Interaction of electrons and positrons with molecular systems of biological interest

Memoria de tesis presentada por

Ana García Sanz

Para optar al Grado de Doctor por la

Facultad de Ciencias,
Universidad Autónoma de Madrid

Director:
Gustavo García Gómez-Tejedor

Trabajo realizado en el

Instituto de Física Fundamental,
Consejo Superior de Investigaciones Científicas

Madrid, Marzo de 2014

Abstract

The aim of this thesis is to study electron and positron interactions with biologically relevant molecules. The study starts with a theoretical investigation on electron collisions with the non-polar targets anthracene and pyrazine and the polar molecules hydrogen-cyanide and pyrimidine, in the gas-phase. Integral and differential electron-molecule cross sections over a broad energy range, typically from 0.1 eV up to 10 keV, are derived using either the R-matrix method or a single-centre expansion-symmetry adapted approach at low energies (below ~10 eV), and a screening corrected form of the independent atom model at higher energies. After a critical comparison with the available experimental sources, theoretical self-consistent electron collisional data sets are recommended for the aforementioned molecules. Furthermore, this combined approach has been adapted to study positron-molecule collisions. In particular, positron scattering cross sections by pyrimidine are for the first time reported.

The calculated interaction parameters find their main practical application in energy deposition models. Accordingly, this thesis also presents a study of electron and positron transport in water in the liquid state using a custom-programmed molecular-level Monte Carlo code, the Low-Energy Particle Track Simulation. Particular emphasis is given to the low-energy processes which are known to be determinant in radiation damage.

In addition, a milestone in the radiation damage field is the investigation of how the fundamental mechanisms of damage are affected and modified under conditions closer to cell. Within this context, an experimental work has been carried out to investigate damage to DNA induced by X-rays and low-energy electrons (LEEs) under standard ambient temperature and pressure (SATP). In particular, thin films of the nucleoside thymidine have been irradiated under dry nitrogen and oxygen. Afterwards, a more complex target, plasmid DNA, has been irradiated under different humidity levels up to solvation. These measurements indicate a much higher efficiency for LEEs relative to X-rays in causing DNA damage under both a hydrated and aerobic environment. This way, this work aims to shed a light on the indirect effects of LEEs. Finally, based on this experimental work, a new experimental apparatus has been designed and constructed which will permit in the future to validate energy deposition models in the condensed phase.

Agradecimientos

En primer lugar, quisiera agradecer a mi director de tesis Gustavo García su tutela durante estos años dedicados a la realización de la presente tesis. Quisiera hacer extensiva mi gratitud a mi compañera de laboratorio Martina Fuss, por su ayuda durante este tiempo.

También quiero expresar mi más sincera gratitud a los profesores Franco Gianturco, Jimena Gorfinkiel y Leon Sanche, por haberme dado la oportunidad de completar mi formación en sus respectivos laboratorios y por la dedicación que mostraron mientras estuve allí. También quiero dar las gracias a todos los miembros de sus equipos, ya que todos contribuyeron a que me sintiera como en casa. Especialmente quiero dar las gracias a Francesco Sebastianelli, Fabio Carelli, Zdenek Masin, Mohammad Rezzaee y Saloua Sahbani, por su ayuda dentro y fuera del laboratorio.

A Amalia Williart, Antonio Muñoz y Diogo Almeida por la ayuda técnica en diferentes ocasiones. También quisiera dar las gracias a Michael Brunger y una vez más a Jimena Gorfinkiel por su asistencia a la hora de revisar los aspectos lingüísticos de los artículos científicos. A mi tutor académico, Luis Méndez, por su ayuda en los procesos burocráticos. Hago extensiva mi gratitud a Raúl Guantes, responsable del programa de Doctorado de Biofísica, a las administraciones del departamento de química y del Instituto Nicolás Cabrera de la Universidad Autónoma de Madrid. A Luis Llorente, por su ayuda en numerosas ocasiones durante los trámites administrativos.

Finalmente, quiero expresar mi más sentido agradecimiento a mis padres, mi tía Pilar y mi hermano Carlos. Muchas gracias por vuestro apoyo incondicional durante estos años. A Álvaro, no hay palabras suficientes para expresar toda mi gratitud. Gracias por la comprensión, ánimo y apoyo que me has brindado este tiempo. A mis amigos, ya que sin duda han hecho estos años más fáciles. Aunque no puedo incluirlos a todos, quisiera nombrar especialmente a Inma, Marina, Elia, Elena, Gema, Virginia, Marta, Rose, Marta Larraona, María, Jon, Julián y Le Bao Chau que en diferentes ocasiones me han acompañado, y animado en momentos de crisis. Por último quisiera dedicar este trabajo a mis abuelos, especialmente a mi abuelo Pablo Sanz. Tu recuerdo siempre me ha animado a seguir. Estés donde estés, gracias.

Contents

1. Introduction **1**

1. Introducción **7**

2. Calculation Methods **13**

2.1. Electron Interactions 13

2.2. Positron Interactions 15

2.3. The Low Energy Region: The SA-SCE and R-Matrix Methods 17

2.3.1. Symmetry Adapted-Single Centre Expansion (SA-SCE) Method . 18

2.3.2. The R-matrix Method 22

2.3.2.1. Adaptation for Positron Physics 26

2.3.3. Resonances Characterization 28

2.3.4. Scattering with Polar Molecules 30

2.4. The High Energy Region: The IAM-SCAR Method 31

2.4.1. Atomic Cross Sections 31

2.4.2. Adaptation to Positron Physics 33

2.4.3. Molecular Cross Sections 35

2.4.4. Scattering with Polar Molecules 37

3. Theoretical Results **43**

3.1. Non-Polar Molecules 44

3.1.1. Anthracene 44

3.1.2. Pyrazine 59

3.2. Polar Molecules 66

3.2.1. Hydrogen Cyanide 67

3.2.2. Pyrimidine 82

3.2.2.1. Electron Scattering from Pyrimidine 83

3.2.2.2. Positron Scattering from Pyrimidine 96

3.3. Summary 108

4. Simulation **119**

4.1. Input Data Requirements 120

4.1.1. Electron Collision Input 122

4.1.2. Positron Collision Input 123

4.2. The Monte-Carlo code 124

4.3. Single Electron and Positron Track Simulation Examples 126

4.4. Summary 130

5. Experimental Methods and Results **133**

5.1. Measurements under UHV Conditions: the Direct Effect 135

5.1.1. Experimental Methods and Materials 136

5.1.2. Results 139

5.2. The Effect of Oxygen Level on Radiation-induced Damage. 142

5.2.1. Experimental Methods and Materials 143

5.2.2. Results and Discussion 150

5.2.2.1. Direct Damage 155

5.2.2.2. Indirect Damage 157

5.2.2.3. Base Release 159

5.2.2.4. Oxidative Base Modifications: 5-FordUrd and 5-HMdUrd 162

5.2.2.5. Oxygen-free Base Modifications: 5,6-dihydrothymidine 164

5.3. The Effect of Hydration Level on Radiation-induced Damage 165

5.3.1. Experimental Methods and Materials 166

5.3.2. Results and Discussion 170

5.3.2.1. Direct Damage 173

5.3.2.2. Indirect Damage 174

5.4. Summary 177

6. Newly Designed Experimental System **185**

6.1. Design and Technical Characteristics 186

6.1.1. UHV Collision Chamber 186

6.1.2. Sample-holder 187

6.1.3. Electron Gun 189

6.1.4. Silicon Detector 190

6.1.5. Hemispherical Electrostatic Analyser 191

6.1.6. Time of Flight 194

6.2. Preliminary Experimental Tests 194
6.3. Summary 197

7. Conclusions **199**

7. Conclusiones **205**

List of Figures **211**

List of Tables **217**

List of Publications **219**

Chapter 1

Introduction

The study of electron and positron interactions with biological matter, and the subsequent damage induced in the media, has attracted a significant amount of scientific interest in recent years, in particular within the molecular physics and biomedical science communities. This is because the key role that these particles play in numerous biomedical applications, for both diagnostic and therapeutic purposes.

Positrons, the antiparticles of electrons, constitute the basis of widely used imaging technologies, such as positron emission tomography (PET) and new therapeutic treatments as positherapy. On the other hand, electrons are always present in any radiation-based technique (e.g. radiotherapy, ion-therapy, brachytherapy, etc).[1] Nowadays, it is well accepted that secondary electrons (SE) are abundantly generated along the primary radiation tracks (~4×10^4 per MeV of energy transferred to the medium)[2] and they are considered as the main source of energy deposition and radiation damage in biological tissue. Apart from ionization processes, which are traditionally related to radiation damage, sub-ionization and even sub-excitation electrons, so-called low-energy electrons (LEEs), can also induce molecular fragmentation via dissociative electron attachment (DEA) or internal excitation, as has been extensively discussed in the literature.[3-545]Within the complex environment of living cells, the scattering processes mentioned above can directly involve DNA building-blocks (i.e., nucleobases, the sugar or the phosphate groups), or other nearby cellular components, such as water or oxygen, producing reactive species which can subsequently damage the DNA components.[6] This results in two

different damage mechanisms, i.e., direct or indirect, respectively. Both types of damage can cause a variety of structural alterations, such as single- and double- strand breaks (SSBs and DSBs), base release or chemical modifications of the DNA components,[7] which can subsequently lead to cell mutation and death.

Due to the great number of processes involved, the damage mechanisms initiated by radiation in the complex DNA molecule (see Figure 1.1) are very difficult to elucidate, and therefore should be tackled in progressive steps. Studies with basic DNA components (for instance, the nucleobases), and model molecules (e.g. pyrimidine, pyrazine, etc.) provide a good insight into the molecular mechanisms leading to DNA damage. This, in turn, helps to correlate the macroscopic effects of radiation with the damage induced at the molecular level.[8]

In an attempt to develop more efficient radiation-based technologies, a deeper understanding is required, at the molecular level, of the fundamental processes underpinning electron and positron interactions with the molecules that form the media. Primarily, it is essential to quantify the relevance of all the accessible scattering processes, in terms of interaction probabilities (cross sections). Such quantification should be conducted over a very broad energy range: from the high energies of the primary radiation down to thermalisation energies. From a fundamental perspective, cross sections are important parameters in their own right. They also constitute the main input data for Monte Carlo simulation methods, which are a very useful tool for modelling the complex sequences of radiation-induced processes.[9] Despite considerable experimental and theoretical work have been carried out to determining electron scattering cross sections, they are incomplete for most molecules of biological interest and often restricted to a limited energy domain, either at low[10] or high energies.[11] This situation is even worse in the case of positron scattering; due to additional difficulties in both theoretical and experimental methods, studies conducted up to now on positron-molecule collisions are very scarce, and consequently e^+-scattering data is only available for few molecules (e.g., water, tetrahydrofuran).[12,13] Within this context, bigger efforts are required for obtaining cross sections for electron and positron collisions over a wide energy range. In this sense, theoretical quantum scattering models are actually an effective tool to derive cross sections, since they provide information on energies and angles which are outside of the scope of the experiments.

Single radiation particle interactions studies are a good starting point and provide valuable information on the basic interaction mechanisms. However, practical biomedical problems require an understanding of how these fundamental mechanisms are affected and modified when the target molecule is embedded in real cellular conditions, i.e., in the condensed-phase and surrounded by other cellular components.[8] As mentioned above, the environment plays a significant role because radiobiological effects are not only caused by the direct impact of

radiation on the target molecule but also through the reactive species produced within the surrounding molecules. Although it has been predicted that indirect effects contribute significantly (about 50-70%) to the overall damage,[6] its underlying molecular mechanisms remain vaguely understood, in particular those governed by LEEs.[7] Consequently, indirect effects are, at present, difficult to introduce into track structure simulations.

Previous studies by our research group were mainly focused on the intermediate and high-energy domains (from ~30 eV up to 10 keV) and, therefore, needed to include tools to analyse the low-energy effects of radiation. This situation prompted the present theoretical and experimental study. It initially concentrates on the calculation of the probabilities of positron and electron interactions with biologically relevant molecules, over a broad energy range. Secondly, it contributes to the development of energy deposition models for electron and positron interactions by combining appropriate input parameters with available Monte Carlo codes. Finally, an experimental investigation into the radiation-induced damage of DNA samples has been carried in a cell-like environment (i.e., a hydrated and aerobic atmosphere). Such experiments have motivated the development of a new experimental setup, specially designed to validate radiation interaction models in the condensed-phase. The specific objectives of this study are listed below:

- To incorporate low-energy electron *ab-initio* scattering calculations into high-energy optical-potential models in order to establish a combined procedure both for non-polar and polar targets capable of generating scattering data over a broad energy range (0-10000 eV).

- To extend this procedure to the study of positron collisions with biomolecules.

- To incorporating low-energy electron and positron effects into Monte Carlo radiation interaction models in order to simulate single electron and positron tracks in biologically relevant media.

- To evaluate the damage induced in irradiated DNA targets by ionizing radiation and LEEs under controlled environmental conditions (pressure, temperature, oxygen and hydration levels).

- To design and construct a portable experimental apparatus to irradiate (with photons, electrons or ions) biological samples in the condensed phase under controlled temperature conditions for the purposes of validating radiation interaction models.

These objectives have been accomplished progressively, as described in the different chapters of this thesis. The content of each chapter can be briefly summarized as follows:

Chapter 2 is dedicated to the description of the quantum scattering methods employed in this work to treat electron/positron-molecule collisions, namely, the symmetry-adapted single-centre expansion (SA-SCE) method and the R-matrix approach for low incident energies (0 - 20 eV), as well as a corrected form of the independent atom model (IAM-SCAR) for intermediate and high energies (1 - 10000 eV).

Chapter 3 describes the calculations and results for electron collisions with the non-polar molecules anthracene and pyrazine, and the polar compounds hydrogen cyanide and pyrimidine. The calculated integral and differential scattering cross sections for these four molecules are presented and discussed. After comparing them with the available experimental and theoretical data, complete sets of integral scattering cross sections are provided from very low energies (~0.1 eV) up to 10 keV. In the case of anthracene and hydrogen cyanide, we also identified and characterized the low-lying resonances. In addition, integral and differential cross sections are computed for positron scattering from pyrimidine by means of the R-matrix procedure and the IAM-SCAR method, using various models to represent the polarization effects.

Chapter 4 presents a simulation procedure for modelling low-energy electron and positron trajectories in biological media. After describing the characteristics of the Low Energy Particle Track Simulation (LEPTS) Monte Carlo code and the sources of the input parameters, we report an application example of electron and positron tracks in liquid water with initial energies of 15 keV.

Chapter 5 reports experimental results on the damaging effects induced by ionizing radiation and LEEs on biomolecular targets subjected to different environmental conditions. We first present a qualitative comparison between damage yields induced directly by fast electrons (10 keV) and by LEEs to a DNA representative sub-unit (thymidine) under vacuum conditions. Subsequently, the simultaneous damage induced by soft X-rays (1.5 keV) and low-energy electrons (0-30 eV) in thin films of thymidine, within pure, dry N_2 and O_2 environments at standard ambient temperature and pressure (SATP) conditions, has been investigated. Additionally, we report on the effect that DNA hydration level has on damage yields induced by soft X-rays and LEEs in thin films of plasmid DNA irradiated at atmospheric pressure with different relative humidity (RH) levels.

Chapter 6 reports the design and construction of a portable and highly-versatile experimental apparatus to irradiate biomolecules in the condensed phase with different primary radiation beams (electrons, photons or ions). The system consists of an ultra-high vacuum chamber, a temperature controlled sample-holder to condense molecular vapours onto metal substrates and a complete system for spectrometric analysis of the primary beam and secondary particles.

Finally, the present work is summarized in the conclusions (Chapter 7), together with some suggestions for future works.

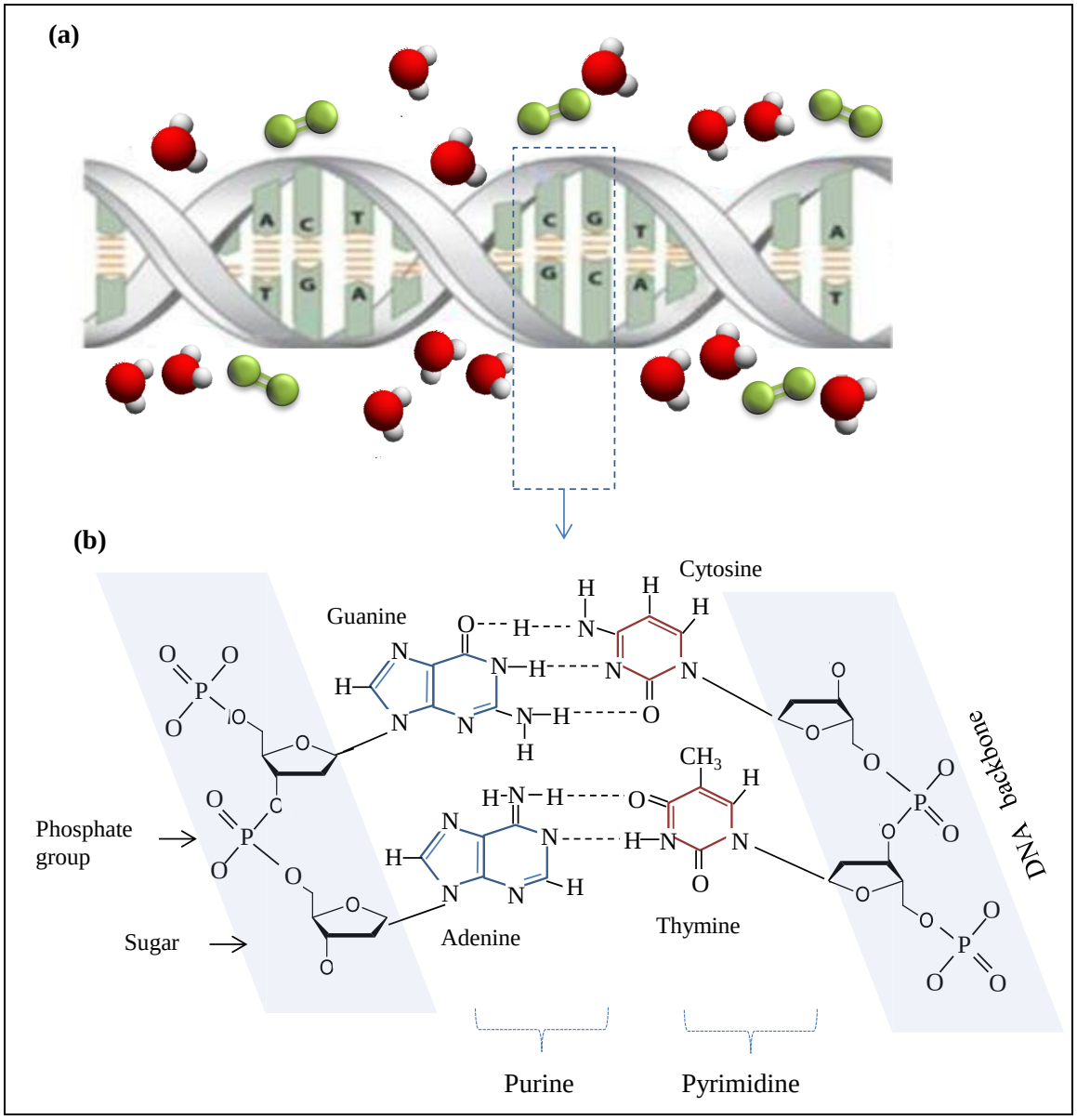

Figure 1.1: (a) Schematic picture of cellular DNA and the local molecular environment (e.g. H_2O and O_2 molecules). (b) Schematic chemical structure of a short double-stranded segment of DNA.

Bibliography

[1] I. Baccarelli, I. Bald, F.A. Gianturco, E. Illenberger and J. Kopyra, *Phys. Rep.* **508**, 1 (2011).

[2] S. M. Pimblott and J. A. LaVerne, *Radiat. Phys. Chem.* **76**, 1244 (2007).

[3] B. Boudaïffa, P. Cloutier, D. Hunting, M. A. Huels and L. Sanche, *Science* **287**, 1658 (2000).

[4] F. Martin, P.D. Burrow, Z. Cai, P. Cloutier, D. Hunting and L. Sanche, *Phys. Rev. Lett*. **93**, 068101 (2004).

[5] H. Abdoul-Carime, S. Gohlke, E. Fischbach, J. Scheike and E. Illenberger, *Chem.Phys. Lett*. **387**, 267 (2004).

[6] C. von Sonntag. *Free-Radical-Induced DNA Damage and its Repair, A Chemical Perspective* (Springer-Verlag, Berlin Heidelberg, 2006).

[7] E. Alizadeh, P. Cloutier, D. Hunting and L. Sanche, *J. Phys. Chem. B* **115**, 4523 (2011).

[8] E. Alizadeh and L. Sanche, *Chem. Rev.* **112**, 5578 (2012).

[9] (a) A. Muñoz, J.M. Pérez, G. García and F. Blanco, *Nucl. Instrum. Meth. A* **536**, 176 (2005); (b) A. Roldán, J. M. Pérez, F. Blanco, A. Williart and G. García, *J. Appl. Phys.* **95**, 5865 (2004).

[10] (a) A. Faure, J.D. Gorfinkiel, and J. Tennyson, *J. Phys. B: At. Mol. Opt. Phys*. **37** 801 (2004). (b) F.A. Gianturco and R.R. Lucchese, *J. Chem. Phys.* **114**, 3429 (2001). (c) M. Rezaee, P. Cloutier, A.D. Bass, M. Michaud, D.J. Hunting, and L. Sanche, *Phys. Rev. E* **86**, 031913 (2012).

[11] (a) A. Faure, J.D. Gorfinkiel, and J. Tennyson, *J. Phys. B: At. Mol. Opt. Phys*. **37** 801 (2004). (b) F.A. Gianturco and R.R. Lucchese, *J. Chem. Phys.* **114**, 3429 (2001). (c) M. Rezaee, P. Cloutier, A.D. Bass, M. Michaud, D.J. Hunting, and L. Sanche, *Phys. Rev. E* **86**, 031913 (2012).

[12] F. Blanco and G. García, *J. Phys. B: At. Mol. Opt. Phys.* **42**, 145203 (2009).

[13] (a) C. Makochekanwa, A. Banković, W. Tattersall, A. Jones, P. Caradonna, D.S. Slaughter, K. Nixon, M.J. Brunger, Z. Petrović, J.P. Sullivan and S.J. Buckman, *New J. Phys*. **11**, 103036 (2009). (b) R. Zhang, A. Faure and J. Tennyson, *Phys. Scr*. **80**, 015301 (2009).

[14] L. Chiari, E. Anderson, W. Tattersall, J.R. Machacek, P. Palihawadana, C. Makochekanwa, J. P. Sullivan, G. García, F. Blanco, R.P. McEachran, M.J. Brunger and S.J. Buckman, *J. Chem. Phys*. **138**, 074301 (2013).

Capítulo 1

Introducción

El estudio de las interacciones de electrones y positrones con materiales de interés biológico, junto con el daño que inducen en los mismos, ha suscitado en los últimos años un gran interés dentro de la comunidad científica, en particular dentro del campo de la radiobiología y la biomedicina, ya que ambas partículas juegan un papel importante en numerosas aplicaciones biomédicas, tanto para terapia como para diagnóstico.

Por un lado, las interacciones de positrones, la antipartícula del electrón, constituyen la base de técnicas de diagnóstico por imagen como la tomografía de emisión por positrones (PET), ampliamente extendida hoy en día para el diagnóstico precoz de tumores, o de nuevas técnicas de tratamiento, como la positerapia. Por otro lado, los electrones están siempre presentes en todas las aplicaciones basadas en el uso de radiaciones ionizantes (radioterapia, hadronterapia, braquiterapia, etc).[1] Hoy es un hecho conocido que una gran cantidad de electrones secundarios son generados a lo largo del haz primario (~4×10^4 de electrones son generados por MeV de energía transferida en procesos primarios)[2]; éstos constituyen la principal fuente del depósito de energía y, por tanto, del daño inducido por radiación. Además de los procesos de ionización, los cuales han sido relacionados tradicionalmente con el daño inducido por radiación, electrones con energías por debajo del límite de ionización (es decir, los llamados electrones de baja energía; LEEs) son también capaces de inducir rupturas moleculares mediante disociación resonante por captura electrónica (DEA), tal y como se ha demostrado extensamente en los últimos años.[3-545]Dentro del complejo ambiente celular, estos procesos pueden tener lugar

directamente con moléculas constituyentes del ADN (daño directo) u otros componentes celulares que lo rodeen, como agua u oxígeno. Esto último genera multitud de radicales e iones que podrían, posteriormente, reaccionar con las subunidades del ADN (daño indirecto).[6] Cualquiera de estas dos vías puede producir lesiones genotóxicas, como roturas de hebra simple (SSB) o doble (DSB).[7]

Debido a la gran cantidad de procesos involucrados, resulta muy difícil esclarecer los mecanismos responsables del daño inducido por radiación en la compleja molécula de ADN (ver Figura 1.1 en página 5). Se hace conveniente, por lo tanto, estructurar su estudio en etapas progresivas. Estudios con biocomponentes básicos (por ejemplo, las nucleobases), y moléculas modelo (v.g. pirimidina, pirazina, etc.) proporcionan una buena idea de los mecanismos moleculares que inducen daño en ADN. Esto, a su vez, ayuda a correlacionar los efectos macroscópicos de la radiación con el daño inducido a nivel molecular.[8]

Con el objetivo de mejorar las tecnologías y dispositivos relacionados con la radiación, resulta evidente que es esencial alcanzar un conocimiento profundo sobre los mecanismos de interacción de electrones y positrones con las moléculas constituyentes del medio. En primer lugar, es imprescindible cuantificar la relevancia de los diferentes procesos de interacción que pueden tener lugar en términos de probabilidad de interacción (secciones eficaces). Dicha cuantificación debe hacerse sobre un amplio rango de energías: desde energías de termalización hasta las energías de la radiación primaria. Estos parámetros de interacción no son importantes únicamente desde un punto de vista fundamental, sino que además constituyen el principal dato de entrada de los modelos de transporte y depósito de energía. De hecho, la precisión de estos datos determinará la fiabilidad de los modelos. Sin embargo, debido a las dificultades que presenta tanto su medición como su cálculo, los datos de secciones eficaces disponibles en la literatura son insuficientes para la mayoría de biomoléculas y, generalmente, están restringidas a un rango de energías limitado (bajas[10] o altas[11] energías). Esta situación es, si cabe, más dramática en el caso de positrones, ya que sólo existen datos de dispersión de positrones con algunas pocas biomoléculas (v.g. agua, tetrahidrofurano).[12,13] Debido a esta situación, es necesario un mayor esfuerzo por parte de la comunidad científica para obtener secciones eficaces de dispersión de electrones y positrones en un rango amplio de energías. Conviene destacar que el uso de modelos de cálculo de cara a la obtención de secciones eficaces resulta una herramienta muy útil, ya que permite el acceso a energías y ángulos, donde los experimentos no son capaces de llegar.

Estos estudios con moléculas aisladas son indispensables ya que proporcionan información sobre las interacciones básicas y constituyen, por tanto, los pilares sobre los que se asientan estudios más complejos. Sin embargo, con el objetivo de incorporar estos conocimientos a

aplicaciones biomédicas, es necesario investigar cómo estos mecanismos fundamentales son modificados cuando las moléculas bajo estudio se encuentran en un ambiente más cercano al celular, es decir, en estado condensado y rodeadas por otras moléculas.[8] Como se ha mencionado anteriormente, la presencia de otros componentes celulares influye significativamente en los efectos de la radiación. En particular, se estima que el daño indirecto supone alrededor de un 60-70% del total. Sin embargo sus mecanismos son todavía parcialmente desconocidos, en particular aquellos gobernados por los electrones de baja energía (LEEs),[7] dificultando su inclusión en los modelos de depósito de energía.

Trabajos anteriores realizados por nuestro grupo de investigación estaban enmarcados principalmente en el rango de energías altas e intermedias (desde 10 eV hasta 10 keV). Por lo tanto, se requiere incorporar herramientas para incluir el rango de bajas energías. Esta situación ha dado lugar a la presente tesis, la cual pretende contribuir al conocimiento actualmente existente de las interacciones de electrones y positrones de varias maneras, desde el punto de vista tanto experimental como teórico. En primer lugar, mediante el cálculo de probabilidades de interacción de electrones y positrones con moléculas de interés biológico cubriendo un amplio rango de energías. Seguidamente, generando modelos de depósito de energía para electrones y positrones mediante la introducción de los datos apropiados en un código de Monte Carlo previamente programado. Finalmente, mediante un estudio experimental del daño inducido por radiación en condiciones cercanas a las encontradas en la célula; en particular, en un ambiente aeróbico e hidratado. Estos experimentos han motivado la construcción de un nuevo dispositivo experimental, diseñado especialmente para validar modelos de depósito de energía en fase condensada. A continuación se enumeran los objetivos específicos de esta tesis:

- Incorporar cálculos *ab-initio* de colisión de electrones de baja energía a otro modelo de potencial óptico válido para altas energías, con el objetivo de establecer un procedimiento combinado que permita generar secciones eficaces en un amplio rango de energías (0.1-10000 eV) para moléculas polares y no polares.

- Extensión del procedimiento anterior para el cálculo de colisiones de positrones con biomoléculas.

- Incorporar los efectos de electrones y positrones de baja energía en un modelo de interacción de Monte Carlo apropiado para la simulación de trayectorias individuales en medio biológico.

- Evaluar el daño inducido en muestras de ADN por radiación ionizante y LEEs bajo condiciones ambientales controladas (oxígenación, hidratación, presión y temperatura).

- Diseño y construcción de una nueva cámara de colisión transportable para la irradiación (con fotones, electrones e iones) de muestras biomoleculares en fase gaseosa o condensada a temperatura controlada, para validar modelos de interacción.

Estos objetivos se han realizado progresivamente, como se describe en los diferentes capítulos de la presente tesis. A continuación, se especifica brevemente el contenido de cada uno de los mismos:

A lo largo del capítulo 2 se describen los modelos cuánticos que se han empleado para tratar las colisiones electrón(positrón)-molécula. En concreto, el modelo de expansión de potencial central para la dispersión por moléculas (SA-SCE) y el método R-matrix para energías incidentes bajas (0-20 eV); así como la forma corregida del modelo de átomos independientes (IAM-SCAR) para energías de impacto intermedias y altas.

El capítulo 3 expone los resultados obtenidos a raíz del estudio de la dispersión de electrones con las moléculas no polares antraceno y pirazina, y las moléculas polares ácido cianhídrico y pirimidina. Las secciones eficaces integrales y diferenciales de dispersión son presentadas y comparadas con otros datos experimentales y teóricos para proporcionar tablas consistentes de datos de dispersión cubriendo un amplio rango de energías (0.1 eV -10000 eV). En paralelo, se presentan datos relativos a secciones eficaces de dispersión de positrones con el blanco molecular pirimidina.

En el Capítulo 4 presentamos una simulación para modelar las trayectorias de electrones y positrones de baja energía. Después de describir las características del código de Monte Carlo LEPTS (del inglés 'Low Energy Particle Track Simulation') y detallar las fuentes de los parámetros de entrada utilizados, se presenta como ejemplo la simulación de las trayectorias individuales de positrones y electrones con energías iniciales de 15 keV hasta su termalización en agua.

En el capítulo 5 se presenta un estudio experimental del daño inducido por radiación ionizante y LEEs en muestras de ADN condensadas en una superficie bajo diferentes condiciones ambientales. Se ha investigado el daño inducido simultáneamente por rayos X (1.5 keV) y electrones de baja energía (0-30 eV) en muestras de ADN, en condiciones de temperatura y presión estándar (es decir, sin aplicar vacío). Durante la irradiación, las muestras han estado sumergidas primeramente en una atmósfera de oxígeno y nitrógeno. En segundo

término, han sido irradiadas bajo diferentes niveles de humedad relativa (RH), en concreto 0, 20, 50, 80 y 100 %RH.

En el capítulo 6 se presenta un nuevo sistema experimental móvil construido para la irradiación con diferentes haces primarios (electrones, fotones o iones) de muestras biomoleculares en fase condensada. Este sistema consta de una cámara de ultra-alto vacío, un porta-muestras con control de temperatura que permite la condensación de moléculas biológicas en superficies inertes y un sistema espectrométrico completo.

Finalmente, se presenta un resumen del presente trabajo en las conclusiones (capítulo 7), junto con algunas sugerencias de cara a futuras investigaciones.

Bibliografía

[1] I. Baccarelli, I. Bald, F.A. Gianturco, E. Illenberger and J. Kopyra, *Phys. Rep.* **508**, 1 (2011).

[2] S.M. Pimblott and J.A. LaVerne, *Radiat. Phys. Chem.* **76**, 1244 (2007).

[3] B. Boudaïffa, P. Cloutier, D. Hunting, M.A. Huels and L. Sanche, *Science* **287**, 1658 (2000).

[4] F. Martin, P.D. Burrow, Z. Cai, P. Cloutier, D. Hunting and L. Sanche, *Phys. Rev. Lett*. **93**, 068101 (2004).

[5] H. Abdoul-Carime, S. Gohlke, E. Fischbach, J. Scheike and E. Illenberger, *Chem.Phys. Lett*. **387**, 267 (2004).

[6] C. von Sonntag. *Free-Radical-Induced DNA Damage and its Repair, A Chemical Perspective* (Springer-Verlag, Berlin Heidelberg, 2006).

[7] E. Alizadeh, P. Cloutier, D. Hunting and L. Sanche, *J. Phys. Chem. B* **115**, 4523 (2011).

[8] E. Alizadeh and L. Sanche, *Chem. Rev.* **112**, 5578 (2012).

[9] (a) A. Muñoz, J.M. Pérez, G. García and F. Blanco, *Nucl. Instrum. Meth. A* **536**, 176 (2005); (b) A. Roldán, J. M. Pérez, F. Blanco, A. Williart and G. García, *J. Appl. Phys.* **95**, 5865 (2004).

[10] (a) A. Faure, J.D. Gorfinkiel, and J. Tennyson, *J. Phys. B: At. Mol. Opt. Phys*. **37** 801 (2004). (b) F.A. Gianturco and R.R. Lucchese, *J. Chem. Phys.* **114**, 3429 (2001). (c) M. Rezaee, P. Cloutier, A.D. Bass, M. Michaud, D.J. Hunting, and L. Sanche, *Phys. Rev. E* **86**, 031913 (2012).

[11] (a) A. Faure, J.D. Gorfinkiel, and J. Tennyson, *J. Phys. B: At. Mol. Opt. Phys*. **37** 801 (2004). (b) F.A. Gianturco and R.R. Lucchese, *J. Chem. Phys.* **114**, 3429 (2001). (c) M. Rezaee, P. Cloutier, A.D. Bass, M. Michaud, D.J. Hunting, and L. Sanche, *Phys. Rev. E* **86**, 031913 (2012).

[12] F. Blanco and G. García, *J. Phys. B: At. Mol. Opt. Phys.* **42**, 145203 (2009).

[13] (a) C. Makochekanwa, A. Banković, W. Tattersall, A. Jones, P. Caradonna, D.S. Slaughter, K. Nixon, M.J. Brunger, Z. Petrović, J.P. Sullivan and S.J. Buckman, *New J. Phys*. **11**, 103036 (2009). (b) R. Zhang, A. Faure and J. Tennyson, *Phys. Scr*. **80**, 015301 (2009).

[14] L. Chiari, E. Anderson, W. Tattersall, J.R. Machacek, P. Palihawadana, C. Makochekanwa, J. P. Sullivan, G. García, F. Blanco, R.P. McEachran, M.J. Brunger and S.J. Buckman, *J. Chem. Phys*. **138**, 074301 (2013).

Chapter 2

Calculation Methods

When considering electron and positron interactions with multi-electron systems, there are many possible outgoing channels. In this chapter, we provide a brief review of the different scattering processes driven by electron and positron collisions. This is followed by a detailed description of the quantum scattering methods employed in this work to obtain scattering observables, namely, the symmetry-adapted single-centre expansion (SA-SCE) method[1,2] and the R-matrix procedure at low energies,[3] together with the IAM-SCAR model[4,5] within the high-energy regime. Adaptation of the R-matrix method and IAM-SCAR model to treat positron-molecule collisions is also discussed. In addition, at low energies special attention is paid to the description of the resonances, which are known to play a very important role in the damage mechanisms induced in biologically relevant molecules. Finally, given that most of the biologically relevant molecules have a strong permanent moment, we also describe the procedure for treating electron/positron scattering from polar target molecules.

2.1. Electron Interactions

When an electron interacts with a target molecule, there is a variety of energy-dependent scattering events that can take place. These processes can be categorized as follows:

1. Elastic Scattering

When an electron suffers elastic scattering no energy is transferred to the internal degrees of freedom of the molecule, therefore the molecule's electronic and nuclear states (rotational and vibrational state) remain unaltered after the collision. However, the scattered electron may be deflected from its original direction.

$$e^- + MN \rightarrow e^- + MN. \quad (2.1)$$

2. Inelastic Scattering

During inelastic scattering, the impinging electron transfers part of its energy to the target molecule´s internal degrees of freedom.

- ***Rotational excitation***

  The collision of a charged projectile induces changes in the rotational state of the molecule. This scattering process is particularly significant in the case of polar target molecules, since strong dipole-induced rotational excitations are generated,

$$e^- + MN(j) \rightarrow e^- + MN(j`). \quad (2.2)$$

- ***Vibrational excitation***

  The interaction changes the vibrational state of the molecule,

$$e^- + MN(v) \rightarrow e^- + MN(v`). \quad (2.3)$$

- ***Electronic excitation***

  After the collision, the target molecule is left in an electronically excited state. In other words, one bound electron promotes to a higher available state.

$$e^- + MN \rightarrow e^- + MN^*. \quad (2.4)$$

- ***Ionization***

  In this case, the scattering electron has enough energy to extract a bound electron from the target,

$$e^- + MN \rightarrow MN^+ + 2e^-. \quad (2.5)$$

  Ionization is the dominant scattering process whenever the incident energy is above the ionization threshold. Ionization events are intimately linked to biological radiation damage, being the main mechanism which generates low-energy electrons.

Some of these scattering processes may lead to dissociation. Additionally, fragmentation can occur through a resonant process, as explained below:

- ***Nonresonant electron-impact dissociation***

Vibrationally and electronically excited molecules may dissociate to produce neutral or ionized atoms,

$$e^- + MN \begin{array}{l} \nearrow M + N + e^- \\ \searrow M^+ + N^- + e^- \end{array} . \qquad (2.6)$$

In addition, after ionization, if the molecular ions are formed in a dissociative state, they can proceed to dissociative reactions, for instance:

$$e^- + MN \rightarrow N^+ + M + 2e^- . \qquad (2.7)$$

- ***Dissociative electron attachment (DEA).***

This is a resonant process that can be represented by,

$$e^- + MN \rightarrow MN^{-*} \rightarrow M + N^- . \qquad (2.8)$$

MN^{-*} is a transitory negative ion (TNI) generated by resonant electron capture and which may dissociate into a neutral radical and a negatively charged fragment. This process is very sensitive to the energy and lifetime of the TNI and is only prone to occur within specific, narrow kinetic energy ranges.

DEA reactions are very important in the study of molecular-level radiation damage,[6] as they not only cause molecular bond fragmentation but also because the radicals produced may initiate other reactions with nearby molecules, inducing further chemical damage.[7]

2.2. Positron Interactions

Positrons (e^+) are the antiparticles of the electrons, i.e., they have the same mass ($m = 9.1 \times 10^{-31}$ kg) and spin ($s = 1/2$) as electrons, but their electric charge is positive rather than negative ($q=+1.6 \times 10^{-19}$ C). The positron was first theoretically predicted by Dirac,[8] and experimentally observed some years later by Anderson.[9]

Despite the common physical properties of electrons and positrons, positron-molecule interactions are very different from electron-molecule interactions due to the opposite charge of the projectiles. The most significant difference is the fact that the incident positron is distinguishable from the target molecule electrons. Thus, electron-electron exchange effects, which are present in electron-molecule collisions, do not occur in positron interactions. Furthermore, in contrast to electrons, the positron is attracted by the target electrons and

repelled by the molecular nuclei. This means that the static interaction between the positron and the target is repulsive, whereas for electrons it is attractive. Regarding polarization effects, they normally present a quadratic dependence on the applied fields, being independent, therefore, of the projectile charge sign. Hence, the total cross section for a given positron-molecule interaction is typically smaller than the corresponding electron interaction at low energies.

Similarly to electrons, a positron in matter may undergo numerous scattering events. With the exception of DEA, the scattering processes described above for electron scattering are also possibilities for positron scattering. Regarding electronic excitation, one should consider that because positrons do not couple target states with different spin symmetries, then only singlet excited electronic states can be reached from a target with a singlet ground state, whereas for electron scattering both singlet and triplet target states could be excited. Additionally, positrons can ionize molecules via three different processes: via direct ionization (equivalent to expression 2.5), or through two new processes which are missing for e^-- scattering, i.e., positronium formation and positron annihilation.[10]

- ***Positronium formation***

Positronium (Ps) is a quasi-stable bound state formed by an electron and a positron.[11] The threshold for positronium formation is placed at 6.8 eV below the ionization threshold:

$$E_{Ps} = E_{ion} - 6.8\ eV. \tag{2.9}$$

Above this threshold, the incident positron can capture an electron from the target molecule to form positronium. The system is unstable and so finally the two particles annihilate to produce gamma rays, with a lifetime of 125 ps for the singlet state (para-Ps) and 142 ns for the triple state (ortho-Ps),

$$e^+ + MN \rightarrow MN^+ + Ps \rightarrow MN^+ + \gamma_{rays}\ . \tag{2.10}$$

The Ps formation rate increases with the energy reaching a maximum and then decaying up to around 100-200 eV. It is quite difficult to incorporate this channel within computational models and relatively little work has been conducted in this area.

- ***Direct annihilation***

Direct positron annihilation with an electron of the target can also occur, which is predominantly 2γ decay,

$$e^+ + MN \rightarrow MN^+ + \gamma_{rays}. \tag{2.11}$$

The probability of this channel occurring is much lower than indirect annihilation via positronium formation[12] and therefore this channel is typically neglected.

2.3. The Low Energy Region: The SA-SCE and R-Matrix methods

The collisional process for the projectile-molecule system is described in terms of the usual time-independent Schrödinger equation,

$$\mathcal{H}\Psi = \mathrm{E}\Psi, \tag{2.12}$$

where Ψ is the total scattering wavefunction of the process, E is the total energy of the system and $\mathcal{H}$ is the non-relativistic Hamiltonian for the projectile-molecule system. In atomic units the Hamiltonian $\mathcal{H}$ has the following form:

$$\mathcal{H}(\boldsymbol{r_{N+1}}, \boldsymbol{r}, \boldsymbol{R}) = \hat{T}_e\,(\boldsymbol{r_{N+1}}) + \hat{V}_{int}(\boldsymbol{r_{N+1}}, \boldsymbol{r}, \boldsymbol{R}) + \hat{H}_N(\boldsymbol{r}, \boldsymbol{R}) \tag{2.13}$$

where $\boldsymbol{r_{N+1}}$ represents the position of the colliding charged particle, $\boldsymbol{r}$ stands for the target electrons coordinates $\mathbf{r_i}$ (i=1,…,N_e) and **R** corresponds to the nuclear coordinates $\mathbf{R_A}$ (A=1,…,N_N) of the molecule. $\hat{T}_e$ is the kinetic energy operator of the incoming particle, $\hat{V}_{int}$ describes the interaction between the incident particle and the target electrons and nuclei with Z_A charge,

$$V_{int}(\boldsymbol{r_{N+1}}, \boldsymbol{r}, \boldsymbol{R}) = q\left(\sum_{A=1}^{N_N} \frac{Z_A}{|\boldsymbol{r_{N+1}} - \boldsymbol{R}_A|} - \sum_{i=1}^{N_e} \frac{1}{|\boldsymbol{r_{N+1}} - \mathbf{r}_i|}\right), \tag{2.14}$$

where the variable q represents the charge of the incident particle (i.e., q=+1 and q= -1 for positrons and electrons, respectively).

Finally, $\hat{H}_N$ is the Hamiltonian of the target, which can be written as,

$$\hat{H}_N(\boldsymbol{r}, \boldsymbol{R}) = -\frac{1}{2}\sum_{i=1}^{N_e} \nabla_i^2 - \frac{1}{2M_A}\sum_{A=1}^{N_N} \nabla_A^2 - \sum_{i=1}^{N_e}\sum_{A=1}^{N_N} \frac{Z_A}{|\boldsymbol{r}_i - \boldsymbol{R}_A|} + \sum_{i=1}^{N_e}\sum_{j>i}^{N_e} \frac{1}{|\boldsymbol{r}_i - \boldsymbol{r}_j|} + \sum_{A=1}^{N_N}\sum_{B>A}^{N_N} \frac{Z_A Z_B}{|\boldsymbol{R}_A - \boldsymbol{R}_B|}, \tag{2.15}$$

where the first and second terms describes the kinetic energy of the N_e-target electrons and the N_N-nuclei, respectively. The third term accounts for the attractive Coulombic interaction between the electrons and the nuclei. The fourth and fifth terms represent the repulsive electron-electron and nuclei-nuclei interaction, respectively.

In this work we use the Oppenheimer (BO) approximation[13,14] to decouple the electronic and the nuclear motion. This allows us to considerably simplify the problem. The BO approximation exploits the great difference in masses of electrons and nuclei ($m_e << m_N$). Because of this

difference, electrons of the molecule can almost respond instantaneously to the movement of the nuclei. Thus, to a good approximation, sufficient for the purposes of this work, we regard the target electrons as moving in the static field created by the fixed nuclei.

We further assume that the target nuclei remain at a frozen geometry during the whole scattering process. This approximation, known as the fixed nuclei approximation (FNA), is valid whenever the incident electron is fast enough to undergo fast collisions, that is, the duration of the collision is shorter than the timescale for the molecular vibrations ($\tau_v \sim 10^{-14}$ s) or rotations ($\tau_r > 10^{-11}$ s).[15] Under these conditions, only the electronic Hamiltonian for the projectile-molecule system needs to be taken into account, which depends parametrically on the nuclear coordinates.[16] The Schrödinger equation and Hamiltonian are rewritten within the fixed-nuclei approximation as,

$$\widehat{H}_{N+1}(\boldsymbol{r_{N+1}}, \boldsymbol{r}|\boldsymbol{R})\, \Psi_{\varepsilon}^{FN}\, (\boldsymbol{r_{N+1}}, \boldsymbol{r}|\boldsymbol{R}) = \mathrm{E}\Psi_{\varepsilon}^{FN}\, (\boldsymbol{r_{N+1}}, \boldsymbol{r}|\boldsymbol{R})\,, \tag{2.16}$$

$$\widehat{H}_{N+1}(\boldsymbol{r_{N+1}}, \boldsymbol{r}|\boldsymbol{R}) = \hat{T}_e\, (\boldsymbol{r_{N+1}}) + \widehat{H}_N^e(\boldsymbol{r}|\boldsymbol{R}) + \widehat{V}_{int}(\boldsymbol{r_{N+1}}, \boldsymbol{r}|\boldsymbol{R}). \tag{2.17}$$

Now $\boldsymbol{R}$ represents the frozen nuclei coordinates and the target Hamiltonian ($\widehat{H}_N^e(\boldsymbol{r}|\boldsymbol{R})$) contains only the electronic terms (i.e., the first, third and fourth term from expression (2.15)).

Both the SA-SCE method[1,2] and R-matrix[3] procedure use the FN approximation. However, the basic interactions between the incident particle and the target nuclei/electrons are represented differently by each method. The single-centre expansion SA-SCE method describes the collision in terms of effective one-particle interaction potentials and, in the case of an incident electron, the exchange interaction is taken into account using a model potential (with local character for the calculations presented in this work). In contrast, the R-matrix theory is an all-electron method which accounts for the exchange interaction exactly using anti-symmetric wavefunctions. In this method the correlation and polarization effects are described by the multi-configurational close-coupling expansion of the total wavefunction.

2.3.1. Symmetry Adapted-Single Centre Expansion (SA-SCE) Method

The SA-SCE procedure was implemented by the groups of Gianturco and Lucchese in the beginning of the 90's in the code known as "ePOLYSCAT".[1,2] This method is based on a single-centre expansion of the scattering wavefunctions around the centre of mass of the projectile-molecule system, what simplifies considerably the quantum scattering equation.[17,18] Since then, this code has been successfully applied to model low-energy electron and positron interaction with numerous polyatomic molecules of biological interest in the gas phase.[19-23] In this work, it has been employed to yield electron-molecule scattering observables.

Accordingly, any arbitrary three-dimensional function describing a given electron, either a bound or the scattered electron, is expanded around a single-centre in a set of symmetry-adapted angular functions $X_{hl}^{p\mu}(\theta,\phi)$:

$$F(\boldsymbol{r_{N+1}}) = \sum_{p\mu} F^{p\mu}(\boldsymbol{r_{N+1}}) = \frac{1}{r}\sum_{hl} F_{hl}^{p\mu}(r_{N+1}) X_{hl}^{p\mu}(\theta,\phi), \tag{2.18}$$

where μ is a component of the *p*th irreducible representation of the point group to which, at the nuclear geometry $\boldsymbol{R}$, the molecule belongs. The index h labels a specific basis function, for a given partial wave l.[24] The radial functions $F_{hl}^{p\mu}(r_{N+1})$ are represented on a numerical grid and the angular functions $\mathrm{X}_{\mathrm{hl}}^{\mathrm{p\mu}}(\theta,\phi)$ are given by the proper linear combination of spherical harmonics $\mathrm{Y_{lm}}(\theta,\phi)$:

$$X_{hl}^{p\mu}(\theta,\phi) = \sum_{m=-l}^{m=+l} b_{hlm}^{p\mu} Y_l^m(\theta,\phi). \tag{2.19}$$

The coefficients $b_{hlm}^{p\mu}$ can be obtained from the character tables for each irreducible representation of the relevant molecular point group.[25]

In a general way, by denoting with $\phi_\alpha^{\mathrm{e}}(\boldsymbol{r}|\boldsymbol{R})$ one generic eigenstate of the target Hamiltonian which fulfils,

$$\widehat{H}_N^e(\boldsymbol{r}|\boldsymbol{R})\phi_\alpha^{\mathrm{e}}(\boldsymbol{r}|\boldsymbol{R}) = \epsilon_\alpha \phi_\alpha^{\mathrm{e}}(\boldsymbol{r}|\boldsymbol{R}), \tag{2.20}$$

where ϵ_α is the electronic eigenvalue for the asymptotic target state α, the many electron problem we are trying to solve can be reduced to a set of coupled one-particle equations if the total $(N+1)$ wavefunction $\Psi(\boldsymbol{r_{N+1}},\boldsymbol{r}|\boldsymbol{R})$ is expanded in terms of these target eigenstates ϕ_α^{e},

$$\Psi(\boldsymbol{r_{N+1}},\boldsymbol{r}|\boldsymbol{R}) = \sum_\alpha \boldsymbol{\mathcal{A}}\{F_\alpha(\boldsymbol{r_{N+1}})\phi_\alpha^{\mathrm{e}}(\boldsymbol{r}|\boldsymbol{R})\}, \tag{2.21}$$

where $\boldsymbol{\mathcal{A}}$ is the antisymmetrization operator, which must be included to fulfil the Pauli exclusion principle when the incident particle is an electron, and $F_\alpha(\boldsymbol{r_{N+1}})$ is the continuum electron wavefunction.

The resulting quantum scattering equations provide us with a way of evaluating the unknown radial coefficients $F_{hl}^{p\mu}$ for the *(N+1)*th continuum electron scattered off the *N*-electron target, which takes the following form:

$$\left[\frac{d^2}{dr_{N+1}^2} - \frac{l(l+1)}{r_{N+1}^2} + 2(\mathrm{E} - \epsilon_\alpha)\right] F_{lh}^{p\mu,\alpha}(\boldsymbol{r_{N+1}}|\boldsymbol{R}) = 2 \sum_{l'h'p'\mu'\alpha'} \int dr' V_{lh,l'h'}^{p\mu\alpha,p'\mu'\alpha'}(\boldsymbol{r_{N+1}}, \boldsymbol{r'}|\boldsymbol{R}) F_{l'h'}^{p'\mu,'\alpha'}(\boldsymbol{r'}|\boldsymbol{R}), \quad (2.22)$$

where E is the collision energy $E = k^2/2$ and the $(\mathrm{p}, \mu, \alpha)$ indices now label the symmetry and the corresponding target state of the continuum wave function.

An additional simple approximation can be now applied to further ease the implementation of the scattering equations: we assume that the target electronic wave function is given by a single-determinant of Hartree-Fock (HF) orbitals of the neutral ground state target. This assumption corresponds to truncating the expansion in Eq. (2.21) over the α target states to only one state (α=1), what leads to the static-exchange (SE) representation of the electron–molecule interaction. The scattering equation (2.22) becomes

$$\left[\frac{d^2}{dr^2} - \frac{l(l+1)}{r^2} + 2(\mathrm{E} - \epsilon)\right] F_{lh}^{p\mu}(\boldsymbol{r}|\boldsymbol{R}) = 2 \sum_{l'h'p'\mu'} \int dr' V_{lh,l'h'}^{p\mu,p'\mu'}(\boldsymbol{r}, \boldsymbol{r'}|\boldsymbol{R}) F_{l'h'}^{p'\mu'}(\boldsymbol{r'}|\boldsymbol{R}). \quad (2.23)$$

The kernel of the integral operator $\hat{V}$ is formed by a set of diagonal (local potential) and non-diagonal (nonlocal potential) terms that in principle fully describe the electron–molecule interaction during the collision. The latter terms are introduced by the nonlocal exchange potential and are difficult to deal with. For the present calculations, the exchange contribution is modelled by a local energy-dependent potential known as the Free-Electron-Gas-Exchange (FEGE) potential,[26,20] proposed by Hara[27] long ago. This potential is known to give fairly good results compare to the exact nonlocal exchange potential,[28,29] whereas being significantly less computational demanding.

The major limitation of the SE model is that the electronic charge of the molecule is not permitted to be altered by the incident electron. This means that neither the correlation nor the polarization effects acting at short and at large electron-target distances, respectively,[30] are taken into account. As mentioned before, within this model, the dynamical response of the target's bound electrons to the impinging electron is included through the addition of a local, energy-independent potential V^{CP}:

$$V^{CP}(\boldsymbol{r_{N+1}}) = \begin{cases} V^{corr}(\boldsymbol{r_{N+1}}), & \boldsymbol{r_{N+1}} \leq r_{match} \\ V^{pol}(\boldsymbol{r_{N+1}}), & \boldsymbol{r_{N+1}} > r_{match.} \end{cases}. \quad (2.24)$$

The V_{CP} model potential contains a short-range correlation contribution V_{corr} which is smoothly connected to the long-range polarization contribution V_{pol} at a certain matching point r_{match}. In this approach, V_{corr} is modelled by a local interaction in the form given by Lee-Yang-Parr[31], obtained by defining an average dynamical correlation energy of a single electron within the formalism of the Kohn and Sham variational scheme. The functional derivative of such a quantity with respect to the N-electron density of the target molecule provides a density functional description of the required short-range correlation term. On the other hand, the long-range part of V_{CP} depends analytically on the static electrical properties of the molecules (i.e., dipole and higher moments and polarizibilities (α)), according to the expression: [32]

$$V^{pol}(\boldsymbol{r_{N+1}}|\boldsymbol{R}) = \lim_{r\to\infty}\left(-\sum_{k=1}\frac{\alpha_k(\boldsymbol{R})}{2{r_{N+1}}^{2k+2}}\right). \tag{2.25}$$

This last step provides the so-called static-model-exchange-correlation-polarization (SMECP) approximation for the scattering event, where the overall interaction is described by the sum of three local terms, namely, the static, exchange and the correlation-polarization potentials, i.e., $V = V^{ST} + V^{FEGE} + V^{CP}$. This local description allows to rewrite the scattering radial equations (2.23) in a simplified form:

$$\left[\frac{d^2}{dr_{N+1}^2} - \frac{l(l+1)}{r_{N+1}^2} + 2(\mathrm{E} - \epsilon)\right] F_{lh}^{p\mu}(r_{N+1}|\boldsymbol{R}) = 2\sum_{l'h'} V_{lh,l'h'}^{p\mu}(r_{N+1}|\boldsymbol{R}) F_{l'h'}^{p\mu}(r_{N+1}|\boldsymbol{R}), \tag{2.26}$$

where the potential coupling elements are given by,

$$\begin{aligned} V_{lh,l'h'}^{p\mu}(r_{N+1}|\boldsymbol{R}) &= \langle X_{hl}^{p\mu}(\theta,\phi)|V(r_{N+1}|\boldsymbol{R})|X_{h'l'}^{p\mu}(\theta,\phi)\rangle \\ &= \int d\hat{r} X_{hl}^{p\mu}(\theta,\phi)\, V(r_{N+1}|\boldsymbol{R}) X_{h'l'}^{p\mu}(\theta,\phi). \end{aligned} \tag{2.27}$$

Finally, the numerical solutions of the coupled equations (2.26), obtained by means of the standard Green's function technique,[32] shall produce the required K-matrix, (and consequently both the T and S matrices elements) from which the integral and differential elastic cross will be derived at a specific collision energy.

From the above description, it is clear that the main drawback of the SA-SCE method is that neither electronic excitations nor ionization events are considered in the calculations. On the other hand, the relatively simple implementation of this approach makes it suitable to treat large polyatomic molecules.

2.3.2. The R-matrix Method

The R-matrix theory was initially established to treat problems of nuclear physics.[33] Afterward, this method was adapted to treat electron scattering from atoms[34-36] and molecular systems.[37,38] In this thesis we employed the UK R-matrix package,[39,40] which is an open-code available for diatomic[36] and polyatomic target molecules.[41] Up to now these codes have been widely used to calculate electron scattering for a number of species, charged and neutral.[42-46] Description of the UK R-matrix model given here is based on those works and some others.[47] Recently, the package was extended to treat also positron-molecule scattering.[48,22] Firstly, we provide details of this procedure when the projectile is an electron. Afterwards, modifications required to treat e^+-molecule collisions are specified (see section 2.3.2.1).

The R-matrix method is based on dividing the coordinate space of the particle-molecule collision problem into an inner and outer region separated by a sphere of radius r=a, which is centred at the centre of mass of the molecule. An indispensable condition is that the sphere is sufficiently large to enclose the electronic density of the target states included in the calculation. Typically, the sphere has radius of 10-15 a_o depending on the target molecule. The main advantage of this division is that the interaction between the incident charged particle and the target can be treated differently in each region. We start solving the more complex inner region scattering problem by diagonalizing the full Hamiltonian for the N+1 system. In this region, the scattering particle is positioned within the molecular electronic cloud, so the short range correlation and exchange effects between the scattering particle and the N-bound electrons become important. The inner region wavefunction is expressed in terms of the R-matrix basis functions ψ_k written in the close-coupling (CC) form:[49]

$$\psi_k = \mathcal{A} \sum_{i,j} a_{ijk} \Phi_i^{\mathrm{N}}(x_1 \dots x_N) u_{ij}(x_{N+1}) + \sum_i b_{ik} \chi_i^{\mathrm{N+1}}(x_1 \dots x_{N+1}), \qquad (2.28)$$

where k represents the kth eigenvector of the *N+1* Hamiltonian in the inner region, x_i represents the spatial and spin coordinates of the ith electron, $\Phi_{\mathrm{i}}^{\mathrm{N}}$ is the wavefunction representing the ith target state, u_{ij} are the continuum orbitals describing the scattering electron. The selection of the symmetry of the continuum orbitals depends on the symmetry of the target states, since the two must couple together to give the correct overall spatial and spin symmetry of the inner wavefunction ψ_k. $\mathcal{A}$ is the anti-symmetrization operator that assures that the Pauli exclusion principle is obeyed and finally, a_{ijk} and b_{ik} are variational coefficients.

The first term in (2.28) runs over the electronic target states coupled with the continuum orbitals. It represents a situation where one electron exists in the continuum (i.e. is unbound), whereas the remaining N electrons stay in the target state ('target+continuum' configurations).

Since the molecular and the continuum orbitals are orthogonal, some important regions of the configuration space could be omitted. To compensate for this effect additional configurations are included in (2.28): the χ_i configurations in which all electrons are placed in target molecular orbitals (L^2- functions). The inclusion of this term is crucial for the representation of the short-range polarization and correlation effects not included in the truncated close-coupling expansion. Note that the wavefunctions (2.28) do not depend on the kinetic energy of the scattering electron and are therefore calculated only once, a feature that provides a substantial advantage over other *ab-initio* methods in terms of computational requirements.

The target wavefunctions $\Phi_{\mathrm{i}}^{\mathrm{N}}$ are represented on the level of the configuration interaction (CI) method. The configurations included in the expansion are generated as anti-symmetrized products (Slater determinants) of molecular orbitals (MOs). One should note that the same set of orbitals must be used for all electronic states. How many and what sort of configurations depends mainly on the system studied. In our R-matrix calculations, we choose a CAS-CI (complete active space configuration interaction: all excitations are performed among a set of orbitals, the active space, and a set of (active) electrons is chosen for which all spin and symmetry restricted excitations are generated.[50] This model has been found to produce a good balance between the target N-particle and the (N+1) particle scattering calculations.[50] Choosing an appropriate size for the active space is important since it determines the quality of the target representation.[47] However, as the number of active orbitals increases, so does the number of configurations, making the computations more demanding. Hence, in practice the size of the active space is restricted by computation limitations.[47a]

In the polyatomic UK *R*-matrix suite both the molecular and the continuum orbitals are expanded in terms of Gaussian-type orbitals (GTOs).[50] The basis functions for the MOs are centred on each nuclei and are adapted from standard quantum chemistry basis sets. In contrast, the 'continuum' GTOs are centred at the centre of mass of the system and generated using the code GTOBAS.[51] In contrast with the target molecular orbitals, they do not vanish on the R-matrix boundary.

The coefficients a_{ijk} and b_{ik} in equation (2.28), are obtained diagonalizing the inner region Hamiltonian,

$$\langle\psi_k|(H_{N+1} + L)|\psi_{k'}\rangle = \delta_{kk'}E_k, \tag{2.29}$$

where L is the Bloch operator that must be included to keep the operator hermitian.[52] In this way, we obtain the inner region eigenfunctions (ψ_k) and their associated eigenvalues, E_k. The next step is to construct the R-matrix which links the inner with the outer region. We can built the R-matrix at the boundary using the inner information (ψ_k and E_k) as,

$$R_{ij}(a,E) = \frac{1}{2a}\sum_{k}\frac{w_{ik}(a)w_{jk}(a)}{E_k - E}, \tag{2.30}$$

where $w_{ik}(a)$ are the amplitudes of the inner wavefunctions evaluated at the boundary r=a, which are defined for the channel i through the following projection, $w_{ik} = \langle \Phi_i^N Y_{l_i m_i} | \psi_k \rangle$. Hence, the energy dependent R-matrix is built from the energy-independent solutions of the inner region. This entity provides the boundary condition at r=a which allows us to obtain the radial wavefunctions, $F_i(r)$, of the scattering particle in the outer region:

$$F_i(a) = \sum_j R_{ij}(a,E)\left(r\frac{dF_j}{dr}\right)_{r=a}. \tag{2.31}$$

Then, the R-matrix is propagated[53] from the boundary up to a large enough radius so that the outer region solutions can be matched to asymptotic solutions.

In the outer region (r > a) the scattering particle is completely separated from the target and therefore the scattering equations have a much simpler form. At large distances both the correlation and exchange forces are negligible and the scattering is dominated by a long-range multipole interaction. A single-centre expansion of the projectile-molecule interaction can be used and the full scattering wavefunction can be written in the form:[54]

$$\Psi = \sum_i \Phi_{\mathrm{i}}^{\mathrm{N}}(\boldsymbol{x}_1 \ldots \boldsymbol{x}_N) Y_{l_i m_i}(\theta,\phi)\frac{F_i(r_{N+1})}{r_{N+1}}, \tag{2.32}$$

where F_i are the reduced radial wavefunctions that represents the scattering electron. Subsequently, a set of n-coupled differential equations for the radial functions $F_i(r)$ are generated by substituting the outer region wavefunction (2.32) in the Schrödinger equation:[34]

$$\left(\frac{d^2}{dr^2} - \frac{l_i(l_i+1)}{r^2} + k_i^2\right)F_i(r) = \sum_j V_{ij}(r)\,F_j(r), \tag{2.33}$$

where the channel energies are $k_i^2 = 2(E - E_i)$, E is the scattering energy and E_i is the energy of the target state associated with the channel i. V_{ij} are potentials obtained from the multipole expansion of the projectile-molecule,

$$V_{ij}(r) = \sum_{\lambda=0}^{\lambda_M} \alpha_{ij}^{\lambda}\, r^{-\lambda-1}, \quad r \geq a \tag{2.34}$$

where the coefficients[36] α_{ij}^{λ}, depend on the target permanent and transition moments $Q_{ij}^{(\lambda)}$, which normally only includes dipoles ($\lambda = 1$), quadrupoles ($\lambda = 2$), and for charged targets the Coulomb potential given by $\lambda = 0$.[39]

Solving equation (2.33) yields n_i (number of open channels) linearly independent solutions whose asymptotic form is,[55,†]

$$F_{ij} \sim \frac{1}{\sqrt{k_i}} \left(sin\left(k_i r - \frac{1}{2} l_i \pi\right) \delta_{ij} + \cos\left(k_i r - \frac{1}{2} l_i \pi\right) K_{ij} \right), \tag{2.35}$$

where K_{ij} are the elements of the K-matrix, which is real, symmetric and, as mentioned before, contains all the scattering information. Additionally, the eigenphase sum, which can be used for the detection and parametrization of resonances as we will see below, can be obtained from the diagonalized K-matrix K_{ii}^D, according to the expression:

$$\delta = \sum_i \arctan\left(K_{ii}^D\right) . \tag{2.36}$$

The collision problem can be described at different levels, depending on the level at which the electron correlation/polarization is described in the calculation. The standard scattering models can be categorized as follows:[56]

(i) The *Static-Exchange model (SE)* is the simplest approximation that has been employed. Exchange between the incident electron and the target electrons is included using the anti-symmetric form of each configuration entering (2.28). In this model the target molecule is described at the Hartree-Fock level including only the ground state of the molecule in the close-coupling expansion. However, at this level the target molecule is not allowed to be distorted in response of the incoming projectile and remains unaltered throughout the collision event. This is reflected in the choice of the L^2 configurations, which take the simple form:

$$X_i^{SE} = (\text{ground state})^N (\text{virtual})^1. \tag{2.37}$$

This means that the N electrons of the target molecule occupy the ground state configuration (HF) orbitals, whereas the incident electron can only occupy one of a selected number of virtual orbitals. Hence, the SE model cannot treat electron impact excitations, and neither can be used to detect Feschbach resonances. Although shape resonances can be described with this model, they usually appear too high in energy due to an incomplete modelling of the correlation/polarization effects.

(ii) At the *Static Exchange plus Polarization (SEP) level*, still the target wavefunction is described on the HF level, but now the molecule is allowed to be polarized by the incoming charged particle. Hence, in addition to the L^2 configurations described before (2.37), we include

† This form is only valid for neutral targets (Z=0)

configurations where one electron from the valence space of the target is promoted to one of a selected number of virtual orbitals (i.e. orbitals that are not occupied in the ground state configuration), which are also available for the incident e^-, that is,

$$X_i^{SEP} = (\text{core})^{N_C}(\text{valence})^{N-N_C-1}(\text{virtual})^{1+1}, \tag{2.38}$$

where N_C are the core electrons which doubly occupy the core orbitals. Although the SEP approximation is capable of describing elastic collisions only, it provides an adequate description of the low-lying shape resonances.

(iii) The most sophisticated model we use is the *Close-Coupling (CC) approximation*. At this level, in addition to the ground state of the target, a number of target electronic excited states are included. We also include L^2 configurations in which the scattering electron occupies either one of the orbitals in the active space or a virtual orbital. Although this procedure is computationally more expensive, it provides a more complete treatment of the low-energy scattering process. For instance, it allows us to calculate electronically inelastic cross sections. In addition, Feschbach resonances can be detected and modelled if the excited "parent" state is included in the close-coupling expansion.

2.3.2.1. Adaptation for Positron Physics

The molecular R-matrix theory was first adapted to positron scattering by Tennyson[57,58] for diatomic targets. More recently, Baluja *et al.*[48] and Franz *et al.*[22] extended the R-matrix code to treat polyatomic targets for energies below the positronium (Ps) formation. A few targets have been studied since then including the calculations reported here for pyrimidine.[59]

In contrast to the electron-molecule case, the exchange interaction between the incoming positron and the target molecule's electrons does not occur. This is reflected in the form of the inner wavefunction, where the $\mathcal{A}$ operator disappears,

$$\psi_k = \sum_{i,j} a_{ijk}\Phi_i^N(x_1 \dots x_N)\tilde{u}_{ij}(x_p) + \sum_i b_{ik}\chi_i{}^N(x_1 \dots x_N)\tilde{\chi}_i{}^1(x_p), \tag{2.39}$$

where now $\tilde{u}_{ij}$ are the continuum orbitals describing the scattering positron built also from GTOs orbitals. As in the electron scattering case, a_{ijk} and b_{ik} are variational coefficients and Φ_i^N are the target wavefunctions. The main difference from (2.28) comes from the second summation, since the L^2 functions are now built as products of two functions: $\tilde{\chi}_i$ denotes a square-integrable spin-orbital occupied by the positron, while χ_i is a N-electron function. At this point, it is important to highlight that in the calculations reported in Section 3.2.2.2 we use an orbital set common to both the electrons and the positron. Due to the absence of the

exchange, the incoming positron can occupy any of the target molecular orbitals, either the virtual orbitals (i.e. unoccupied) or those already doubly occupied by electrons. In analogy to the SE and SEP models for electron-molecule scattering, we define the Static (S) and the Static-Polarization (SP) models for positron-molecule collisions in the following way:

$$X_i^S = (\text{Ground state})^N(\text{Ground state} + \text{virtual})^1. \tag{2.40}$$

$$X_i^{SP} = (\text{core})^N(\text{core})^{N-N_c-1}(\text{virtual})^1(\text{Ground state} + \text{virtual})^1. \tag{2.41}$$

Since the incoming positron can occupy also the orbitals already occupied by the electrons, the scattering models for positrons lead to a larger number of configurations than the equivalent electron-molecule models and, consequently, the positronic calculations are more computationally demanding. In addition, although exchange effects vanish within the inner region, the strong attraction between the scattered positron and target electrons results in great difficulty in accurately modelling the correlation effects. Hence, building the inner wavefunction for positron-molecule collisions is more difficult. On the other hand, the formulation of the scattering potential in the outer region is similar to the electron-molecule case once adjusted for the opposite charge the positron.[47c]

Although the R-matrix method has proved to be a powerful method,[39,45] it is not free of drawbacks. For instance, no ionized states of the target were considered, as this would have required the inclusion of pseudostates[60] and would have therefore increased drastically the computational requirements, leading to unaffordable calculations for the target molecules treated here. Consequently, one should take into account that cross sections calculated in this work for energies above the ionization threshold are less accurate than those calculated at lower energies. Additionally, SEP (SP) calculations suffer from the presence of a large number of non-physical pseudoresonances that blurs the cross section curves in the higher energy range. These artefacts are typical of SEP (SP) calculations which use a multi-configuration description for the N+1 wavefunction. Finally, the requirement that the R-matrix sphere must contain the whole target electronic density implies that the R-matrix method is restricted to medium-sized biomolecules. On the other hand, the clear advantage of the R-matrix method is that the complex inner region problem needs to be solved only once since the inner equations are energy-independent, whereas the simpler outer region problem can be solved easily for different energy domains.

2.3.3. Characterization of Resonances

Generally the eigenphase sum $\delta(E)$, and consequently the cross sections, vary smoothly with the energy of the incident particle. However, in the presence of a resonance, $\delta(E)$ shows a

dramatic rise at certain kinetic energy E_R over an energy interval Γ. This behaviour is reflected in the corresponding cross sections, which vary strongly around the resonant energy E_R. A resonance can be described as a long lived metastable state of the system, where the incident electron remains partially bound to the target for a time much longer than that actually needed to traverse the area occupied by the molecule itself. During that time, the scattering electron occupies one of the empty molecular orbital, leading to the formation of a transient negative ion (TNI). The lifetime (τ) of this process, which is typically in the range $\tau \sim 10^{-10}$ - 10^{-15} s, is related to the width (Γ) of the resonant state through the time-energy uncertainty principle, $\Delta t \Delta E \geq \hbar/2$. Being $\Delta t \sim \tau$ and $\Delta E \sim \Gamma$, it follows that:

$$\tau \cong \frac{\hbar}{\Gamma}, \tag{2.42}$$

which means that narrow resonances correspond to long-lived resonant states.

The formation of resonance may initiate various molecular processes. For instance, TNIs may decay through ejection of the extra electron (called autodetachment), leaving the target molecule in an electronically/vibrationally/rotationally excited state, or via dissociative electron attachment (see section 2.1).

There are different types of resonances according to the internal excitation of the intermediate ion:

(i) *Shape resonances* occur when the incident electron gets trapped by the "shape" of the effective interaction potential between the incident e^- and the target molecule, which results from the combination of the attractive polarization potential and the repulsive centrifugal potential. The extra electron occupies a low-lying unoccupied orbital in the target molecule, usually the energetically lowest unoccupied orbital (LUMO), without electronic excitation of the target molecule. Shape resonances are typically short-lived so that they appear as broad structures in the scattering cross sections.[61]

(ii) *Core-excited resonances* occur when trapping of the incoming electron proceeds via electronic excitation of the molecule.[62] In particular, a target electron leaves a hole in a normally occupied orbital and occupies a free orbital. Depending on whether they lie either below or above their parent states they can be classified as Feshbach or core-excited shape resonances, respectively.

Resonances are characterised principally by the position where they are placed (E_r), the width (Γ_r), the corresponding lifetime, and their symmetry. Getting precise values for these parameters is a challenging task for theory. Typically, resonances are identified in the calculated eigenphase sum curves since they introduce a rapid π-jump at the energy where the resonance

occurs. The standard procedure of analysis is by fitting the eigenphase sum to the well-known Breit-Wigner form,[63]

$$\delta(E) = \ arctan\ \frac{\Gamma_r/2}{(E_r - E)} + \delta_b(E), \tag{2.43}$$

where $\delta_b(E)$ is the background eigenphase which normally varies slowly with energy.

This is the approach followed in the R-matrix calculations, in which resonances are detected and fitted using the module RESON.[64] Although this method is sometimes limited (for instance, in case of overlapping resonances for which the Breit-Wigner form is not really suitable), for the targets investigated in this thesis with the R-matrix method, namely pyrazine and pyrimidine, RESON is reasonably fast and reliable.

The analysis of the eigenphase sums is not the only method that can be employed for finding resonances in calculated scattering data. In fact, the SA-SCE method employs a different procedure which is based on the idea that the resonances are associated with a long time-delay, according to the Q-matrix formalism proposed by Smith.[65] The time-delay matrix Q can be calculated directly from the scattering matrix S at given energy:

$$Q(E) = i\hbar S\frac{dS^\dagger}{dE}. \tag{2.44}$$

Smith[65] showed that the eigenvalues of the Q-matrix represent the delay time of the scattered particle. For a multichannel scattering process, the trace of the time-delay matrix is associated to the eigenphase sum, i.e., $2\hbar\frac{d\delta_{sum}}{dE} = TrQ(E)$. The derivative of the eigenphase sum is given by a sum of Lorentzian functions, each one associated with a resonance feature characterized in turn by an energy E_r and Γ_r,

$$\frac{d\delta_{sum}(E)}{dE} = \sum_{v=1}^{N}\frac{\Gamma_r/2}{(E - E_r)^2 + \ (\Gamma_r/2)^2} + \frac{d\delta_b(E)}{dE}. \tag{2.45}$$

The advantage of this method is that it allows characterizing closely-spaced resonances. Note, however, that within the SA-SCE approach only shape resonances can be identified.

2.3.4. Scattering with Polar Molecules

The study of interaction of charged particles with polar molecules plays an important role in radiation-induced damage research since many biologically relevant molecules have a strong permanent dipole moment.

However, electron/positron scattering calculations from polar systems are generally more difficult to perform than from non-polar targets. This is because the long-range nature of the dipole potential implies that a large number of partial waves should be included in the wave function expansion. This in turn normally increases significantly the computational requirements. As mentioned before, both the R-matrix approach and the SA-SCE method treats the scattering problem within the Fixed Nuclei Approximation (FNA). Although this approximation gives reliable results for non-polar targets, it is known to fail for molecules with a high permanent dipole moment, leading to divergences in the elastic DCS mainly in the forward direction caused by the lack of convergence in the partial-wave expansion for large *l*. A widespread procedure to avoid these undesirable divergences is based on using the first Born approximation (FBA) for a charged particle in a point-dipole potential,[66] since the contributions from all the partial waves, both individually and as summed quantities, can be calculated analytically within the FBA. A variety of Born 'top-up' procedures have been developed in the past, as described in detailed by Zhang *et al*.[59] Among them we have chosen the frame-transformation method, implemented by Sanna and Gianturco[67] POLYDCS code, which is in turn based on the multipole-extracted adiabatic-nuclei (MEAN) procedure proposed by Norcross and Padial.[66b] Within this approach, after applying a frame transformation scheme from the Body-Fixed to the Space-Fixed frame of reference in order to allow for rotational motion, slow convergence of the partial-wave expansion can be avoided by using the following expression:

$$\frac{d\sigma}{d\Omega} = \frac{d\sigma^B}{d\Omega} + \sum_{l} \left(A_l - A_l^B\right) P_l(\cos\,(\theta)). \qquad (2.46)$$

Note that dσ/dΩ is now obtained for an initial rotational state as a sum over final rotational states. The above expression basically indicates that the contribution to the DCS from low partial waves up to l_{max} is calculated *ab-initio*, in this work either by the UKR-mol or ePOLYSCAT suites, so that short-range effects are considered. In this way, collisions leading to (dipole-forbidden) transitions with $\Delta j \neq 1$, which are known to be dominated by low-partial waves,[68] are also taken into account. On the other hand, contribution from higher partial waves is introduced by calculating the cross sections using the Born approximation and then subtracting the partial cross sections for the low-partial waves already considered ($l < l_{max}$). Hence, the formula given by equation (2.46) can be understood as a short-range correction to the original Born approximation.[67]

Although still an approximate approach, the Born correction implemented in POLYDCS has been shown to produce consistent rotationally summed integral and differential cross sections for various biomolecules of arbitrary geometry.[59,39]

2.4. The High Energy Region: The IAM-SCAR Method

It was customary in the past to use the Born-Bethe theory[69] within the high energy region which considers an asymptotic behaviour of the system. Within this approach, the scattered particle is described as a set of plane waves and it is assumed that during the collision event neither the molecule nor the incident particle is disturbed. However, it has been shown[70,71] that, in the case of electrons, this approximation overestimates the total cross sections, and especially the elastic part, even at 5 keV for simple atoms and molecules. This is also likely to be true for positrons. As a consequence, it is necessary to distinguish two energy regions: (i) above 10 keV where the Born approximation constitutes a simple and accurate tool and (ii) below 10 keV where a more sophisticated approach should be employed between this upper limit and the energies where the low-energy methods previously described start to fail, i.e., above the ionization threshold. The procedure we employ here, developed by Blanco and Garcia,[72,73,4,5] is based on optical potential calculations assuming an independent atom representation of the molecule. Such approximation is valid only when the incident energy is high enough to ensure that the scattering cross sections of the different atoms do not interfere between each other. For energies where it commences to fail (typically below ~100 eV), a simple procedure based on the calculation of the overlap of the atomic cross sections according to their positions in the molecule is introduced. Sequential details on the IAM-SCAR calculation method are given in the next subsections.

2.4.1. Atomic Cross Sections

In contrast to the aforementioned low-energy quantum scattering R-matrix and SA-SCE methods, the present procedure does not consider the molecule as a single target but, instead, substitutes it by its constituent atoms in their corresponding molecular positions by assuming that the molecular binding does not affect the electronic distribution of the atoms. Each atom is supposed, therefore, to scatter independently. This approximation, known as the independent atom model (IAM), introduces considerable simplifications to the calculations since we do not need to solve the complicated molecular scattering equations, but instead the Schrödinger dispersion equations for atoms which are simpler. Thus, the first issue of this calculation is to describe e^-/e^+ interactions with the constituting atoms of the target molecule.[72-74] For this purpose, we represent scattering from atoms by an interacting complex optical:

$$V_{opt}(\mathbf{r}) = V_{\mathbb{R}}(\mathbf{r}) + iV_{abs}(\mathbf{r}), \tag{2.47}$$

whose real part, $V_{\mathbb{R}}(\mathbf{r})$, accounts for the elastic scattering of the incident electrons/positrons, whereas the imaginary part, $V_{abs}(\mathbf{r})$, accounts for the inelastic collisions considered as absorptions from the incident positron beam.

For electron scattering, this optical potential is given for each atom by:

$$V_{opt}(\mathbf{r}) = V_s(\mathbf{r}) + V_{ex}(\mathbf{r}) + V_{pol}(\mathbf{r}) + iV_{abs}(\mathbf{r}), \qquad (2.48)$$

where $V_s(\mathbf{r})$ is the static term derived from a Hartree-Fock calculation of the atomic charge distribution,[75] $V_{ex}(\mathbf{r})$ is the exchange contribution given by the semiclassical energy-dependent formula derived by Riley and Truhlar[76] and $V_{pol}(\mathbf{r})$ represents the target polarization in the form given by Zhang et al.[77]. The absorption potential $V_{abs}(\mathbf{r})$ accounting for the inelastic processes is based on Staszewska´s et al.[78] quasifree model. Within this procedure, inelastic processes are considered as binary collisions between the incident particles and the target electrons. The target properties are introduced through boundary conditions, which are determined by means of the spatial and momentum density distributions of the target particles and by the Pauli's principle which introduces restrictions to the final states permitted after the collision. The resulting absorption potential is local, energy dependent and is a function of the electron density of the target,

$$V_a(r,E) = -\frac{1}{2}\rho(r)u(r,E)\bar{\sigma}(r,E) \qquad (2.49)$$

where $\rho(r)$ is the electron charge density, $u(r,E)$ is the velocity corresponding to the local kinetic energy ($E - V(r)$) and $\bar{\sigma}$ is the effective cross section for an electron traversing that density $\rho(r)$. $\bar{\sigma}$ is calculated from the integration of the binary electron-electron differential cross sections over all the continuum final states (p', k') which are energetically allowed, i.e., $\left(p'^2/2 > k_F^2/2 + \Delta\right)$ and $\left(k'^2/2 > k_F^2/2 + \Delta\right)$. The most controversial part of this potential is the procedure to define the threshold energy Δ to initiate the absorption process. In this case, the Δ parameter is given by the energy gap between the ground state and the first optically allowed state, in concordance with the original framework.[78] However, the initial description of the absorption potential suffered from some inherent limitations.[74] For instance, the differentiated treatment given to the incident particle and the electrons from the target, what is incompatible with the Pauli exclusion principle. Blanco and García[72,73] incorporated the description of the electron's indistinguishability, together with further improvements to the original formulation, such as the inclusion of screening effects and local velocity corrections. These corrections finally led to a model that provides a good approximation for electron–atom scattering over a broad energy range.

For each atom, the corresponding radial scattering equation is numerically integrated, and the resulting complex partial wave phase shifts δ_l are used, to generate the atomic scattering amplitudes $f(\theta)$,

$$f(\theta) = \frac{1}{2ik}\sum_{l=0}^{l_{max}}(2l+1)\left(e^{2i\delta_l}+1\right)P_l(\cos\theta), \tag{2.50}$$

where θ is the scattering angle, k denotes the incident electron's momentum and P_l are the Legendre polynomials. Subsequently, differential ($d\sigma_{el}/d\Omega$) and integral (σ_{el}) elastic cross sections and the total (σ_{tot}) scattering cross sections can be derived from the partial wave expansion and the optical theorem,[79]

$$\frac{d\sigma_{el}}{d\Omega} = |f(\theta)|^2, \tag{2.51}$$

$$\sigma_{el} = \int \frac{d\sigma_{el}}{d\Omega}\, d\Omega = \frac{4\pi}{k^2}\sum_{l=0}^{l_{max}}(2l+1)sin^2\delta_l\ , \tag{2.52}$$

$$\sigma_{tot} = \frac{4\pi}{k^2}Im(f_{\theta=0}), \tag{2.53}$$

where l_{max} has been chosen to assure the convergence of the results within a 1%.

2.4.2. Adaptation to Positron Physics

To calculate positron-atom scattering cross sections, we employed an adapted version of the above optical potential (2.48).[80] In this case, the real part $V_{\mathbb{R}}$ (**r**) consists only of the electrostatic $V_s(r)$ and the polarization $V_{pol}(r)$ terms. The former has been derived following the scheme proposed by Reid and Wadehra[81-83] by performing standard Hartree-Fock calculations of the atomic charge density. The choice of the polarization term becomes relatively more important in this case than for electron scattering, as it is the only attractive contribution to the positron-target interaction to counteract the repulsive nature of the static potential since no exchange term exists. In other words, the computed cross sections are very sensitive to the procedure chosen to model the polarization potential. That is why instead of employing the polarization potential of the form given by Zhang *et al.*[77], usual for electron scattering,[72] we use a new polarization potential based on that proposed by McEachran *et al.*[84] for nobles gases. In particular, we have employed the dipole potential (V_d) and the dipole plus quadrupole polarization (V_{d+p}) potentials for Ne, as described in McEachran *et al.*[84], but scaled by a constant parameter to diffuse the charge density of each target orbital, which in turn reproduces the known dipole (α_d) and quadrupole polarizibility (α_q) of the atomic target in question.[85] It has

been shown that the inclusion of the dipole plus quadrupole polarization potential (V_{d+p}) in the positron-neon calculations provided results in better agreement with the experimental data[86] than if only the dipole polarization term (V_d) was included; this fact has therefore encouraged us to consider the V_{d+p} potential in our study.

Regarding the absorption potential, we follow the scheme developed by Reid and Wadehra[81-83] which is in turn based on the procedure proposed by Staszewska *et al*.[78] for electron scattering. As far as the inelastic cross sections are concerned, the main difference between electron and positron scattering is the positronium formation channel. As mentioned before, the threshold energy (Δ) should be the energy of the first excited level. However, the Ps formation threshold (Δ_p) lies below the first electronic-state excitation energy, where it constitutes the dominant inelastic scattering channel. Since Ps formation cannot be described in terms of a binary collision,[78] it cannot be explicitly introduced into the original formulation of the absorption potential as an independent inelastic event. In an earlier attempt to deal with this problem, Reid and Wadehra[82] proposed to define the threshold absorption parameter as the Ps formation energy, i.e., $\Delta = \Delta_p$. However, it was later shown that the main drawback of this approach is that the total cross sections are overestimated for energies above 100 eV.[80] The solution that we adopt is therefore to define an energy-dependent parameter for the absorption threshold $\Delta(E)$:

$$\Delta(E) = \Delta_e - (\Delta_e - \Delta_p) e^{-\left(\frac{E-\Delta_p}{E_m}\right)}, \tag{2.54}$$

where Δ_e is the lowest excitation energy of the atomic targets, Δ_p is the Ps formation threshold and E_m is a characteristic energy at which the inelastic cross section, without considering the Ps formation, reaches its maximum (generally located at ~20 eV). This expression provides values between the limit conditions: $\Delta(E) = \Delta_p$ for energies close to Ps formation threshold, whereas for higher energies it turns to be $\Delta(E) = \Delta_e$. A smooth transition between both limits is modulated by the negative exponential, which is governed by the E_m parameter.[85]

2.4.3. Molecular Cross Sections

Once the e^--atom or e^+-atom scattering problem has been solved, molecular cross sections are calculated from the atomic data by applying a coherent addition, commonly known as the additivity rule (AR). Within this approximation the molecular scattering amplitude $F(\theta)$ can be derived from the sum of all the relevant atomic amplitudes $f_i(\theta)$, thus leading to the molecular elastic differential cross sections (DCS) for the target in question as follows:

$$F(\theta) = \sum_{atoms} f_i(\theta) e^{iq.r_i}, \tag{2.55}$$

$$\frac{d\sigma_M^{elast}}{d\Omega} = \sum_{i,j} f_i(\theta) f_j^*(\theta) \frac{sin\, qr_{ij}}{qr_{ij}}, \tag{2.56}$$

where q is the momentum transferred in the scattering process, r_i are the atomic positions and r_{ij} is the distance between the i and j atoms. Integral elastic cross sections (CSs) can then be determined by integrating those DCS (2.56). Alternatively, integral cross sections can be also derived from the atomic scattering amplitudes in combination with the optical theorem,[79]

$$\sigma_M^{elast} = \sum_i \sigma_i^{elast}, \tag{2.57}$$

However, an inherent contradiction was initially found between the integral CSs derived from these two procedures what indicated that the optical theorem was being violated.[87] This problem was solved by applying a normalization procedure to the differential cross sections, so that integral cross section derived from the two approaches are now entirely consistent.[87]

This procedure gives reasonable results for energies above 100 eV, as the incident particles are fast enough to effectively "see" the target molecule as a sum of the individual atoms. For lower energies, the atomic cross sections are sufficiently large to overlap, leading to an overestimation of the molecular cross sections.[4] To reduce this limitation, a modified AR approach was developed to account for the low-energy screening effects.[4,5] The method, named SCAR (screening-corrected additivity rule), accounts for the geometry of the target molecule by introducing some screening coefficients (s_i):

$$\sigma_M^{elast} = \sum_i s_i \sigma_i^{elast} \quad and \quad \sigma^{inelast} = \sum_i s_i \sigma_i^{inelast}. \tag{2.58}$$

The screening coefficients are within the range $0 \leq s_i \leq 1$, so that they reduce the contribution of each atom to the total cross section. Calculation of s_i coefficients requires only information on the position and individual cross sections σ_i of each atom in the molecule. They can be calculated in a recurrent way as a sum of N terms, where each $\varepsilon^{(k)}$ arises from the k-atoms overlapping,

$$s_i = \varepsilon_i^{(1)} - \frac{\varepsilon_i^{(2)}}{2!} + \frac{\varepsilon_i^{(3)}}{3!} - \frac{\varepsilon_i^{(4)}}{4!} + \cdots \pm \frac{\varepsilon_i^{(N)}}{N!}\ , \tag{2.59}$$

$$\varepsilon_i^{(1)} = 1, \qquad \varepsilon_i^{(k)} \cong \frac{N-k+1}{N-1} \sum_{j(\neq i)} \frac{\sigma_j \varepsilon_j^{(k-1)}}{\alpha_{ij}} \qquad (k = 2, \dots, N). \tag{2.60}$$

In these expressions N is the number of atoms in the molecule and $\alpha_{ij} = max\,(4\pi r_{ij}^2, \sigma_i, \sigma_j)$, where r_{ij} is, as abovementioned, the distance between atoms i and j.

These screening corrections can be applied similarly to elastic differential cross sections. Instead of the standard form (2.56), now we have:

$$\frac{d\sigma_M^{elast}}{d\Omega} \cong (1 - X_s) \frac{\sigma^{elast} - \sigma_D}{4\pi} + \left[1 + X_S \left(\frac{\sigma^{elast}}{\sigma_D} - 1\right)\right] \frac{d\sigma_D}{d\Omega}, \tag{2.61}$$

where σ_D, $d\sigma_D/d\Omega$, and X_S are defined by:

$$\frac{d\sigma_D}{d\Omega} = \sum_i s_i^2 \frac{d\sigma_i^{elast}}{d\Omega} + \nu \sum_{i \neq j} s_i s_j f_i(\theta) f_i^*(\theta) \frac{sin\, qr_{ij}}{qr_{ij}},$$

$$\sigma_D = \sum_i s_i^2 \sigma_i^{elast},$$

$$X_S \approx \frac{\int_0^{45°} \frac{d\sigma_D}{d\Omega}\, sin\theta\, d\theta}{\int_0^{180°} \frac{d\sigma_D}{d\Omega} sin\theta\, d\theta}, \tag{2.62}$$

where ν is the normalization parameter mentioned above.

The main advantage of this model is the possibility of obtaining cross sections for a wide variety of molecules of any geometry from the data of a reduced number of atoms. This characteristic is particularly valuable in the field of the radiobiology, since biomolecules are constituted essentially by H, N, C and O atoms. Thus, cross sections for electron and positron collisions with these atoms need to be calculated only once. Afterward, scattering cross sections from a great variety of molecules, such as DNA components or proteins, can be generated by changing the geometrical conditions and applying the screening corrections (SCAR), what is fairly inexpensive in computational terms. The target molecules under study in the present work are anthracene, pyrazine, HCN and pyrimidine, whose constituting atoms are C, H and N. The corresponding atomic cross sections have been calculated and discussed before in Blanco and García[73] and references therein. The IAM-SCAR method permits to calculate integral and differential elastic cross sections, inelastic cross sections including electronic-state excitations and ionization events, and the corresponding total cross sections. With the above mentioned corrections, the range of validity of this method is extended down to about 30 eV, with an

estimated accuracy of 10%.[87,89] Note that this calculation is averaged over all the incident angles. Thus, effects depending on the direction of the incident particle are not considered here.

2.4.4. Scattering with Polar Molecules

From the previous description it is clear that both vibrational and rotational excitations are ignored in the IAM-SCAR method. However, in the case of polar molecules the dipole-induced rotational excitations are not negligible and must be included in the scattering calculations. The method we follow in this case, based on the one suggested by Jain,[88] assumes the interaction of a charged particle with a free electric dipole in the framework of the First Born approximation (FBA). Then, the calculated differential and integral rotational excitation cross sections are incorporated to our IAM-SCAR calculation in an incoherent way, i.e. by just adding the results as an independent channel. Although rotational excitation energies are, in general, fairly small (typically a few meV) in comparison with the energy of the incident projectile, the latter energy should be in practice higher than ~20 eV in order for the FBA to be valid. Under these circumstances, differential $\left(d\langle\sigma_j\rangle_T/d\Omega\right)$ and integral $\left(\langle\sigma_j\rangle_T\right)$ rotational excitation cross sections are calculated by weighting the population for the jth rotational quantum level at an operation temperature (T) of 300 K and estimating the average excitation energy $\left(\Delta E_{rot}^{eff}\right)$ from the corresponding rotational constants. A unique transition starting from this j averaged state with Δj=±1 is considered and the resulting cross sections are given by:

$$\frac{d\langle\sigma_j\rangle_T}{d\Omega} = \frac{2\mu^2}{3E}\frac{1}{\left(\Delta E_{rot}^{eff}(T)/2E\right)^2 + 4sin^2\theta/2}, \tag{2.63}$$

$$\langle\sigma_j\rangle_T \approx \frac{4\pi\mu^2}{3E} ln\frac{4E}{\left|\Delta E_{rot}^{eff}(T)\right|}, \tag{2.64}$$

where μ is the permanent dipole moment of the molecule and θ the scattering angle. The complete approach, referred in this work as the IAM-SCARD method, has been shown to be successful when applied to some polar molecules such as water.[89]

However, when the target molecule has a strong permanent dipole moment, as is the case of many biomolecules (e.g. hydrogen cyanide and pyrimidine), it is known that the FBA fails for medium and large scattering angles. In order to partially solve this problem, we have incorporated a correction based on that suggested by Dickinson.[90] Essentially, this procedure introduces a first-order corrective term to the differential cross sections $\left(d\sigma^{Dck}/d\Omega\right)$ for medium and large angles, while maintaining the FBA correction $(d\sigma^{B}/d\Omega)$ for lower angles:

$$\frac{d\sigma^{B}}{d\Omega} \approx \frac{|\mu|^2}{6E_i}\frac{1}{sin^2(\theta/2)} \quad \theta < \theta_c\,, \tag{2.65}$$

$$\frac{d\sigma^{Dck}}{d\Omega} \approx \frac{\pi|\mu|}{64E_i}\frac{1}{sin^3(\theta/2)} \quad \theta < \theta_c\,. \tag{2.66}$$

From these equations is easy to see that the Dickinson correction is equivalent to multiply the Born cross section (2.65) by the factor $f^{Dick} = min\,(1{,}3\pi/32Dsin(\theta/2))$. This correction only affects to molecules with a permanent dipole moment larger than μ=0.75 D, and scattering angles larger than θ_c, i.e., the critical angle where both curves cross each other.

Bibliography

[1] F.A. Gianturco, R.R. Lucchese and N. Sanna, *J. Chem Phys.* **100**, 6464 (1994).

[2] A.P.P.Natalense and R.R.Lucchese, *J. Chem. Phys.* **111**, 5344 (1999).

[3] P.G. Burke, *R-Matrix Theory of Atomic Collisions: Application to Atomic, Molecular and Optical Processes* (Springer, 2011).

[4] F. Blanco and G. Garcia, *Phys. Lett*. A **317**, 458 (2003).

[5] F. Blanco and G. Garcia, *Phys. Lett.* A **330**, 230 (2004).

[6] B. Boudaïffa, P. Cloutier, D. Hunting, M. A. Huels and L. Sanche, *Science* **287**, 1658 (2000).

[7] P.A.M. Dirac, *Proc. Roy. Soc. Lond*. A **117**, 610 (1928).

[8] L. Sanche, *Mass Spect. Rev*. **21**, 349 (2002).

[9] C.D. Anderson, *Phys. Rev*. **43**, 491 (1933).

[10] J.P. Marler and C.M. Surko, *Phys. Rev. A* **72**, 062713 (2005).

[11] M. Deutsch, *Phys. Rev*. **83**, 207 (1951).

[12] J.P. Marler, L.D. Barnes, S.J. Gilbert, J.P. Sullivan, J.A. Young and C.M. Surko, *Nucl. Instr. and Meth. in Phys. Res.* B **221**, 84 (2004).

[13] M. Born and J.R. Oppenheimer, *Ann. Phys. (Leipzig)* **84**, 457 (1927).

[14] M.A.Morrison, T.L. Estle and N.F. Lane, *Quantum states of Atoms, Molecules and Solids.* (Prentice-Hall, Englewood Cliffs, NJ, USA, 1977).

[15] N.F. Lane, *Rev. Mod.Phys*, **52**, 29 (1980).

[16] W.H. Flygare, *Molecular Structure and Dynamics.* (Prentice-Hall, Englewood Cliffs, NJ, USA, 1978).

[17] F.H.M. Faisal, *J. Phys. B: At. Mol. Opt. Phys.* **3**, 636 (1970).

[18] P.G. Burke and A.L. Sinfailam, *J. Phys. B: At. Mol. Opt. Phys.* **3**, 641 (1970).

[19] F.A. Gianturco, R.R. Lucchese and N. Sanna, *On the Scattering of Low-Energy Electrons by Sulphur Hexafluoride, J. Chem. Phys.* **102**, 5743 (1995).

[20] F.A. Gianturco and R.R. Lucchese, *J. Chem. Phys.* **108**, 6144 (1998).

[21] F.A. Gianturco and R.R. Lucchese, *J. Chem. Phys.* **114**, 3429 (2001).

[22] J. Franz, F.A. Gianturco, K.L. Baluja, J. Tennyson, R. Carey, R. Montuoro, R.R. Lucchese, T. Stoecklin, P. Nicholas, T.L. Gibson and R.R. Lucchese, *Nucl. Instr. and Meth. in Phys. Res. B* **266**, 425 (2008).

[23] F. Carelli, F. Sebastianelli, I. Baccarelli and F.A. Gianturco, *Int. J. Mass. Spectrom.* **277**, 155 (2008).

[24] F.A. Gianturco, D.G. Thompson and A. Jain, *Computational Methods for Electron-Molecule Collisions*. (Plenum, New York, 1995).

[25] S.L. Altman and P. Herzig, *Point-Group Theory Table.* (Oxford University Press, Oxford, 1994).

[26] S. Telega and F.A. Gianturco, *Eur. Phys. J. D.* **36**, 271 (2005).

[27] S.J. Hara, *J. Phys. Soc. Jpn.* **22**, 710 (1967).

[28] S. Salvini and D.G. Thompson, *J. Phys. B: At. Mol. Opt. Phys.* **14**, 3797 (1981).

[29] A. Jain and D.G. Thompson, *J. Phys. B: At. Mol. Opt. Phys.* **16**, 3077 (1983).

[30] F.A. Gianturco, A. Jain and L.C. Pantano, *J. Phys. B* **20**, 571 (1987).

[31] C. Lee, W. Yang and R. G. Parr, *Phys. Rev. B* **37**, 785 (1998).

[32] R.R. Lucchese and F.A. Gianturco, *Int. Rev. Phys. Chem.* **15**, 429 (1996).

[33] E.P. Wigner and L. Eisenbud , *Phys.Rev.* **72**, 29 (1947).

[34] P.G. Burke, A. Hibbert and W.D. Robb, *J. Phys. B: At. Mol. Phys.* **4**, 153 (1971).

[35] P.G. Burke and W.D. Robb, *Adv. At. Mol. Phys.* **11**, 143 (1975).

[36] P.G. Burke, I.Mackey and I. Schimamura, *J. Phys. B: At. Mol. Phys.* **10**, 2497 (1977).

[37] B.I. Schneider, *Chem. Phys. Lett.* **31**, 237 (1975).

[38] B.I. Schneider and P.J. Hay, *Phys. Rev. A* **13**, 2049 (1976).

[39] J. Tennyson, *Phys. Rep.* **491**, 29 (2010).

[40] J.M. Carr, P. Galiatsatos, J. Gorfinkiel, A. Harvey, M. Lysaght, D.Madden, Z. Mašín, M. Plummer, J. Tennyson and H. Varambhia, *Eur. Phys. J. D.* **66**, 1 (2012).

[41] L.A. Morgan, C.J. Gillan, J.Tennyson and X. Chen, *J. Phys. B* **30**, 4087 (1997).

[42] H.N. Varambhia, M. Gupta, A. Faure, K.L. Baluja and J. Tennyson, *J. Phys. B: At.Mol. Opt. Phys.* **42**, 095204 (2009).

[43] S. Harrison and J. Tennyson, *J. Phys. B: At. Mol. Opt. Phys.* **45**, 035204 (2012).

[44] A. Faure, H.N. Varambhia, T. Stoecklin and J. Tennyson, *Mon. Not. R. Astron. Soc*. **382**, 840 (2007).

[45] Z. Mašín and J.D. Gorfinkiel, *J. Chem. Phys.* **135**, 144308 (2011).

[46] A. Dora, L. Bryjko, T.van Mourik and J. Tennyson, *J. Chem. Phys.* **136**, 024324 (2012).

[47] (a) I. Rozum, *PhD Thesis* (University College London, 2003); (b) H.N. Varambhia, *PhD Thesis* (University College London, 2010); (c) R. Zhang, *PhD Thesis* (University College London, 2010).

[48] K.L. Baluja, R. Zhang, J. Franz and J. Tennyson, *J. Phys. B: At. Mol. Opt. Phys*. **40**, 3515 (2007).

[49] R. Fandreyer, P.G. Burke, L.A. Morgan and C.J. Gillan, *J. Phys. B: At. Mol. Opt. Phys*. **26**, 3625 (1993).

[50] D. Bouchiha, J.D. Gorfinkiel, L.G. Caron and L. Sanche, *J. Phys. B: At. Mol. Opt. Phys*. **40**, 1259 (2007).

[51] A. Faure, J.D. Gorfinkiel, L.A. Morgan and J. Tennyson, *Comput. Phys. Commun*. **144**, 224 (2002).

[52] C. Bloch, *Nuclear Phys***. 4**, 503 (1957).

[53] K.L. Baluja, P.G. Burke, and L.A. Morgan. *Comput. Phys. Commun.*, **27**, 307 (1982).

[54] C.J. Gillan, J. Tennyson and P.G. Burke, *Computational methods for Electron Molecule Collisions.* (Ed. W. M. Huo and F. A. Gianturco, Plenum Press, New York, 1995).

[55] C.J. Noble and R.K. Nesbet, *Comput. Phys. Commun.* **33**, 399 (1984).

[56] J.M. Carr, P. Galiatsatos, J.D. Gorfinkiel, A. Harvey, M. Lysaght, D. Madden, Z. Mašín, M. Plummer, J. Tennyson and H. Varambhia, *Eur. Phys. J. D*. **66**, 58 (2012).

[57] J. Tennyson, *J. Phys. B: At. Mol. Phys.* **19**, 4255 (1986).

[58] G. Danby and J. Tennyson, *J. Phys. B: At. Mol. Opt. Phys*. **23**, 1005 (1990).

[59] R. Zhang, A. Faure and J. Tennyson, *Phys. Scr*. **80**, 015301 (2009).

[60] (a) J.D. Gorfinnkiel and J. Tennyson *J. Phys. B: At. Mol. Opt. Phys*. **37** L343 (2004).(b) J.D. Gorfinnkiel and J. Tennyson *J. Phys. B: At. Mol. Opt. Phys*. **38** 1607 (2005).

[61] W. Domcke, *Phys. Rep*. **208**, 97 (1991).

[62] H. Feshbach *Ann. Phys. (N.Y.)* **5**, 357 (1958).

[63] G. Breit and E. Wigner, *Phys. Rev*. **49**, 519 (1936).

[64] J. Tennyson and C.J. Noble, *Comput. Phys. Comm*. **33**, 421 (1984).

[65] F.T. Smith, *Phys. Rev*. **118**, 349 (1960).

[66] (a) M.A. Morrison, *Adv. At. Mol. Phys*. **24,** 51 (1988). (b) D.W. Norcross and N.T. Padial, *Phys. Rev. A.* **25**, 226 (1982). (c) F.A. Gianturco and A. Jain, *Phys. Rep.* **143**,347 (1986).

[67] N. Sanna and F.A. Gianturco, *Comput. Phys. Commun*. **114**, 142 (1998).

[68] Y. Okamoto, K. Onda and Y. Itikawa, *J. Phys. B* **26**, 745 (1993).

[69] M. Inokuti, *Rev. Mod. Phys*. **43**, 297 (1971).
[70] G. García and F. Manero, *Phys. Rev. A* **57**, 1096, (1998).

[71] G. García and F. Blanco, *Phys. Rev. A* **62**, 044702 (2000).

[72] F. Blanco and G. García, *Phys. Lett*. *A* **295**, 178 (2002).

[73] F. Blanco and G. García, *Phys. Rev*. *A* **67**, 022701 (2003).

[74] F. Blanco and G. García, *Phys. Lett. A* **255,** 147 (1999).

[75] R.D. Cowan, *The Theory of Atomic Structure and Spectra* (University of California Press, London, 1981).

[76] M.E. Riley and D.G. Truhlar, *J. Chem. Phys*. **63**, 2182 (1975).

[77] X.Z. Zhang, J.F. Sun and Y.F. Liu, *J. Phys. B.* **25**, 1893 (1992).

[78] G. Staszewska, D.W. Schwenke, D. Thirumalai and D.G. Truhlar, *Phys. Rev. A* **28**, 2740 (1983).

[79] F. Mott and H.S.W. Massey, *The Theory of Atomic Collision* (Oxford University Press, Oxford, 1965).

[80] R.P. McEachran, J.P. Sullivan, S.J. Buckman, M.J. Brunger, M.C. Fuss, A. Muñoz, F. Blanco, R.D. White, Z.Lj. Petrović, P. Limão-Vieira and G. García, *J. Phys. B* **45**, 045207 (2012).

[81] D.D. Reid and J.M. Wadehra, *Phys. Rev. A* **50**, 4859 (1994).

[82] D.D. Reid and J.M. Wadehra, *J. Phys. B: At. Mol. Opt. Phys*. **29**, L127 (1996).

[83] D.D. Reid and J.M. Wadehra, *J. Phys. B: At. Mol. Opt. Phys*. **30**, 2318 (1997).

[84] (a) R.P. McEachran, D.L. Morgan, A.G. Ryman and A.D. Stauffer, *J. Phys. B* **10**, 663 (1977); (b) R.P. McEachran, A.G. Ryman and A.D. Stauffer, *J. Phys. B: Atom. Molec. Phys.* **11**, 511 (1978).

[85] L. Chiari, A. Zecca, S. Girardi, E. Trainotti, G. García, F. Blanco, R. McEachran and M. Brunger, *J. Phys. B: At. Mol. Opt. Phys*. **45**, 215206 (2012).

[86] A.C.L. Jones, C. Makochekanwa, P. Caradonna, D.S. Slaughter, J.R. Machacek, R.P. McEachran, J.P. Sullivan, S.J. Buckman, A.D. Stauffer, I. Bray and D.V. Fursa, *Phys. Rev. A* **83**, 032701 (2011).

[87] A.R. Milosavljević, F. Blanco, J.B. Maljković, D. Šević, G. García and B.P. Marinković, *New J. Phys*. **10**, 103005 (2008).

[88] A. Jain, *J. Phys. B* **21**, 905 (1988).

[89] A. Muñoz, J.C. Oller, F. Blanco, J.D. Gorfinkiel, P. Limão-Vieira and G. García, *Phys. Rev. A* **76**, 052707 (2007).

[90] A.S. Dickinson, *J. Phys. B* **10**, 967 (1977).

Chapter 3

Theoretical Results

In this chapter we report the integral elastic, electronically inelastic and total cross sections (CS), plus the elastic differential cross sections (DCS), for electron-molecule collisions calculated by means of the computational methods described in Chapter 2. Two of these methods, namely, the single-centre expansion (SA-SCE) approach (implemented in the ePOLYSCAT code)[1,2] or the R-Matrix method,[3] provide meaningful scattering data at low scattering energies, whereas the IAM-SCAR method[4,5] provides valuable information at intermediate and high energies. The main objective of this chapter is to combine the scattering cross sections obtained from the different procedures and provide complete sets of integral elastic, inelastic and total cross sections from thermalized energies up to 10 keV. The interactions of four different molecules were computationally investigated: hydrogen cyanide, anthracene, and the diazines pyrimidine and pyrazine. Due to their different sizes, geometrical structures and physico-chemical properties, they constitute representative examples for testing the present combination of procedures. Moreover, cross section data available for these target molecules is rather incomplete or restricted to a limited energy region. Hence, the present calculations provide an important contribution to the electron-molecule scattering data pool.

Finally, given the scarcity of positron scattering data available in the literature, we have extended the scheme developed for electron scattering, which combines different quantum scattering models, to treat positron collisions. Of particular note, we provide the first ever report theoretical cross sections for positron scattering from pyrimidine for energies of 1-10000eV.

3.1. Non-Polar Molecules

3.1.1. Anthracene

Anthracene is a polycyclic aromatic hydrocarbon (PAH) which is of considerable interest in various fields of study. Firstly, anthracene is of great environmental concern since it is known to be a widespread atmospheric and soil contaminant[6,7] produced, for instance, by an incomplete combustion of fuels containing carbon, such as wood, diesel, coal, etc. Also, relatively recent studies have reported the anthracene compound to be a hazardous chemical and a potential human carcinogen.[8,9] Anthracene molecules, together with other PAHs, are believed to be a major component in the interstellar medium (ISM) since they have been shown to be responsible for the infrared emission features that dominate the spectra of many galactic and extragalactic sources.[10,11] Additionally, anthracene is broadly used as a scintillator for detectors of high energy radiation. On the other hand, given that computational tasks become significantly more demanding as the number of molecular electrons increase, computational analysis of electron scattering with polyatomic molecules have been generally limited to few-atoms and few-electrons molecular structures, in particular at low energies. It is therefore important, from a more fundamental perspective, to analyze electron collisions for increasingly more complicated targets as anthracene.

Electron collisions with anthracene have been the subject of several investigations. Experimental studies on the excited states of anthracene were firstly reported by Von Jager[12] who measured energy-loss spectra of condensed-phase anthracene with high-energy electrons (35 keV). Further energy-loss measurements for gaseous anthracene were carried out initially by Koch *et al.*[13] and more recently by Allan[14] and Man *et al.*[15] Measurements on electron attachment were provided firstly by Christophorou *et al.*[16], who derived cross sections for electron attachment resonances by means of an electron swarm experiment. Burrow *et al.*[17] utilized electron transmission spectroscopy to determine the vertical electron affinities and to characterize the short-lived temporary anion states of gaseous anthracene. Tobita *et al.*[18] studied the formation of long-lived parent negative ions and fragments from anthracene following low energy electron impact. In particular, they detected a sharp peak in the parent negative ion yield curve at energies close to 0 eV. Subsequently, Canosa and co-workers[19] verified the presence of a strong maximum at energies ~0 eV. Regarding integral elastic or total cross sections, neither theoretical nor experimental data appear, to our knowledge, to be available in the literature. Differential cross sections have been only measured by Boechat-Roberty *et al.*[20], who provided absolute elastic and inelastic differential cross sections at the incident electron energy of 1 keV.

It is particularly noticeable that theoretical cross sections have not been calculated before for this target, probably, due to the significant size of this system. Hence, this work[21,22] constitutes the first theoretical study on electron-anthracene collisions.

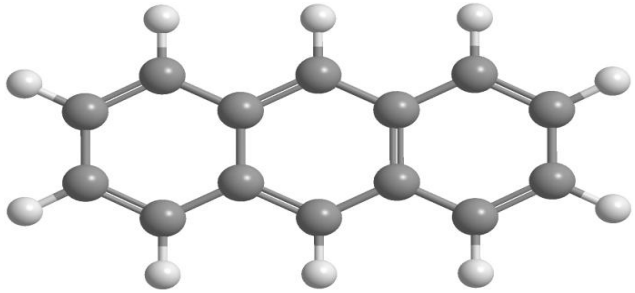

Figure 3.1: Equilibrium geometrical configuration of the present target molecule anthracene.

Low-energy Calculation Details

Anthracene ($C_{14}H_{10}$) is a polycyclic aromatic hydrocarbon (PAH) formed by three linearly condensed carbon rings (see Figure 3.1). Fixed-nuclei calculations have been performed in the equilibrium geometry of anthracene, placed in the YZ plane.[23] In the low energy range, elastic cross sections have been computed with the ePOLYSCAT code. The initial N-electron target wavefunction was generated using the Gaussian 03 suite of codes[24] at the Hartree-Fock level and expanded in the 6-311++G (3df, 3pd) basis set. These *ab-initio* calculations yielded for the neutral molecule an optimized geometrical configuration in fair agreement with earlier calculations.[23] Anthracene belongs to the D_{2h} point group and has no permanent dipole moment, consistent with its centro-symmetric geometry. However, it possesses a strong polarizibility, whose tensorial components calculated with the present model are α_{xx} = 12.8 Å^3, α_{yy} = 39.4 Å^3 and α_{zz} = 23.4 Å^3; such values are in reasonable agreement with earlier theoretical values[25] α_{xx} = 12.1 Å^3, α_{yy} = 39.4 Å^3 and α_{zz} = 23.4 Å^3.

In order to get converged cross sections, it is important to ensure the numerical convergence of all the necessary parameters (e.g., size of the partial wave expansion for the scattered electron l_{max}, size of the multipolar expansion for the scattering potential, size of the physical box limitating the area where the collision takes place, etc.).[26] Figure 3.2a shows the partial integral elastic CSs associated with the A_g symmetry, computed using different values of l_{max}, namely, 20, 30, 40, 60 and 80 (using a radial box size of 50 Å). In practice, the optimum l_{max} value is given as a compromise between the quality of the results and the running time of the calculations. In this case, we noted that increasing the maximum angular momentum from l_{max} = 60 to l_{max} = 80 had no significant effect on the final results, but made calculations too much demanding (1 point ~4 hours of CPU time). We also report partial CS computed using different values for the interaction box size i.e., B = 50 Å and B = 100 Å; we found no

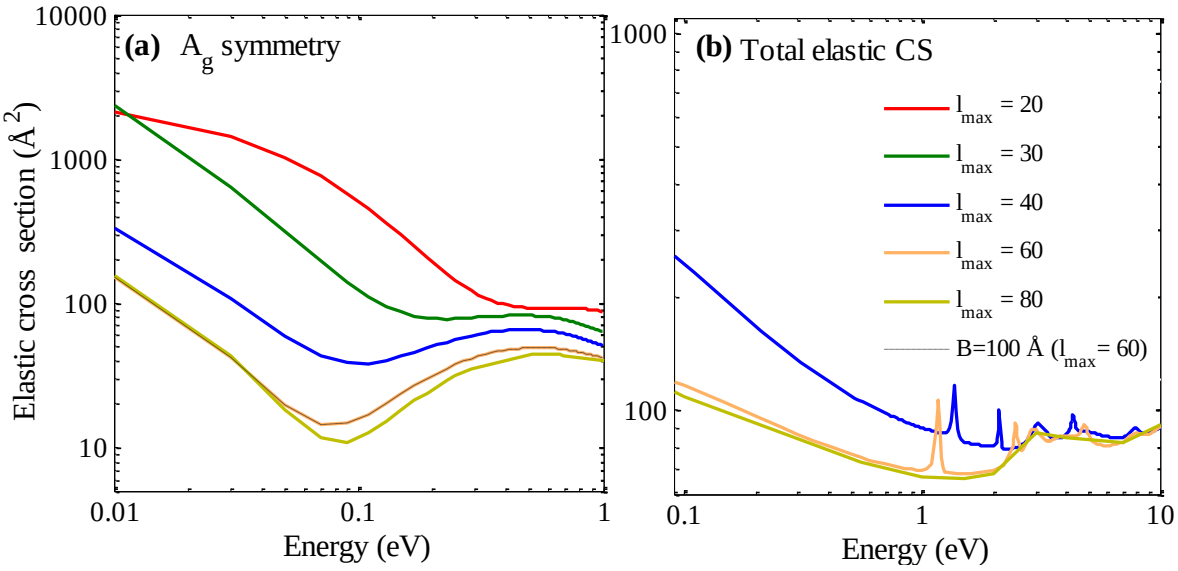

Figure 3.2: (a) Partial elastic cross sections for the A_g symmetry and (b) total integral elastic CSs (summed over contributions from all irreducible representations) calculated using different l_{max} (i.e., 20, 30, 40, 60, and 80), with a radial interaction box of 50 Å. Also shown, partial elastic CSs calculated using a radial interaction box of 100 Å and l_{max}=60.

appreciable differences between them, as can be seen in Figure 3.2. Same tests of convergence were performed for the remaining symmetries, showing the same behaviour (for the sake of brevity we show in Figure 3.2b the total elastic CSs, i.e., summed over contributions from all irreducible representations). According to this discussion, for the present calculations we have employed a partial wave expansion up to l_{max} = 60 both for the bound molecular orbitals and for the scattering wave functions and a physical box with a radius of 50 Å. The multipolar expansion of the interaction potential V^{SMECP} included terms up to λ_{max}=120.

Low-lying Resonant States

Partial integral elastic CS calculated for each of the contributing IRs (i.e., the symmetric A_g, B_{1g}, B_{2g}, B_{3g} and the antisymmetric A_u, B_{1u}, B_{2u}, B_{3u}) of the D_{2h} point group are reported in Figure 3.3 from threshold up to 10 eV. It can be appreciated the presence of several maxima at various energies below 10 eV for different symmetries. As mentioned in section 2.3.3, the unambiguous signature of a physical resonance is a π-jump in the eigenphase sum at the resonance energy position. Figure 3.4 shows the behaviour of the eigenphase sums, together with their first derivatives, for each symmetry in which we find a maximum in the corresponding partial cross section. It can be seen that the seven eigenphase sums, which we have fitted to a Breit-Wigner formula (Equation 2.43),[27] show a sharp π-jump.

The computed resonant parameters are listed in Table 3.1, where is reported the symmetry, energy position where the resonance is formed, the width and the corresponding lifetime. The lowest resonant state, the B_{3u} state of anionic metastable anthracene, is located around 1 eV. The next resonance has A_u symmetry and occurs around 2.46 eV. Both resonances turn out to have very narrow widths and, thus, are fairly stable. The partial cross sections of Figure 3.3 additionally show the presence of three further resonances in the low-energy range (below ~5 eV) that correspond to metastable negative ions of anthracene, which have B_{1g}, B_{3u} and B_{2g} symmetry, respectively. The earlier experiments reported on electron transmission spectra by Burrow *et al.*[17], also indicate various resonance features, which are however downshifted in energy around 1-2 eV with respect to our data (see Table 3.1). As stated in previous works, the model potentials employed in the SA-SCE approach are known to show only semi-quantitative agreement with available experiments,[28,29] although always being able to locate all the resonances experimentally observed.

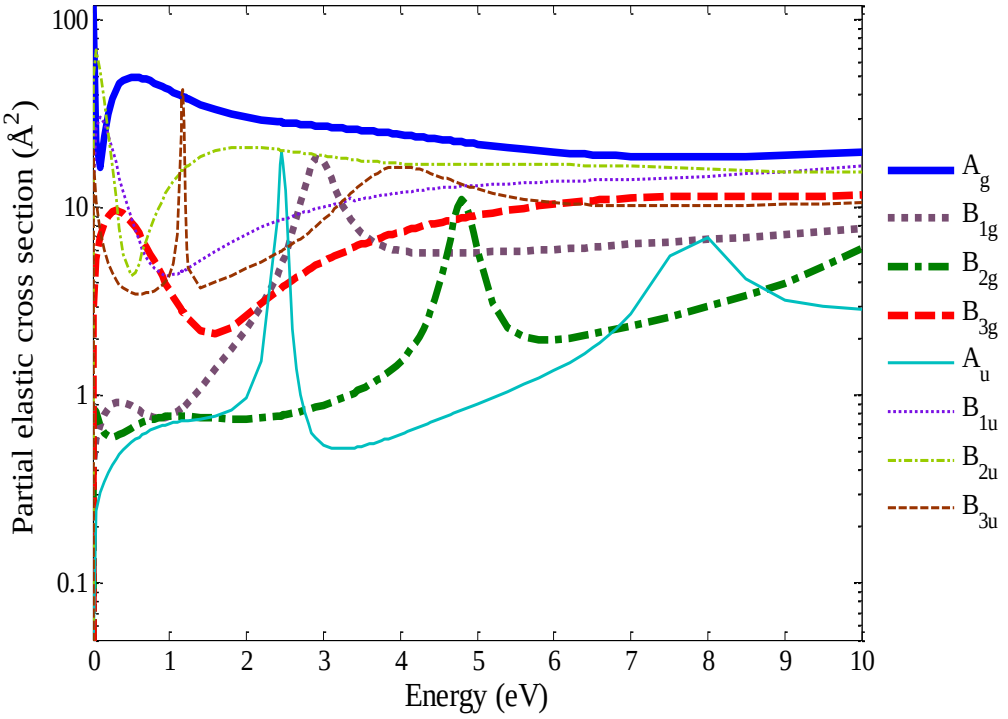

Figure 3.3: Partial elastic cross sections for electron scattering from anthracene for the contributing symmetries A_g, B_{1g}, B_{2g}, B_{3g}, A_u, B_{1u}, B_{2u} and B_{3u}.

Table 3.1. Computed resonant parameters for the anthracene molecule.

Symmetry	Energy (eV)		Width (eV)	Lifetime (s)
	Present work	Experiments[17]		
B_{3u}	1.16	~0.6	0.035	$1.88.10^{-14}$
A_u	2.46	~1.5	0.098	$6.71.10^{-15}$
B_{1g}	2.91	~1.67	0.510	$1.29.10^{-15}$
B_{3u}	3.76	~1.80	1.974	$3.34.10^{-16}$
B_{2g}	4.81	~2.67	0.360	$1.83.10^{-15}$
A_u	7.77	-	0.982	$6.70.10^{-16}$
B_{2g}	10.46	-	2.218	$2.97.10^{-16}$

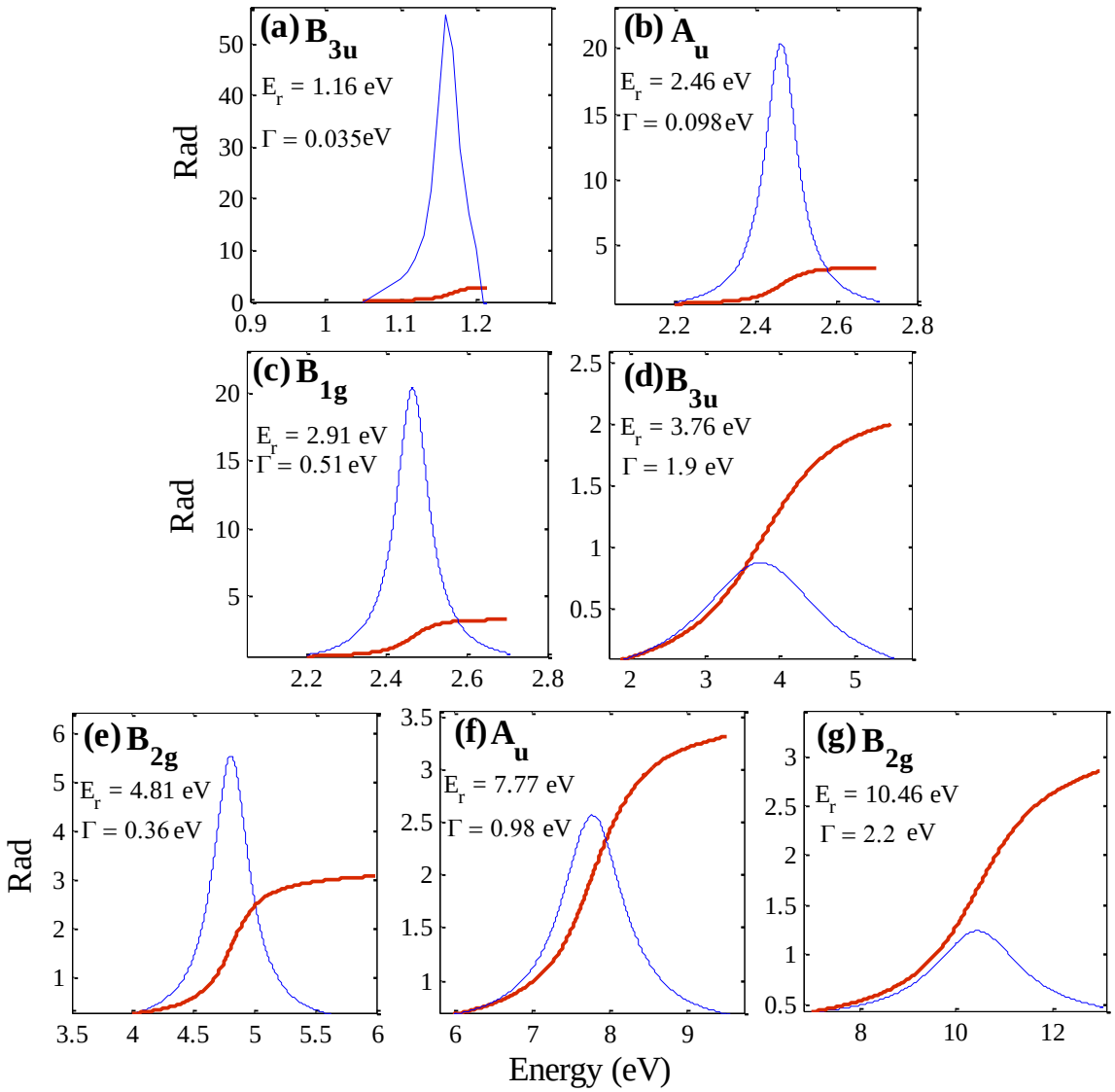

Figure 3.4: Computed eigenphase sums, fitted to a Breit-Wigner formula, together with their first derivatives, for the symmetries in which we found a maximum in the corresponding cross sections. See text for further details.

It is interesting to note that these low-energy resonances follow the symmetry sequence of the virtual MO obtained from a minimal basis set (MBS) calculation of the Hartree–Fock energy for the equilibrium geometry. However, the latter are located much higher in energy, as can be seen in Figure 3.5. This figure shows the spatial distributions of the metastable anion states lying below 5 eV (left panel). In other words, they show the distribution of the electronic charge associated with the scattered electron. They are compared with the corresponding virtual MOs of the same symmetry[30] (right panel). There is a strong similarity between the two wavefunctions in every case. All the resonant states found up to 5 eV are essentially of π*-type nature; the excess electron is chiefly localized on the carbon atoms along some specific bonds, but not on the terminal H atoms. Earlier calculations of π*-type resonances in polycondensed aromatic rings performed by the group of Gianturco (see e.g. Carelli and Gianturco[31]) had indicated that such resonances are not likely to induce ring-breaking fragmentations. On the other hand, the absence of any extra charge located on the H atoms suggests that a possible fragmentation path could be the detachment of one of the external H atoms, as observed in other aromatic systems.[32,33]

Interestingly, the presence of virtual state formation during electron scattering from anthracene has been suggested in the experimental work reported by Field *et al*.[34,35] who measured backward scattering processes down to meV of collision energy. In qualitative terms, such states occur at very low scattering energies near the zero-threshold and when the overall attractive potentials are considerably strong.[36,37] In this case the polarization potential plays this role since anthracene possesses a fairly large spherical dipole polarizability (α_o=188 a.u.[3]). The virtual state formation, in fact, is a property also found for benzene other polycondensed aromatic ring systems.[38,31] Thus, in this work, we try to verify such phenomenon by following the scattering features using quantum scattering calculations, as already performed successfully for benzene. In first place, a necessary condition for virtual state scattering is that that the scattering length (α) is negative.[35] It can be seen in Table 3.2 that the scattering length decreases as a negative quantity with vanishing energies. In addition, at ultralow scattering energies, the distribution of the scattered electron becomes nearly isotropic, as expected from the dominance of the s-wave (l=0) in the scattering event (see Figure 3.6a).

Other effects of the virtual state formation can be seen in the data reported in Figure 3.6b. The upper panel of the figure shows the dramatic increase at zero energy of the elastic integral CSs in the totally symmetric IR A1g. This corresponds to a rapid drop in the eigenphase sum very close to vanishing energies, which continues up to a maximum as one moves away from the threshold. Afterward, the eigenphase sum shows a rapid decrease and becomes negative, indicating the presence of an attractive potential that allows the formation of a virtual state at

B_{3u} resonance E_r = 1.16 eV Γ_r = 0.035 eV	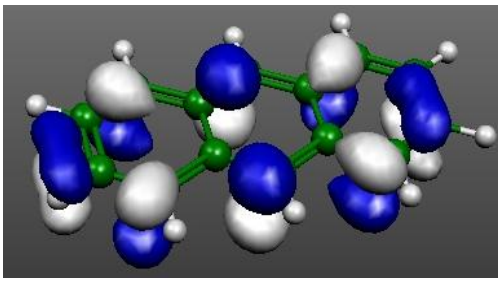	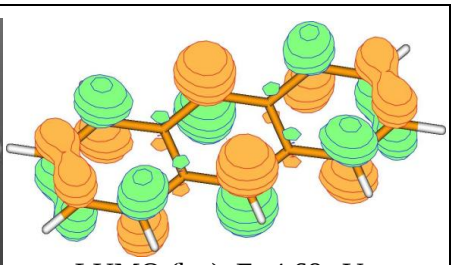 LUMO (b_{3u}) E=4.68 eV
A_u resonance E_r = 2.46 eV Γ_r = 0.098 eV	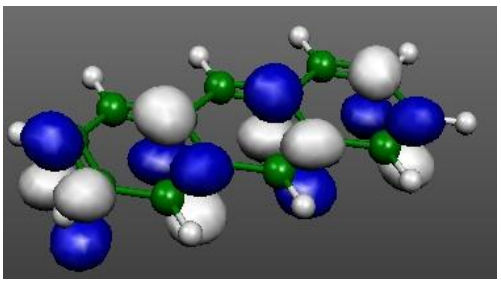	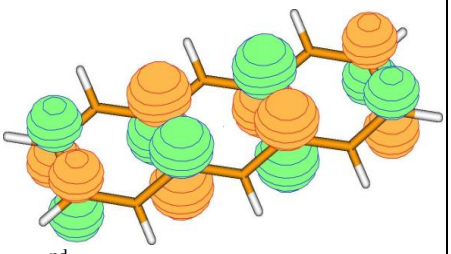 2nd virtual MO (a_u) E=6.47 eV
B_{1g} resonance E_r = 2.91eV Γ_r = 0.51 eV	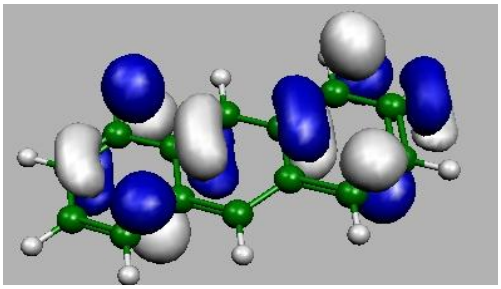	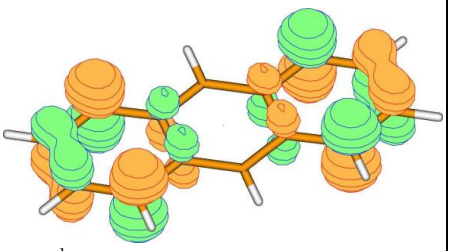 3rd virtual MO (b_{1g}) E=7.65 eV
B_{3u} resonance E_r = 3.76 eV Γ_r = 1.97 eV	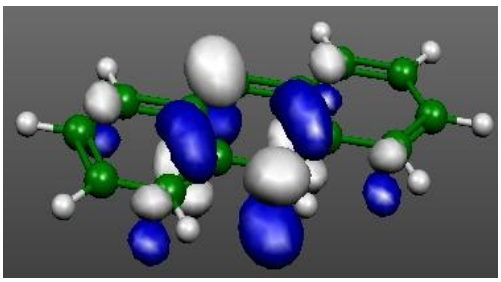	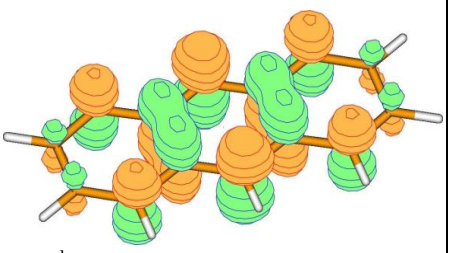 4rd virtual MO (b_{3u}) E=9.71 eV
B_{2g} resonance E_r = 4.81eV Γ_r = 0.36 eV	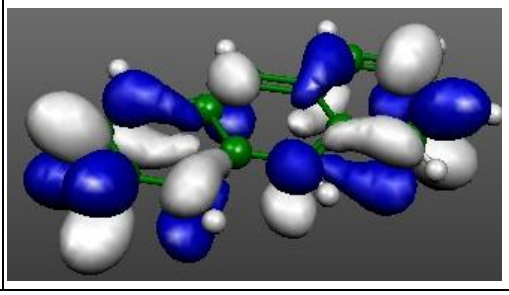	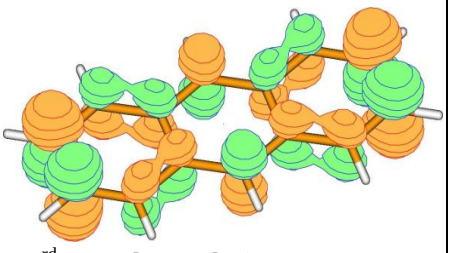 5rd virtual MO (b_{2g}) E=10.05 eV

Figure 3.5: (left panel) Computed wavefunctions (real part) for the resonant electron in anthracene associated with the metastable anions found at energies below ~5 eV. Their locations and widths are given in eV. The right panels report the corresponding virtual molecular orbitals (MO) of the same symmetry.

threshold (see bottom panel in Figure 3.6b). Moreover, both the total elastic CSs, σ_{tot}, and the backward scattering CSs, σ_{back}, exhibit a marked increase in size at vanishing collision energies (see Figure 3.7a).Our computed σ_{back} is compared with the experimental σ_{back} measured by Field *et al*.[34] There is good quantitative agreement with the experiments down to about 100 meV, although for lower energies there is only qualitative agreement. Given the approximation of our model potential, the accord is rather good. Moreover, the ratio between σ_{back} and σ_{tot} should go to 1/2 at vanishing electron impact energies, since the distribution of electrons for dominant s-wave scattering is isotropic in the space frame. This ratio was reached in the case of benzene,[35] and is also produced here (see Figure 3.7b).

Therefore, the present results indicate that the observed low-energy behaviour is indeed associated with virtual state scattering, as suggested by the experiments.[34,35]

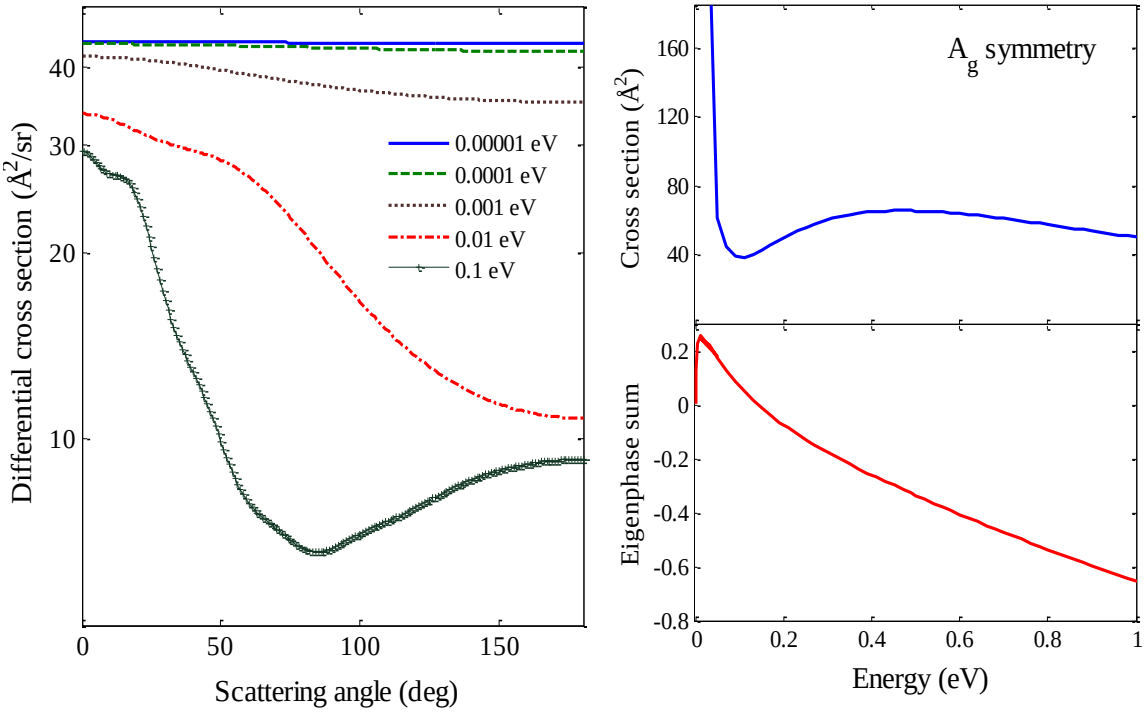

Figure 3.6: (Left panel) Computed elastic DCS for electron-anthracene collisions down to 10^{-6} eV of incident energy. (Right panel) Computed integral elastic cross sections (upper panel) in the totally symmetric IR *A*1g, together with the corresponding eigenphase sum behaviour (bottom panel). See text for further details.

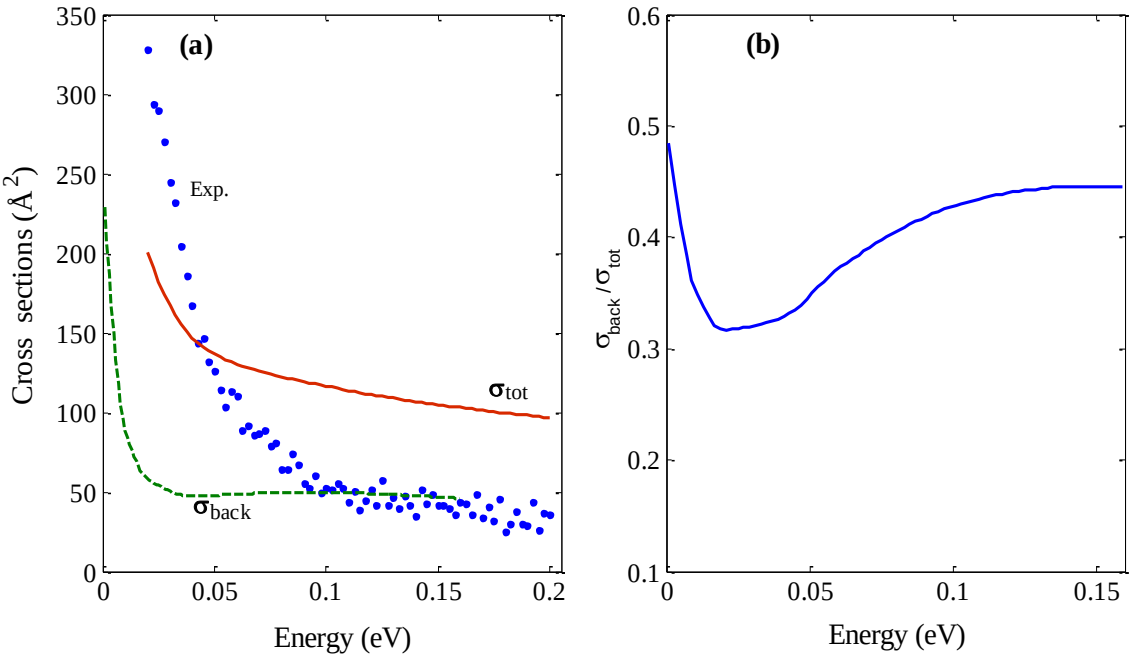

Figure 3.7: (a) Present calculated total integral and backward scattering CS for electrons impacting on anthracene as a function of electron impact energy. Also shown the experimental backward cross sections, as obtained after integrating the corresponding DCSs from 90º to 180º. (b) Computed ratio between the σ_{back} and σ_{tot} values from the present work.

Table 3.2: Computed scattering length for scattering in the A_{1g} IR.

Energy	Scattering Length α
10^{-6}	-12.53
10^{-5}	-12.52
10^{-4}	-12.40
10^{-3}	-11.40
0.5×10^{-2}	-8.72
10^{-2}	-6.96

Elastic Cross Sections

Elastic differential cross sections (DCSs) calculated with the ePOLYSCAT code and the IAM-SCAR method over the energy range 0.00001−100 eV and 1−10000 eV, respectively, are shown in Figure 3.8 at some selected electron incident energy values. It is observed that the elastic DCSs computed with the ePOLYSCAT method are characterized by a shoulder around 40°-60° and a broad minimum around 140° at 5 eV which progressively shifts to lower angles as the impact energy increases (around 80° at 30 eV). The IAM-SCAR angular distribution

shows also this broad minimum around 90°-110°, which is fairly pronounced around 100 eV but tends to disappear at higher energies. At energies below 15 eV, there is poor agreement between both methods as is to be expected from the low-energy failings of the IAM approximation (Figure 3.8a). At 15 eV of incident energy both calculations are almost identical, within 4 %, for scattering angles between 80° and 160° (Figure 3.8d). At higher incident energies there is still reasonable agreement between both elastic DCS curves, within 15 % from 60° to 180° and within 20 % from 50° to 180° at 20 eV and 30 eV, respectively. The elastic DCSs for higher incident energies as calculated with the IAM-SCAR method are shown in Figure 3.8f. Experimental elastic DCS have been only provided by Boechat-Roberty *et al.*[20] at 1 keV incident electron energy and in the angular range from 0° to 20°. This experimental data is reported in Figure 3.9 together with the present elastic DCS computed with the IAM-SCAR method, showing excellent agreement.

As aforementioned, there are no other calculations or experimental data available in the literature to compare our results with. In order to give an estimation of the reliability of the calculations, we can consider as a comparison the benzene molecule which is formed by a single aromatic ring. Additionally, accurate experimental data for e^--benzene collisions have been recently provided. In the low energy domain, Cho *et al.*[39] and Gulley and Buckman[40] showed that their experimental elastic DCS values were in good agreement with the ePOLYSCAT results for angles below 60°, in the energy range 1.1-40 eV and 8-20 eV, respectively. At higher energies, DCS for elastic scattering from benzene were measured by Kato *et al.*[41]. These authors reported good agreement with the corresponding IAM-SCAR results in the 20–70 eV region for angles above 50°, whereas some discrepancies were detected for smaller angles. In addition, excellent agreement was found at energies above 100 eV over the entire angular range.

Present calculated DCS for anthracene are compared to experimental DCS results for benzene[41] at incident energies of 50, 100 and 200 eV in Figure 3.10. Although anthracene cross sections are quantitatively higher (by a factor of 3, 2.5 and 2.3, at 50, 100 and 200 eV, respectively), both molecules have DCS with very similar shape, as better appreciated when scaling our present anthracene calculated data.

From the above discussion we can, therefore, conclude that for low energies we can safely rely on the data obtained with the ePOLYSCAT model. At intermediate energies (10-70 eV), we expect the ePOLYSCAT code to give a more realistic picture in the lower angular range (below ~50°), while the IAM-SCAR procedure provides instead a better agreement for higher angles up to 180°. For energies above 100 eV, theoretical DCS derive with the IAM-SCAR theory are recommended.

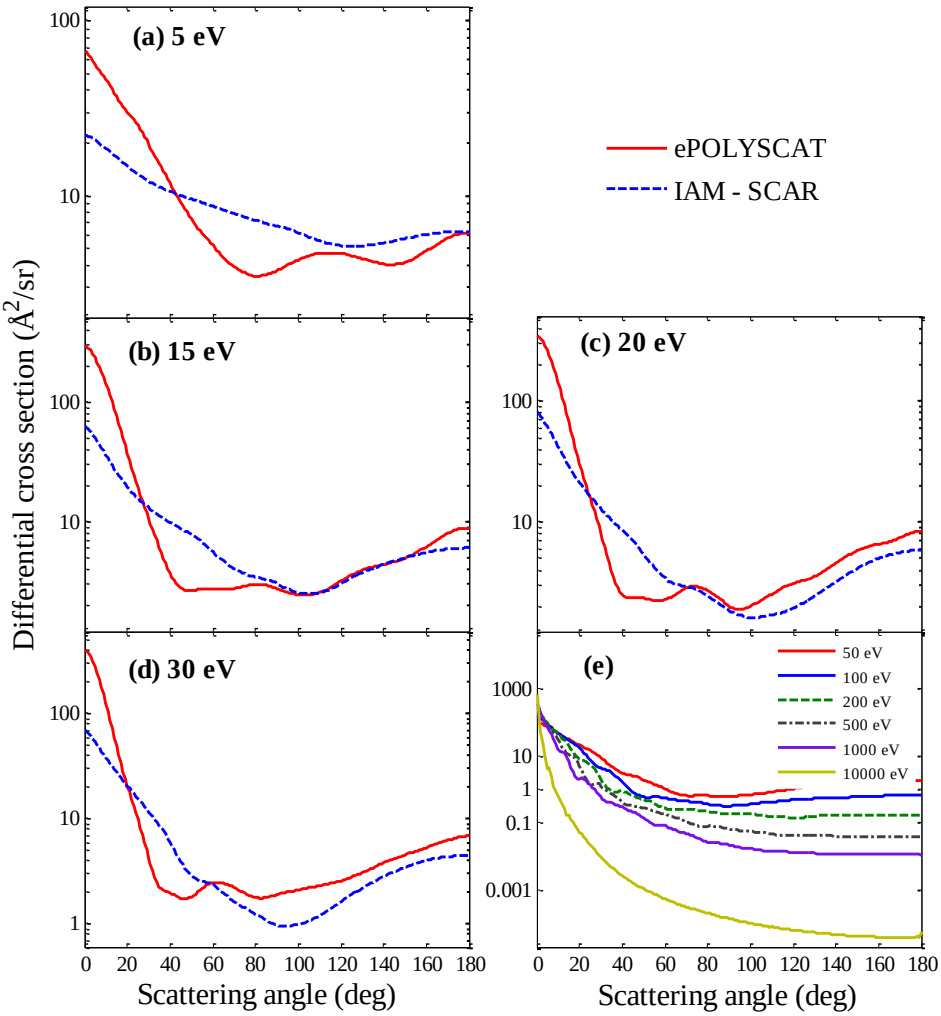

Figure 3.8: Angular differential cross sections for elastic electron scattering from anthracene at the incident energies indicated in the panels, computed with the ePOLYSCAT code (SA-SCE method) and the IAM-SCAR model.

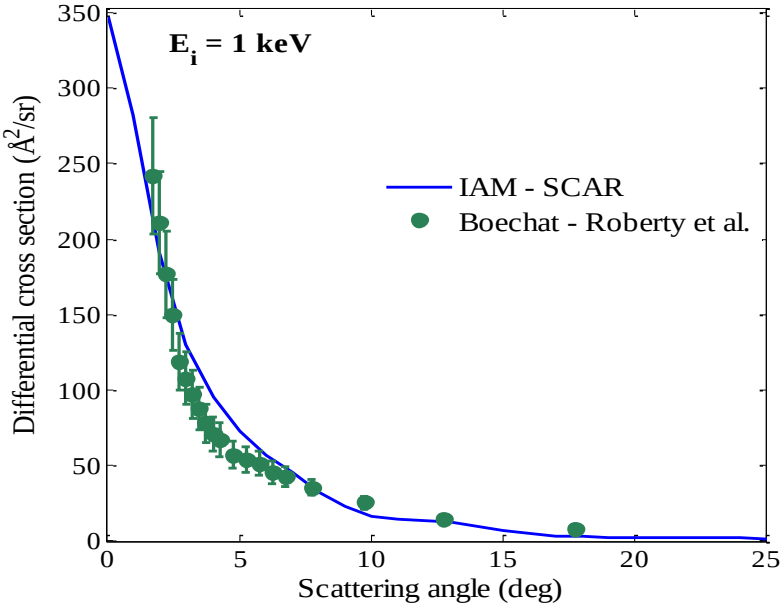

Figure 3.9: Elastic DCS for electron scattering from anthracene at 1 keV incident energy obtained with IAM-SCAR and comparison to the experimental elastic DCS reported by Boechat-Roberty *et al.*[20]

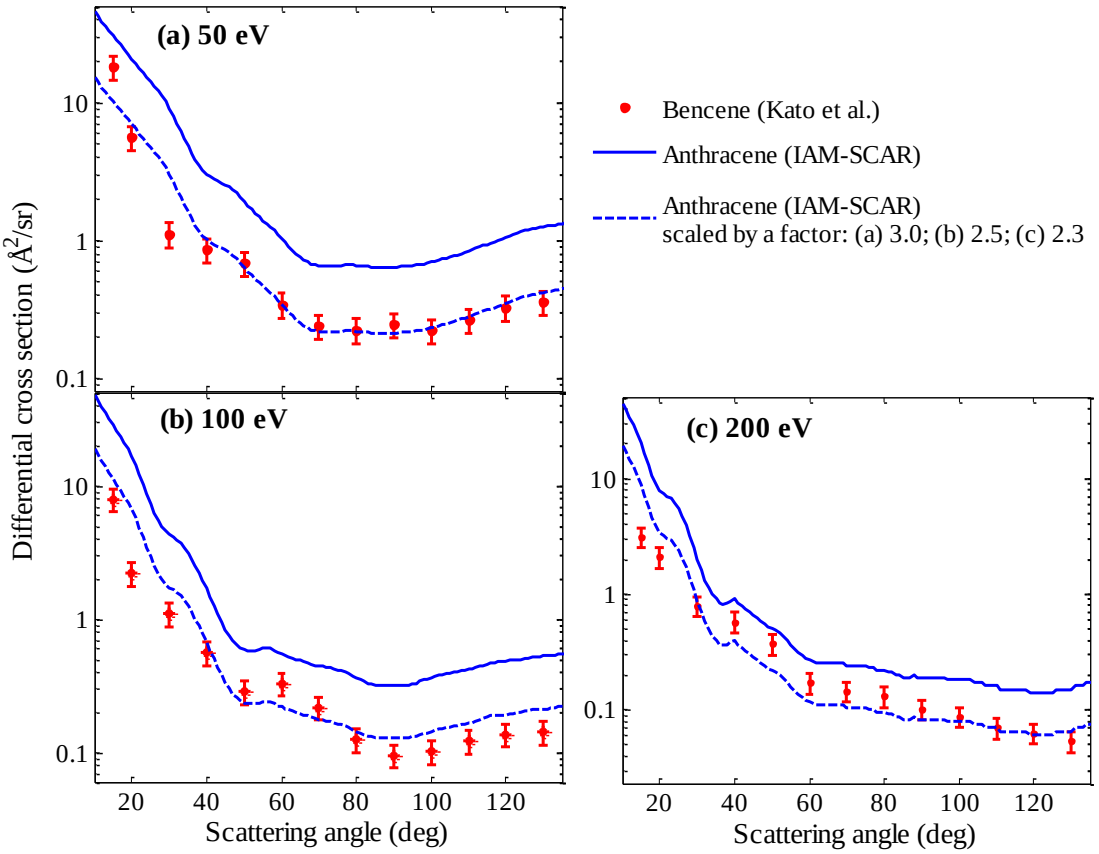

Figure 3.10: Elastic DCS for electron scattering from anthracene computed with the IAM-SCAR method and comparison to experimental data for benzene[41] at 50 eV (panel a), 100 eV (panel b) and 200 eV (panel c) incident energies. Anthracene elastic DCSs scaled by a factor of 3.0 (panel a), 2.5 (panel b) and 2.3 eV (panel c) are also shown.

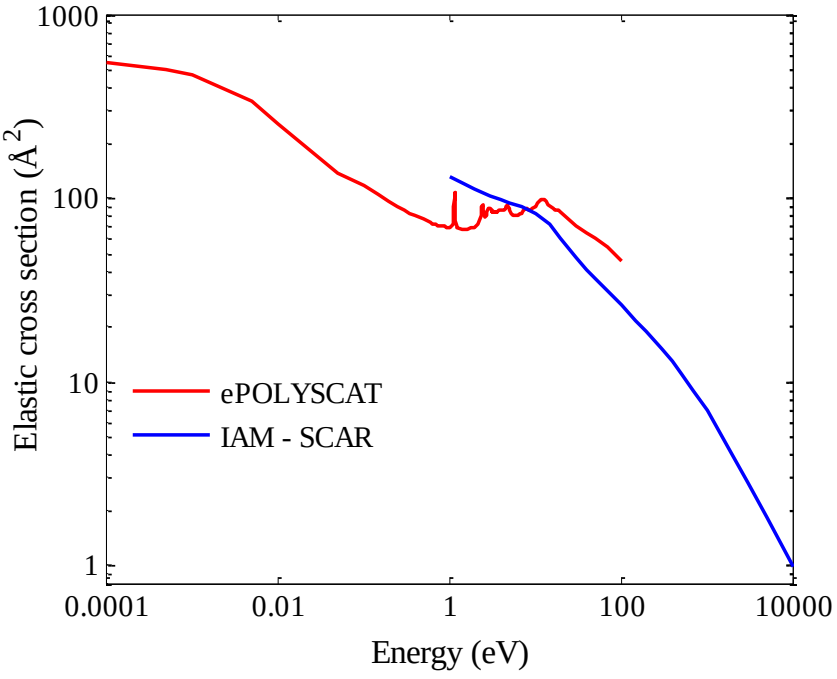

Figure 3.11: Elastic cross sections computed with the ePOLYSCAT code and with the IAM-SCAR method.

Integral elastic CS calculated with the ePOLYSCAT code and the IAM-SCAR model are shown in Figure 3.11. After crossing each other at an incident energy close to the ionization threshold, which lays around 7.44 eV, the elastic CSs obtained with the ePOLYSCAT code suffer a significant rise and deviate from the IAM-SCAR data at intermediate incident energies. The origin of this behaviour resides in the optical potential employed by the SA-SCE theory which does not include an absorption term. The exclusion of the inelastic processes from the scattering calculations leads to an overestimation of the integral elastic CS at incident energies above ionization threshold. This behaviour has been also observed in the computational study of electron-HCN collisions and is discussed more in detail in Section 3.2.1.

Inelastic and Total Cross Sections

Total cross sections (TCS) computed with the IAM-SCAR model, in the energy range 1-10000 eV, are shown in Figure 3.12. In addition, inelastic integral CS calculated through the $V_{abs}(r)$ absorption term of the IAM-SCAR optical potential are also shown in Figure 3.12. This method accounts for the electronically inelastic scattering events occurring within that energy range, that is, electronic-state excitations and ionization. Although the first electronic excited state of the anthracene molecule lays around 3.6 eV,[20,15] the IAM-SCAR onset for the inelastic events occurs at ~10 eV, followed by a noticeable rise of the summed inelastic CS for increasing energies. The fact that electronically excited states lying below 10 eV are underestimated in our IAM-SCAR approach reflects the intrinsic limitations of the present independent-atom model in the low-energy region. Additionally, it should also be noted that processes involving nuclear motion, i.e. rotational and vibrational excitations, have not been considered in this study. Nevertheless, this restriction is not thought to be significant, at the energy range we are interested in, due to the non-polar nature of the present target molecule.

Given that no further integral CS are available in the literature, as mentioned above, we have to rely on the good agreement achieved by both the SA-SCE method and IAM-SCAR approach when applied to the benzene molecule. In the low energy regime, elastic CS for benzene computed with the ePOLYSCAT code were in good agreement with the earlier measurements reported by Sueoka,[42] within the error limits of the experiments. At intermediate and high energies, total and integral CSs calculated with IAM-SCAR for electron-benzene scattering[43] agree well with experimental data from Cho *et al.*[39], Mozejko *et al.*[44], Makochekanwa *et al.*[45] and Sueoka[42]. Hence, we expect that future experimental integral CS for electron scattering from anthracene will be in agreement with the present calculations.

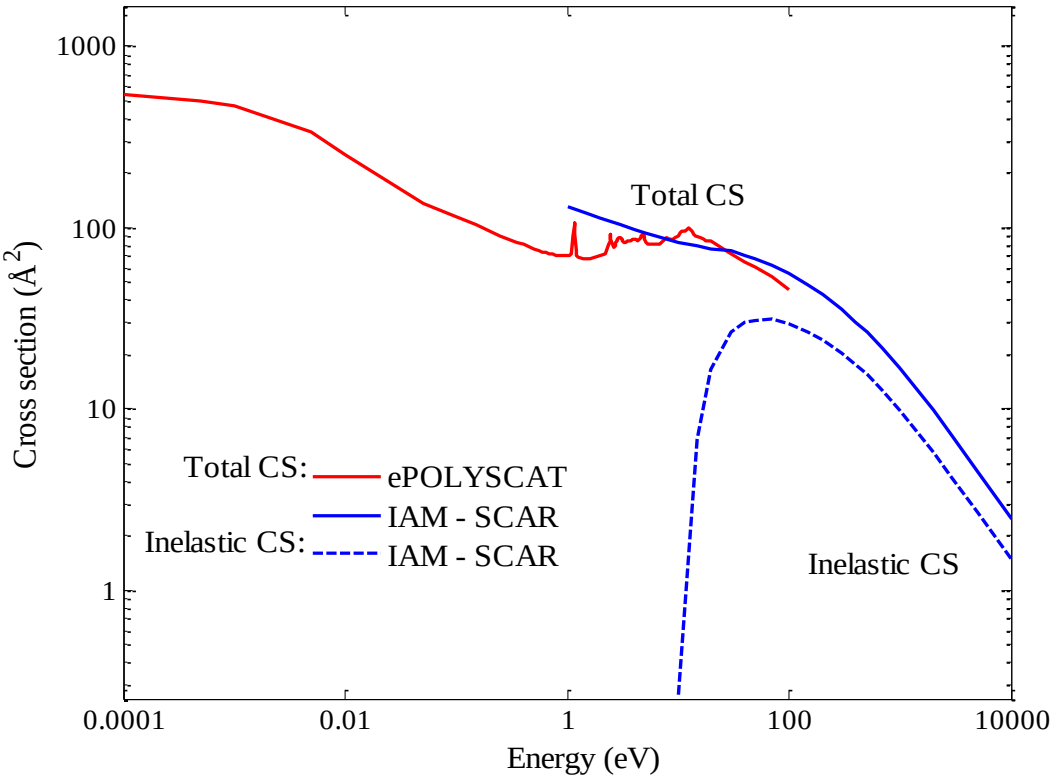

Figure 3.12: Present integral inelastic and total cross section for electron scattering from anthracene computed with the ePOLYSCAT code and the IAM-SCAR method.

Recommended Set of Integral Cross Section Data

As a result of the precedent discussion, a complete set of recommended integral cross section data for electron scattering from anthracene in the energy range from 0.00001 eV to 10000 eV is proposed in Table 3.3. Within the low energy region, from thermalized energies up to the ionization threshold (7.44 eV), integral CS computed with the SA-SCE model have been shown to be reliable. Regarding TCS, this approximation is considered to be fairly accurate since, up to the ionization threshold, elastic collisions constitute the main scattering process. For higher energies, integral CSs computed with the IAM-SCAR model are recommended in the incident energy range 30-10000 eV. Although the accuracy of the ePOLYSCAT model and the IAM-SCAR approach is hard to gauge, the good agreement observed previously between these scattering procedures and experimental measurements for various molecules,[46-48] suggests that we can estimate a numerical uncertainty of about10% for each method within its own region of applicability. At intermediate energies, the cross sectional data is derived from a smooth interpolation between both curves by means of a double logarithmic fitting. The estimated error increases from 5% at E=10 eV up to 25% and 28% at 30 eV, for the integral elastic CS and TCS, respectively, evaluated as half-value of the absolute difference between both models.

Table 3.3: Recommended elastic, electronically inelastic (electronic excitation and ionization) and total integral cross sections for electron scattering from anthracene in the energy range from 10^{-5} to 10000 eV.

Energy (eV)	Elastic (Å^2)	Electronically Inelastic (Å^2)	Total (Å^2)
0.00001	551.37		551.37
0.0001	540.95		540.95
0.001	472.21		472.21
0.01	251.78		251.78
0.1	116.42		116.42
0.2	96.66		96.66
0.3	86.41		86.41
0.4	80.44		80.44
0.5	76.55		76.55
0.7	71.97		71.97
1	69.63		69.63
1.17	106.8		106.80
2	69.62		69.62
2.46	92.49		92.49
2.91	88.67		88.67
3	88.68		88.68
3.76	84.66		84.66
4	85.67		85.67
4.81	91.88		91.88
5	86.03		86.03
6	80.82		80.82
7	82.43		82.43
8	87.68		87.68
9	84.82		84.82
10	82.88	0.27	83.15
15	72.52	6.78	79.30
20	60.48	16.63	77.11
30	47.32	26.82	74.14
40	40.88	29.96	70.84
50	36.40	31.08	67.48
70	31.08	31.36	62.44
100	26.24	29.68	55.92
200	18.82	24.22	43.04
300	15.15	20.33	35.48
500	11.17	15.46	26.63
700	8.96	12.54	21.50
1000	6.92	9.83	16.74
2000	4.00	5.82	9.83
3000	2.86	4.17	7.03
5000	1.84	2.71	4.55
10000	0.99	1.47	2.47

3.1.2. Pyrazine

Pyrazine is a heterocyclic aromatic molecule that belongs to the group of the diazines ($C_4H_4N_2$). Diazines are derivatives of the benzene molecule where two C-H bonds have been replaced by a nitrogen atom. Pyrazine (also named 1,4-diazine) contains two nitrogen atoms at positions 1 and 4 in the six-member ring (see Figure 3.13) and belongs to the point group D_{2h} in its equilibrium geometry. Pyrazine is a structural isomer of pyrimidine, and therefore a close analogue of the pyrimidinic" DNA/RNA nucleobases, i.e., thymine, cytosine and uracil. Although pyrimidine and pyrazine share quite similar physico-chemical properties, the symmetric geometry of pyrazine confers this molecule a non-polar nature. This characteristic is considerably advantageous for computational investigations since it makes the calculations less computationally demanding than for pyrimidine. That is why pyrazine provides an alternative and convenient model for the pyrimidinic bases.

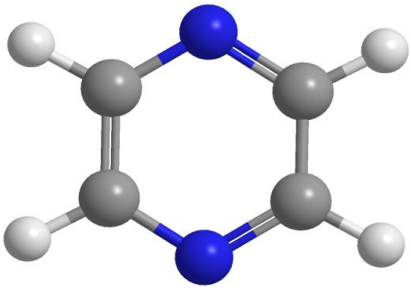

Figure 3.13: Equilibrium geometrical configuration of the present target molecule pyrazine.

Despite the advantages of employing pyrazine as a benchmark system, electron collisions with this target have been studied only by a few groups. Early electron transmission experiments performed by Nenner and Schulz[49] showed the formation of three low-lying π^* resonances for incident electron energies below 5 eV: the two lowest-lying resonances centred at 0.065 and 0.87 eV were identified as pure shape resonances, whereas the more energetic one, localized at around $\sim$ 4.1 eV, was suggested to have a mixed shape and core-excited character. Palihawadana *et al.*[50] have measured absolute differential and integral elastic CSs for electron scattering from pyrazine in the incident energy range 3 - 50 eV. Just recently, TCS have been measured, for the first time, with a newly-built apparatus[51] in the incident energy range from 10 eV to 500eV.[52] From the theoretical point of view, two groups have provided a detailed analysis on low-energy electron collisions with pyrazine. Firstly, Winstead and McKoy[53] computed differential elastic cross sections by means of the Schwinger Multichannel (SMC) method.[54,55] These authors also reported strong evidence for the mixed character of the third low-lying resonance. These findings are important since mixed resonances exist also in nucleobases and may play an important role in DNA damage (e.g. base release), as we will see in Chapter 5.

More recently, Mašín and Gorfinkiel[56] calculated elastic and electronically inelastic CS by means of the R-Matrix method,[3] at both the SEP and close coupling (CC) levels of approximation.

It is noteworthy that the abovementioned scattering studies have been restricted to a limited energy domain. In fact, previous theoretical investigations have been focused on the energy region below the ionization threshold. In view of this, the main purpose of the present section is to report computed integral and differential CS for electron scattering from pyrazine over a broad energy range (1-10 keV).[52] In the low energy region, the R-matrix calculations provided by Mašín and Gorfinkiel[56] have shown to give the best agreement with the experiment up to now (note the SA-SCE technique cannot be applied to identify core-excited resonances). The R-matrix data presented here are the result of combining the SEP model, for energies below the first electronic excitation state (~4eV),[57] and the CC model for energies above this threshold.[†] Following the approach we used for anthracene (section 3.1.1), the resulting low-energy CSs are combined with the present CS computed with the IAM-SCAR procedure, as shown below.

Elastic Cross Sections

Elastic differential cross sections obtained with the IAM-SCAR calculation for pyrazine are plotted in Figure 3.14 at some selected electron incident energy values, together with other experimental[50] and theoretical data[56,53] available in the literature. The angular dependence obtained in the experimental DCSs is characterized by a broad minimum at around 120°-80º, which is progressively shifted to lower angles as the impact energy increases. In addition, a characteristic shoulder appears at around 20°-60° in the measured DCS, which has been related with the ring of the aromatic molecules. Below 20 eV, the IAM-SCAR approach fails to reproduce the shape of the experimental angular distribution; our computed DCS becomes flatter with decreasing energies and do not reproduce the broad minima. In addition, it predicts a shallower rise of the cross section as one goes towards 0º, and therefore underestimates the forward-angle contribution. As the energy increases up to 50 eV, the IAM-SCAR results come into better agreement, both in shape and magnitude, with the experimental data from Palihawadana *et al.*[50] at scattering angles above 40º. Although no further experimental data is available in the literature for incident energies >50 eV, it is expected that for energies above 100 eV the IAM-SCAR approach provides reliable cross sections, in analogy to benzene[41] (and to pyrimidine, as we will see in section 3.2.2). Summarizing, present elastic DCS results can be recommended for incident energies $\geq$ 30 eV, in the angular range above ~40º. For lower energies, a more sophisticated model, as the R-matrix procedure, is needed.

[†] The author of this work did not participate in the calculation of this data. Both SEP and CC cross section have been provided by Mašín and Gorfinkiel.

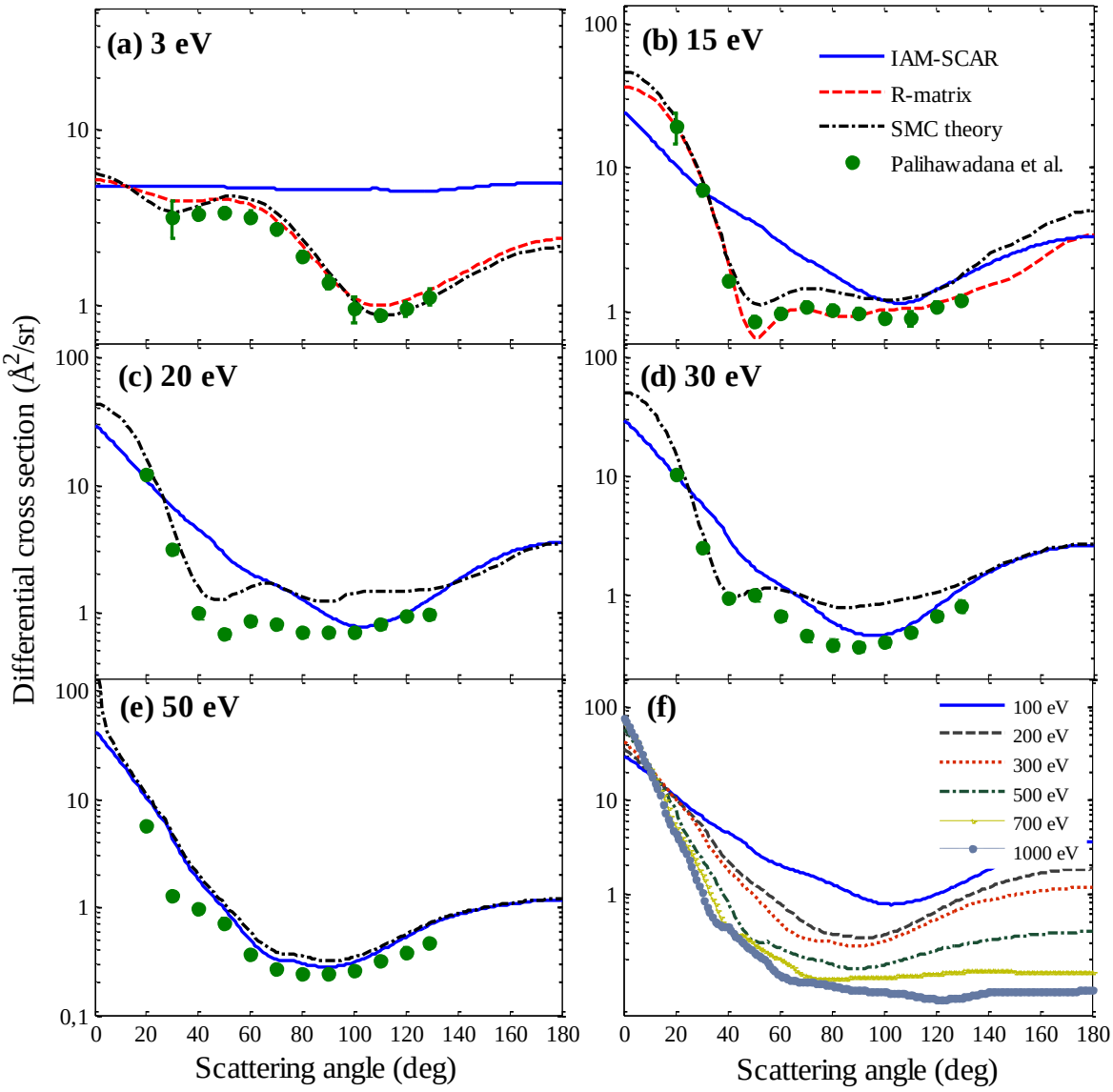

Figure 3.14: Angular differential cross sections for elastic electron scattering from pyrazine computed with the IAM-SCAR model for the incident energies indicated in the panels. For comparison, DCSs computed with the R-matrix theory[56] and SMC approach[53], and experimental measurements provided by Palihawadana *et al.*[50] are also shown.

Integral elastic CS computed with the IAM-SCAR approach are shown in Figure 3.15 together with the results derived with the R-matrix method.[56] At the common energies of overlap, very good agreement is found between both theoretical approaches, within a 7% and 12% at 10 and 15 eV, respectively. Also, fairly good agreement is found with earlier SMC calculations[53] in the 10 - 20 eV energy range. In addition, there is a very good level of accord between the present IAM-SCAR calculations and the experimental data from Palihawadana *et al.*[50], for the entire energy range where such a comparison is possible, i.e., from 3 to 50 eV. At this point, one should keep in mind that integral elastic CS reported by Palihawadana *et al.*[50], as in most experimental studies on elastic scattering, have been derived by extrapolating the

measured DCS towards 0° and 180°, as the experiments were conducted in a limited angular range. In this case, experimental DCSs were extrapolated following the shape of the corresponding SMC results[53] at each energy. Whereas at energies above 20 eV the SMC procedure somewhat overestimates the experimental values, the IAM-SCAR results lies within the experimental uncertainty bars.

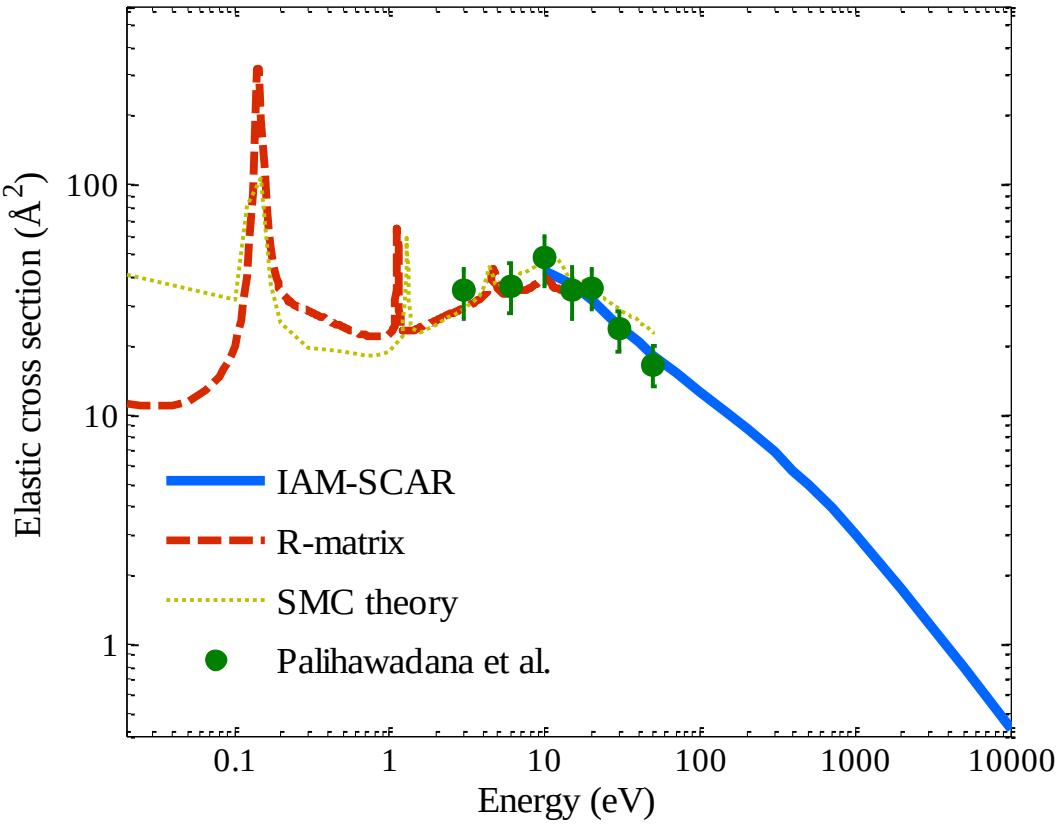

Figure 3.15: Integral elastic cross sections for electron scattering from pyrazine computed with the IAM-SCAR method. For comparison, elastic CS computed with the R-matrix theory[56], SMC approach[53] and experimental measurements provided by Palihawadana *et al.*[50] are also shown.

Inelastic and Total Cross Sections

Inelastic CSs computed with the IAM-SCAR method are shown in Figure 3.16 together with the R-matrix data.[56] As mentioned in Chapter 2, the R-matrix values account for the electronic excitations but ignores the ionization processes. Thus, these results are merely indicative above the ionization threshold (~9.4 eV).[58] Whereas the R-matrix method shows an onset of 4.0 eV (compatible with the location of the first electronic excitation state of pyrazine),[57] the IAM-SCAR onset for the inelastic events occurs at ~10 eV, as for anthacene. Despite this initial discrepancy, both methods are in good agreement at around 10-15 eV and the IAM-SCAR method provides a smooth continuation for the R-matrix calculation at higher energies. As

discussed in section 3.1.1, although rotational and vibrational excitations are ignored, this restriction is not thought to be significant, at the energy range of interest, for the present non-polar molecule.

Present TCS computed with the IAM-SCAR method are in excellent agreement with the R-matrix[56] results at the common energies of overlap, as can be seen in Figure 3.17. Note, in fact, that both curves merge each other around 20 eV. Additionally, further TCS have been measured in the Madrid's laboratory in the 10-500 eV energy range, by means of a newly-built experimental setup developed by Fuss *et al.*[51]. The system consists on the magnetic confinement (0.2 T) of the incident electron beam during the entire path within the collision chamber up to reaching the detector, formed by two microchannel plates. It can be seen that the experimental and theoretical results show a general agreement, to within 11-25%, over the whole energy range where the measurements were performed, i.e., 10-500 eV. When comparing theoretical and experimental TCS, one should keep in mind that the experimental values are dependent on the angular restrictions, since the experimental apparatus does not perfectly discriminate against elastically and rotationally scattered electrons to the forward ($0 \leq \theta \leq \delta\theta$) and backward angles ($180-\delta\theta \leq \theta \leq 180$). Thus, experimental TCS represent a lower bound on the true TCS values. In order to provide a more realistic comparison, both R-matrix and IAM-SCAR elastic DCS have been partially integrated in the angular range covered by the experiment, in the attempt to mimic the experimental conditions. Subsequently, the inelastic contribution has been added to obtain the theoretical partially integrated TCS. It can be seen in Figure 3.17 that, in the low energy region, the experimental TCS lay between the partially integrated CS obtained from the R-matrix and IAM-SCAR methods. With increasing energies, the level of accord between the experimental TCS and the IAM-SCAR partially integrated CS markedly improves and, above ~70 eV, becomes excellent.

Recommended Set of Integral Cross Section Data

As a summary of the previous discussion, a set of recommended values for integral elastic, inelastic and total cross sections at various selected energies from 0.1 eV up to 10000 eV are given in Table 3.4. From thermalized energies up to the ionization threshold, cross sectional data is reliably provided by the R-matrix method.[56] The numerical uncertainty of this method is estimated to be also around 10%, according to the good agreement observed between this method and experimental measurements for various molecules.[59] Above the ionization potential, integral CSs calculated with the IAM-SCAR model are recommended. At intermediate energies, where both approaches are smoothly joined together, the numerical error is estimated to be of ~10 %, given the good agreement found between both models.

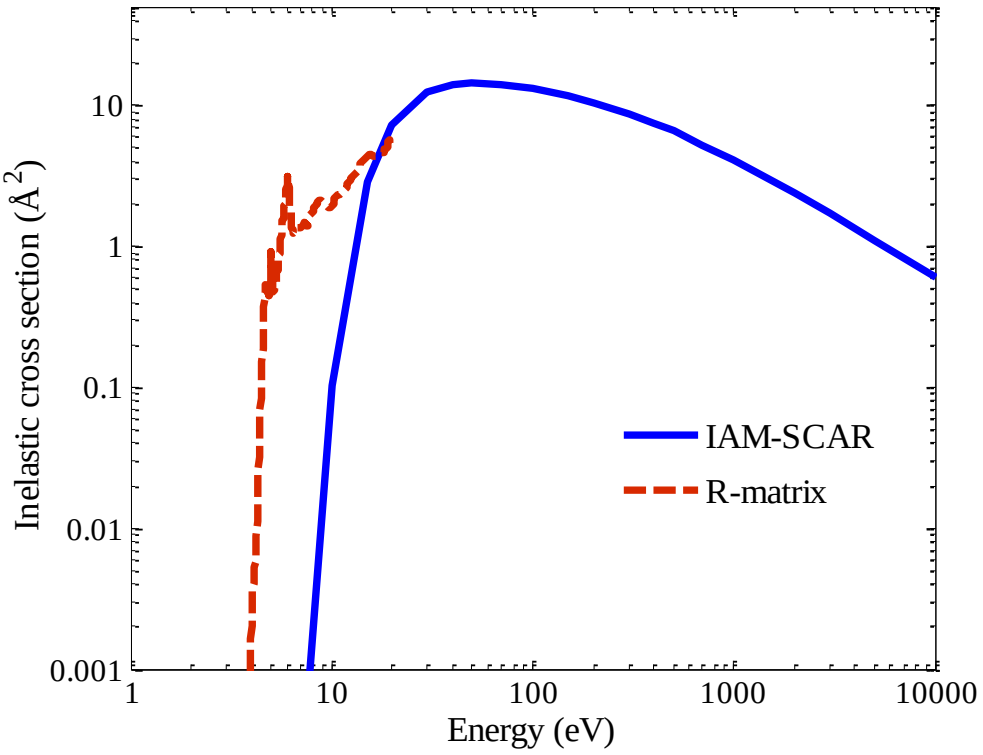

Figure 3.16: Integral inelastic cross section for electron scattering by pyrazine computed with IAM-SCAR method and the R-matrix theory[56].

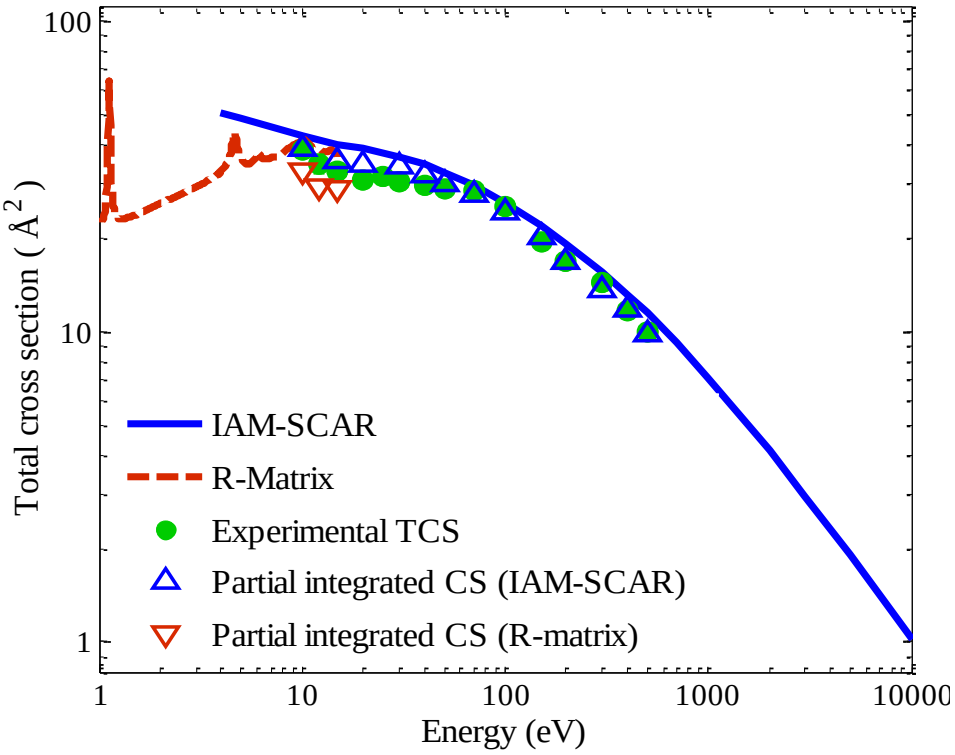

Figure 3.17: TCS for electron scattering by pyrazine: present IAM-SCAR calculations, R-matrix theory,[56] experimental TCS.[52] Partially integrated CS values (i.e. emulating the experimental conditions) are given for the theoretical IAM-SCAR and R-matrix results.

Table 3.4: Recommended elastic, electronically inelastic (electronic-state excitation and ionization) and total integral cross sections for electron scattering from pyrazine in the energy range from 0.1 to 10000 eV.

Energy (eV)	Elastic (Å2)	Electronically Inelastic (Å2)	Total (Å2)
0.1	19.88		19.88
0.3	28.34		28.34
0.4	25.94		25.94
0.5	24.11		24.11
0.7	22.23		22.23
1.0	22.15		22.15
1.5	23.59		23.59
2	25.66		25.66
3	29.07		29.07
4	32.56	0.0022	32.57
5	35.55	0.8735	36.43
7	34.68	1.35	36.04
10	39.21	1.8991	41.11
15	36.96	4.2256	41.19
20	31.36	7.308	38.67
30	24.16	12.348	36.51
40	20.55	13.86	34.41
50	18.20	14.252	32.45
70	15.18	14.14	29.32
100	12.52	13.3	25.82
200	8.62	10.5	19.12
300	6.83	8.68	15.51
500	4.96	6.524	11.48
1000	3.02	4.06	7.08
2000	1.75	2.3828	4.13
3000	1.24	1.7024	2.95
5000	0.80	1.1004	1.90
10000	0.43	0.59	1.02

3.2. Polar Molecules

The study of collisions between charged particles and polar molecules is of main interest in radiation biological physics, since the majority of molecules of biological interest have a considerably high permanent dipole moment (e.g., water,[60] DNA subunits,[61-63] etc; see Table 3.5). Polar targets, however, normally entail extra complications in experimental studies. The main reason for this is that the angular distribution of the scattered charged particles is strongly peaked in the forward direction, but the angular resolution of the experimental apparatus is normally not good enough to distinguish the scattered particles from the primary beam, since they are deflected within the finite width of the detector apertures. Furthermore, the excitation energy of the rotational levels is so small that the energy resolution of the experiments does not allow these inelastic processes to be distinguished from the elastic events.

Theoretical scattering studies involving polar molecules also have their difficulties and are harder to model than the equivalent calculations with non-polar targets. This is mainly due to the long-range nature of the dipole potential, which implies that a large number of partial waves should be included in the wave function expansion. This, in turn, normally leads to a significant increase in the computational requirements.

As a computational test for such types of molecules, calculations involving two polar molecules, hydrogen cyanide (HCN) and pyrimidine (1,3-diazine, $C_4H_4N_2$), have been carried out. The computational approach followed in order to calculate CS is based on the scheme proposed in section 3.1, although additional rotational excitations have been calculated. At low energies, either the ePOLYSCAT model or the R-matrix method is employed in combination the POLYDCS code, yielding dipole-corrected cross sections. The present CSs were calculated assuming the molecule is a symmetric top. We have considered transitions from the ground state ($j = 0$) to rotational states up to $j = 3$ and $j = 9$, for HCN and pyrimidine, respectively. At high energies, rotational excitation was included in our IAM-SCAR calculations as an independent dipole interaction channel, as described in section 2.4.4.

Table 3.5: Dipole moment of various biomolecules.

Molecule	Dipole moment (μ)
Water[60]	1.8 D
Adenine[62]	2.5 D
Thymine[61]	4.1 D
Guanine[62]	7.1 D
Cytosine[61]	7.0 D
THF[63]	1.6 D

3.2.1. Hydrogen Cyanide

Hydrogen cyanide (HCN) is a simple polyatomic molecule with linear structure. HCN is present frequently as a component of numerous systems of biological interest. In addition, this molecule is of main interest in the astrophysical community, since it has been postulated as an initial compound for the formation of more complex organic molecules in the Interstellar Medium (ISM)[64] and in Titan's atmosphere.[65,66] Hence, studies on electron collisions with HCN are important to understand the evolution mechanisms on these environments. From a fundamental point of view, hydrogen cyanide is of significant interest since it possess a strong permanent dipole moment[67] of $\mu = 2.98$ D.

Electron collisions with HCN have been the subject of numerous studies in the low energy domain focused on identifying the low-lying shape resonances and fragmentation pathways via dissociative electron attachment. Early experiments performed by Inoue,[68] revealed the formation of the anion CN^- around 2.5 eV of electron collision energy. Then, Edard *et al.*[69] provided vibrational excitation CSs and showed the existence of a resonance associated with a π^* triple-bond orbital at around 2.3 eV and another one associated with a $\sigma^*_{C\text{-}H}$ orbital at ~6.7 eV. Similarly, Burrow *et al.*[70] characterized the temporary anion state of HCN and identified a low-lying π^*-resonance of shape character at around 2.26 eV. More recently, May *et al.*[71], using a time-of-flight ion spectrometer, measured absolute partial cross sections for the formation of vibrationally excited CN^- fragments via DEA channel, which peaked at ~1.85 eV. Despite all these investigations, electron scattering studies at energies out of the region where resonances take place are scarce. To the best of our knowledge, integral and differential elastic CS have been only measured by Srivastava *et al.*[72] at the energy range 3 - 50 eV and angles from 20º to 130º by means of a crossed electron-molecular beam technique. From the theoretical point of view, various studies have also been performed. Firstly, Jain and Norcross[73,74] located a π^*-type TNI at the equilibrium geometry and found that the stretching of the C–H and C≡N bonds, as well as the bending of the molecule, led to the appearance of a σ^* broad resonance. Varambhia and Tennyson[75] calculated the resonance parameters using the R-Matrix technique. Chourou and Orel[76] studied the low-energy resonance structures and dissociation mechanisms of HCN using the complex-Kohn variational method in a three-dimensional space. Calculations on electron-HCN collisions CS have been performed by Jain and Baluja[77], who reported elastic CS and TCS up to 5000 eV. Alternatively, differential and integral rotational excitation CS can be found in a recent study published by Faure *et al.*[78] who employed the R-matrix method in combination with the adiabatic-nuclei-rotation approximation.

Previous works have been all limited to a rather restricted energy range. Thus, the main objective of the present work[79] is to provide scattering data over a broader region of electron energies, from 0.1 eV up to 10000 eV.

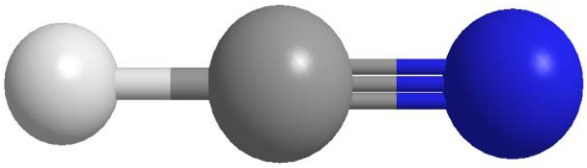

Figure 3.18: Equilibrium geometrical configuration of the present target molecule HCN.

Low-energy Calculation Details

HCN belongs to the $C_{2\infty}$ point group and contains 14 electrons. The electronic configuration of the ground state of HCN is $(1\sigma)^2(2\sigma)^2(3\sigma)^2(4\sigma)^2(5\sigma)^2(1\pi)^4\ ^1\Sigma^+$. Cross sections have been calculated within the fixed-nuclei approximation at the equilibrium geometry[80] (CN = 1.11 Å and CH = 1.06 Å; see Figure 3.18), by means of the ePOLYSCAT model. Although the $C_{\infty v}$ point group possesses infinite IRs, only the contribution of the dominant ones are considered in the present calculations, i.e., Π, Σ, Δ and Φ. The neutral N-electron target wavefunction was generated with the Gaussian 03 suite of codes[24] at the Hartree-Fock level using two customary basis sets: 6-311++G(3df, 3pd) and aug-cc-pVTZ. The molecular structure and the dipole moment generated with both basis sets are listed in Table 3.6. It can be seen that these parameters are in close agreement with the experimental values[80,67] when the 6-311++G(3df,3pd) basis set is employed. The tensorial components of the dipole polarizability obtained with this model are $\alpha_{xx} = \alpha_{yy} = 1.93$ Å^3 and $\alpha_{zz} = 3.18$ Å^3. The resulting computed spherical polarizability is $\bar{\alpha} = 2.34$ Å^3, which is in fair agreement with earlier calculations reported by Grain *et al.*[81] ($\bar{\alpha} = 2.32$ Å^3). The present polarizability values calculated by us are employed to define the correlation-polarization model potential V^{CP} (2.25).

Table 3.6: Computed geometrical properties (bond lengths) and dipole moment (μ) of HCN, obtained with the ePOLYSCAT code using the basis sets 6-311++G(3df, 3pd) and aug-cc-pVTZ. Experimental values are given for comparison.

	6-311++G(3df, 3pd)	**aug-cc-pVTZ**	**Experiments**
C≡N (Å)	1.057	1.056	1.06[a]
C–H (Å)	1.124	1.124	1.11[a]
μ (D)	3.17	3.26	2.98[b]

[a] From Sutton.[80]
[b] From DeLeon and Muenter.[67]

We perform further tests concerning the size of the partial wave expansion for the scattered electron (l_{max}) and the size of the radial integration box. Partial elastic CSs associated with the Π symmetry have been calculated using different number of partial waves, i.e., l_{max} = 10, 20, 60 and 100. In addition, three different sizes for the interaction physical box have been tried, i.e., B = 25, 100 and 500 Å. It can be seen in Figure 3.19 that calculations including partial waves up to l_{max} = 60 and a physical box with a radius of 25 Å, provide numerical converged results. The multipolar expansion of the potential included terms up to λ_{max} = 120.

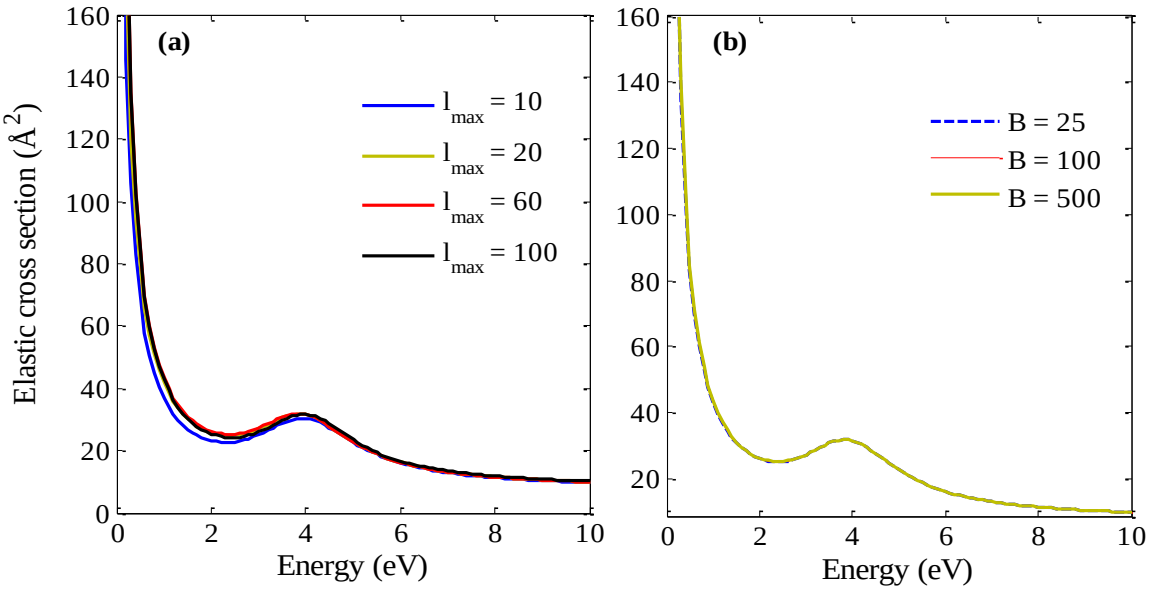

Figure 3.19: (a) Partial elastic cross sections for the Π symmetry computed including l_{max} = 10, 20, 60 and 100 in the partial wave expansion with the physical box fixed at B = 25 Å. Panel (b) shows elastic cross sections computed with three different radial box sizes, i.e., B = 25, 100 and 500 Å.

Low-lying Resonant States

Partial elastic cross sections computed for the different IRs are reported in Figure 3.20. One low-lying shape resonance of π*-type character is identified at ~4 eV. Interestingly, when one allows both the C–H and C≡N bonds to be stretched by about a 40% of its equilibrium value, i.e., C–H ≥ 1.6Å and C≡N ≥ 1.7Å, the scattering calculations revealed the presence of a second resonance of σ*-type character at ~7 eV. This finding is in accordance with previous experimental and theoretical investigations.[69,73] Figure 3.21 reports the eigenphase sums which shows a clear π-jump at the resonance energy position, both for the π* and σ* resonances. The resonant parameters (energy position, width and the corresponding lifetime), derived from the Breit-Wigner formula (Eq. 2.43), are listed in Table 3.7. Similar to what was has been observed for anthracene (section 3.1.1), the resonance positions are shifted towards higher energies (~1 eV) compared to the energy proposed by the experimentalists.

The data in Figure 3.22 report the features of the computed π* (top panel) and σ* (bottom panel) resonant electron: on the right side-panel the real part of the scattering wavefunction is shown, which can be compared with the corresponding virtual MO of the same symmetry from the neutral calculations (left side-panel). In both cases, a strong similarity is observed between the two spatial features, since both the virtual and the scattering wavefunctions are chiefly located over the two bond regions.

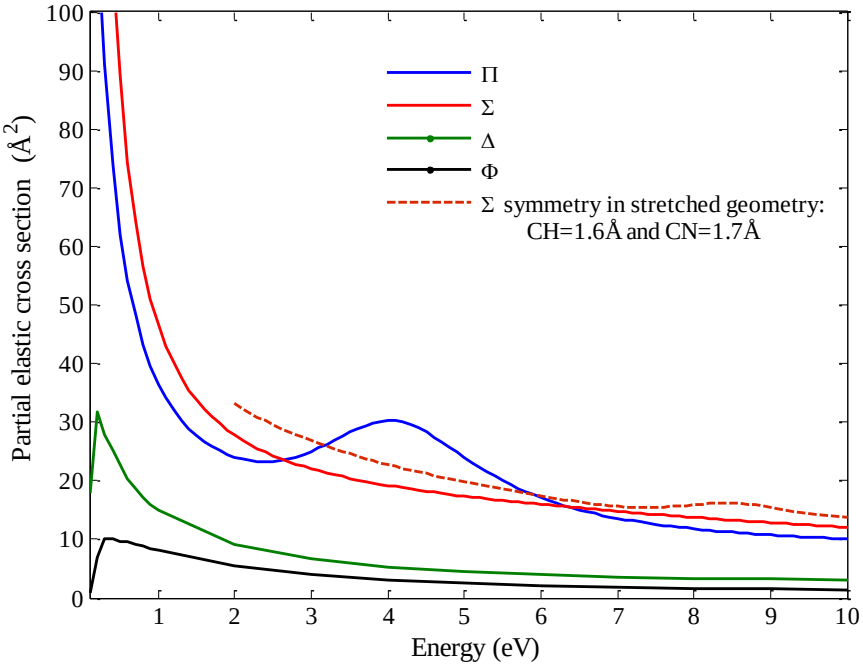

Figure 3.20: Partial elastic cross sections for electron scattering from HCN for the contributing symmetries Π, Σ, Δ and Φ.

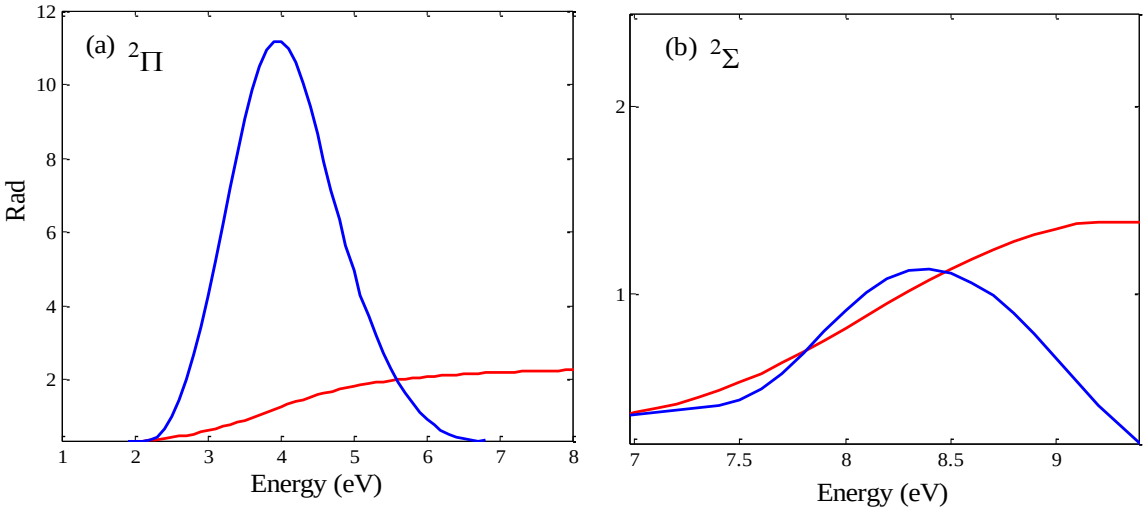

Figure 3.21: Computed eigenphase sums, fitted to a Breit-Wigner formula, together with their first derivatives, for the symmetries of HCN in which we found a maximum in the corresponding cross sections. See text for further details.

Table 3.7: Computed resonant parameters for HCN.

Symmetry	Energy (eV)		Width (eV)	Lifetime (s)
	Present work	Experiments[69,71]		
$^2\Pi$	4.1	2.3	0.59	$1.17.10^{-15}$
$^2\Sigma$	7.7	6.7	0.53	$1.24.10^{-15}$

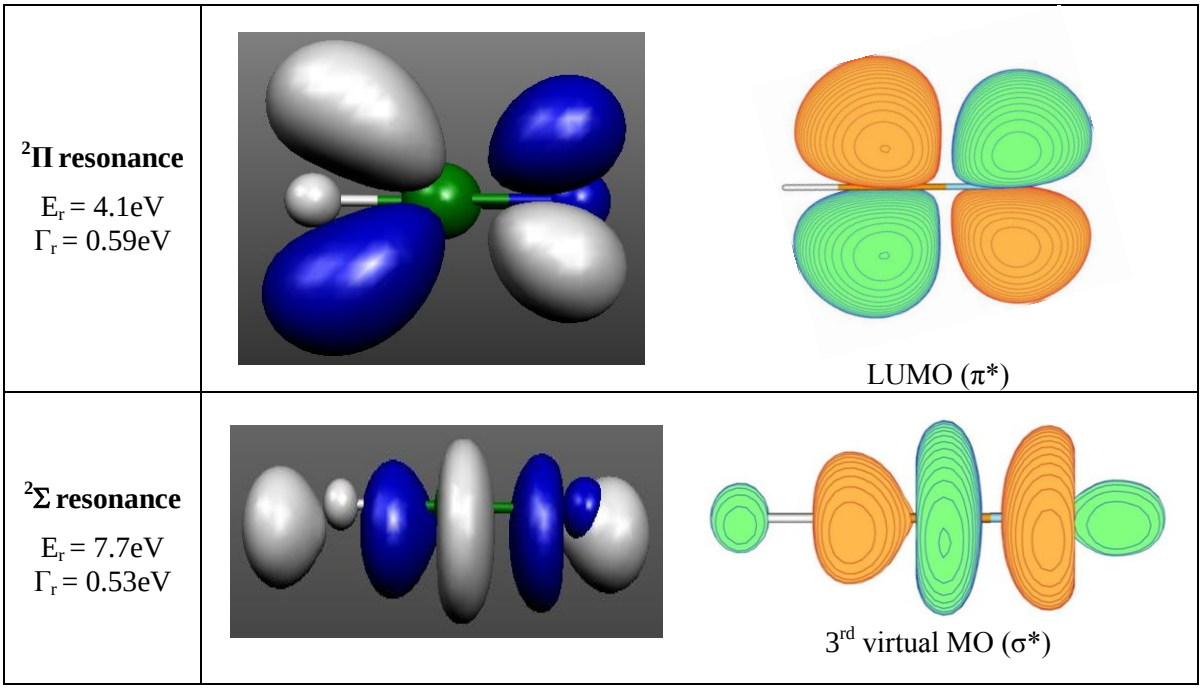

Figure 3.22: Computed scattering wavefunction (right side) and the corresponding virtual orbital wavefunction (left side) for the $^2\Pi$ resonant state at the equilibrium geometry (top panel), and for the $^2\Sigma$ resonant state at the stretched geometry: C–H = 1.6Å and C≡N = 1.7Å (bottom panel).

Evolution of the Metastable Anionic States.

Once the shape resonances have been characterized, we are further interested in examining their behaviour upon bond deformation to identify potential dissociative electron attachment pathways in HCN.[82] During a resonant collision, the energy of the excess electron may be transferred into the internal degrees of freedom of the molecular bonds.Various experimental works[69,71] have reported strong C≡N stretching activity accompanied by bending vibrations during the resonant attachment of the excess electron to hydrogen cyanide, which may cause ultimately the fragmentation of the parent molecule,

$$HCN(^1\Sigma^+, v) + e^-(E) \rightarrow HCN^{-*}(^2\Pi_g) \rightarrow CN^-(^1\Sigma^+, v') + H(^2S). \quad (3.1)$$

In this section we show how the SA-SCE model can be successfully employed to follow the behaviour of shape resonances, as stretching and bending deformations are taking place.

Whenever a single specific bond is responsible for the breakup of the metastable anion, one then observes shifts in the computed resonance position and width while that bond is stretched, with a further dissociative behaviour of the one-dimensional (1D) potential energy curve (PEC) associated to the (N+1)-electron molecular anion formed during the resonant process. Note, however, that this is an approximate description since the dynamical coupling between the resonant electron and the bound nuclei is not explicitly included, but instead, we adiabatically follow a selected bond deformation. Previous studies carried out by Gianturco and co-workers[83] indicated that our procedure preserves the qualitative picture of the fragmentation paths.

Firstly, a series of calculations regarding the π* resonance were performed: (i) stretching of the C-H bond while maintaining the C≡N bond at the equilibrium value, (ii) stretching of the C≡N bond while the C-H bond remains at the equilibrium geometry, (iii) simultaneous stretching of both bonds. Figure 3.23 reports the resonance energy upon C-H and C≡N stretching, where the error bars represent the width of the resonant state. It is clearly seen that when the C≡N is lengthen beyond the equilibrium geometry, the resonance energy moves towards the zero-energy threshold and becomes progressively narrower, i.e., longer lived. In contrast, stretching of the C-H bond cause the resonant state to shift to higher energies with broader width, in other words, it becomes more instable and is prone to decay via electron detachment. In Figure 3.24 we examine the spatial modifications of the resonant wavefunction upon bond deformation, which show that the excess electron is mainly localized on the CN^- spatial region.

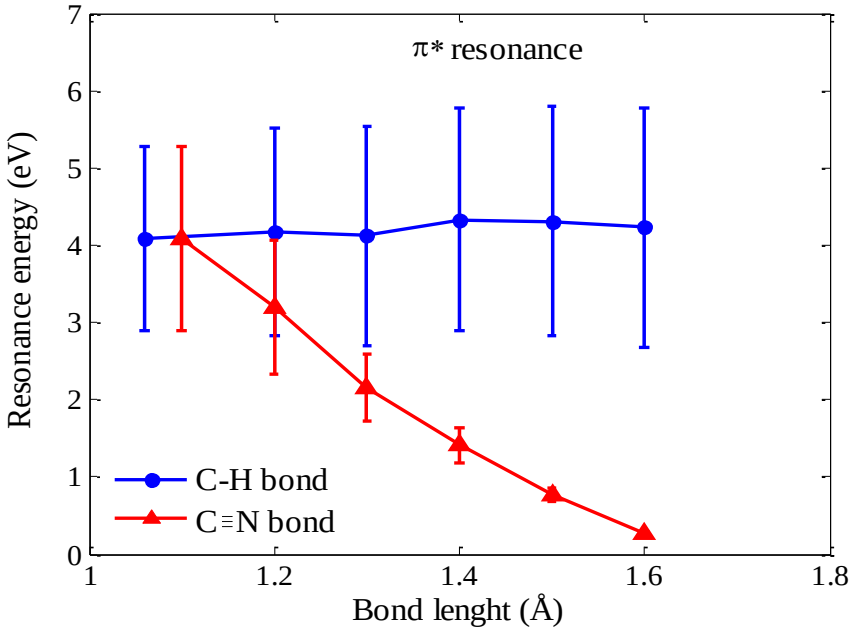

Figure 3.23: Computed variations in the resonant features (E_r and Γ_r) of the π* resonance as function of both C-H and C≡N stretching.

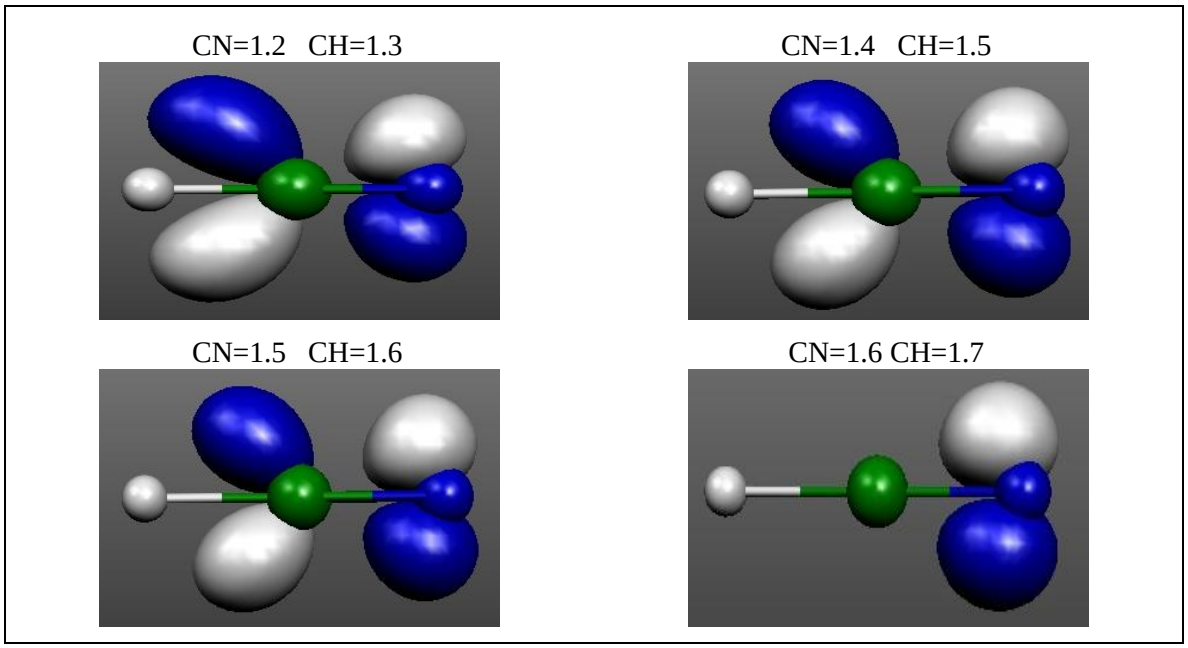

Figure 3.24: Spatial resonant wavefunctions (real part) for the π* resonance as function of the stretching of both C-H and C≡N bonds (all distances are in Å).

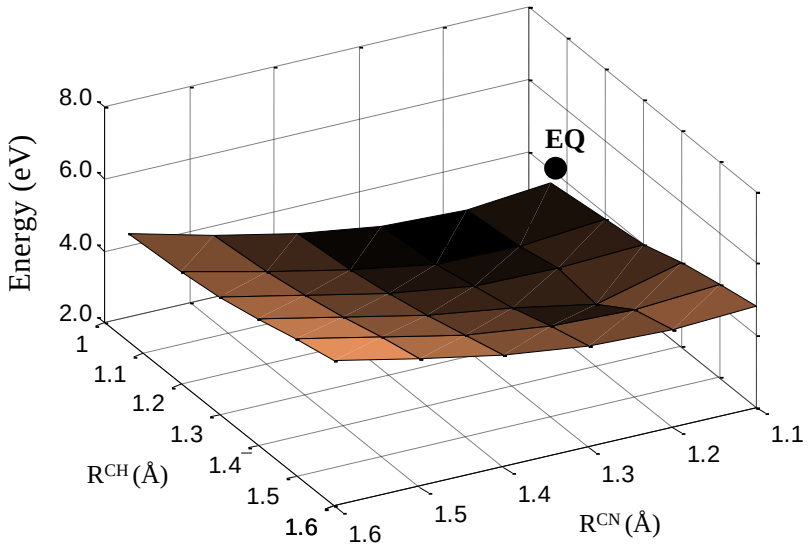

Figure 3.25: Computed real part of the PES for the $^2\Pi$ (N+1)-electron resonant state as function of the stretching of both C-H and C≡N bonds.

Figure 3.25 shows the 2-dimensional potential energy surface (PES) for the $^2\Pi$ (N+1)-electron resonant state. The computed potential energy values are given by the familiar expression (see e.g. Carelli *et al.*[84] and references therein),

$$E_{tot}(R) = E_{res}(R) + E_N(R) - E_N(R_{eq}), \tag{3.2}$$

where E_N are the electronic energies of the parent molecule (at the equilibrium geometry R_{eq} and at a set of geometries identified as R) and $E_{res}(R)$ is the energy location of the resonant electron. It can be seen in Figure 3.25 that the associated potential energy initially decreases upon bond stretching, but then rapidly produces a repulsive region. This indicates that, although the excess charge is localized over the C≡N region, the nuclei do not dissociate upon bond stretching, in agreement with the findings of other groups.[74,76]

A similar procedure is now applied to the σ* resonance. Figure 3.26 shows that the resonance moves down in energy and becomes narrower when both C-H and C≡N bonds are stretched (starting from the geometry where this resonance first appears, i.e., CH = 1.6Å and CN = 1.7Å). This effect is more dramatic if both bonds are stretched simultaneously (not shown). However, in this case, the excess electron is distributed over the whole molecule (see Figure 3.27). Figure 3.28 reports the corresponding 2-dimensional PES for this metastable state (real component) of (N+1) electrons, which shows a dissociative behaviour. In this case, the σ* resonance is strongly coupled with the C≡N stretch vibrational mode, in agreement with the experimental results.[69,71] As suggested by Chorou and Orel,[76] it is expected that the $^2\Sigma$ curve will cross the potential energy curve of the $^2\Pi$ state, in regions outside the areas shown.

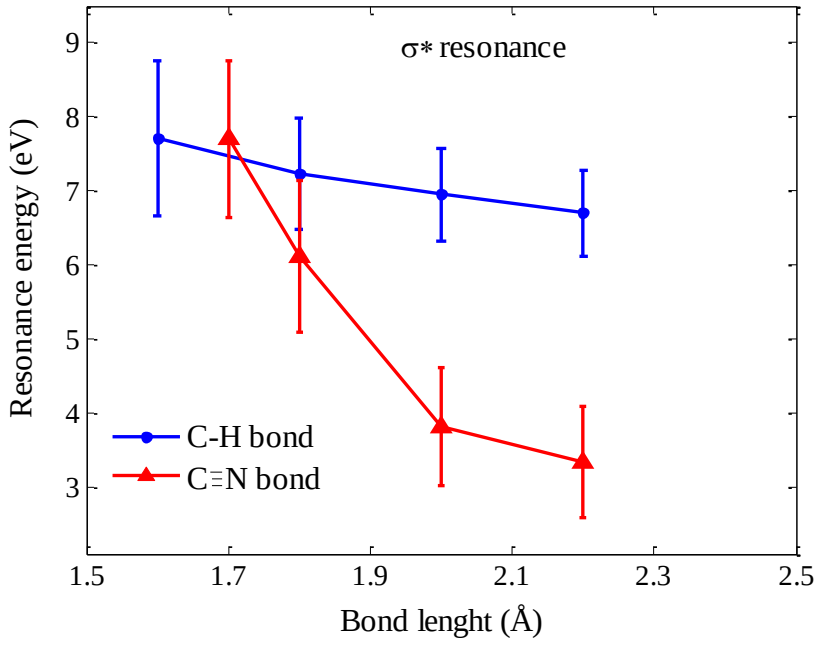

Figure 3.26: Computed variations in the resonant features (E_r and Γ_r) of the σ* resonance as function of both C-H and C≡N stretching.

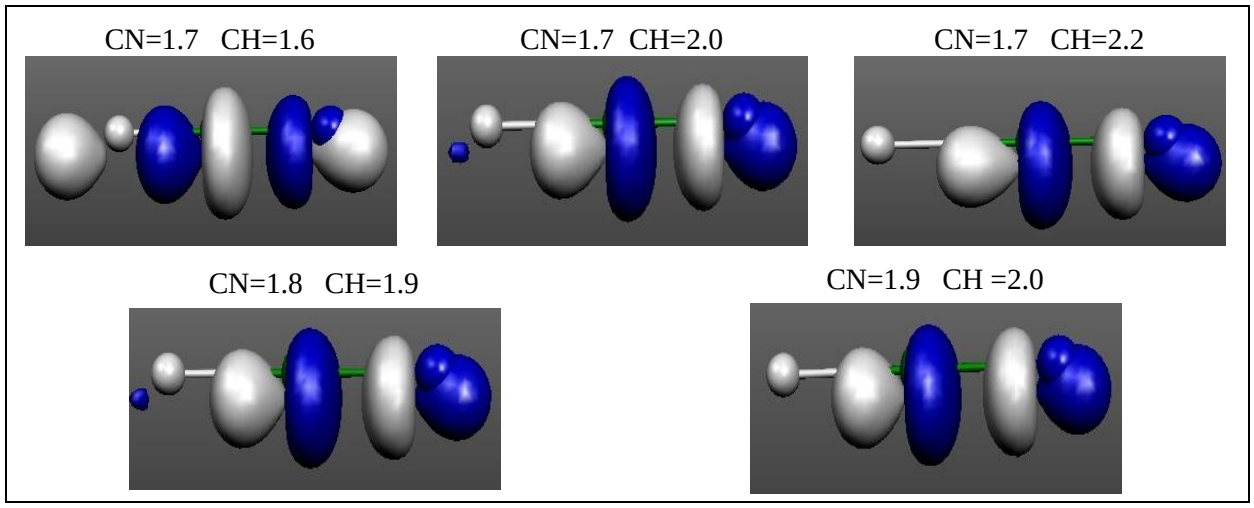

Figure 3.27: Spatial resonant wavefunctions (real part) for the σ* resonance as function of the stretching of both C-H and C≡N bonds (all distances are in Å).

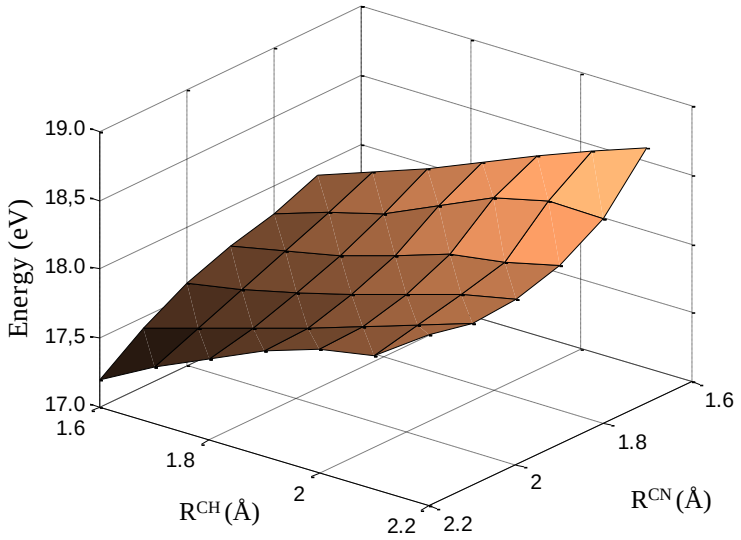

Figure 3.28: Computed real part of the PES for the $^2\Sigma$ (N+1)-electron resonant state as function of the stretching of both C-H and C≡N bonds.

On the other hand, earlier experimental studies on vibrational excitation effects,[69,71] found strong C≡N and bending excitations during the resonant attachment into the π*-orbital. Also, a computational study reported recently by Chorou and Orel[76] indicated that, by moving the HCN molecule away from linearity, the ensuing crossing between the two initial $^2\Pi$ and $^2\Sigma$ PESs will become avoided and the initial resonant compound can now undergo H-tunnelling to dissociation into CN^- +H, producing a vibrationally excited CN^- fragment. [71] Accordingly, we further analyse the effects of bending on the π* resonance with the SA-SCE model. This action reduces the symmetry of the molecule to the C_s point group and removes the π-degeneracy into A' and A'' components. Figure 3.29 shows the changes in the π* resonance as the molecule is progressively bent from linearity, while keeping the C≡N bond stretched up to CN=1.7 Å. It can

be seen that whereas the A'' component maintains its original π*-character and therefore does not suffer appreciable changes as the molecule in bent, the A' component, which acquires now σ*-like character, decreases rapidly in energy and becomes significantly more stable. The corresponding resonant wavefunction (real part) for the A' component at θ=60º is also reported in Figure 3.29 (right panel). It can be seen that the excess electron is mainly located along the C≡N part of the molecule, indicating the above process to be likely the doorway state to CN^- stabilization.

The fact that our findings are in agreement with earlier experimental[69] and theoretical works,[76] indicate the feasibility of the SA-SCE method to model the dissociation dynamics in small polyatomic targets. This kind of information is particularly important in radiation-induced damage studies, since the radicals and ions formed via DEA can further react with other molecules in the media generating multiple-sites damage (as we will see in more detail in Chapter 5).

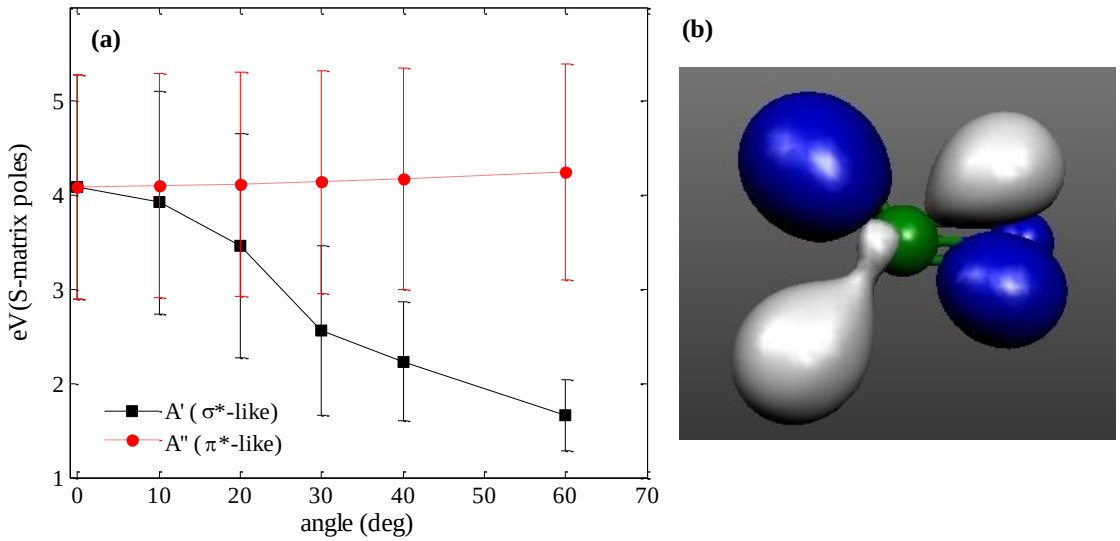

Figure 3.29: (a) Computed variations in the resonant features (E_r and Γ_r) of the π* resonance as the molecule is bent from linearity up to θ=60º. (b) Spatial resonant wavefunction (real part) at θ=60º for the A' resonant state. See text for further details.

Elastic Cross Sections

Calculated elastic CS computed with the ePOLYSCAT code and the IAM-SCAR approach in the energy range 0.1−100 eV and 1−10000 eV, respectively, are shown in Figure 3.30. Note that at intermediate energies, from 15 up to 30 eV, both curves differ from one another in almost 50%. This behaviour is not unexpected and has been already observed in the study of electron collisions with anthracene (section 3.1.1). The origin of this discrepancy is attributed to the omission of the absorption term in the potential used by the SA-SCE theory. It has been proved

that the exclusion of the inelastic processes, leads to an overestimation of the integral elastic CS, especially at energies above the ionization threshold[85] (which in this case it is at 13.6 eV).[86] This behaviour has been checked by removing the absorption contribution from the IAM-SCAR optical potential: when only the elastic channel is considered, the IAM-SCAR CS increase considerably and both methods tend to converge to the same values for increasing energies, as can be seen in Figure 3.30.

In the case of polar targets, special attention must be given when comparing theoretical and experimental data. As mentioned before, experiments do not usually have enough resolution to distinguish electrons scattered after having excited a target molecule rotationally from those elastically scattered. This means that experimental elastic CSs are, to some extent, contaminated by rotational excitations, leading to overestimated elastic CS. Thus, a realistic comparison to the experiments can be only made when including the dipole interaction to our calculations.

Accordingly, elastic CSs dipole-corrected provided by the ePOLYSCAT-POLYDCS approach and the IAM-SCAR+rotations method are also plotted in Figure 3.30. Firstly, it should be highlighted that the agreement between both methods is now markedly improved at intermediate energies. In addition, they are in very good level of accord with the theoretical elastic CSs reported by Faure *et al.*[78], also dipole-corrected. For energies above 11.6 eV up to 50 eV, present calculated CS show good agreement with the experimental results from Srivastava's *et al.*[72]. However, for lower energies (3 and 5 eV), the experimental elastic CS falls below the calculated data. The origin of these differences can be, in part, attributed to the extrapolation method applied to the experimental DCS values, which only cover a limited angular range (see section 3.1.2). To facilitate a direct comparison in equal conditions, both the experimental and theoretical DCS (dipole-corrected) have been partially integrated over the angular range where the experimental data has been measured, i.e., 20º-130º, as shown in Figure 3.31. It can be seen that the agreement between the experiment and theory markedly improves, in particular with the IAM-SCAR method.

This indicates that, in scattering studies involving polar molecules, it is important to compare the experimental DCS at the angles technically accessible by the apparatus with the theoretical DCS dipole-corrected. The present elastic DCSs computed for the electron impact energies 3, 5, 11.6, 21.6 and 50 eV are shown in Figure 3.32. At low energies (3, 5 and 11.6 eV), ePOLYSCAT-POLYDCS shows qualitative agreement with the experimental results.[72] There is also a reasonable good agreement between this calculation and those of Jain and Norcross[73] and Faure *et al.*[78] At these low energies, DCSs calculated with the IAM-SCAR+rotations procedure are somewhat larger, but they come into a better agreement with increasing energies. In particular, the IAM-SCAR+rotations results and the experimental data

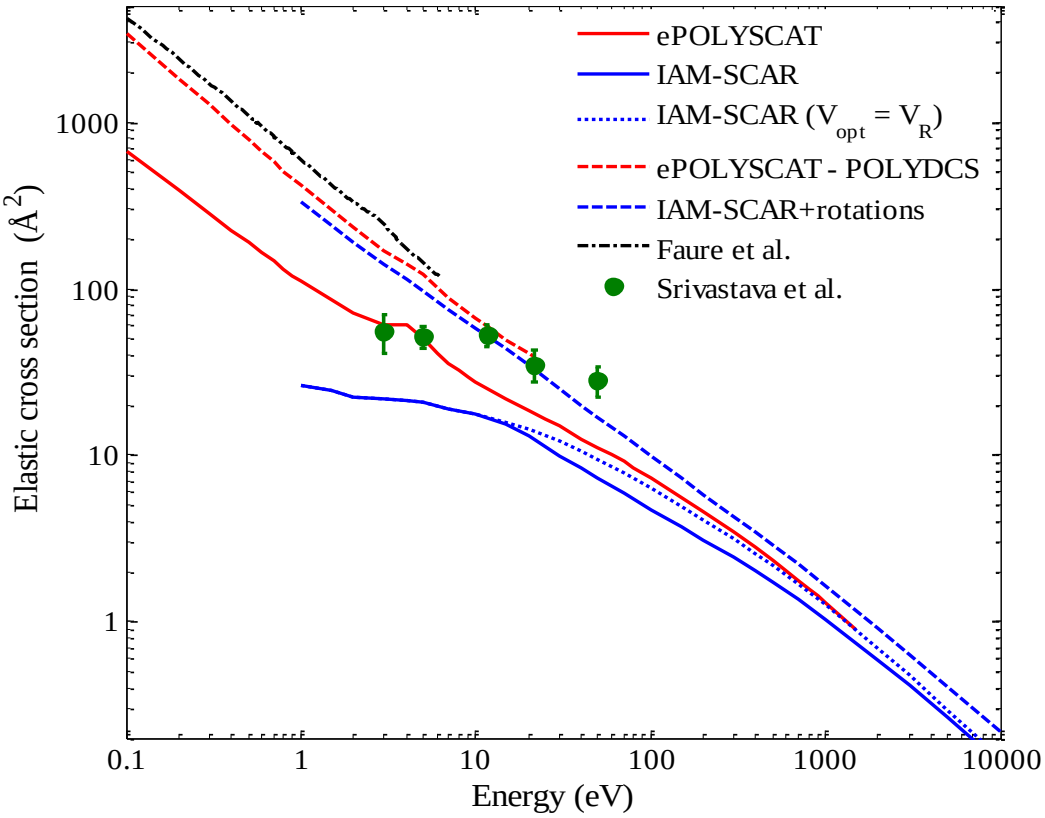

Figure 3.30: Integral elastic cross section for electron scattering from HCN computed with the ePOLYSCAT code and the IAM-SCAR method (the latter with and without the absorption term). Also plotted are the corresponding dipole-corrected cross sections. For comparison, previous theoretical results from Faure *et al.*[78] and experimental measurements from Srivastava *et al.*[72] are also shown.

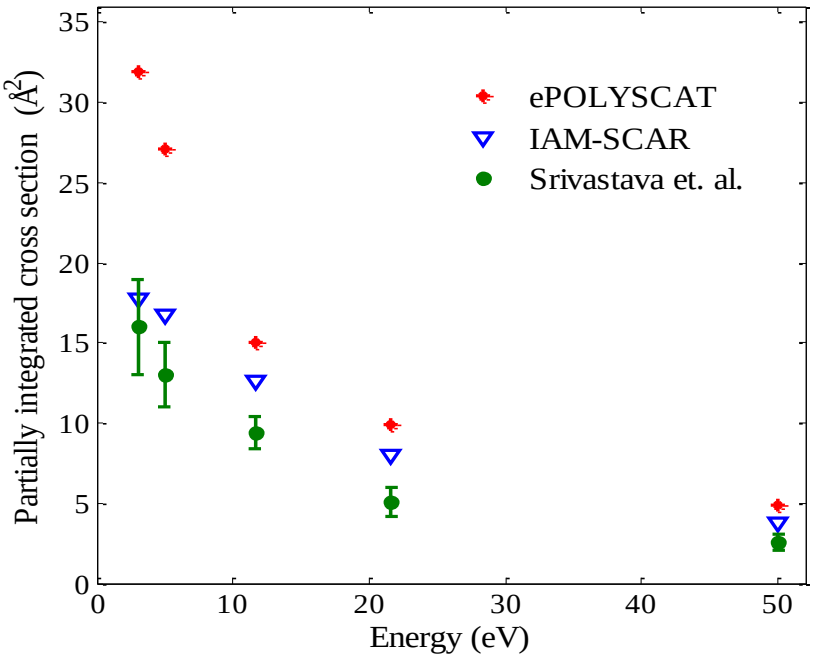

Figure 3.31: Elastic CS values for HCN integrated over the angular range 20º-130º (i.e. emulating the experimental conditions) for the theoretical IAM-SCAR and ePOLYSCAT results, and the experimental measurements from Srivastava *et al.*[72]

are in agreement, within ~10 %, for angles above 90º and 50º, at 21.6 eV and 50 eV, respectively. As discussed in section 2.4.4, the Born approximation is known to fail for relatively large scattering angles whenever the permanent dipole moment of the target molecule is very large, as is the case of HCN. In view of this situation, we introduced a correction based on that suggested by Dickinson,[87] which brings a substantial improvement to the calculated DCS at medium and large angles, as can be seen in Figure 3.32.

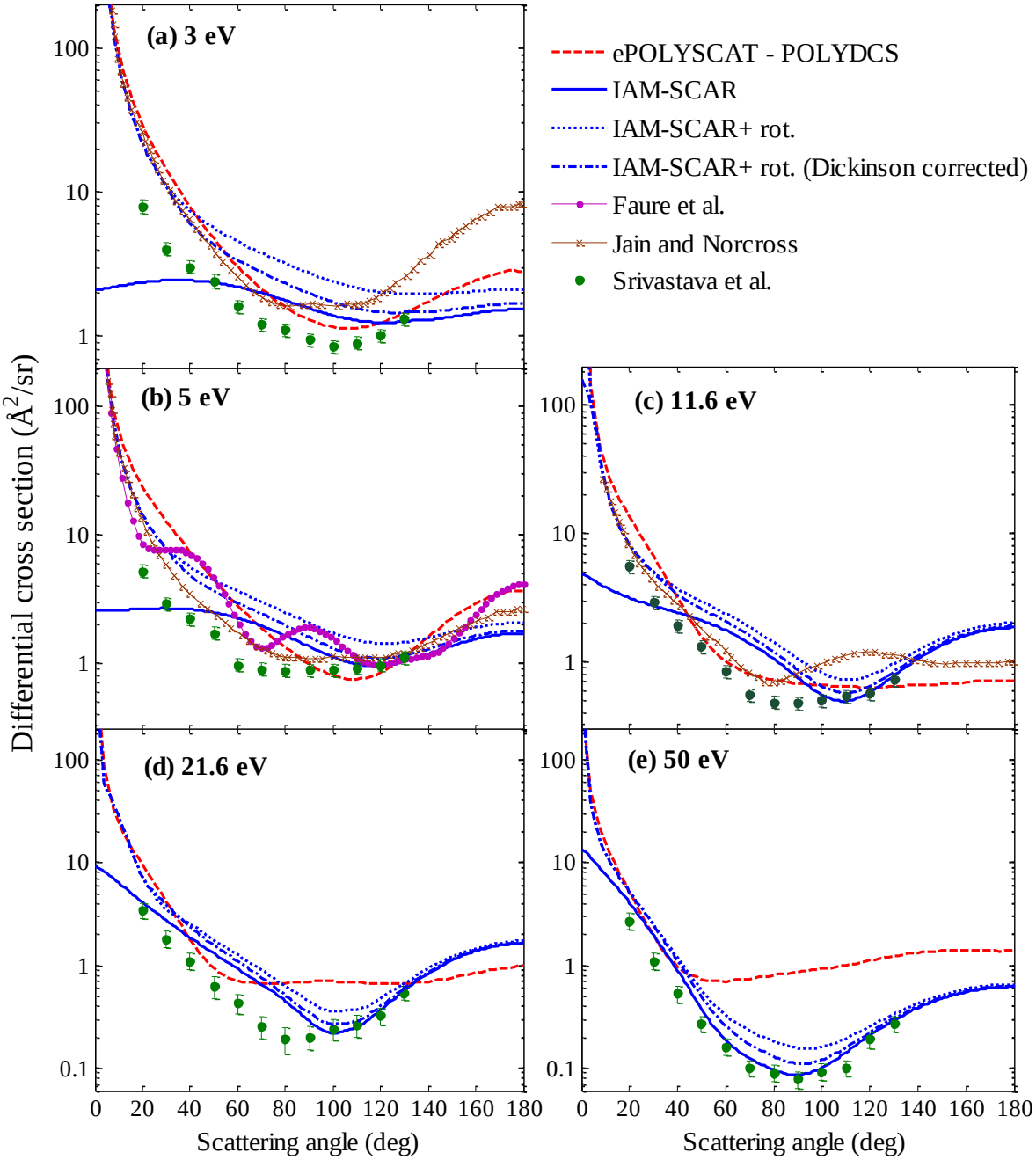

Figure 3.32: Elastic DCS for electron scattering from HCN computed with the ePOLYSCAT–POLYDCS procedure and the IAM-SCAR+rotations model at the incident energies indicated in the panels. The results of the latter model are given with and without a dipole correction. For comparison, previous theoretical results from Faure *et al.*[78] and Jain and Norcross[73], and experimental measurements from Srivastava *et al.*[72] are also shown.

For comparison, DCSs computed with the IAM-SCAR model without including the dipole-induced rotational excitations are also shown in Figure 3.32. Whereas the uncorrected DCSs tend to be flat for small angles, the dipole-corrected elastic DCSs present large gradients in the forward direction. The non-negligible contribution of the forward-angle scattering in the case of polar targets, makes clear why the experimental integral CSs are so sensitive to the extrapolation procedure applied to the measured DCS values to the extreme angles.

Inelastic and Total Cross Sections

Figure 3.33 shows present inelastic CS computed with the IAM-SCAR procedure. TCS are also reported in Figure 3.33 showing good agreement between the ePOLYSCAT-POLYDCS and IAM-SCAR+rotations calculations at the overlapping energy region. This indicates the dominant role of the dipole-induced rotational excitations at these energies. In addition, IAM-SCAR+rotations results show good qualitative agreement with earlier theoretical TCS computed by Jain and Baluja[77] at the 10 - 5000 eV energy range. Although at high energies (above ~2000 eV), TCS computed by Jain and Baluja[77] tend to decay faster, the discrepancies remain within the estimated error of the calculations over the whole energy range.

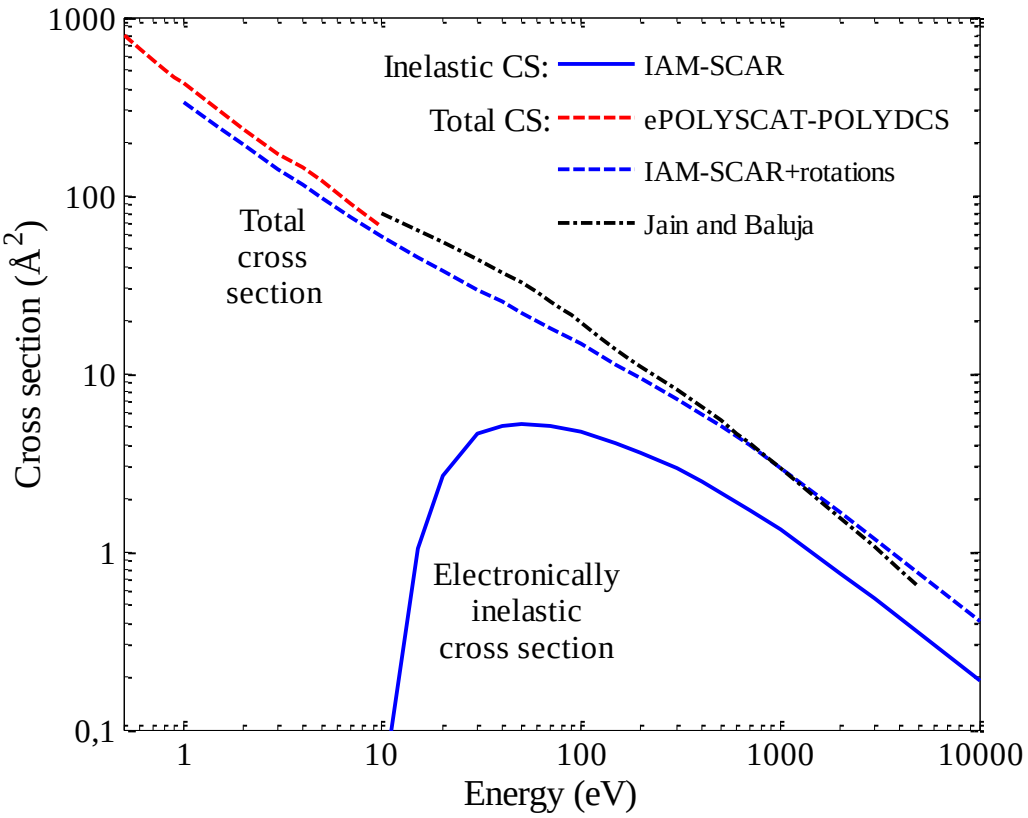

Figure 3.33: Present integral inelastic cross sections computed with IAM-SCAR method. Total cross sections computed with the ePOLYSCAT-POLYDCS and IAM-SCAR+rotations procedures are also shown. For comparison, previous TCS calculated by Jain and Baluja[77] are also plotted.

Recommended Set of Integral Cross Section Data

As a result of the previous discussion, a set of recommended integral elastic, inelastic and total cross sections has been generated from 0.1 eV up to 10000 eV for electron collisions with HCN (see Table 3.8). Up to the ionization threshold (~ 13.6 eV), recommended CSs are given by the SA-SCE model, with the rotational excitations computed by means of the POLYDCS code. Regarding TCS, this approximation is not believed to introduce significant error since elastic scattering and rotational excitations are the dominant processes at these energies, being the electronic excitations a small contribution. On the other hand, CSs computed with the IAM-SCAR model are recommended above ~ 30 eV. At intermediate energies, the cross sectional data is derived from a smooth interpolation between both curves by means of a double logarithmic fitting with an estimated error between 10% - 25%.

Table 3.8: Recommended elastic, rotational excitations, electronically inelastic (electronic-state excitations and ionization) and total integral cross sections for electron scattering from HCN in the energy range from 0.1 to 10000 eV.

Energy (eV)	Elastic ($Å^2$)	Rotational ($Å^2$)	Electronically Inelastic ($Å^2$)	Total ($Å^2$)
0.1	668.95	2765.47		3434.42
0.2	389.05	1416.22		1805.27
0.3	282.14	1005.86		1288.00
0.4	224.79	749.21		974.00
0.5	188.44	597.56		786.00
0.7	145.31	431.49		576.80
1	111.60	311.84		423.44
2	70.73	163.76		234.50
3	60.86	109.41		170.26
4	60.42	81.50		141.92
5	50.50	70.20		120.71
7	35.48	53.62		89.10
10	26.72	39.75	0.04	66.51
15	19.36	27.75	1.05	48.16
20	15.41	21.57	2.69	39.67
30	11.05	15.22	4.59	30.86
50	7.54	9.54	5.21	22.29
70	6.00	6.87	5.07	17.94
100	4.73	5.10	4.68	14.51
200	3.11	2.72	3.58	9.41
300	2.42	1.88	2.91	7.21
500	1.72	1.15	2.15	5.02
1000	1.04	0.61	1.32	2.97
2000	0.59	0.32	0.76	1.68
3000	0.42	0.22	0.54	1.18
5000	0.27	0.14	0.35	0.75
10000	0.14	0.07	0.19	0.40

3.2.2. Pyrimidine

Pyrimidine is another member of the diazines group (1,3-diazine; $C_4H_4N_2$), with the nitrogen atoms situated at positions 1 and 3 of the six-member ring (see Figure 3.34). This structure confers pyrimidine a high permanent dipole moment[88] of 2.334 D and a significant spherical polarizibility[89] of around 8.9 $Å^3$. Pyrimidine is of interest in many fields of study since it forms the molecular basis of several biological molecules, such as cytosine, thymine and uracil. Although these species are potentially more interesting, their low-symmetry and electron-rich make the more symmetric pyrimidine computationally preferable. Thus, pyrimidine is normally used as a model compound to investigate electron and positron interactions with DNA and RNA bases. It is noteworthy that pyrimidine and all the nucleobases show the presence of three low-lying resonances of π^* character, as for pyrazine.[49] These resonances, which are associated with the aromatic ring, play a crucial role in LEEs-induced damage, as we will see more in detail in Chapter 5.

Several studies on electron collisions with pyrimidine have been reported up to now. Elastic DCS were firstly measured by Maljković *et al.*[90] in the gas phase at the incident energy range 50-300eV. Recently, this experimental data have been completed by Palihawadana *et al.*[91], who measured the elastic angular distributions at lower impact energies, ranging from 3 eV up to 50 eV. In the latter work, the authors also measured electronically inelastic cross sections within the same energy range. In addition, Jones *et al.* [92] reported experimental DCSs for electron impact electronic excitation in the energy range 15−50 eV. Studies on (e^-,$2e^-$) ionization have been carried out by Builth-Williams *et al.*[93]. Additionally, electron energy-loss measurements in the energy range between 2 and 15 eV have been reported by Ferreira da Silva *et al.*[94]. Experiments have been also run in the condensed phase by Levesque *et al.*[95] who measured vibrational and electronic excitation cross sections. Theoretical elastic CSs were calculated at low energies by means of the Schwinger multichannel technique.[91] Mašín *et al.*[96] determined both elastic and electronically inelastic CSs using the R-matrix method. More recently, scaled quasi-free scattering calculations have been reported by Ferraz *et al.*[97] In the high energy domain, integral elastic CS and TCS have been calculated using the IAM-SCAR method.[90,91,98]

In the case of positron scattering, experimental studies encounter similar problems plus some additional difficulties due to the significantly reduced incident positron fluxes. From the theoretical point of view, despite the fact that no exchange effects are present, positron collisions are harder to model than the equivalent scattering of electrons. This is mainly due to the occurrence of positronium formation and the strong correlation-polarization interaction. This is reflected in the data available in the literature for positron-pyrimidine collisions, which is much scarcer than in the electron case. In particular, Zecca *et al.*[99] measured TCS in the incident

energy range 0.3- 45 eV, using a positron transmission beam technique. Just recently, Palihawadana *et al.*[100] have measured, for the first time, integral and differential elastic CS, together with integral inelastic CS, for energies for from 1 to 180 eV. These authors have also reported experimental CS for the Ps formation. However, to the best of my knowledge, no theoretical data for positron scattering was available prior to this work.

Therefore, the purpose of this section is to firstly complete the study on electron collisions with pyrimidine and provide a set of recommended cross sections over a much wider energy range.[98] Subsequently, the first theoretical cross sections are presented for positron scattering from pyrimidine.[101]

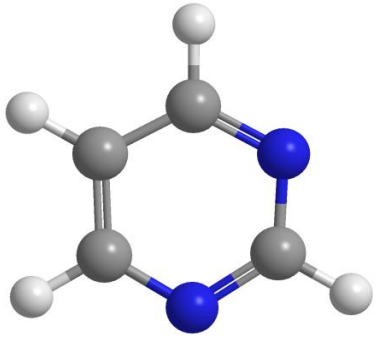

Figure 3.34: Equilibrium configuration of the present target molecule pyrimidine.

3.2.2.1. Electron Scattering from Pyrimidine

Low-energy Calculation Details

Pyrimidine has 42 electrons and belongs to the C_{2v} point group. Fixed-nuclei calculations have been performed at its equilibrium geometry[102] for the corresponding IRs, i.e., A_1, B_1, B_2 and A_2. Consistent with the e^--scattering study with the non-polar structural isomer pyrazine (section 3.1.2), the R-matrix method is preferred at low energies. The main parameters that affect an R-matrix scattering calculation are the number of continuum partial waves included, the R-matrix radius, the choice of the atomic basis set, and the number of virtual orbitals. The target orbitals were generated by Mašín *et al.*[96] using the Hartree-Fock self-consistent field (SCF) and the state-averaged CASSCF (SA-CASSCF) methods for the SEP and CC calculations, respectively. Tests of convergence for the target description and scattering calculations were also performed by Mašín *et al.*[96] According to that work, the most physical results are obtained when using the compact basis set cc-pVDZ, an R-matrix radius of $a=13a_o$ and $l = 4$ partial waves in the continuum basis set.[103] Maintaining these parameters, some more tests have been performed at the SEP and CC level of approximation, as shown below.

- ***Static-Exchange plus polarization (SEP) calculations***

Within this model, the target orbitals were divided in a frozen core with 12 electrons arranged in double occupied orbitals, and a valence space with 29 movable electrons. These orbitals together with the selected space of virtual orbitals constitute the target space. Calculations were performed with the maximum size of the target space: (44, 17, 32, 11), i.e., 44 molecular orbitals of a_1 symmetry, 5 of b_1, 12 of b_2 and 3 of a_2. Considering that (11, 2, 7, 1) of them are occupied orbitals in the ground state of target, this target space is associated with 83 virtual orbitals. In addition, cross sections were calculated with target orbital spaces of ($19a_1$, $5b_1$, $12b_{12}$, $3a_2$), ($26a_1$, $8b_1$, $17b_{12}$, $5a_2$) and ($37a_1$, $12b_1$, $24b_{12}$, $8a_2$), which are associated with 18, 35 and 60 virtual orbitals, respectively. Partial elastic CSs for the four IRs of the C_{2v} point group are plotted in Figure 3.35 for the different target space sizes.

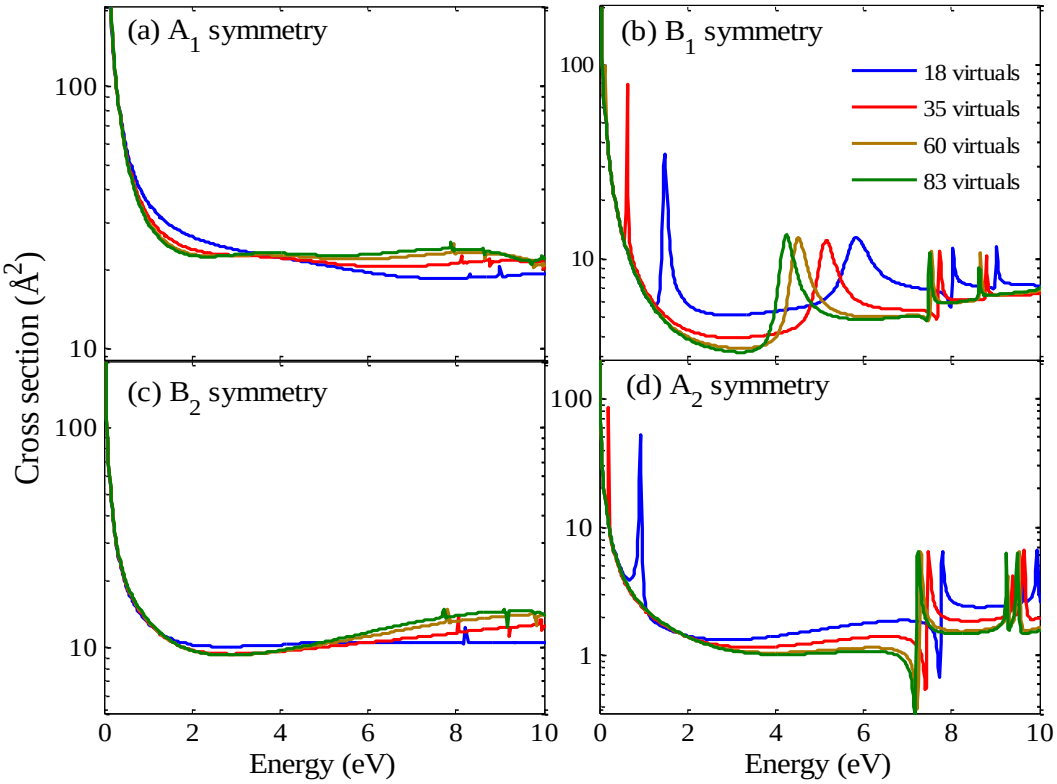

Figure 3.35: Partial elastic cross sections for the symmetries A_1 (panel a), B_1 (panel b), B_2 (panel c) and A_2 (panel d) computed at the SEP level including 18, 35, 60 and 83 virtual orbitals.

- ***Close-coupling (CC) calculation***

Close-coupling calculations were performed using the model developed by Mašín *et al.*[96] The active space for the SA-CASSCF calculations was chosen by the authors to be (10,8), i.e., 10 electrons distributed among 8 orbitals, in accordance with previous calculations for pyrazine.[56] The target orbitals obtained with the SA-CASSCF method were then used to generate all electronic excited states with excitation energies lying below ~10 eV. Masin *et*

al.[96] included the lowest-lying 14 singlet and 15 triplet electronic excited states in the description of the target. In the present calculations, we included only the 14 singlet electronic excited states. The resulting CSs are reported in Figure 3.36. It can be observed that the inclusion of triplet states has no significant effect on the absolute value of the elastic CSs, however it causes a shift in the calculated position of the resonances towards lower energies**.** As expected, the electronically inelastic CSs are slightly larger when the triplet excited states are considered (Figure 3.36b).

The integral total elastic CSs, summed over contributions from all irreducible representations, computed with the SEP and CC models are shown in Figure 3.37. Additionally, the positions of the low-lying resonances calculated with each model are reported in Table 3.9, together with the corresponding experimental values.[49]

Cross sections computed with the different R-matrix methods have shapes and magnitude similar to each other. However, they differ on the positions of resonant structures. It should be noted that the R-matrix scattering calculations do not exhibit convergence of the positions of resonant structures as the number of virtual orbitals included in the calculation is increased.[104] The optimal number of virtual orbitals is that which gives positions of the π* resonances in an acceptable agreement with the experimental data.[104] The smallest virtual space (18 virtual orbitals) places the position of the three resonances too high in energy compared with the experimental values. On the other hand, when 60 virtual states are employed the π_1^* resonance of A_2 symmetry became a bound state. Similarly, the use of the largest virtual space (83 virtuals), brings both the π_1^* (A_2) and π_2^* (B_1) resonances to a bound state. Therefore our preferred model includes 35 virtuals, since the two lowest-lying π* resonances lie within the experimental range reported by Nenner and Schulz.[49] It is appreciated in Table 3.9 that the SEP model provides positions for the low-lying shape resonances in better agreement with experiment than the CC model. One should note that the third π* resonance is found at energies higher than in the experiment in all the models.

For energies below the first excitation threshold, which for pyrimidine is around 4 eV,[105] the SEP model is preferred, since it provides a better representation of the short-range polarization and correlation effects. Above this limit, it is more convenient to employ the CC model as it accounts for the electronic-state excitations and, therefore, provides a more realistic representation of the scattering processes at this energy region. Hence, the choice of the appropriate scattering model for a given target molecule depends essentially on the energy range of the incident particle. The most accurate R-matrix cross sectional data has been reported by Mašín.[104] Therefore, in order to generate a set of recommended cross sections, those results are used here as the low-energy contribution to the IAM-SCAR calculations.

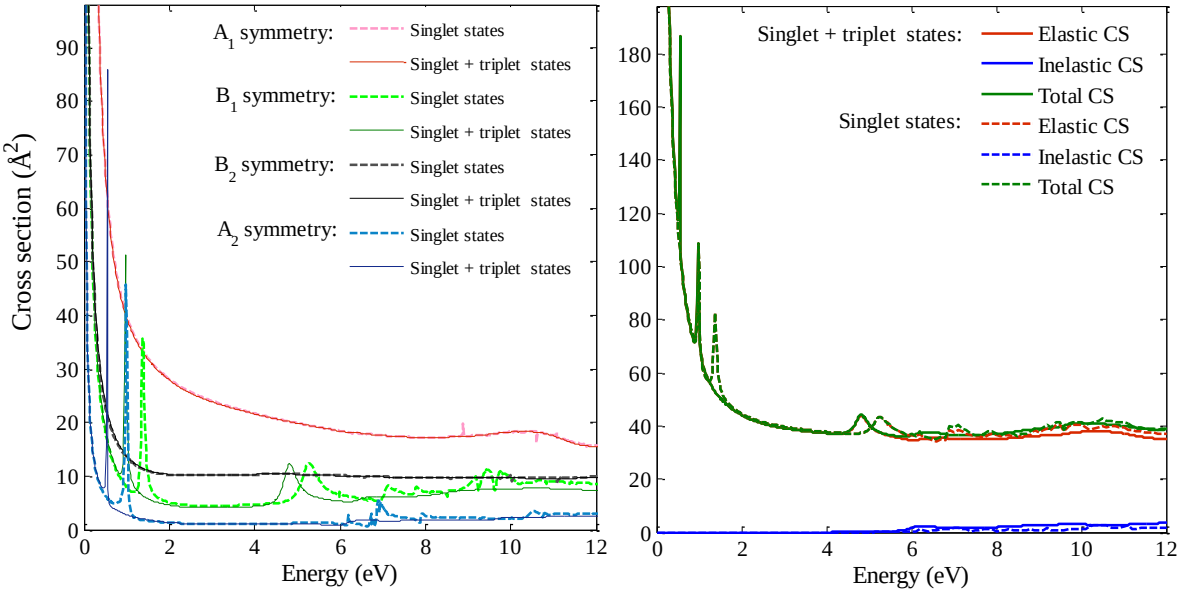

Figure 3.36: (Panel a) CC partial elastic cross sections for the symmetries A_1 (red), B_1 (green), B_2 (black) and A_2 (blue). (Panel b) Total, elastic and inelastic cross sections computed at the CC level.

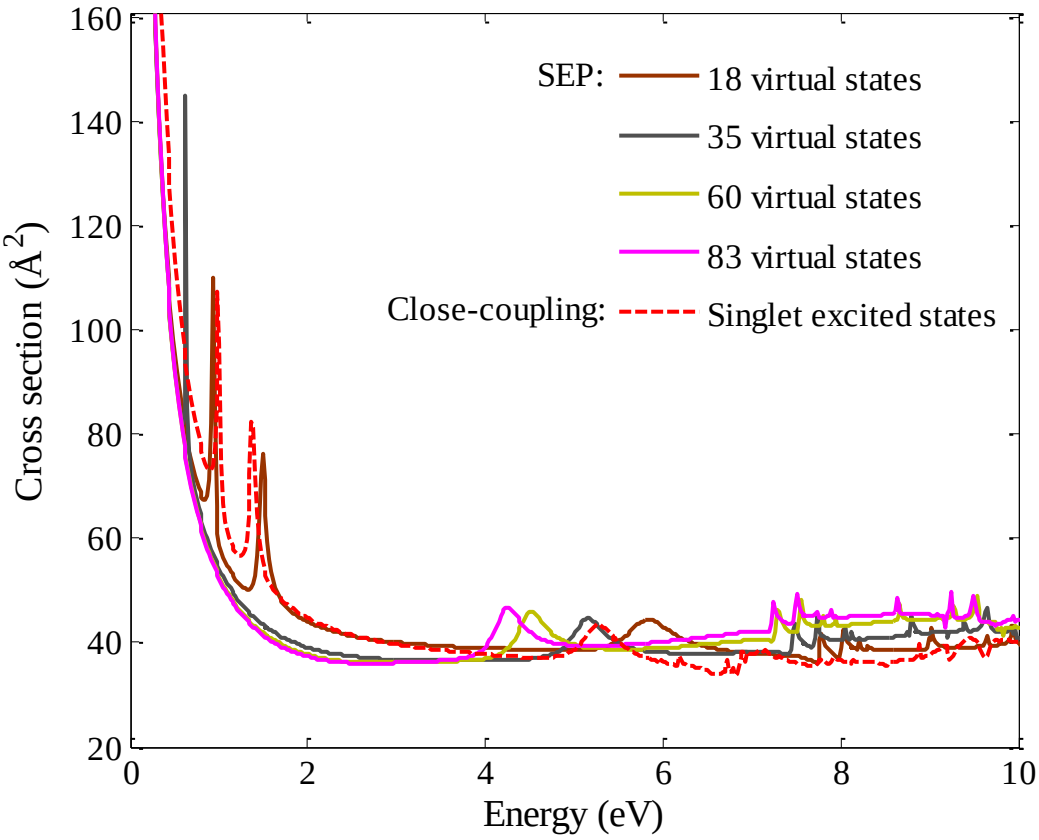

Figure 3.37: Summed elastic cross sections computed at the SEP and Close-Coupling level of approximation.

Table 3.9: Resonance parameters (eV) computed for the different SEP and CC models, compared with the experimental resonance positions.[49]

Model	π_1^* ($\mathbf{A_2}$)		π_2^* ($\mathbf{B_1}$)		π_3^* ($\mathbf{B_1}$)	
	Energy	Width	Energy	Width	Energy	Width
SEP (18 virt.)	0.93	0.035	1.48	0.090	5.79	0.61
SEP (35 virt.)	0.21	0.001	0.63	0.015	5.12	0.44
SEP (60 virt.)	-	-	0.13	0.002	4.48	0.39
SEP (83 virt.)	-	-	-	-	4.21	0.36
CC	0.99	0.043	1,37	0.078	5.34	0.01
Experiments	0.25-0.7		0.77-1.6		4.24±0.6	

Elastic Cross Sections

Elastic DCSs computed with the IAM-SCAR method are shown in Figure 3.38 for some selected incident electron energy values. We report the dipole-corrected cross sections, appropriate for comparison with experiments. Since pyrimidine is also a strong polar molecule, the Dickinson-correction has been applied for medium and large angles. In the same fashion of pyrazine, at low energies there is poor agreement between the IAM-SCAR approach and other experimental[91] and theoretical works,[96,97] as expected. At energies above 20 eV, the independent-atom model comes into better agreement with the experimental data from Palihawadana *et al.*[91] and Maljković *et al.*[90], although some discrepancies exist in the angular region below ~40°. However, for energies ≥100 eV (Figure 3.38f-g) these discrepancies disappear and there is excellent agreement throughout the whole overlapping angular range with the measurements from the Belgrade group.[90]

Figure 3.39 report the elastic integral CS, both dipole-corrected and uncorrected, for electron scattering from pyrimidine. In this case, even when the dipole-induced rotational excitations are not considered, there is good agreement between the R-matrix approach and the IAM-SCAR method at intermediate energies (solid lines). Also good agreement is found with the SMC calculations which do not include any dipole correction.[91] Once the elastic CSs are dipole-corrected, the agreement is excellent and both methods essentially coincide in magnitude and shape. As stated before, a realistic comparison with the experimental results can be made only if the dipole-induced rotational excitations are included in the calculations (see section 3.2.1). It is interesting to note that whereas theoretical and experimental DCS are in good level of agreement (Figure 3.38), calculated integral CSs are significantly larger than the

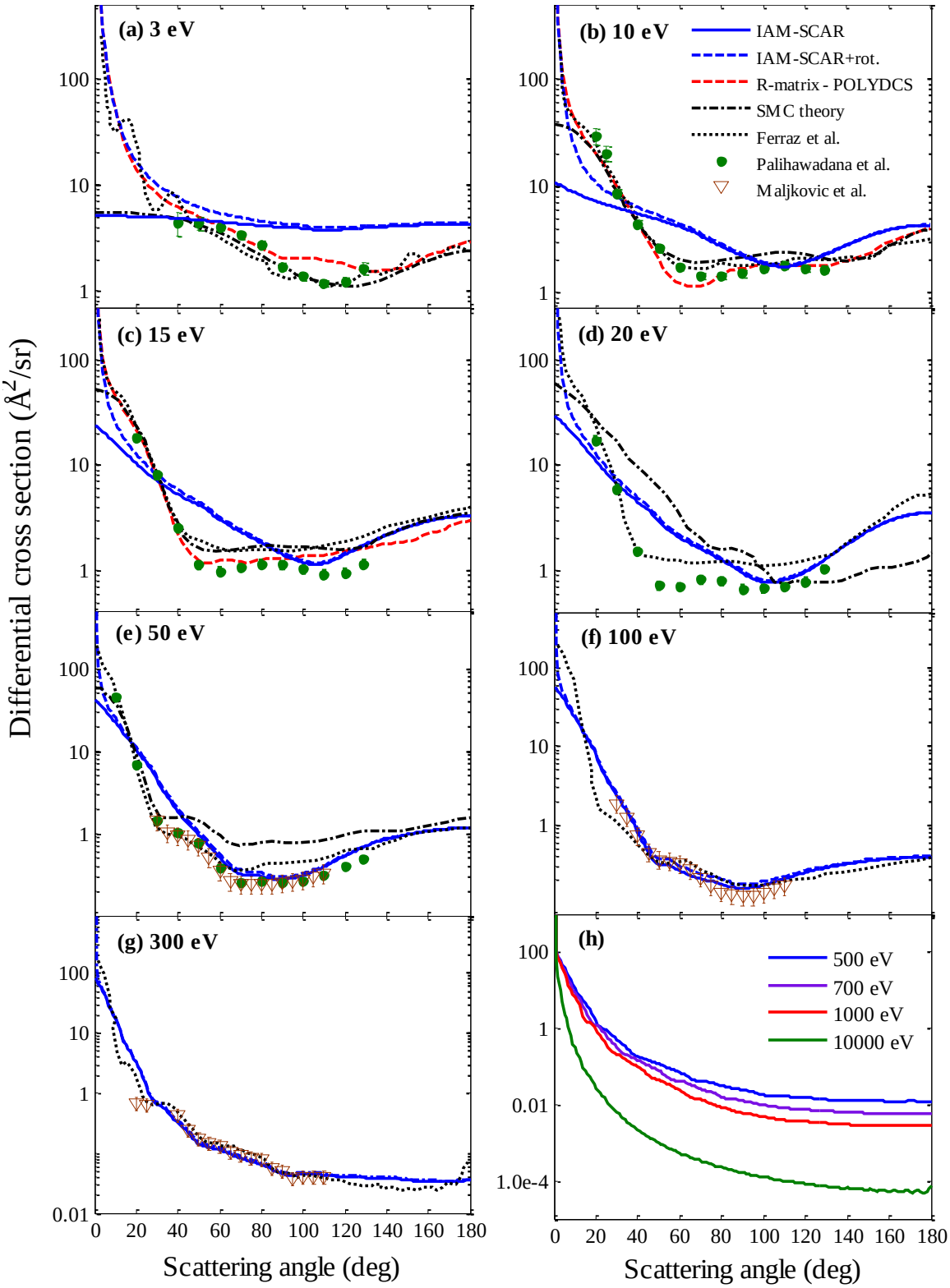

Figure 3.38: Elastic DCSs for electron scattering from pyrimidine computed the IAM-SCAR+rotations (Dickinson-corrected) model at the incident energies indicated in the panels. For comparison, elastic DCSs computed with the R-matrix method,[96] SMC theory[91] and calculations from Ferraz *et al.*[97], together with the experimental data from Palihawadana *et al.*[91] and Maljković *et al.*[90], are also shown.

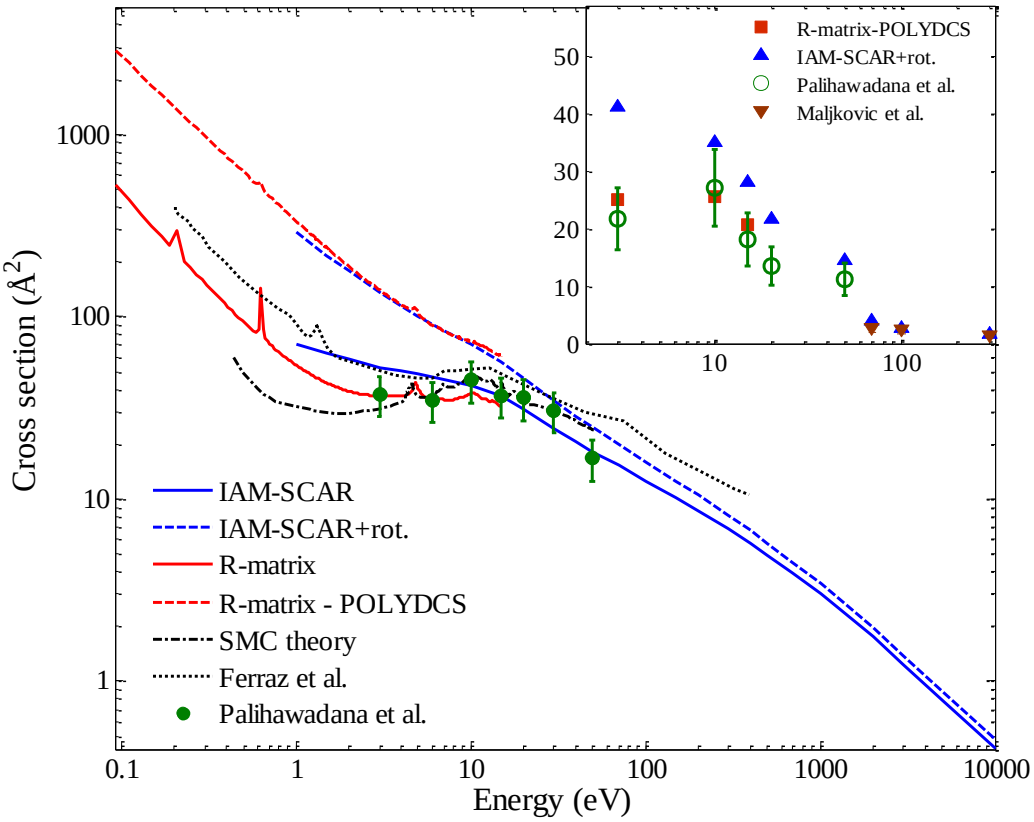

Figure 3.39: Integral elastic cross section, with and without the dipole-correction, computed with the IAM-SCAR procedure. Also shown, cross sections computed with the R-matrix theory,[96] SMC approach[91] and calculations from Ferraz *et al.*[97], together with earlier measurements.[91,90] The top-right panel shows the cross sections partially integrated over the restricted experimental angular range (i.e. emulating the experimental conditions) for the theoretical IAM-SCAR and R-matrix results.

experimental values. Similar to what has been observed for the molecules discussed in the previous sections, this seems to be an effect of the angular extrapolation of the measured DCS values to the forward and backward angles. It can be observed on the top-right panel of Figure 3.39 that, when the experimental and calculated DCS are integrated over the angular range where the measurements were performed, i.e., mimicking the experimental conditions, the good agreement between the experiment and the calculation is restored.

Inelastic and Total Cross Sections

Electronically inelastic CSs computed with the IAM-SCAR method are plotted in Figure 3.40. As for pyrazine, the IAM-SCAR cross sections exhibits a late onset (10 eV) compared to the R-matrix results (4 eV).[96] Note, however, that both methods are in good agreement at intermediate energies (10 - 15 eV). In addition, at 15 eV there is good agreement between the IAM-SCAR results and the experimental values presented in Mašín *et al.*[96] With increasing energies, although computed and experimental results show a similar trend, the IAM-SCAR

CSs are significantly larger in magnitude. These differences are partially attributed to the fact that whereas the calculations take into account the ionization processes, these are neglected by the experiments.

Figure 3.41 shows that the theoretical TCS data computed with the IAM-SCAR and R-matrix methods are in excellent agreement at intermediate energies. These results are compared with the experimental TCS measured by Fuss *et al.*[51] using a magnetically confined electron scattering system. As discussed for pyrazine (section 3.1.2), these experimental TCS effectively neglects the elastic and rotational excitation contribution of the lowest and highest scattering angles, and so constitutes a lower bound on the true TCS values. In order to provide a more realistic comparison, the theoretical cross sections have been computed mimicking the experimental conditions. As can be appreciated in Figure 3.41, there is good agreement between the experimental TCS and the partially integrated IAM-SCAR CS in the low energy region (~below 30 eV), even though it falls beyond the recommended range of application of the computational method, and becomes excellent with increasing energies. It is also observed that the partially integrated R-matrix results are in pretty good agreement with the experimental TCS, although as expected, they tend to be slightly smaller in magnitude due to the omission of the ionization states.

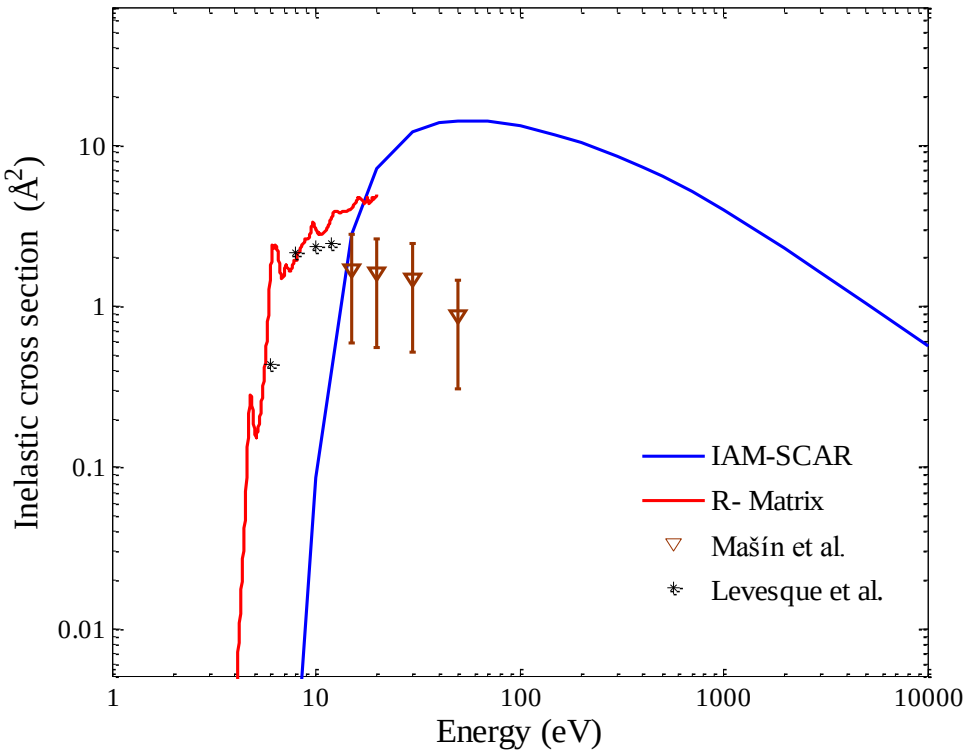

Figure 3.40: Electronically inelastic cross sections computed with the IAM-SCAR method. Also shown, R-matrix calculations,[96] and experimental data reported by Levesque *et al.* [95] and Mašín *et al.*[96]

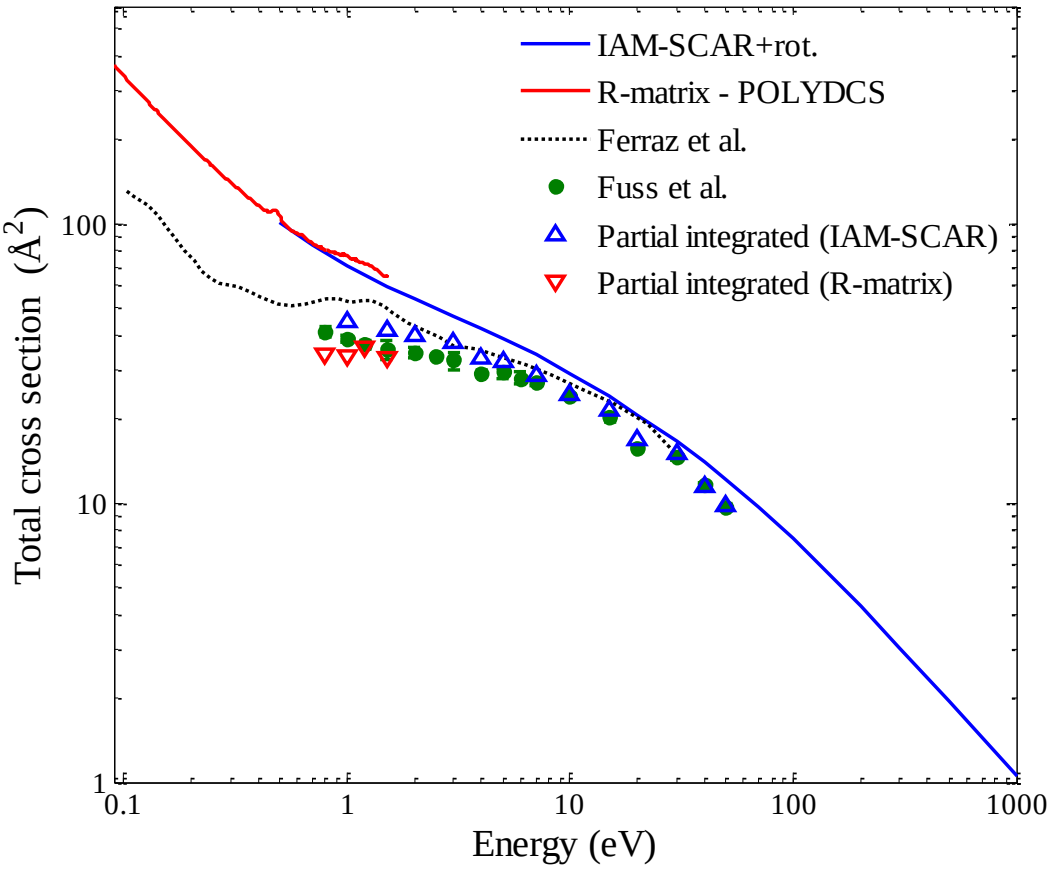

Figure 3.41: Total cross sections (dipole-corrected) for electron scattering by pyrimidine computed with the IAM-SCAR+rotations procedure. Also shown: cross sections computed with the R-matrix theory,[96] calculations from Ferraz *et al.*[97], and the experimental data provided by Fuss *et al.*[51] TCS. Cross sections partially integrated over the restricted experimental angular range (i.e. emulating the experimental conditions) are given for the theoretical IAM-SCAR and R-matrix results.

Recommended Set of Integral Cross Section Data

As a result of the previous discussion, a set of recommended elastic, inelastic and total integral cross sections has been generated from 0.1 eV up to 10000 eV for electron collisions from pyrimidine (see Table 3.10). From thermalized energies up to the ionization threshold, cross sectional data is reliably provided by the R-matrix method,[96] with the rotational excitations computed by means of the POLYDCS approach. Above the ionization potential, integral cross sections obtained by the IAM-SCAR+rotations model can be recommended. At intermediate energies, where both methods are smoothly joined together, the estimated error is ~10%, since both approaches are in excellent agreement.

Table 3.10: Recommended elastic, rotational excitations, electronically inelastic (electronic-state excitations and ionization) and total integral cross sections for electron scattering from pyrimidine in the energy range from 1 to 10000 eV.

Energy (eV)	Elastic ($Å^2$)	Rotational ($Å^2$)	Electronically Inelastic ($Å^2$)	Total ($Å^2$)
1.0	54.40	281.37		335.77
1.5	43.40	203.60		247.00
2	39.08	149.93		189.00
3	36.84	103.31		140.15
4	36.74	78.94	0.0015	115.68
5	40.48	61.72	0.1722	102.37
7	35.12	48.59	1.61	85.32
10	37.74	31.55	3.02	72.32
15	36.96	19.54	4.04	60.55
20	31.36	15.04	7.17	53.56
30	24.25	10.39	12.12	46.76
40	20.61	7.98	13.64	42.22
50	18.26	6.50	14.03	38.78
70	15.20	4.79	13.92	33.91
100	12.57	3.44	13.08	29.09
150	10.11	2.38	11.56	24.05
200	8.65	1.82	10.30	20.78
300	6.83	1.23	8.51	16.58
500	4.96	0.78	6.36	12.10
700	3.95	0.56	5.10	9.60
1000	3.05	0.42	3.95	7.42
2000	1.75	0.21	2.29	4.25
3000	1.24	0.15	1.63	3.02
5000	0.80	0.09	1.05	1.93
10000	0.43	0.05	0.57	1.04

Comparison with Non-Polar Molecules: Pyrazine and Anthracene

As pyrazine and pyrimidine are structural isomers they possess very similar physico-chemical properties (for instance, the spherical polarizabilities for pyrimidine[106,107] and pyrazine[89] are $\bar{\alpha} \sim 8.78$ Å^3 and $\bar{\alpha} \sim 8.88$ Å^3, respectively), so the main difference between them is their permanent dipole moments, 2.33 D for pyrimidine[88] and 0 D for pyrazine. It is therefore of interest, from a fundamental perspective, to compare the electron interaction probabilities of pyrazine and pyrimidine, and to evaluate the effect of the permanent dipole moment of the latter on the electron scattering dynamics. In addition to this, the inclusion of the anthracene molecule in such a comparative study would also provide useful information. Given that anthracene and pyrazine are non-polar derivatives of benzene (see the discussion in section 3.1.2), they are expected to show similar electron scattering responses, in qualitative terms.

Our calculated elastic differential cross sections (DCS) for pyrimidine, pyrazine and anthracene (according to the recommended values, taken from the results presented in previous sections) are plotted in Figure 3.41. We found very good qualitative agreement between anthracene and pyrazine DCS over the entire angular range for energies above 10 eV (which is better appreciated when the anthracene cross sections are scaled). In addition, similar behaviour is observed in the DCS results from pyrimidine and pyrazine for angles larger than 20°. However, noticeable differences arise at angles of less than 20º, where the pyrimidine elastic DCS results tend to be significantly larger in magnitude.

Figures 3.43 and 3.44 report the integral elastic and total cross sections, respectively. Calculated cross sections are given by the cross sections recommended in the current study (Tables 3.3, 3.4 and 3.10 for anthracene, pyrazine and pyrimidine, respectively). It is evident that there is a strong qualitative resemblance between pyrazine and anthracene elastic CS and TCS over the entire energy range, even coinciding in the presence of two low-lying resonances ($E_r \sim 0.9$ and 4.5 eV). For energies above 15 eV, good qualitative agreement is observed between the non-polar molecules and the pyrimidine integral CS. Moreover, pyrazine and pyrimidine CS are in excellent quantitative agreement at this energy range. However, at lower incident energies pyrimidine cross sections show a stepwise increase.

Thus, the main difference between these molecules is the large rotational excitation contribution for pyrimidine which is not observed for pyrazine or anthracene, especially at low incident energies and in the forward direction, as expected. It is worth noting that whereas these differences are clearly appreciated in the calculated cross sections, experiments yield almost equal cross sections for pyrimidine and pyrazine, to within the experimental uncertainty. This can essentially be interpreted as being due to the experimental angular acceptance that effectively ignores part of the small angle distribution, which is exactly where the dipole effects

are most significant. Thus, particularly in the case of polar targets, calculations constitute a very helpful complement to experimental results.

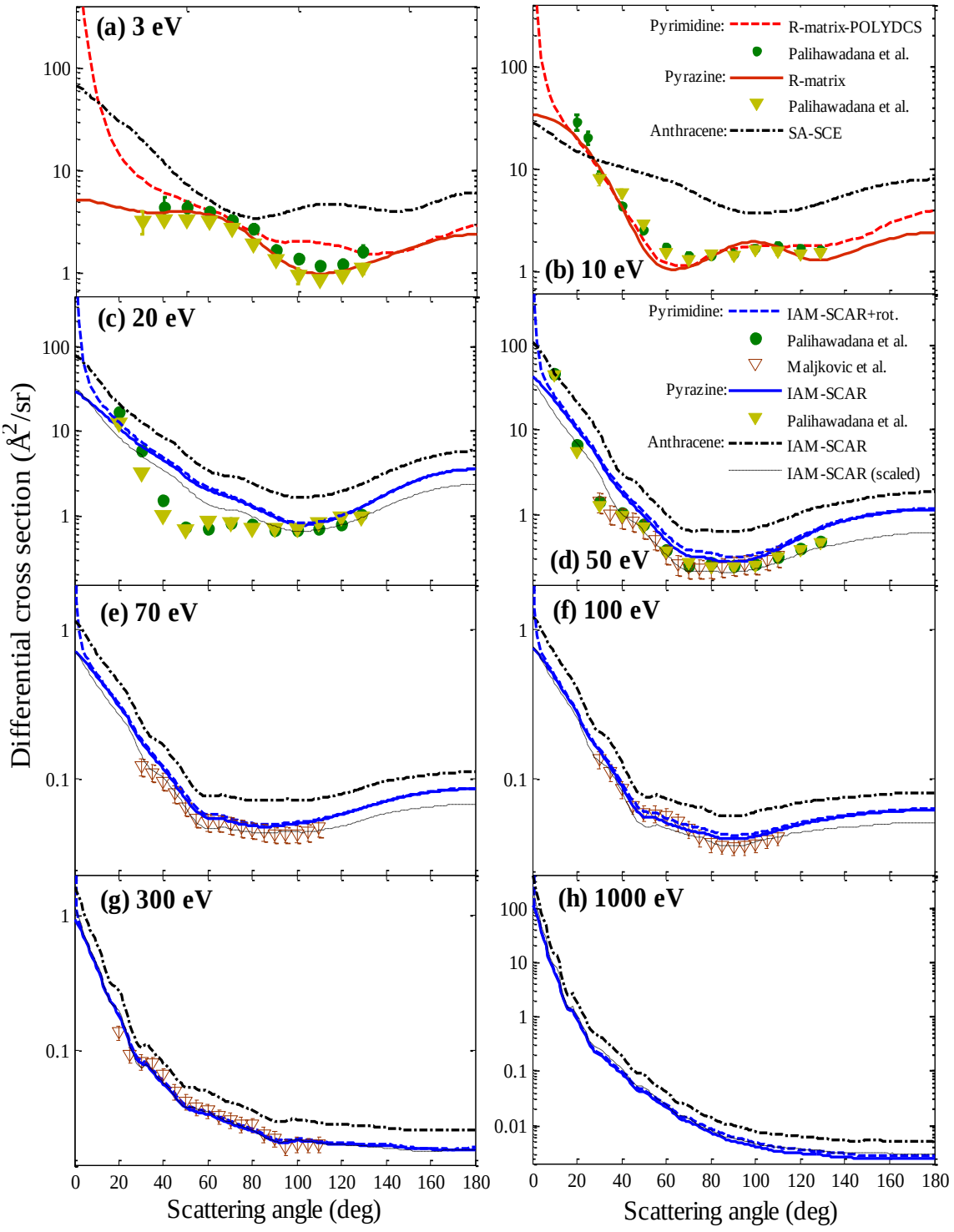

Figure 3.42: Present elastic DCS for electron scattering from anthracene, pyrazine and pyrimidine for the incident energies indicated in the panels. For comparison, experimental cross sections for pyrimidine[91,90] and pyrazine[50] from other sources are plotted. Also shown, present anthracene DCSs scaled by a factor between 2.0-3.0.

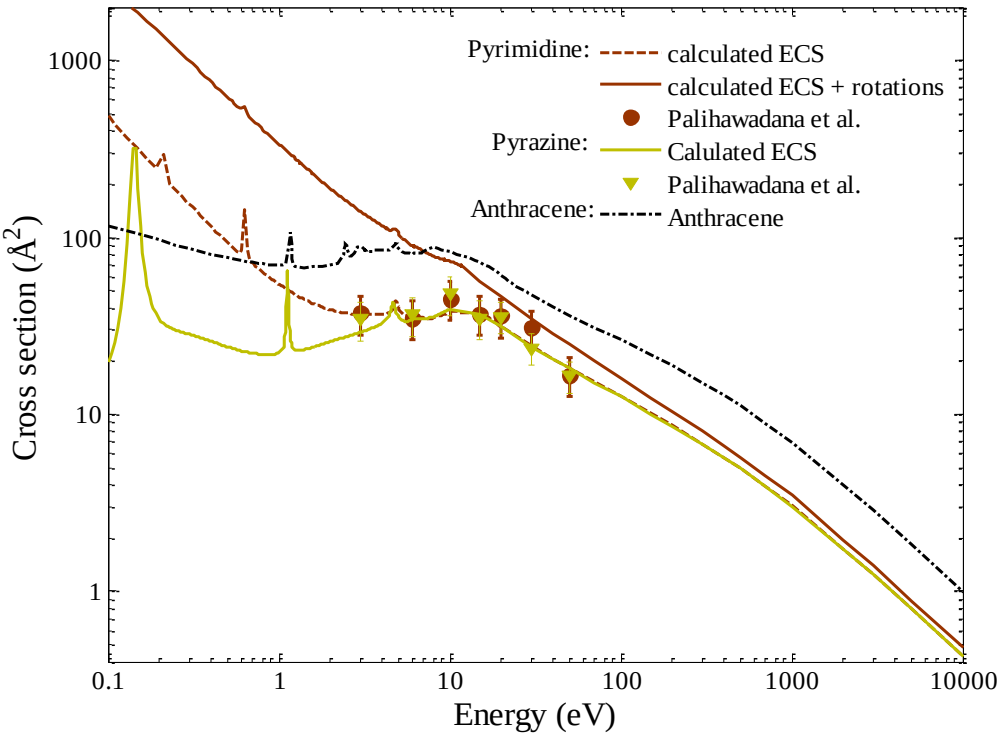

Figure 3.43: Present recommended elastic CS for electron scattering from anthracene (Table 3.3), pyrazine (Table 3.4) and pyrimidine (Table 3.10), with and without dipole-correction. For comparison, experimental cross sections for pyrimidine[91] and pyrazine[50] from other sources are plotted.

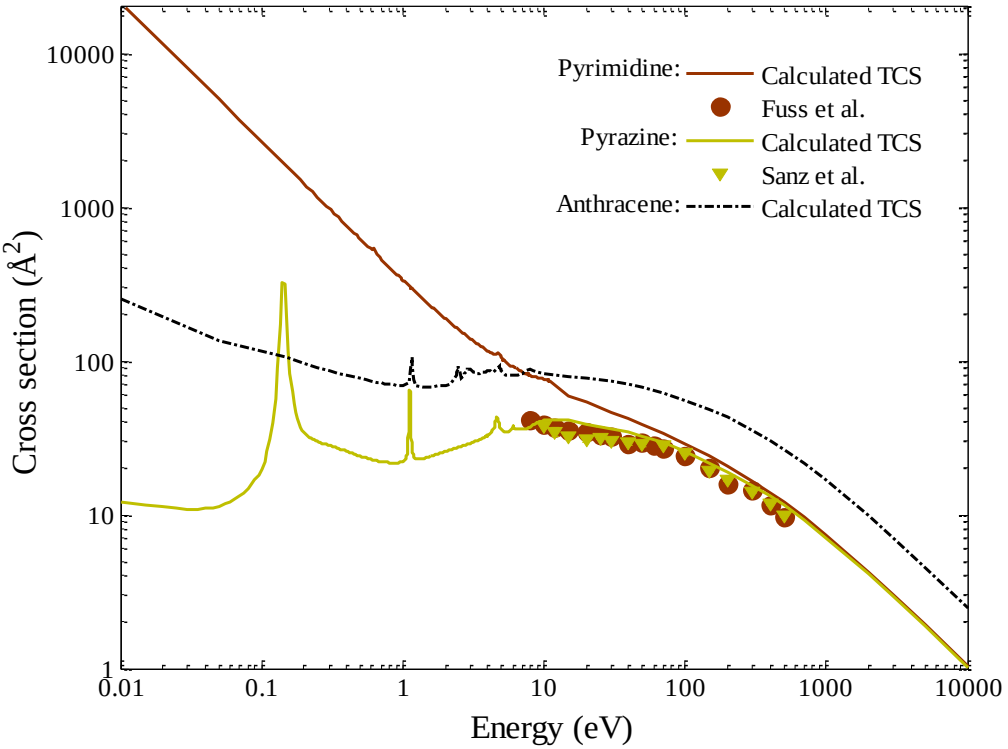

Figure 3.44: Present recommended TCS for electron scattering from anthracene (Table 3.3), pyrazine (Table 3.4) and pyrimidine (Table 3.10). For comparison, experimental cross sections for pyrimidine[51] and pyrazine[52] are plotted.

3.2.2.2. Positron Scattering from Pyrimidine

Low-energy Calculation Details

All positron-pyrimidine scattering calculations have been also performed at the equilibrium geometry of pyrimidine.[102] In the low energy region, CSs have been computed with the R-matrix method after adapting the models employed for electron collisions[104] to positron scattering. In this case, one should consider that the scattered positron can occupy all orbitals including those which are already occupied by electrons. In order to evaluate how sensitive e^+ scattering calculations are to the polarization effects, we have employed various levels of approximation: the static (S), static plus polarization (SP) and close-coupling (CC) models.

Using the experience gained for electron-pyrimidine collisions (section 3.2.2.1), we performed various stability tests in order assure the numerical convergence of the positron scattering CSs. A summary of all the computational tests carried out for e^+-pyrimidine collisions is given in Table 3.11. Within the SP model, two different basis sets were used: the compact cc-pVDZ basis set and the diffuse 6-311+G** basis set. In order to guarantee that the electronic density of all the target states included in the calculation is negligible outside the R-matrix sphere, we have used an R-matrix radius of a=13ao and a=18ao, for the compact and the diffuse basis sets, respectively. In addition, two different target orbital spaces were tested, i.e., ($26a_1$, $8b_1$, $17b_2$, $5a_2$) and ($37a_1$, $12b_1$, $24b_2$, $8a_2$), which correspond to 35 and 60 virtual orbitals. Finally, the scattered positron is described by a continuum basis set developed by Faure *et al.*[103] which has been extended up to l=4 or l=5. One should note that the target description does not depend on the charge of the projectile. Thus, we used the target wavefunctions generated previously for electron-pyrimidine calculations by Mašín[104] (i.e. Hartree-Fock SCF and state-averaged CASSCF orbitals, for the SP and CC calculation, respectively). The dipole moment obtained with the compact basis was 2.31 D and 2.36 D for the SEP and CC models, respectively, in fair agreement with the experimental value of 2.334 D,[88] whereas for the diffuse basis set the value obtained was slightly higher with both models: 2.53 D.

Table 3.11: Details of the optimization tests performed for the positron-pyrimidine scattering study.

Model	**Basis set**	**Target orbital space** (a_1, b_1, b_2, a_2)	**Continuum basis set**	**R – matrix radius**
Static	cc-pVDZ	22, 7, 14, 3	$l = 4$	13 a.u.
SP	cc-pVDZ	26, 8, 17, 5 37, 12, 24, 8	$l = 4, 5$ $l = 4$	13 a.u.
	6-311++G**	26, 8, 17, 5	$l = 4$	18 a.u.
CC	cc-pVDZ	28, 11, 19, 6	$l = 4$	13 a.u.

- ***Static (S) calculations***

We used the model developed by Mašín[104] for e^--pyrimidine as a template for the present calculations. We used the 25 lowest-lying virtual orbitals, the compact (cc-pVDZ) atomic basis set, the R-matrix radius was set to $13a_0$ and the continuum basis set included functions up to l=4. Partial elastic CSs for the four symmetries A_1, B_1, B_2 and A_2 are shown in Fig. 3.41, together with the total (summer over all the IRs contributions) elastic cross sections.

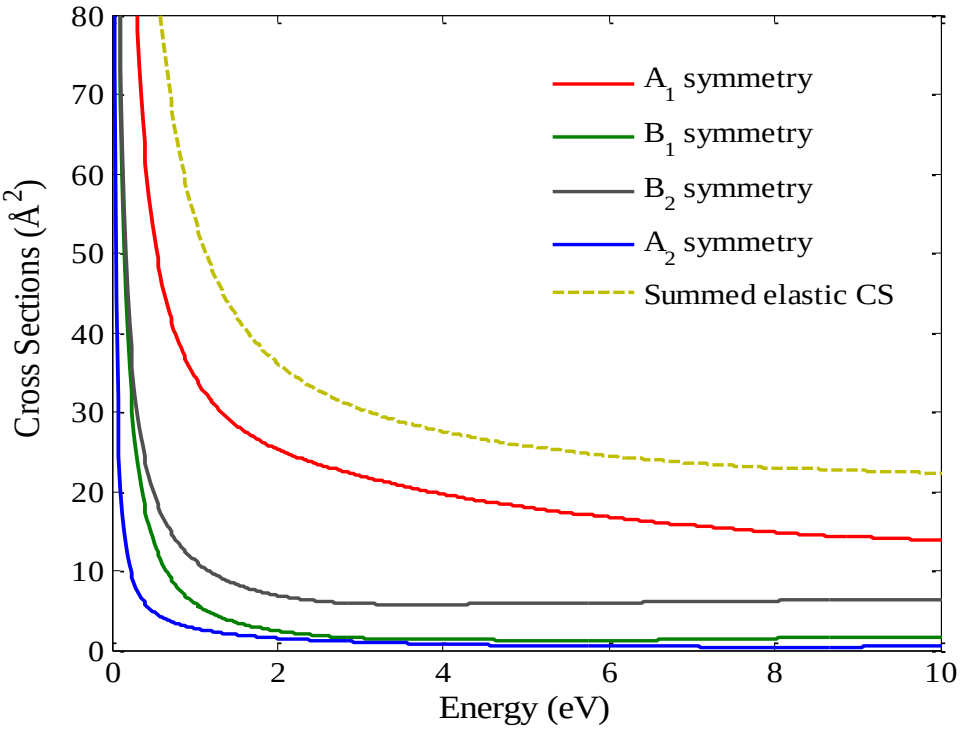

Figure 3.45: Partial elastic cross sections for the A_1, B_1, B_2 and A_2 symmetries computed at the Static (S) level of approximation. The total (summer over all the IRs contributions) elastic CSs are also plotted.

- ***Static and Polarization (SP) calculations***

In analogy to the SEP model for electron-molecule scattering, within the SP model one electron from the valence space is allowed to promote to a selected number of virtual orbitals. Target calculations have been performed with two different basis sets, a compact basis set, cc-pVDZ and a diffuse one, 6-311+G**. It can be observed in Figure 3.46a-d that the cross sections obtained with the diffuse basis set are bigger in magnitude than those for the compact basis set. This indicates that these calculations are very sensitive to the nature of basis set used, as already pointed out in the electron scattering case.[96] For instance, the virtual orbitals, important for modelling correlation/polarization effects, were found to be considerably different in energy and shape when using the compact or the diffuse basis set. These differences manifest themselves in the number of virtual orbitals used to generate L^2 functions for the different models, which increases from 35 up to 40 when the compact basis

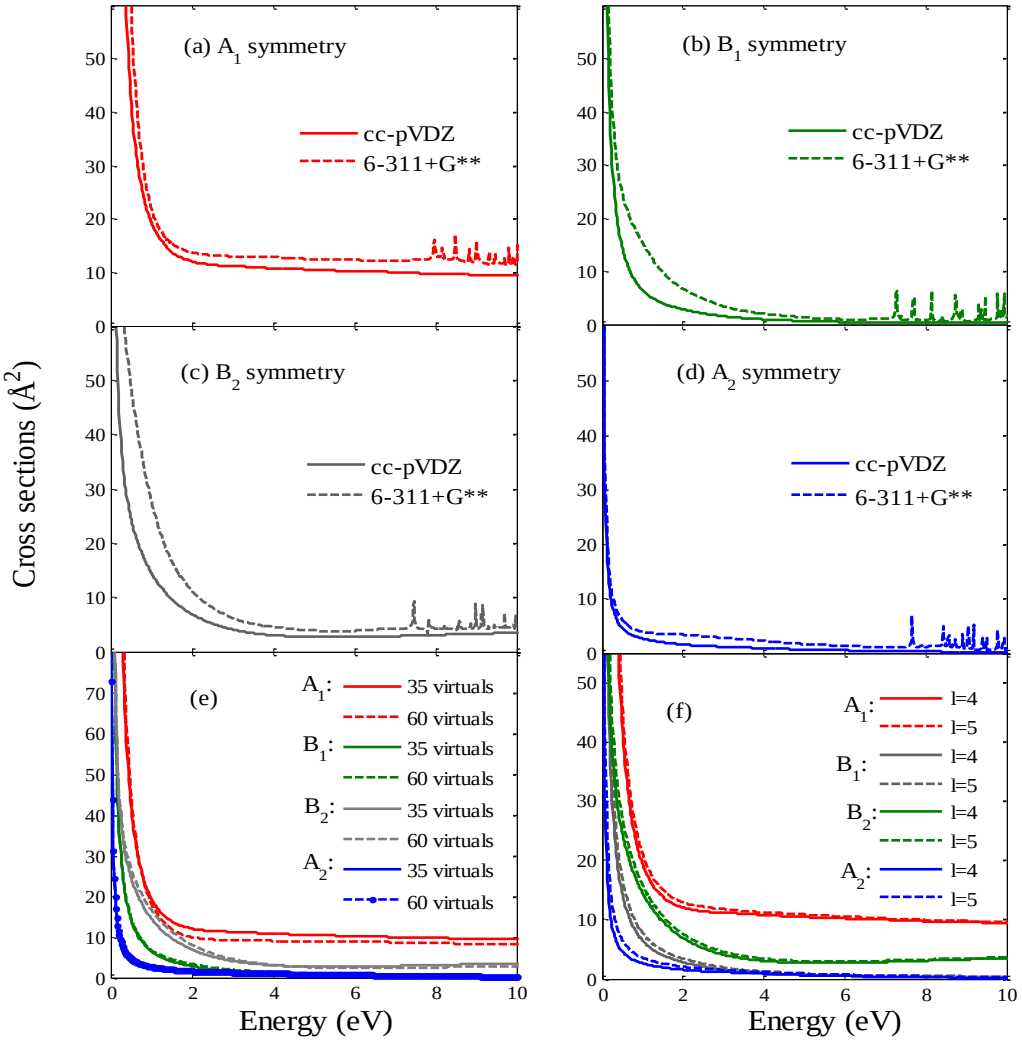

Figure 3.46: Partial elastic cross sections at the SP level for the symmetries A_1, B_1, B_2 and A_2 computed with: (panel a-d) the compact cc-pVDZ and the diffuse 6-311+G** basis sets, (panel e) a target space containing 35 and 60 virtual orbitals, (panel f) continuum partial waves up to l=4 and l=5.

set is changed for the diffuse basis set. One should note that calculations using the compact basis set less computationally demanding than those using the diffuse one.

Previous electron-pyrimidine calculations (section 3.2.2.1), showed that using 18 or 83 virtual orbitals in total give very poor results. Therefore, these sizes of the virtual space are not anymore considered. Partial elastic CSs calculated for each contributing IR (i.e., A_1, B_1, B_2 and A_2) using the lowest-lying 35 and 60 virtual orbitals are shown in Figure 3.46e. From this plot it is inferred that enlarging the virtual space does not cause significant differences in the scattering results. Note that the electron-pyrimidine scattering study showed that changing the size of the virtual space affects mainly to the position of the resonances. In that case using 35 lowest-lying virtual orbitals was found to be optimal, giving positions of the

π* resonances in fairly agreement with the experimental data. However, no shape resonances are present when the incident particle is a positron. In the present calculations, our preferred model also includes 35 virtuals for consistency and in order to realistically compare electron and positron cross sections.

Finally, the GTOs basis set used to describe the scattered positron was expanded up to $l = 4$ and $l = 5$. It can be seen in Figure 3.46f that increasing the partial waves included in the *ab-initio* calculations up to *l*=5 has no discernible effect on the cross sections. Hence, $l = 4$ is preferred, as it conducts to less computationally demanding calculations.

- ***Close-coupling calculation***

The model employed in the CC calculation was again based on that developed by Mašín *et al.*[96] for electron-pyrimidine collisions. In particular, we used 40 virtual orbitals and the size of the complete active space was (10,8). Calculations have been performed with the cc-pVDZ basis set. We included the 14 lowest singlet electronic states (4^1A_1, 3^1B_1, 4^1B_2, 4^1A_2) of pyrimidine in the close-coupling expansion. As mentioned in Chapter 2, the R-matrix calculation does neither include the Ps formation description, nor a description of ionization, and therefore the inelastic CS calculated with this model accounts only for the electronic excitations.

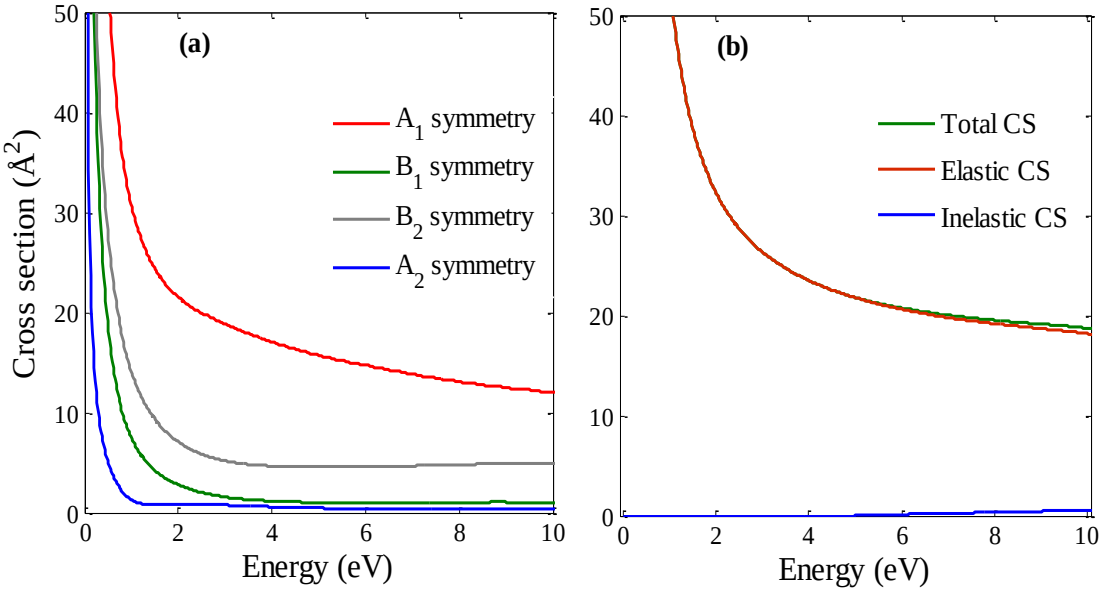

Figure 3.47: (a) partial CC elastic cross sections for the symmetries A_1, B_1, B_2 and A_2. (b) Integral elastic, inelastic and total cross sections at the CC level of approximation.

Elastic Cross Sections

Figure 3.48 shows present integral elastic CS computed with the R-matrix model and the IAM-SCAR approach over the energy ranges 0.1 – 15 eV and 1 – 10000 eV, respectively. These refer to elastic integral CSs that are not dipole-corrected. In the low energy region, R-matrix CSs computed with the SP model, using the compact and diffuse basis sets, and at the CC level of approximation are reported. As mentioned before, R-matrix results are quite sensitive to the nature of the basis set employed: it can be appreciated that the elastic CS calculated with the diffuse basis set are bigger in magnitude than those obtained with the compact basis set. Moreover, the SP and CC approximations produce very similar results for the compact basis set, in particular at low energies. The numerous narrow peaks visible for energies above ~5 eV in the *ab-initio* SP cross sections correspond to (non-physical) pseudoresonances, an inherent feature of the SP approximation when using a multi-configuration description for the (N+1)-particle wavefunction. We also observe that these structures tend to appear at lower energies when the diffuse basis set is employed. At higher energies, the IAM-SCAR cross sections have been computed using two different models for the polarization potential: the dipole (V_d) and the dipole plus quadrupole (V_{d+p}) polarization potentials. Although both models show in general similar qualitative behaviour, cross sections computed with the V_{d+p} potential are slightly larger in magnitude. Note that in this optical model calculation the polarization potential is the only attractive interaction between the positron and the target. Consequently, the attractive interaction is enhanced when the quadrupole term is included, leading to larger cross sections in particular at low energies. However, at higher energies the results from both methods converge.

Despite the different R-Matrix and IAM-SCAR models are in reasonable agreement with one another, to within their respective ranges of validity, we clearly discern in Figure 3.48 some discrepancies between the uncorrected cross sections for both methods at intermediate energies. The origin of these discrepancies may be due to the different methods for treatment of the polarization effects, since the results are very sensitive to the description of the polarization potential. However, once the elastic ICS are Born corrected, allowing therefore for the rotational motions induced by the strong permanent dipole moment, excellent agreement is found between the R-matrix approach and IAM-SCAR procedure (see Figure 3.49). Moreover, the agreement between the different R-matrix models (SP and CC) improves significantly. Similarly, IAM-SCAR dipole-corrected cross sections calculated with V_d and V_{d+p} are now almost identical. This is because positron scattering from polar molecules is essentially dominated by the dipole interaction, being correlation and polarization weaker effect. Under these circumstances, CSs from the polar target pyrimidine show therefore very little dependence on the method used and thus on the treatment employed to model the polarization interaction, as observed for water.[108]

Present calculated results are compared with the experimental data reported recently by Palihawadana *et al.*[100]. Similarly to electron scattering measurements, the energy resolution of the experimental apparatus is not enough to resolve the dipole-induced rotational excitations, what means that the experimental elastic CS are contaminated by rotational excitations. Hence, they are compared with the calculated elastic CS dipole-corrected (see Figure 3.49). Large discrepancies are found between theory and experiment, which according to the results presented in throughout this Chapter, are attributed to the angular restrictions of the experimental apparatus: the minimum measurable angle of scattering is 8° at 20 eV of incident energy and increases up to 26° at 2 eV, thus leading to underestimated CS. When calculated cross sections are partially integrated under experimental conditions, the agreement between theory and experiment markedly improves, in particular with the R-matrix calculations at the CC level (red triangles) at low energies and with the IAM-SCAR calculations using the V_{d+p} potential (blue triangles) at higher energies (remaining models are not shown for the sake of clarity).

The elastic DCSs computed with the R-matrix-POLYDCS procedure and the IAM-SCAR+rotations model with the dipole Dickinson correction are reported in Figure 3.50 for some selected positron incident energies. The angular dependence of the R-matrix DCSs is characterized by a shoulder at around 40° - 60°, which is progressively shifted to lower angles as the impact energy increases (it lays around 20º for 10 eV). On the other hand, the IAM-SCAR+rotations angular distribution shows a broad minimum at around 90°-110° for low energies, which tends to disappear at higher energies. Note that all our calculated curves, converging in value for angles below 20º, are strongly peaked in the forward direction, as expected due to the strong polar nature of pyrimidine. This behaviour is in fact more dramatic as the incident positron energy decreases. Our calculations are compared with the experimental DCSs reported by Palihawadana *et al.*[100]. At the lowest positron incident energies (i.e., E_i = 1 and 3 eV), theory and experiment are in good qualitative agreement up to around 60°, and also in good quantitative agreement up to ~40°, in particular with the IAM-SCAR+rotations method. However in the angular range 60° - 80°, the experimental measurements lay somewhat below the theoretical data. With increasing energies the agreement is markedly improved. For instance, at 10 eV the IAM-SCAR+rotations procedure is in good agreement with the experiments for angles below 50°, whereas at higher angles the R-matrix calculations are in better qualitative and quantitative agreement with the measurements. At 15 and 20 eV the agreement between the experiments and the IAM-SCAR+rotations approach improves over the entire angular range. Note that the experimental uncertainty is higher than in the electron scattering case and some fluctuations in the experimental data are observed. In summary, given the difficulties

encountered in both experimental and theoretical works, the agreement attained is reasonably good.

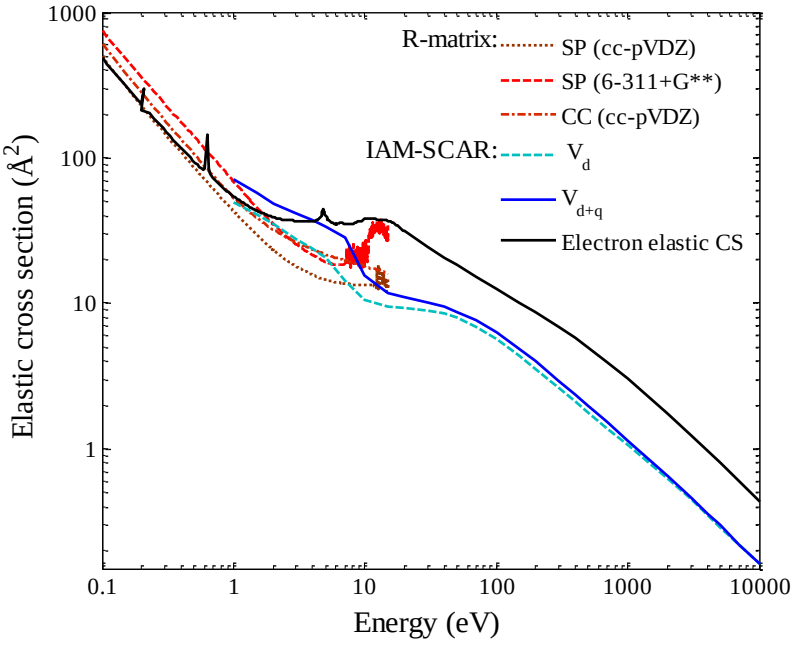

Figure 3.48: Integral elastic cross sections for positron scattering from pyrimidine computed with the R-matrix method (at the SP and CC levels of approximation) and the IAM-SCAR model (using the dipole polarization potential, V_d, and dipole plus quadrupole polarization potential,V_{d+p}). Additionally we have plotted, for comparison, the electron scattering elastic integral cross sections.

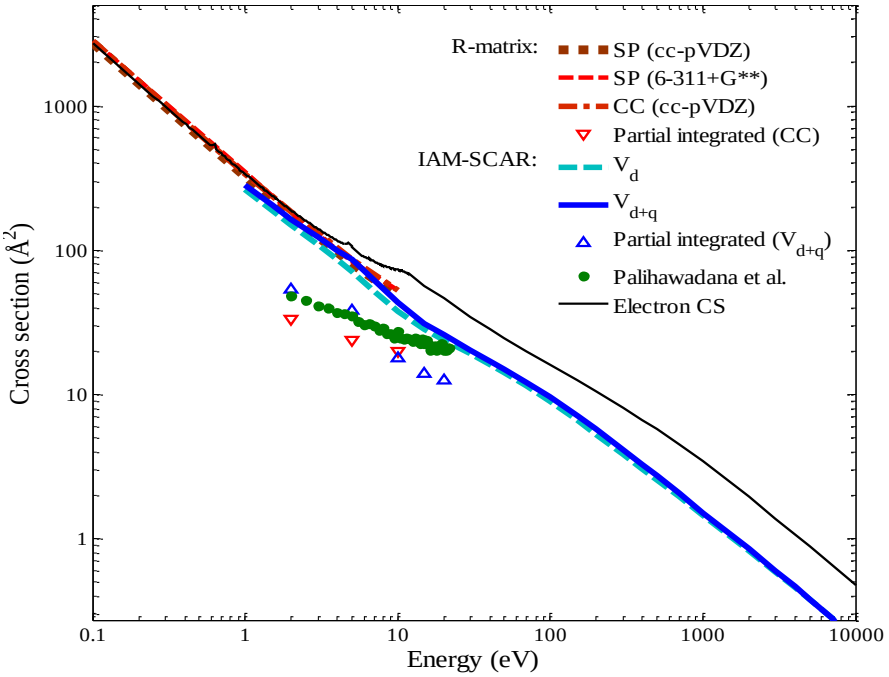

Figure 3.49: Integral elastic cross sections for positron scattering by pyrimidine, including the Born dipole allowed rotational excitations, computed with the R-matrix-POLYDCS procedure and with the IAM-SCAR+rotations (Dickinson corrected) method. Partially integrated CS values (i.e. emulating the experimental conditions) are given for the theoretical IAM-SCAR and R-matrix results. Also plotted for comparison, the experimental data from Palihawadana *et al.*[100] Additionally, we have plotted the recommended electron scattering elastic integral cross sections, dipole-corrected (Table 3.10).

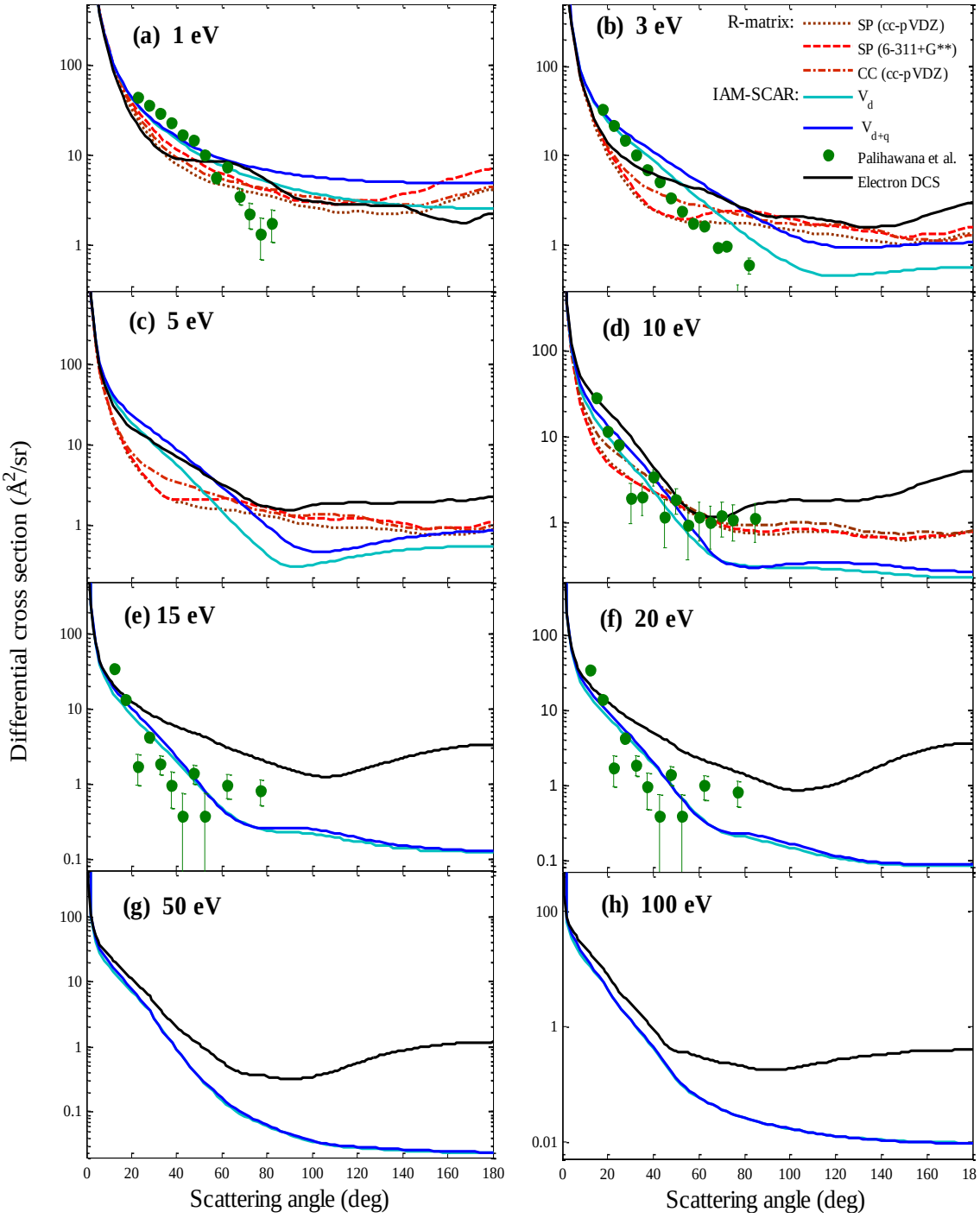

Figure 3.50: Elastic DCS for positron scattering from pyrimidine, computed with the R-matrix-POLYDCS method (at the SP and CC levels of approximation) and the IAM-SCAR model (using the V_d and V_{d+q} polarization potentials). All the R-matrix results are Born corrected and all the IAM-SCAR results are Dickinson corrected. Also plotted are the experimental data from Palihawadana *et al.*[100] Additionally, we have plotted the electron elastic DCS, dipole-corrected (see text for further details).

Inelastic and Total Cross Sections

Inelastic integral CSs computed with the present models are shown in Figure 3.51. As mentioned before, inelastic CS calculated with the R-matrix at the close-coupling level of approximation comprises only the electronic-state excitations. A Born correction has been added to the inelastic CS, so that the higher partial waves (i.e., $l > 4$) initially not included in the *ab-initio* calculation are also considered.[104] On the other hand, inelastic CSs computed with the IAM-SCAR comprise electronic excitations, ionization and Ps formation, which were calculated through the atomic $iV_a(r)$ absorption potential and are, therefore, equal for both the V_d and V_{d+q} potentials. Regarding Ps formation, CSs calculated with the IAM-SCAR method are in qualitative agreement with the corresponding experimental values, however the latter are larger in absolute value. These differences are attributed can be attributed to the difficulties to properly include the Ps formation in the theory. Looking now to the electronically inelastic CS, it can be observed that there is fairly good agreement between the experimental measurements of Palihawadana *et al.*[100] and the R-matrix theory at low energies (up to ~10 eV). At higher energies, the R-matrix results fall below the experimental results as expected, since ionization channels are missing from those calculations. In contrast, in the 15-30 eV energy range there is excellent agreement between the measurements[100] and the IAM-SCAR data.

The present TCS (Born-corrected as these account fully for the projectile-dipole interaction) computed with the R-matrix-POLYDCS procedure and the IAM-SCAR+rotations method are in very good agreement at intermediate energies, due to the dominance of the dipole interaction (Figure 3.52). Calculated TCS are compared with the experimental TCS available in the literature from Zecca *et al.*[99] and Palihawadana *et al.*[100]. It is clearly appreciated that the computed TCS are higher in magnitude than the measured TCS. This apparent experimental underestimation is attributed, as before, to the angular discrimination of the experimental spectrometer. This provokes that the measurements miss part of the forward angle scattering contribution, where is concentrated most of the dipole-induced rotational excitations. In a recent investigation, Makochekanwa *et al.*[109] claimed that the forward effect neglects an important contribution to the positron CS for polar molecules, in particular at low energies. For instance, the TCS measured for water at 0.5 eV should be increased by around ~ 67%, and that for formic acid at 4 eV by around ~ 45 % in order to account for this effect. Since the permanent dipole moment of pyrimidine is higher than in these targets, it is expected the forward angle scattering correction to be even more significant here. When a partial integration is performed to the calculated CS emulating the experimental angular conditions, excellent agreement is now achieved between the IAM-SCAR theory and the measurements reported by Palihawadana *et al.*[100] from ~1 eV up to ~100 eV of incident energy. On the other hand, measurements from Zecca *et al.*[99] lay significantly below Palihawadana's *et al.*[100] data. This marked discrepancy is

believed to be caused by the different angular acceptance of the experimental apparatuses they employed.[100] However, Zecca *et al.*[99] did not report any information about the angular acceptance of their experimental setup, and therefore is not possible to give any realistic quantitative comparison with these measurements. The above discussion demonstrates the importance of correctly account for the forward angle effects of the experiments in order to give a realistic comparison with the calculations.

Given the general good agreement found between the present IAM-SCAR calculations and the experimental data, the level of accuracy of these calculations is estimated be similar to that found for electron collisions, ~10%. Regarding the R-matrix procedure, one should note that above ~3 eV the accuracy of the R-matrix cross sections is inevitably lower than that of electron scattering cross sections for the same target, due to the absence of the Ps formation channels from the calculations. The Ps formation cross section peaks around 10 eV, where its contribution is about 20% that of the elastic cross section. This is approximately the additional uncertainty that applies to the R-matrix elastic and total positron cross sections.

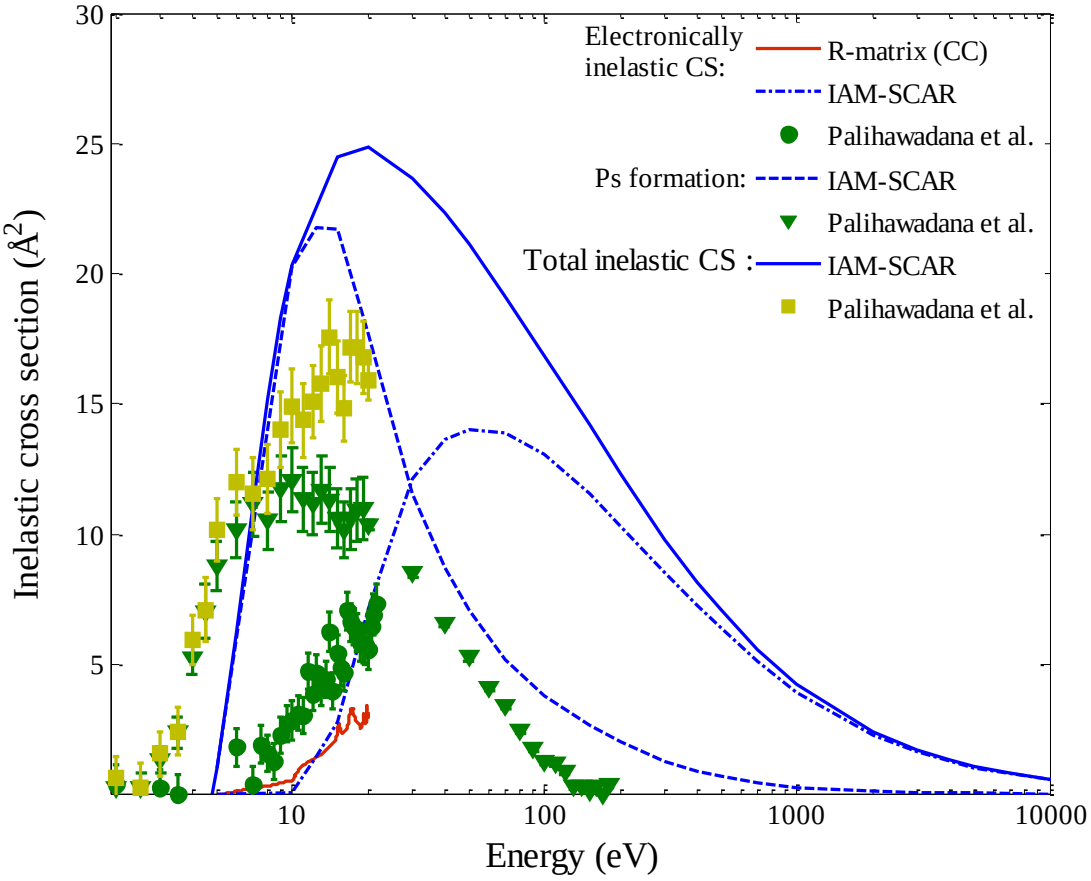

Figure 3.51: Electronically inelastic integral cross sections computed with the R-Matrix approach at the CC level and the IAM-SCAR method, together with the Ps formation cross sections from IAM-SCAR theory. These data is compared with the experimental measurements reported by Palihawadana *et al.*[100]

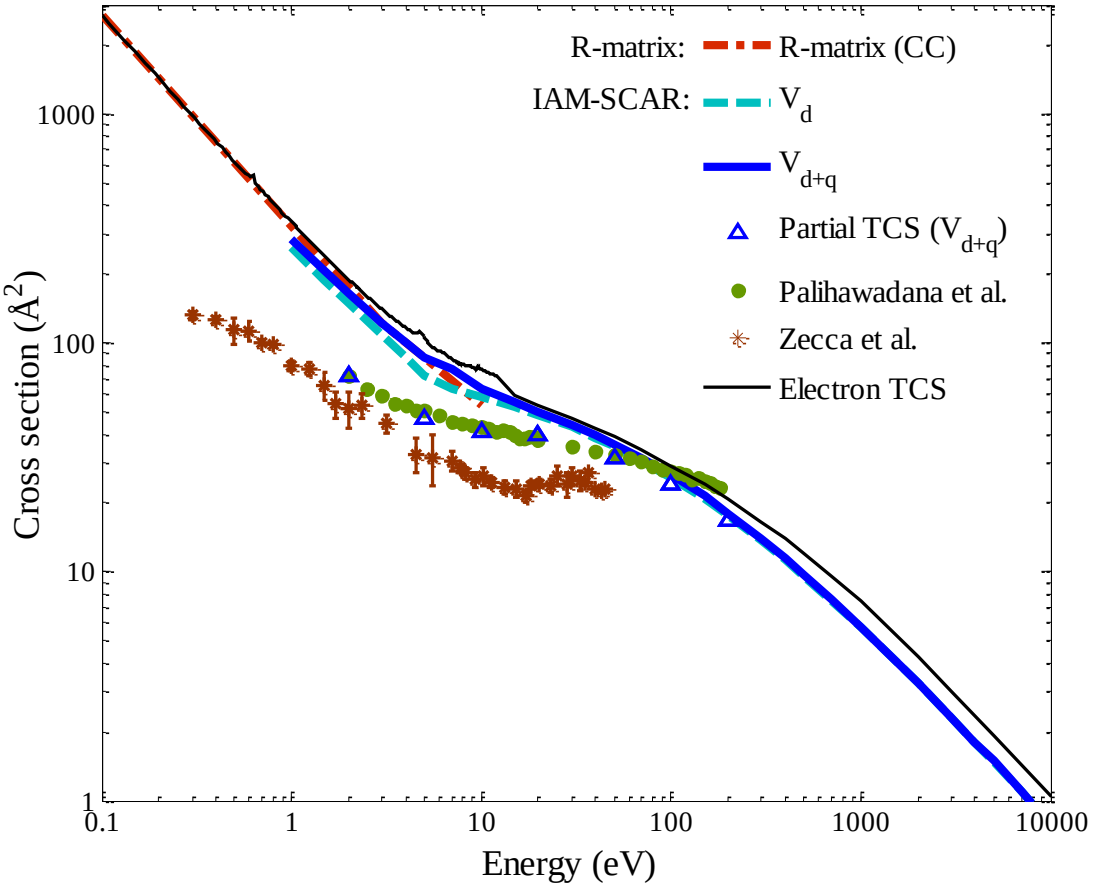

Figure 3.52: Total cross sections (dipole corrected) computed with the R-matrix-POLYDCS procedure (at the CC level) and the IAM-SCAR approach using the V_d and V_{d+q} polarization potentials. Partially integrated CS values (i.e. emulating the experimental conditions) are given for the theoretical IAM-SCAR results, together with the experimental data from Palihawadana *et al.* [100] and Zecca *et al.*[99] Additionally, we have plotted the recommended electron scattering TCS, dipole-corrected (Table 3.10; see text for further details).

Table 3.12: Elastic and elastic dipole-corrected cross sections computed with the R-matrix approach at the SP and CC levels (cc-pVDZ basis set and l=4).

	R-matrix SP model (Å^2)		R-matrix CC model (Å^2)	
Energy (eV)	Elastic	Elastic-dipole corrected	Elastic	Elastic-dipole corrected
0.50	84.26	616.22	103.52	635.13
1.00	42.62	326.71	53.13	338.35
1.50	29.43	225.94	38.58	235.98
2.00	23.35	174.77	32.20	184.08
2.50	20.02	143.46	28.64	152.30
3.00	17.98	122.56	26.34	131.04
5.00	14.52	79.91	21.78	86.65
10.00	13.38	47.85	18.18	52.61

Table 3.13. Integral elastic, inelastic (comprising rotational excitations, electronic-state excitations, positronium formation and ionization) and total cross sections for positron scattering from pyrimidine in the energy range from 1 to 10000 eV, calculated with the IAM-SCAR approach both with the V_d and V_{d+q} polarization potential.

Energy (eV)	IAM-SCAR with V_d			IAM-SCAR with V_{d+q}		
	Elastic (Å^2)	Inelastic (Å^2)	Total (Å^2)	Elastic (Å^2)	Inelastic (Å^2)	Total (Å^2)
1.0	49.56	212.52	262.08	71.12	212.80	283.92
1.5	40.32	148.96	189.28	57.40	148.96	206.36
2	34.72	115.36	150.08	48.72	115.36	164.08
3	27.78	80.36	108.36	41.72	80.36	122.08
4	23.60	62.16	85.96	37.24	62.16	99.40
5	20.38	52.08	72.24	33.88	53.02	86.90
7	14.08	48.72	62.72	28.00	58.49	86.49
10	10.53	47.6	57.96	15.46	47.60	63.06
15	9.44	43.4	52.64	11.82	43.40	55.22
20	9.30	39.48	48.72	10.92	39.48	50.40
30	8.96	33.88	42.84	10.08	33.88	43.96
40	8.46	29.96	38.64	9.41	29.96	39.37
50	7.92	27.412	35.28	8.76	27.41	36.18
70	6.86	23.744	30.52	7.62	23.74	31.36
100	5.63	20.216	25.844	6.30	20.22	26.52
150	4.34	16.52	20.86	4.87	16.52	21.39
200	3.56	14.084	17.64	3.98	14.08	18.06
300	2.64	11.004	13.664	2.94	11.00	13.94
400	2.13	9.1	11.228	2.36	9.10	11.46
500	1.80	7.812	9.604	1.98	7.81	9.79
700	1.39	6.104	7.504	1.52	6.10	7.62
1000	1.06	4.62	5.684	1.14	4.62	5.76
2000	0.62	2.632	3.248	0.65	2.63	3.28
3000	0.45	1.862	2.31	0.46	1.86	2.32
4000	0.35	1.4476	1.8004	0.36	1.45	1.81
5000	0.29	1.1872	1.4812	0.30	1.19	1.49
7000	0.22	0.8764	1.0976	0.22	0.88	1.10
10000	0.16	0.63	0.7896	0.16	0.63	0.79

Electron and Positron Scattering

Finally, it is interesting to compare the present positron cross sections with the previous results on electron scattering (given by the recommended values, as explained in Section 3.2.2.1). When comparing electron and positron elastic CSs, the most obvious difference is that no shape resonances are present when the incident particle is a positron (see Figure 3.48 and 3.49). With this exception, electron and positron CSs are similar, although the positron CSs tend to be lower in magnitude. Accordingly, this decrease in size is also observed in the elastic DCS (Figure 3.50) and is not unexpected: firstly, no exchange interaction exists when the incident particle is a positron. In addition, whereas both the static and the polarization interaction are attractive for electrons, the static interaction becomes repulsive for positrons. The weaker attractive forces acting between the incident positron and the target molecule lead therefore to smaller cross sections than those for electron scattering. We also note that both the electron- and positron- impact cross sections are strongly peaked in the forward direction, confirming therefore that the dipole interaction dominates over the static interaction, in particular at low energies, independent of the sign of the incident particle charge. However, it can be seen that positrons are more forward-scattered than electrons.

In accordance with the above discussion, the positron TCSs lie somewhat below the corresponding electron TCS, in particular at low energies, as can be seen in Figure 3.52. The most significant processes that distinguish positron and electron scattering, i.e. the exchange interaction and Ps formation, become small at energies above 100-200 eV. Despite the fact that the interaction probabilities for electron and positron scattering are therefore expected to converge at higher energies, we observe in Figure 3.52 that the electron TCS remains slightly larger, to within 20%. These small discrepancies are not considered to be important, and can be attributed to the different atomic absorption potentials employed for positron and electron scattering.[110]

3.3. Summary

In this chapter we have presented a quantum scattering study on electron collisions with a variety of representative molecules, namely, anthracene,[21,22] HCN,[79,82] and the diazines, pyrazine[52] and pyrimidine.[98] Previous scattering investigations with these molecules were either nonexistent, as is the case of anthracene, or incomplete in terms of the energy range covered by the study. Hence, this study has provided, and completed, useful scattering information about these relevant biomolecules. In particular, complete sets of recommended integral elastic, inelastic and total cross sectional data have been reported over a broad energy range, from 0.1 eV (0. 01 meV in the case of anthracene) up to 10 keV, for electron collisions with the

abovementioned molecules. Elastic DCSs have also been reported over the same energy ranges. The present sets of integral and differential CS values find their main application as input data for single-track structure simulations (e.g., the LEPTS code, see Chapter 4).

In order to cover a wide energy range, a computational approach based on a combination of quantum scattering methods has been employed. In the low-energy domain, either the single-centre expansion (SA-SCE) approach[1,2] or the R-Matrix method,[3] was employed. The cross sections calculated from these models generally demonstrated good agreement with experimental data collected by other research groups, thus confirming the reliability of both methods up to the ionization threshold. On the other hand, for incident energies below ~30 eV, the IAM-SCAR theory[4,5] is not expected to provide accurate cross sections, and therefore, our data should be taken as merely indicative within this energy range. In fact, this approach is not capable of localizing low-lying resonant structures because of the premises used in the theory which do not consider the molecular structure. At higher energies, we have shown that the IAM-SCAR method starts to form a closer agreement with previous experimental and theoretical sources of data for the four molecules being studied. Thus, the IAM-SCAR results are recommended in the 30-10000 eV energy range. At intermediate energies, the low-energy cross sections computed with the SA-SCE approach and the R-matrix method, were joined together with the IAM-SCAR results through a double logarithmic fitting. When the SA-SCE method was employed (i.e., for the target molecules anthracene and HCN), the uncertainty increased from ~ 10% at 10 eV up to ~ 30% at 30 eV. On the other hand, for the diazines (i.e., pyrimidine and pyrazine) we found excellent agreement between the low-energy R-matrix results and the IAM-SCAR model, with an estimated error of ~10% over the range where the energies overlapped. The larger discrepancies encountered with the SA-SCE theory are attributed to the interaction potential model employed in this method, which does not include the absorption term and therefore yields overestimated cross sections, as confirmed in section 3.2.1.

Our present results indicate that the IAM-SCAR data is generally in better agreement with the cross sections calculated by the R-matrix method, across the overlapping energy region. In addition, the R-matrix method (at the close-coupling level) affords the possibility of calculating electronically inelastic cross sections, which cannot be calculated with the SA-SCE method. However, the condition that the R-matrix sphere must contain the entire electron density of the target implies that the R-matrix method is restricted to relatively small biomolecules. Furthermore, one of the main disadvantages of the R-matrix approach is that it is not a priori clear how many virtual orbitals should be included in the calculations (in the case of medium-sized molecules).[104] This implies that a comparison with experimental data is required in order to establish the optimal size of the virtual space. Whereas on the other hand, the SA-SCE

method does not suffer from the latter disadvantage and, moreover, it can be employed when the target molecules are relatively complex, as is the case of anthracene. Therefore, the choice of the low-energy scattering method for future calculations will depend on the size of the target, the scattering processes we are interested in and the availability of previous experimental data.

In this chapter, we have also presented a quantum scattering analysis of the features of low-energy electrons interacting with anthracene and HCN by means of the SA-SCE method. For the former molecule, we have found the existence of several shape resonances with a π^* character (as inferred from the computed wavefunction (real part) for the resonant electron) at energies below ~5 eV. The presence of a virtual state at vanishing energies was detected, in agreement with the predictions of an earlier experimental investigation.[34] With regard to HCN, our calculations corroborated the two resonances reported by the experimentalists: a low-lying π^*-type resonance located at ~4 eV at the equilibrium geometry of HCN, and a broad σ^* resonance at ~7 eV, when both the CH and CN bonds were stretched.[69,70,74] In addition, we have studied the dissociation dynamics of this small polyatomic target by means of a simple qualitative analysis by adiabatically following a selected bond deformation. Our results indicated that dissociation into CN^-+H is not likely to occur if the molecule is restrained to be linear, but in contrast such process is favoured if the bending coordinate is taken into account, as suggested by other experimental and theoretical sources.[76,74]

In this Chapter we have also paid special attention to polar targets because numerous biomolecules have a strong polar nature, such as HCN and pyrimidine, and the dipole interaction plays an important role in the scattering dynamics, especially at low energies. For such targets, comparison of the calculated integral CS with experimental results is not straightforward. Typically, the energy resolution of the experiments is too low to be able to distinguish between the rotational excitation processes and the elastic events. In addition, due the angular acceptance of the apparatus, part of the forward angle scattering contribution is not detected, such as the dipole-induced rotational excitations. These limitations have noticeable effects on the experimentally determined cross sections. On one hand, experimental elastic CSs are somewhat contaminated by rotational excitation processes, leading to overestimation of the 'elastic' CS. This caused some confusion in the past when comparing experimental and theoretical data, since reasonable agreement was generally observed between the measurements and the calculated cross sections that were not dipole-corrected. Nevertheless, although dipole-induced rotational excitations are rather small over the angular range for which the experimental measurements can be made, they cannot be neglected; for consistency, experimental elastic CS should be compared with the theoretical dipole-corrected elastic CS. On the other hand, experimental TCS represent a lower limit to the true value, as electrons scattered by very small

angles after rotationally exciting a target molecule cannot be discerned from the non-scattered ones. Therefore, due to this, experimental TCSs for pyrazine and pyrimidine were found to be almost identical, despite the strong polar nature of the latter molecule. We have shown that the apparent disagreement observed between theoretical and experimental data (at the level of integral elastic and total CS) was not present when the calculated cross sections were partially integrated emulating the experimental conditions. It can be concluded that theoretical scattering studies are a very useful complement to the experiments, as they can describe energy (and angular) regions which are often inaccessible for experiments.

Finally, we have also reported the first computational investigation on positron collisions with the polar target pyrimidine (see section 3.2.2.2). We have provided elastic, inelastic and total integral CSs, together with the elastic DCS, over a broad energy range (0.1 – 10000 eV). CSs have been calculated at low energies with the R-matrix method using the SP and CC models, and at higher energies with the IAM-SCAR procedure using the dipole potential (V_d) and the dipole plus quadrupole potential (V_{d+p}). We observed that the calculations were quite sensitive to the description of the polarization potential, when dipole effects were not considered, as was expected (see Figure 3.48). However, once the cross sections were Born corrected to properly account for the effects of pyrimidine's large permanent dipole moment (and therefore the dipole-induced rotational excitations), we noted that our results were rather insensitive to the model employed. This is a consequence of the dominant role played by the dipole interaction over the static potential (see Figure 3.49). Despite the limitations of the experimental procedures and of our calculations, reasonable agreement was found between the measured CS[99,100] and the CS computed in the present study, particularly in the case of the dipole plus quadrupole polarization (V_{d+p}) IAM-SCAR model.

Bibliography

[1] F. A. Gianturco, R. R. Lucchese and N. Sanna, *J. Chem. Phys.* **100**, 6464 (1994).

[2] A. P. P. Natalense and R. R. Lucchese, *J. Chem. Phys.* **111**, 5344 (1999).

[3] P.G. Burke, *R-Matrix Theory of Atomic Collisions: Application to Atomic, Molecular and Optical Processes* (Springer, 2011).

[4] F. Blanco and G. García, *Phys. Lett. A* **317**, 458 (2003).

[5] F. Blanco and G. García, *Phys. Lett. A* **330**, 230 (2004).

[6] L.H. Keith and W.A. Telliard, *Environ. Sci. Technol.* **13**, 416 (1979).

[7] H. Hamdi, L. Manusadzianas, I. Aoyama and N. Jedidi, *Chemosphere* **65**, 1153 (2006).

[8] A. Tuvikene, *Ann. Zoo. Fen*. **32**, 295 (1995).

[9] J.E. Stein, T.K. Collier, W.L. Reichert, E. Casillas, T. Hom and U. Varanasi, *Environ. Toxicol. Chem.* **11**, 701 (1992).

[10] U.P. Vijh, A.N. Witt and K.D. Gordon, *ApJ.* **606**, L65 (2004).

[11] T.P. Snow and V. M. Bierbaum, *Annu. Rev. Anal. Chem.* **1**, 229 (2008).

[12] J. von Jager, *Ann. Phys., Lpz.* **7**, 147 (1969).

[13] E.E. Koch, S. Kunstreich and A. Otto, *Opt. Commun.* **2**, 365 (1971).

[14] M. Allan, *J. Electron Spectrosc. Relat. Phenom.* **48**, 219 (1989).

[15] K.F. Man, S. Trajmar, J.W. McConkey, J.M. Ratliff and M. Khakoo, *J. Phys. B: At. Mol. Opt. Phys.* **25**, 5245 (1992).

[16] L.G. Christophorou, D.L. McCorkle and J.G. Carter, *J. Chem. Phys.* **54**, 253 (1971).

[17] P.D. Burrow, J.A. Michejda and K.D. Jordan, *J. Chem. Phys.* **86**, 9 (1987).

[18] S. Tobita, M. Meinke, E. Illenberger, L. Christophorou, H. Baumgartel and S. Leach, *Chem. Phys.* **161**, 501 (1992).

[19] A. Canosa, D. C. Parent, D. Pasquerault, J. C. Gomet, S. Laubé and B. R. Rowe, *Chem. Phys. Lett.* **228**, 26 (1994).

[20] H.M. Boechat-Roberty, M.L.M. Roccoz, C.A. Lucas, M.B. Fernandes and G.G.B. de Souza, *J. Phys. B: At. Mol. Opt. Phys.* **30**, 3369 (1997).

[21] *Appl Rad. Isot.* **83**, 68 (2014).

[22] A.G. Sanz, F. Carelli, F. Sebastianelli, F.A. Gianturco and G. García, *New J. Phys.* **15,** 013018 (2013).

[23] J. Tobik and A. Dal Corso, *J. Chem. Phys.* **120**, 9934 (2004).

[24] M.J. Frisch, G.W. Trucks, H.B. Schlegel, *et al*. *Gaussian 03* (Wallingford, CT: Gaussian Inc., revision c.02, 2004).

[25] Z.G. Soos, E.V. Tsiper and R.A. Pascal, *Jr.*, *Chem. Phys. Lett.* **342**, 652 (2001).

[26] F. Carelli, *PhD Thesis* (University of Rome "Sapienza", 2012).

[27] F.T. Smith, *Phys. Rev.* **118**, 349 (1960).

[28] R.R. Lucchese and F.A. Gianturco, Int. Rev. Phys. Chem. **15**, 429 (1996).

[29] R. Curik, F.A. Gianturco, R.R. Lucchese and N. Sanna J. Phys. B: At. Mol. Opt. Phys. B **34**, 59 (2001).

[30] Virtual molecular orbitals (MOs) profiles in Figure 3.5 are courtesy of F. Sebastianelli.

[31] F. Carelli and F.A. Gianturco, *Comput. Theor. Chem.* **990**, 67 (2012).

[32] T. Shida and S.J. Iwata, *Am. Chem. Soc.* **95**, 3473 (1973).

[33] S. Denifl, S. Ptasinska, M. Probst, J. Huesak, P. Scheier and T.D. Maerk, *J. Phys. Chem. A* **108**, 6562 (2004).

[34] D. Field, S.L. Lunt, S.V. Hoffmann, J.P. Ziesel and R.J. Gulley, *in The Physics and Chemistry of the Interstellar Medium* (edited by V Ossenkopf *et al.*, Herdecke: GCA, p. 367, 1999).

[35] D. Field, J.P. Ziesel, S.L.Lunt, R. Parthasarathy, L. Suess, S.B. Hill, F.B. Dunning, R.R. Lucchese and F.A. Gianturco, *J. Phys. B.: At. Mol. Phys.* **34,** 4371 (2001).

[36] C.J. Joachain, *Quantum Collision Theory* (New York, North-Holland, 1987).

[37] R.G. Newton, *Scattering Theory of Waves and Particles* (New York, Springer, 1982).

[38] F. Carelli and F.A. Gianturco, *Mon. Not. R. Astron. Soc.* **422**, 3643 (2012).

[39] H. Cho, R.J. Gulley, K. Sunohara, M. Kitajima, L.J. Uhlmann, H. Tanaka and S.J. Buckman. *J. Phys. B: At. Mol. Opt. Phys.* **34**, 1019 (2001).

[40] R.J. Gulley and S.J. Buckman. *J. Phys. B: At. Mol. Opt. Phys.* **32**, L405 (1999).

[41] H. Kato, M.C. García, T. Asahina, M. Hoshino, C. Makochekanwa and H. Tanaka, *Phys. Rev. A* **79**, 062703 (2009).

[42] O. Sueoka, *J. Phys. B: At. Mol. Opt. Phys.* **21**, L631 (1988).

[43] F. Blanco and G. García, *Phys. Lett. A* **360**, 707 (2007).

[44] P. Mozejko, G. Kasperski, C. Szmytkowski, G.P. Karwasz, R.S. Brusa and A. Zecca, *Chem. Phys. Lett.* **257**, 309 (1996).

[45] C. Makochekanwa, O. Sueoka and M. Kimura, *Phys. Rev. A* **68**, 032707 (2003).

[46] (a) F.A. Gianturco and R.R. Lucchese, J. Chem. Phys. **108**, 6144 (1998). (b) F.A. Gianturco and R.R. Lucchese, J. Chem. Phys. **114**, 3429 (2001).

[47] A.R. Milosavljević, F. Blanco, J.B. Maljković, D. Šević, G. García and B.P. Marinković, *New J. Phys*. **10**, 103005 (2008).

[48] A. Muñoz, J. C. Oller, F. Blanco, J. D. Gorfinkiel, P. Limão-Vieira and G. García, *Phys. Rev*. *A* **76**, 052707 (2007).

[49] I. Nenner and G.J. Schulz, *J. Chem. Phys.* **62**, 1747 (1975).

[50] P. Palihawadana, J.P. Sullivan, S.J. Buckman and M.J. Brunger, *J. Chem. Phys.* **137**, 204307 (2012).

[51] M.C. Fuss, A.G. Sanz, F. Blanco, J.C.Oller, P. Limão-Vieira, M.J. Brunger and G. García, *Phys. Rev. A* **88**, 042702 (2013).

[52] A.G. Sanz, M.C. Fuss, F. Blanco, Z. Mašín, J.D. Gorfinkiel, M.J. Brunger and G. García, *J. Chem. Phys*. **144**, 128 (2013).

[53] C. Winstead and V. McKoy, *Phys. Rev. A* **76**, 012712 (2007).

[54] K. Takatsuka and V. McKoy, *Phys. Rev. A* **24**, 2473 (1981).

[55] K. Takatsuka and V. McKoy, *Phys. Rev. A* **30**, 1734 (1984).

[56] Z. Mašín and J.D. Gorfinkiel, *J. Chem. Phys.* **135**, 144308 (2011).

[57] P. Weber and J. Reimers, *J. Phys. Chem. A* **103**, 9821 (1999).

[58] D.M.P. Holland, A.W. Potts, L. Karlsson, M. Stener and P. Decleva, *Chem. Phys.* **390**, 25 (2011).

[59] J. Tennyson, *Phys. Rep.* **491**, 29 (2010).

[60] S. J. Suresh and V. M. Naik, J. Chem. Phys. **113**, 9727 (2000).

[61] (a) Kulakowski, I., Geller, M., Lesyng, B., Wierzcho, K. L. Biochim Biophys Acta, **361**, 119 (1974). (b) Weber, H.P., Craven, B. M. Acta Crystallogr. B, **46**, 532 (1990).

[62] H. DeVoe and I. Jr. Tinoco, J. Mol. Biol. **4**, 500 (1962).

[63] Jr. R. D. Nelson, D. R.Lide and A.A. Maryott, Selected Values of Electric Dipole Moments for Molecules in the Gas Phase, NSRDS-NBS Series Vol. 10 (US GPO, Washington, DC, 1967).

[64] R.V. Yelle, *Astrophys. J.* **383**, 380 (1991).

[65] V. Vuitton, P. Lavvas, R.V. Yelle, M. Galand, A. Wellbrock, G.R. Lewis, A.J. Coates and J.E. Wahlund, *Planet Space Sci.* **57**, 1558 (2009).

[66] S. Gupta, E. Ochiai and C. Ponnamperuma, *Nature* **293**, 725 (1981).

[67] R.L. DeLeon and J.S. Muenter, *J. Chem. Phys.* **80**, 3992 (1984).

[68] M. Inoue, *J. Chem. Phys.* **63**, 1061 (1966).

[69] F. Edard, A.P. Hitchcock and M. Tronc, *J. Phys. Chem.* **94**, 2768 (1990).

[70] P.D. Burrow, A.E. Howard, A.R. Johnston and K.D. Jordan, *J. Phys. Chem.* **96**, 7570 (1992).

[71] O. May, D. Kubala and M. Allan, *Phys. Rev. A* **82**, 010701 (2010).

[72] S.K. Srivastava, H. Tanaka and A. Chutjian, *J. Chem. Phys.* **69**, 1493 (1978).

[73] A. Jain and D.W. Norcross, *Phys. Rev. A* **32**, 134 (1985).

[74] A. Jain and D.W. Norcross, *J. Chem. Phys.* **84**, 739 (1986).

[75] H.N. Varambhia and J. Tennyson, *J. Phys. B* **40**, 1211 (2007).

[76] S.T. Chourou and A.E. Orel, *Phys. Rev. A* **80**, 032709 (2009).

[77] A. Jain and K.L. Baluja, *Phys. Rev A* **45**, 202 (1992).

[78] A. Faure, H.N. Varambhia, T. Stoecklin and J. Tennyson, *Mon. Not. R. Astron. Soc.* **382**, 840 (2007).

[79] A.G. Sanz, M.C. Fuss, F. Blanco, F. Sebastianelli, F.A. Gianturco and G. García, *J. Chem. Phys.* **137**, 124103 (2012).

[80] L.E. Sutton, *Tables of Interatomic Distances and Configuration in Molecules and Ions;* (Chemical Society London, London, p M106, 1958).

[81] J.E. Gready, G.B. Bacskay and N.S. Hush, *Chem. Phys.* **31**, 467 (1978).

[82] A.G. Sanz, F. Sebastianelli and F.A. Gianturco, *in Radiation Damage in Biomolecular systems* (edited by G.García and M.C. Fuss, pp. 71-86, Springer, 2012).

[83] (a) T.P.M. Goumans, F.A. Gianturco, F. Sebastianelli, I. Baccarelli and J.L. Rivail, *J. Chem. Theory Comput.* **5**, 217 (2009). (b) F.A. Gianturco, F. Sebastianelli, R.R. Lucchese, I. Baccarelli, and N. Sanna, *J. Chem. Phys*. **128**, 174302 (2008).

[84] Carelli, F. Sebastianelli, I. Baccarelli, and F.A. Gianturco, *Int. J. Mass Spectrom*. **277**, 155 (2008).

[85] M.T. Lee, I. Iga, L.E. Machado, L.M. Brescansin, E.A. y Castro, I.P. Sanches and G.L.C. de Souza, *J. Elect. Spectrosc. Rel. Phenom.* **155**, 14 (2007).

[86] D.C.Frost, S.T. Lee and C.A. McDowell, *Chem. Phys. Lett.* **23**, 472 (1973).

[87] A.S. Dickinson, *J. Phys. B* **10**, 967 (1977).

[88] G.L. Blackman, R.D. Brown and F.R. Burden, *J. Mol. Spectrosc.* **35**, 444 (1970).

[89] NIST Computational Chemistry Comparison and Benchmark Database, NIST Standard Reference Database Number 101 Release 15b, August 2011, Editor: Russell D. Johnson III http://cccbdb.nist.gov/.

[90] J.B. Maljković, A.R. Milosavljević, F. Blanco, D. Šević, G. García and B.P. Marinković. *Phys. Rev. A.* **79**, 052706 (2009).

[91] P. Palihawadana, J.P Sullivan, M.J. Brunger, C. Winstead, V. McKoy, G. García and F. Blanco, S.J. Buckman, *Phys. Rev. A* **84**, 062702 (2011).

[92] (a) D. B. Jones, S. M. Bellm, P. Limão-Vieira, M. J. Brunger, Chem. Phys. Lett. 535, 30 (2012). (b) D.B. Jones, S. M. Bellm, F. Blanco, M. C. Fuss, G. García, P. Limão - Vieira, M. J. Brunger, J. Chem. Phys. **137**, 074304 (2012).

[93] J.D. Builth-Williams, S.M. Bellm, D.B. Jones, H. Chaluvadi, D.H. Madison, C.G. Ning, B. Lohmann and M.J. Brunger, *J. Chem. Phys.* **136**, 024304 (2012).

[94] F. Ferreira da Silva, D. Almeida, G. Martins, A.R. Milosavljevic, B.P. Marinkovic, S.V. Hoffmann, N.J. Mason, Y. Nunes, G. García and P. Limão-Vieira, *Phys. Chem. Chem. Phys.* **12**, 6717 (2010).

[95] P.L. Levesque, M. Michaud and L. Sanche, *J. Chem. Phys.* **122**, 094701 (2005).

[96] Z. Mašín, J.D. Gorfinkiel, D.B. Jones, S.M. Bellm and M.J. Brunger, *J. Chem. Phys.* **136**, 144310 (2012).

[97] J.R. Ferraz, A.S. dos Santos, G.L.C. de Souza, A.I. Zanaleto, T.R.M. Alves, M.T. Lee, L.M. Brescansin, R.R. Lucchese and L.E. Machado, *Phys. Rev. A* **87**, 032717 (2013).

[98] A.G. Sanz, M.C. Fuss, F. Blanco, Z. Mašín, J.D. Gorfinkiel, F. Carelli, F. Sebastianelli, F.A. Gianturco and G. García, *Appl. Rad. Isot.* **83**, 57 (2014).

[99] A. Zecca, L. Chiari, G. García, F. Blanco, E. Trainotti and M.J. Brunger, *J. Phys. B: At. Mol. Opt. Phys.* **43**, 215204 (2010).

[100] P. Palihawadana, R. Boadle, L. Chiari, E.K. Anderson, J.R. Machacek, M.J. Brunger, S.J. Buckman and J.P. Sullivan, "*Positron scattering from pyrimidine*" (Submitted for publication).

[101] A.G. Sanz, M.C. Fuss, F. Blanco, Z. Mašín, J.D. Gorfinkiel, M.J. Brunger and G. García, *Phys. Rev.A* **88**, 062704 (2013).

[102] M. Schreiber, M.R. Silva-Junior, S.P.A. Sauer and W. Thiel, *J. Chem. Phys.* **128**, 134110 (2008).

[103] A. Faure, J.D. Gorfinkiel, L.A. Morgan and J. Tennyson, *Comput. Phys. Commun.* **144**, 224 (2002).

[104] Z. Mašín, *PhD Thesis* (The Open University, 2012).

[105] G. Fischer, Z.L. Cai, J.R. Reimers and P. Wormell, *J. Phys. Chem. A* **107**, 3093 (2003).

[106] C. Hattig, O. Christiansen, S. Coriani and P. Jorgensen, *J. Chem. Phys.* **109**, 9237 (1998).

[107] B. Jansik, D. Jonsson, P. Salek and H. Agren, *J. Chem. Phys.* **121,** 7595 (2004).

[108] K.L. Baluja, R. Zhang, J. Franz and J. Tennyson, *J. Phys. B: At. Mol. Opt. Phys.* **40**, 3515 (2007).

[109] C. Makochekanwa, A. Banković, W. Tattersall, A. Jones, P. Caradonna, D.S. Slaughter, K. Nixon, M.J. Brunger, Z. Petrović, J.P. Sullivan and S.J. Buckman, *New J. Phys.* **11**, 103036 (2009).

[110] L. Chiari, E. Anderson, W. Tattersall, J.R. Machacek, P. Palihawadana, C. Makochekanwa, J. P. Sullivan, G. García, F. Blanco, R.P. McEachran, M.J. Brunger and S.J. Buckman, J. Chem. Phys. **138**, 074301 (2013).

Chapter 4

Simulation

As we have seen in previous chapters, electrons and positrons interact with biological media via diverse energy-dependent events, such as elastic scattering, ionization, electronic and rotational excitations, or DEA, with different probabilities of interaction. Due to the random nature of these interactions, charged particles do not experience the same sequence of scattering events as they thermalize. The stochastic character of the problem means that it must be described with event-by-event Monte Carlo (MC) calculations.[1] Such approach permits to follow the history of an incident particle and its products in a medium of interest, providing an instructive picture of the damage processes taking place, at the molecular level.

During the last two decades various MC codes[2-5] have been developed for modelling electron, positron and photon track structures, among which we should highlight GEANT4 (Geometry And Tracking)[4] and PENELOPE (PENetration and Energy Loss of Positrons and Electrons)[5]. The fundamentals are essentially the same for each of these methods but differ in the cross section databases which they use to represent the different scattering processes. In an attempt to reduce the computational tasks, those simulations generally treat matter as a continuum of atomic constituents and force low-energy electrons to instantly deposit their remaining energy when they reach a certain energy cut-off value. In addition, energy deposition in a given target volume is assumed to be directly proportional to the number of ionization events that have occurred therein. This means that potentially damaging interactions driven by electrons at very low-energies (e.g., dissociations induced by electronic and vibrational

excitations of the molecule or by electron attachment) are simply ignored. As mentioned earlier, these low-energy processes contribute significantly to DNA damage.[6]

For these reasons, the Low Energy Particle Track Simulation (LEPTS)[7] was developed with the main objective of improving the available Monte Carlo codes by incorporating the effects of low-energy particles. This requires an appropriate set of input parameters, mainly formed from experimental and theoretical cross sections (CS) for each of the possible scattering processes, as well as suitable energy-loss distribution functions. Under these conditions, the LEPTS code gives a molecular-level description of electron/positron transport accounting for all the collision events occurring during the thermalization process.

Water is one of the most abundant substances in the universe. It is also the most relevant component in living organisms (cells are comprised of 70-80% water)[8] and so is often used as a surrogate for modelling human tissue.[9] Due to the general importance of this compound within various fields of research, it has been extensively studied[10-12] in the past and reliable input probability distribution functions are available in the literature. Furthermore, water shares some physico-chemical properties with other DNA subunits, for example a strong dipole moment (which dramatically affects the scattering dynamics, as we saw in section 3.2), making it a very representative target molecule for modelling biological compounds. In this chapter we present an example to describe how the LEPTS procedure is used to simulate electron and positron tracks in liquid water. As this simulation code mainly focuses on the low-energy domain, we have chosen an initial energy of 15 keV.[13,14] Details about the simulation procedure and the input data are given below.

4.1. Input Data Requirements

The main parameters which are required for modelling single e^- and e^+ tracks in biological matter can be summarized as follows:

- *Total scattering cross section*: This constitutes a critical reference value since it represents the sum of all the possible interaction processes accounted for. It also defines the mean free path of the incident particle in a certain absorber.

- *Differential and integral elastic CS*: Elastic processes are relevant at any energy. Albeit they are not important in terms of energy deposition, they cause large angular deflections of the projectile. Hence, they are crucial parameters to determine the direction of the primary and secondary particles until their final thermalization.

- *Differential and integral inelastic CS*: Integral CS for the different inelastic interactions that can take place are necessary, namely, ionization, electronic excitation, rotational excitation (which is particular important in the case of polar targets), vibrational excitation, neutral dissociation, and electron attachment (only in case of electron scattering). Additionally, when the impinging particle is a positron, positronium (Ps) formation is also considered.

  Given that inelastic differential cross sections are generally available only for a small range of scattering angles and energies, we can derive the inelastic angular distributions from the elastic DCS in combination with the energy loss spectra.[15] From the general trend observed in angular distributions of electrons scattered inelastically, which show smaller differences in magnitude (i.e., 'flatter' distributions) together with larger scattering at backwards angles for increasing energy loss, the following empirical formula was derived by Fuss *et al.*,[15]

$$\frac{d^2\sigma(E)}{d\Omega\Delta E} \propto \left(\frac{d\sigma(E)}{d\Omega}\right)_{el}^{1-\frac{\Delta E}{E}}, \tag{4.1}$$

  where σ is the scattering cross section and Ω is the solid angle. One can easily see that this approximation leads to the elastic DCS for $\Delta E = 0$, and generates gradually the observed flattening effect up to reaching an isotropic distribution for the extreme case of complete energy loss (i.e., $\Delta E = 0$).[15] Although this formula is a rough approximation to a complex problem, it can be implemented easily into the simulation and provides reasonable results as we showed in earlier works.[15-17]

- *Energy-loss distribution functions*: In order to model the energy transferred in a scattering event, we use the energy loss distribution functions derived from the experimental energy loss spectra. It has been shown that for relatively high energies (above 100 eV) the energy loss spectra are almost independent of the incident energy and scattering angle, thus a unique energy loss function is needed. In contrast, for lower energies different energy loss distribution functions should be considered for different energies and angles.

When the number of processes considered in the calculation is big enough to minimise statistical fluctuations, the numerical uncertainties linked to the Monte Carlo procedures are negligible compared to the uncertainties affecting the input parameters.[14] This means that the reliability of a MC simulation is determined mainly by the accuracy of the input data sets. Given that above 10 keV the standard Born-Bethe theory is valid (see Chapter 2), we will focus on procedures to derive scattering cross sections and energy loss data for incident energies below 10 keV. Note that the set of data employed for the present simulation is related to water in the gaseous phase. The absorbing matter is considered to be liquid water by setting the density to

1 g/cm^3 but without accounting for any other properties of the liquid phase. This assumption is not expected to introduce major uncertainties in the calculations for intermediate and high energies (> 100 eV), given that electron mass stopping powers obtained for water in both phases in the keV range are very similar.[10] For low energies, larger discrepancies could arise between both phases due to shifts in the electronic excitation and ionization energies.[14]

One should note that it is not possible to measure all the data required by a nano-scale simulation. Hence, cross sections data sets are built by combining measurements and calculated results. In general, CS data calculated by means of the scattering procedures described in Chapter 2 are considered the main source, once validated by experiments. Experimental data is then used to provide information about processes and energies out of the scope of the theoretical methods we use.

4.1.1. Electron Collision Input

Integral scattering CS for e^--H_2O collisions are shown in Figure 4.1. An extensive analysis on the sources of these data and their associated uncertainties was reported by Muñoz *et al*.[10,11] Essentially, TCS were measured with a transmission beam experiment placed at CSIC-Madrid for energies above 50 eV up to 5000 eV.[10] Below 50 eV, we used a compromised value between our calculated TCS and the experimental data from Curík *et al*.[18] and Szmytkowski.[19] Total ionization CSs, as well as partial ionization CSs corresponding to different ionic fragments, were measured in a pulsed crossed beam experiment in combination with a time of flight (TOF) spectrometer for energies between 50 eV and 10 keV.[10, 20] For lower energies, data were completed with experimental results from Straub *et al*.[21] For elastic collisions and the remaining inelastic channels, integral CSs were derived by combining experimental data available in the literature[12,22] with theoretical calculations performed with the IAM-SCAR method. In addition, angular distribution functions for elastic processes were derived from our differential elastic cross section calculation.[13]

Note that our calculation method IAM-SCAR does not provide cross section data as a function of the energy transfer in the collision, and therefore all the energy loss information required by the model is provided by experiments.[14] At low energies, up to 50 eV, a crossed-beam set-up placed at Flinders University in Australia was used to obtain high resolution (50 - 100 meV) electron energy loss spectra as a function of energy and scattering angle.[11] For higher energies, from 50 to 10000 eV, energy loss spectra measured with the previously mentioned transmission beam experiment were used.[10]

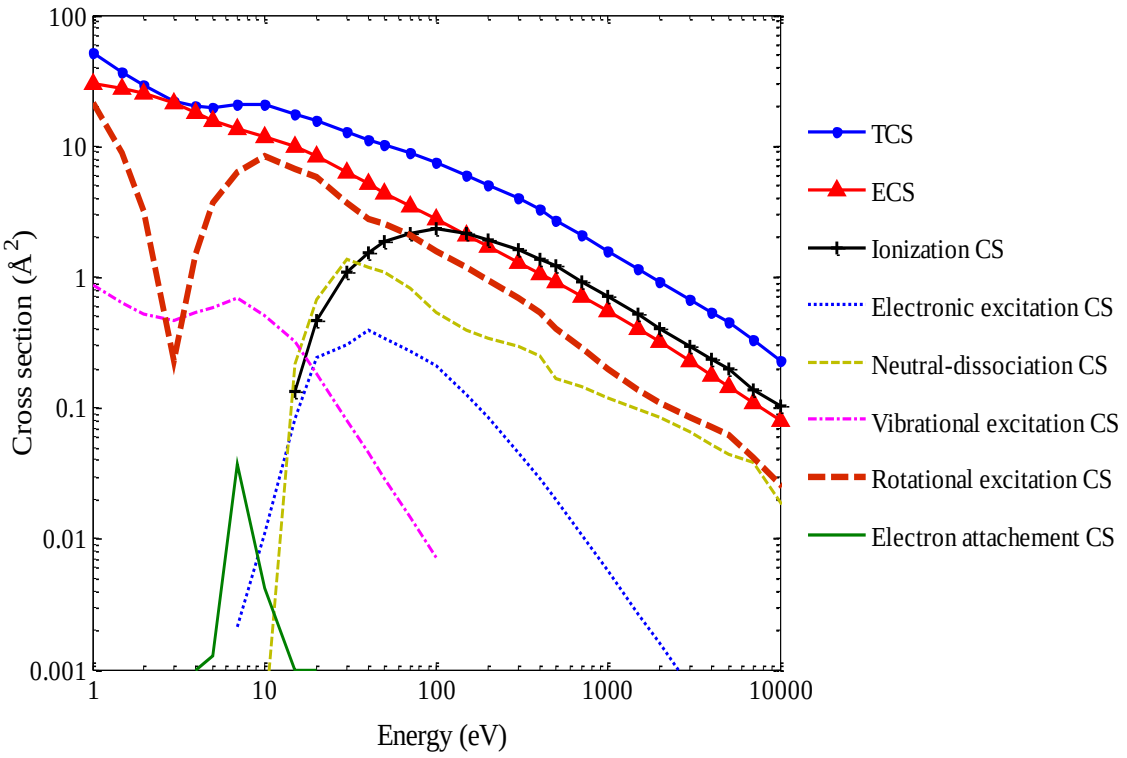

Figure 4.1: Integral cross section values for electron scattering from vapour water employed for the present simulation (these input data represent a synthesis of previous studies).[7]

4.1.2. Positron Collision Input

As discussed in Chapter 3, additional difficulties arise when attempting to measure or calculate positron interaction data. Most of the experimental cross sections used in the present model were provided by the Centre for Antimatter-Matter Studies at the Australian National University.[23] In particular, TCS and Ps formation cross sections were measured with a modified beam attenuation technique (further details of the experimental set-up can be found in Sullivan *et al.*[14,23]). Ionization CS data was taken from the literature and especially from the extensive work carried out by the positron group at University College London.[24] Integral and differential elastic CSs were derived by means of the IAM-SCAR method adapted for positron scattering, as explained in Chapter 2.[13]

Unfortunately, the remaining parameters required to model e^+ tracks are not available in the literature. In such cases, it is customary to use modified electron scattering data to complete the input data sets required by the simulation.[14] In particular, vibrational and rotational excitation CSs were assumed to be the same as those corresponding to the electron case. Electronic excitations of the target are restricted to those states which do not involve spin flip.[14] In addition, we assumed the same energy-loss distribution functions for positrons as for electrons

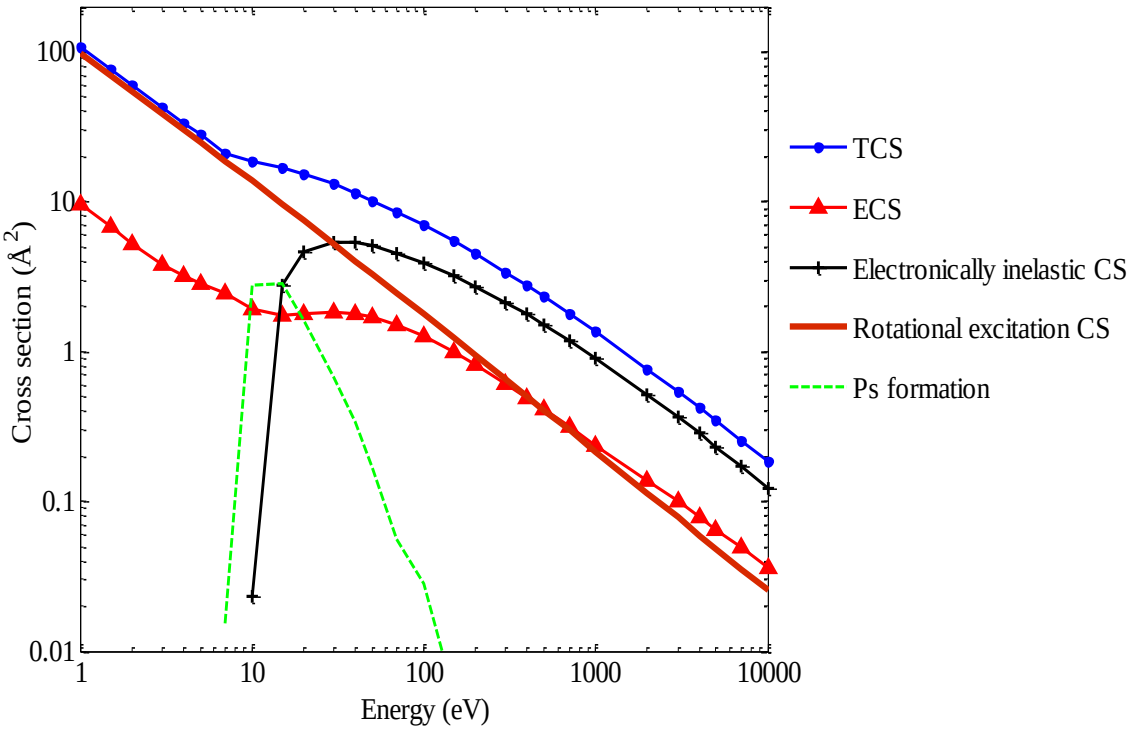

Figure 4.2: Integral cross section values for positron scattering from vapour water employed for the present simulation.

This assumption seems reasonable since the main expected difference, i.e. Ps formation, rapidly leads to positron annihilation without any contribution to the energy-loss spectrum.

4.2. The Monte Carlo code

Our Monte Carlo code (LEPTS) is an event-by-event simulation procedure written in C++ specifically designed for processing low-energy electron and positron interactions, typically in the energy range from 1eV to 1keV. LEPTS is compatible and can be combined with other general purpose Monte Carlo codes commonly in use for radiation dosimetry, such as GEANT4[4] and PENELOPE.[5] It takes sampling mechanisms and some graphical output functions from the GEANT4 toolkit.[4] Additionally, other related tools, such as GAMOS (Geant4-based Architecture for Medicine-Oriented Simulations)[25] have been used to define target composition and geometries. LEPTS also incorporates a graphical tool (LEPTS-Visor) which permits the analysis and visualization of collisional data over the whole irradiated area or within a selected nano-region. The option menu offers the users all the relevant information related to the region of interest, i.e., energy deposited (absorbed dose), total number of interactions, the amount of specific processes (ionizations, dissociations, elastic events, etc...) and secondary particles generated. The main advantage of this combined procedure is that

GEANT4 or PENELOPE can be used as complement to expand upwards the energy range or to simulate other types of radiation, such as photons, whereas electrons and positrons with energies below 10 keV (whether occurring as primary or secondary particles) are tracked with LEPTS, thus providing an accurate modelling of low-energy processes on the nano-scale.

The track simulation procedure for an incoming e^- or e^+ with energies below 10 keV is illustrated schematically in Figure 4.2. The first step consists on sampling the mean free path of the charged particle in the biological medium under study according to the TCS corresponding to its collision energy. Once the location of a collision event is defined, elastic and inelastic integral CS are sampled to determine which kind of collision is taken place and the appropriate routine is called. In the case of elastic collisions, although no energy is deposited in the medium, the charged particle is deflected from the incident beam direction. The code samples the outgoing particle's angle according to the angular distribution functions (normalised probability as a function of the scattering angle) derived from the corresponding elastic DCS. For inelastic collisions, the programme samples the partial integral inelastic CS (ionization, excitation, attachment, etc.) to decide the type of interaction that is taking place and the energy loss distribution function to evaluate the energy transferred to the molecule. Subsequently, the particle's outgoing direction is sampled using the inelastic differential CS.[15] Once the interaction event has finished, the charged projectile is ready to undergo another collision (unless the incident particle has been absorbed via attachment to a molecule, in the case of electrons, or Ps formation for positrons). Additionally, if ionization has taken place, a new secondary e^- is automatically generated. This electron enters in the simulation procedure with an energy given by the difference between the energy transferred by the incident particle and the ionization potential of the molecule and moving in the direction derived from linear momentum conservation. Note that all the SEs generated along the primary track are equally followed until their final absorption or thermalization. According to the energy loss spectrum used, most of the secondary electrons produced are non-ionizing (except for Auger electrons which have much higher energies but representing only a very small percentage of these secondary electrons).

At the present moment, a complete collection of interaction data, including energy-loss distribution functions, is available for various charged particle-molecule systems: electrons - water,[11, 26] electrons - methane,[27] electrons - ethylene,[15] electrons -THF,[17] electrons - SF_6 and positrons - argon.[28] Additionally, complete sets of theoretical cross sectional data are currently available for electron-anthracene,[29] electron-pyrazine,[30] electron-HCN,[31] electron-pyrimidine[32] and positron-pyrimidine[33] (as reported in Chapter 3). To date, the LEPTS code has been employed to simulate electron and positron tracks in some of the aforementioned biomolecular systems. It has also been applied to common treatments used in brachytherapy, with photons emitted by I-125 seeds[34] and electrons emitted by Ru-106 eye applicator plaques.[6,35]

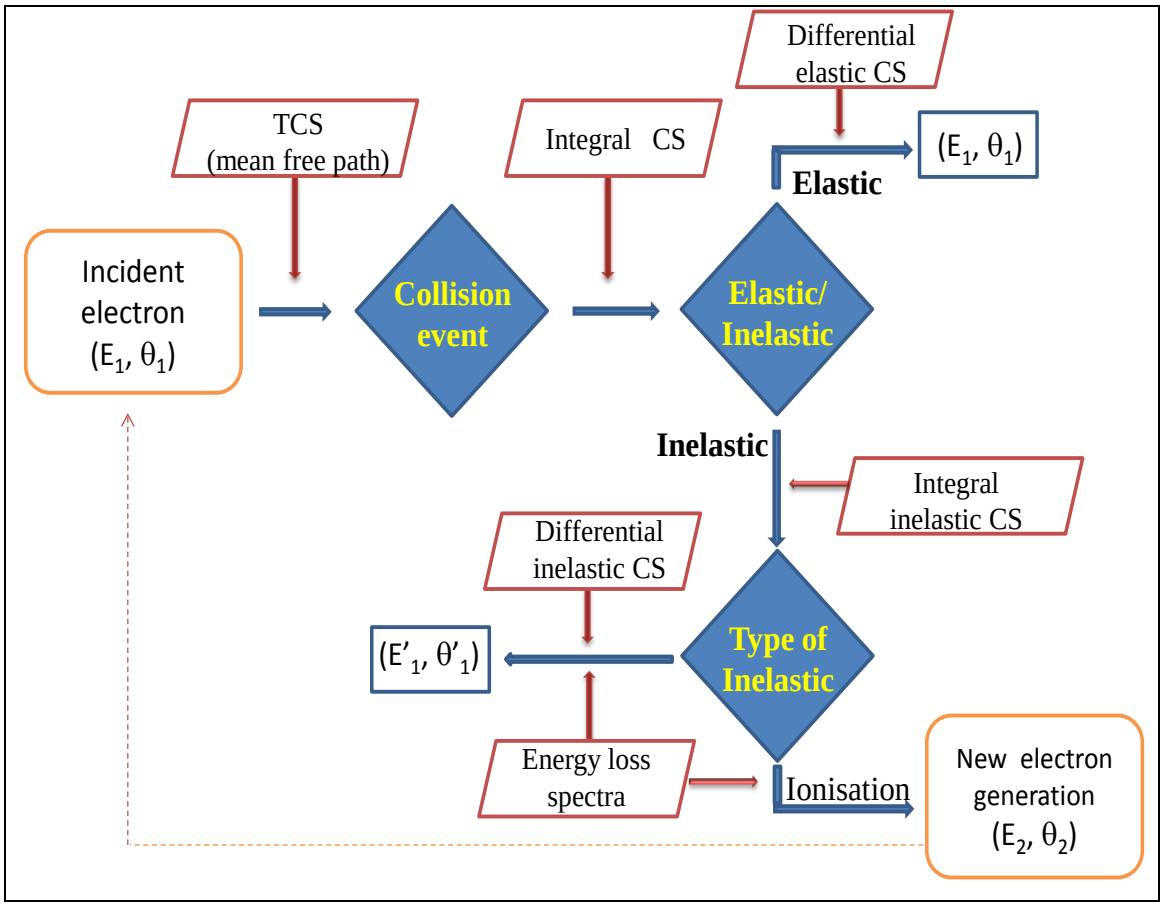

Figure. 4.3: Flow diagram of a single track simulation with the LEPTS code.

4.3. Single Electron and Positron Track Simulation Examples

In order to show the characteristics of the present modelling procedure, we have simulated some electrons and positrons tracks in liquid water with initial energies of 15 keV. As an example, single tracks for 50 e^- until their final thermalization are shown in Figure 4.4a. We also report a zoom-up of a three-dimensional nano-volume near the end of an electron track (panel b). Each dot in the figure represents a collision event and its colour describes a particular type of interaction. It can be seen in Figure 4.4a that the electron tracks are fairly straight at the beginning (high-energy region) but tend to curve as they progressively lose their energy. It can be also appreciated that multiple secondary electrons are produced along the primary particle's path. These low-energy electrons undergo further collisions and their remaining energy is mostly deposited through rotational or vibrational excitations. At the very end of the track, when no other inelastic processes are energetically available, electrons are considered thermalized after undergoing a certain number of successive elastic collisions (see Figure 4.4b).

Relevant information provided by the LEPTS model for both the whole irradiated volume and the selected nano-volume is summarized in Table 4.1. It specifies the total number of

interactions, the number of events for each considered process, the frequency of each process relative to the total number of events and the energy imparted. It can be seen that the energy deposition in the selected nano-volume is ~ 2480 eV, which will lead to a meaningless absorbed dose in it. However, several tens of dissociative processes occur in the nano-volume. In addition, one should note that the frequency of each scattering process found within the nano-volume differs from the average found in the total volume. This is a consequence of the energy dependence of the cross sections for the different scattering channels. Note that these numbers vary considerably from one to another chosen nano-volume along different tracks. In order to obtain reliable information about the type and number of interactions much better statistics than that of the example shown in Figure 4.4 would be required.

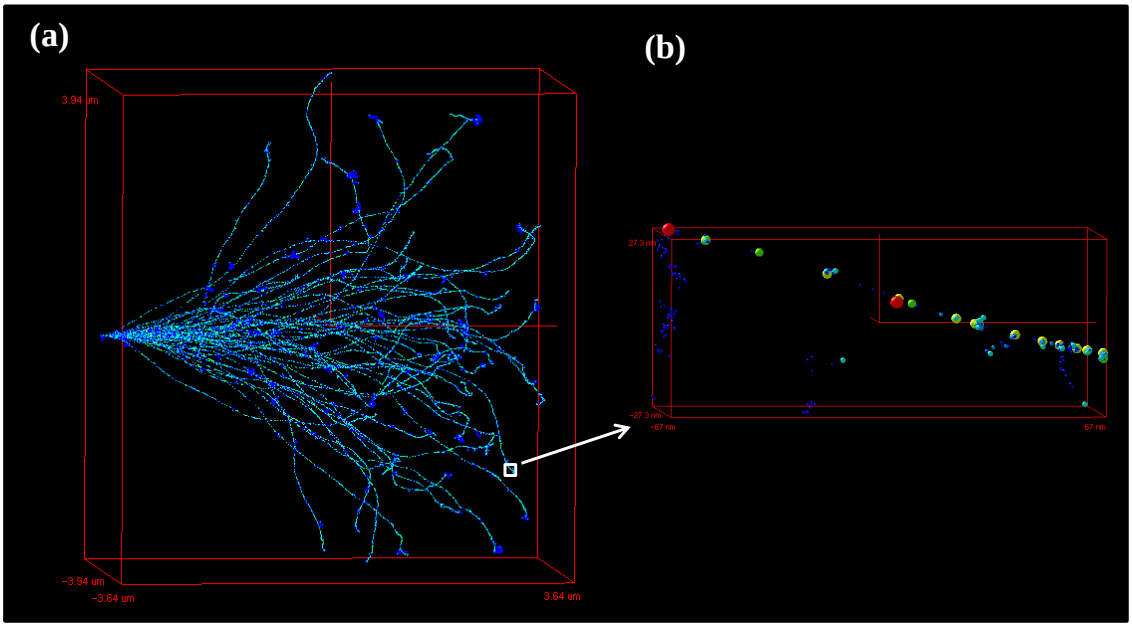

Figure 4.4: Single electron tracks simulation in water. (a) Fully simulated trajectories for 50 electrons with an initial energy of 15 keV. (b) Nano-volume detail obtained by zooming-up the end of a selected track. The colour of the balls indicates the type of interaction event: ●, elastic scattering; ●, rotational excitation; ●, vibrational excitation; ●, electronic excitation; ●, neutral dissociation; ●, ionisation; ●, electron attachment.

Table 4.1: Information about energy deposition and type of interactions derived from the simulation of 50 e^- tracks of 15 keV incident energy in H_2O, both for the total irradiated volume and a selected nano-volume. Percentages in brackets describe the frequency of the respective process relative to the total number of events.

	Whole irradiated area	Nano-volume (zoom)
Volume	472 μm^3	7903 nm^3
Total number of interactions:	1469316	3131
Elastic	1083812 (73.8%)	2152 (68.7%)
Rotational excitation	310899 (21.2%)	778 (24.8%)
Vibrational excitation	35177 (2.4%)	90 (2.8%)
Electronic excitation	2122 (0.14%)	7 (0.22%)
Neutral dissociation	11773 (0.80%)	36 (1.1%)
Ionization	25028 (1.70%)	67 (2.1%)
Auger e- generation	197 (0.013%)	-
Electron attachment	309 (0.021%)	1 (0.031%)
Energy imparted (in inelastic collisions)	738.3 keV	2481 eV

LEPTS code has been also employed to simulate single tracks for 50 positrons having incident energies of 15 keV (Figure 4.5a). A nano-volume detail obtained by zooming-up the end of a selected positron track is shown in Figure 4.5b. As in the case of electrons, each dot accounts for a collision event and its particular colour indicates the type of interaction taking place (see Fig 4.5 for details). It can be seen that positrons can also induce ionization of the H_2O molecules, resulting in SEs generation which can ultimately undergo attachment. Relevant information derived both for the whole irradiated volume and a selected nano-volume is summarized in Table 4.2.

When comparing the electron and positron tracks, we observe various differences. Firstly, the total number of interactions undergone by e^+ is significantly lower than the number for e^-. According to the results presented in Chapter 3, where it was discussed that the weaker interaction between the incident positron and the target molecule at low energies leads to smaller scattering CSs for positrons compared to electrons, this behaviour is to be expected. In addition, the elastic angular distributions shown in Chapter 3 indicate that positrons scatter principally in the forward direction, whereas for electrons scattering is more significant at larger angles. This is reflected in the shape of the positron tracks which experience less deflection from the primary path. Finally, the main difference can be found at the end of the tracks where low-energy positrons are able to form a positronium state and then annihilate.

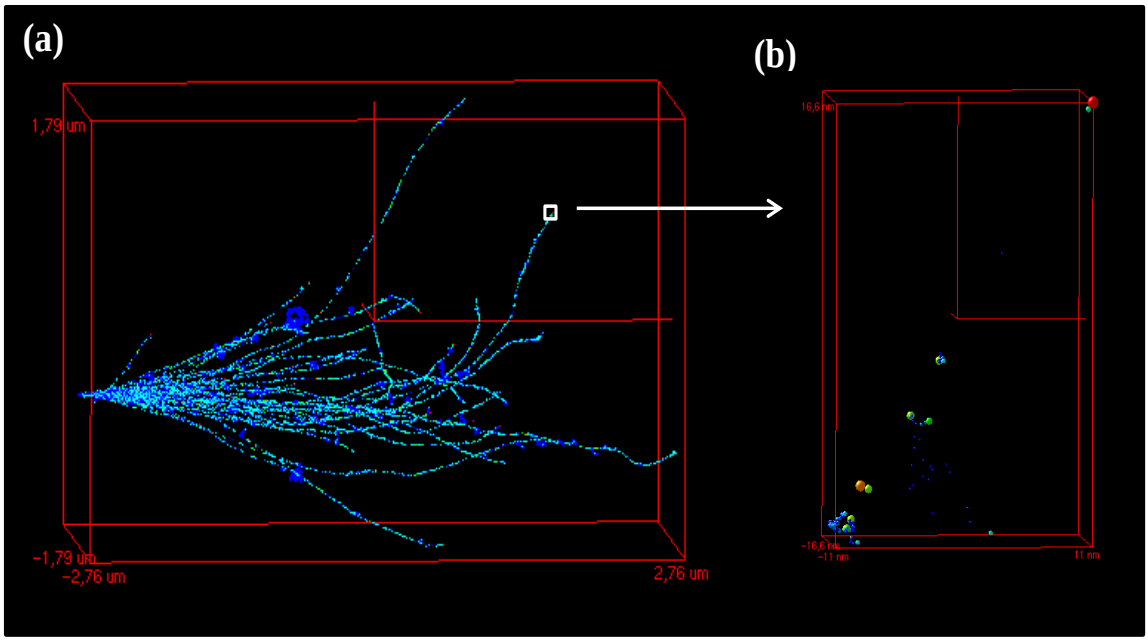

Figure 4.5: Single positron tracks simulation in water. (a) Fully simulated trajectories for 50 positrons with an initial energy of 15 keV. (b) Nano-volume detail obtained by zooming-up the end of a selected track. The colour of the balls indicates the type of interaction event: •, elastic scattering; •, rotational excitation; •, vibrational excitation; •, electronic excitation; •, neutral dissociation; •, ionisation; •, Auger electron generation; •, electron attachment (of secondary electrons); • Ps formation.

Table 4.2: Information about energy deposition and type of interactions derived from the simulation of 50 e^+ of 15 keV incident energy in H_2O, both for the total irradiated volume and a selected nano-volume. Percentages in brackets describe the frequency of the respective process relative to the total number of events.

	Whole irradiated area	**Nano-volume (zoom)**
Volume	76.4 μm^3	9716 nm^3
Total interactions:	466731	286
Elastic	343119 (73.5%)	215 (75.2%)
Rotational excitation	99981 (21.4%)	57 (19.9%)
Vibrational excitation	11174 (2.4%)	4 (1.4%)
Electronic excitation	1000 (0.21%)	1 (0.34%)
Neutral dissociation	3231 (0.69%)	2 (0.69%)
Ionization	8025 (1.72%)	5 (1.7%)
Auger e- generation	62 (0.013%)	-
Electron attachment	89 (0.019%)	1 (0.035%)
Positronium formation	50 (0.011%)	1 (0.035%)
Energy imparted (in inelastic collisions)	745.9 keV	6245 eV

4.4. Summary

In this chapter we have presented a radiation interaction model for low-energy charged particles, LEPTS, which provides molecular-level information about the energy imparted and the types of interactions that take place, including those experienced by secondary electrons. In this sense, LEPTS permits characterization of the induced damage in terms of molecular dissociations instead of absorbed dose and thus, it can be considered as a useful nano-dosimetric tool for applications which may require such a level of detail. Additionally, a main advantage of this procedure is its compatibility with other general purpose Monte Carlo simulation tools, such as GEANT4[4] or PENELOPE,[5] which are commonly used to model radiation effects for energies above 10 keV. Hence, through this combined procedure, we can cover a broad energy range from the high energy of the primary radiation, typically in the order of MeVs, down to their final thermalization including the tracks of all the secondary electrons generated.

Whilst this simulation procedure describes all of the interaction processes mediated by both the incident particles and the subsequently generated secondary electrons, it should be noted that it does not, however, consider the damaging effects induced by other secondary species, such as charged or neutral radicals, but merely accounts for their generation. The indirect damage produced by these species remains partially unknown (see Chapter 5), making difficult its inclusion in the radiation interaction models. Bearing this in mind, the simulation procedure presented above is sufficiently flexible to allow us to incorporate the results of new investigations as they become available.

Bibliography

[1] E. Alizadeh and L. Sanche, *Chem. Rev*. **112**, 5578 (2012).

[2] I. Kawrakow, *Med. Phys*. **27**, 485 (2000).

[3] S. Jan et al., *Phys. Med. Biol* .**49**, 4543 (2004).

[4] S. Agostinelli et al., *Nucl. Instrum. Meth. A* **506**, 250 (2003).

[5] J. Baró, J. Sempau, J.M. Fernández-Varea and F. Salvat, *Nucl. Instrum. Meth. B* **100**, 31 (1995).

[6] M.C. Fuss, A. Muñoz, J.C. Oller, F. Blanco, A.Williart, P. Limão-Vieira, M.J.G. Borge, O.Tengblad, C. Huerga, M. Téllez and G. García, *Appl. Rad. Isot.* **69**, 1198 (2011).

[7] (a) A. Muñoz, J.M. Pérez, G. García and F. Blanco, *Nucl. Instrum. Meth. A* **536**, 176 (2005); (b) A. Roldán, J.M. Pérez, F. Blanco, A. Williart and G. García, *J. Appl. Phys.* **95**, 5865 (2004).

[8] C. von Sonntag, *Free-Radical-Induced DNA Damage and its Repair, A Chemical Perspective* (Springer-Verlag, Berlin Heidelberg, 2006).

[9] R.D. White, W. Tattersall, G. Boyle, R.E. Robson, S. Dujko, Z.Lj. Petrovic, A.Bankovic, M.J. Brunger, J.P. Sullivan, S.J. Buckman and G.Garcia, *App. Rad. Isot*. **83**, 77 (2014).

[10] A. Muñoz, J.C. Oller, F. Blanco, J.D. Gorfinkiel, P. Limão-Vieira and G. García, *Phys. Rev. A* **76**, 052707 (2007).

[11] A. Muñoz, F. Blanco, G. García, P.A. Thorn, M.J. Brunger, J.P. Sullivan and S.J. Buckman, *Int. J. Mass Spectrom.* **277**, 175 (2008).

[12] Y. Itikawa and N.J. Mason, *J. Phys. Chem.* Ref. Data **34**, 1 (2005).

[13] A.G. Sanz, M.C. Fuss, A. Muñoz, F. Blanco, P. Limão-Vieira, M.J. Brunger, S.J. Buckman and G. García, *Int. J. Rad. Biol.* **88**, 71 (2012).

[14] F. Blanco, A. Muñoz, D. Almeida, F. Ferreira da Silva, P. Limão-Vieira, M. Fuss, A.G. Sanz and G. García, *Eur. Phys. Jour. D* **67**, 199 (2013).

[15] M.C. Fuss, A.G. Sanz, A. Muñoz, T.P.D. Do, K. Nixon, M.J. Brunger, M.-J. Hubin-Franskin, J.C. Oller , F. Blanco and G. García, *Chem.Phys. Lett.* **560**, 22 (2013).

[16] M.C. Fuss, A.G. Sanz, A. Muñoz, F. Blanco, M.J. Brunger, S.J. Buckman and G. García. *App. Rad. Isot.* **83B**, 159 (2014).

[17] M.C. Fuss, R. Colmenares, A.G. Sanz, A. Muñoz, J.C. Oller, F. Blanco, T.P.D. Do, M.J. Brunger, D. Almeida, P. Limão-Vieira and G. García, *J. Phys. Conf. Ser*. **373,** 012010 (2012).

[18] R. Curík, J.P. Ziesel, N.C. Jones, T.A. Field and D. Field, *Phys. Rev. Lett*. **97**, 123202 (2006).

[19] C. Szmytkowski, *Chem. Phys. Lett*. **136**, 363 (1987).

[20] M. Fuss, A. Muñoz, J. C. Oller, F. Blanco, D. Almeida, P. Limão-Vieira, T.P.D. Do, M.J. Brunger and G. García, *Phys. Rev. A* **80**, 052709 (2009).

[21] H.C. Straub, B.G. Lindsay, K.A. Smith and R.F. Stebbings, *J. Chem. Phys*. **108**, 109 (1998).

[22] P.A. Thorn, M.J. Brunger, P.J.O. Teubner, N. Diakomichalis, T. Maddern, M.A. Bolorizadeh, W.R. Newell, H. Kato, M. Hoshino, H. Tanaka, H. Cho and Y.-K. Kim, *J. Chem. Phys*. **126**, 064306 (2007).

[23] (a) J.P. Sullivan, S. J. Gilbert, J.P. Marler, R.G. Greaves, S.J. Buckman and C.M. Surko, *Phys. Rev. A* **66**, 042708 (2002); (b) J. P. Sullivan, A. Jones, P. Caradonna, C. Makochekanwa and S.J. Buckman, *Rev. Sci. Instrum.* **79**, 113105 (2008).

[24] G. Laricchia, S. Armitage, D.E. Leslie, M. Szhuinska and P. Van Reeth, *Rad. Phys. Chem.* **68**, 21 (2003).

[25] http://fismed.ciemat.es/GAMOS/

[26] A. Muñoz, J.C. Oller, F. Blanco, J.D. Gorfinkiel, P. Limão-Vieira, A. Maira-Vidal, M.J.G. Borge, O. Tengblad, C. Huerga, M. Téllez and G. García, *J. Phys. Conf. Ser*. **133**, 012002 (2008).

[27] M. Fuss, A. Muñoz, J. Oller, F. Blanco, M.-J. Hubin-Franskin, D. Almeida, P. Limão-Vieira and G. García, *Chem. Phys. Lett*. **486,** 110 (2010).

[28] R.P. McEachran, J.P. Sullivan, S.J. Buckman, M.J. Brunger, M.C. Fuss, A. Muñoz, F. Blanco, R.D. White, Z.Lj. Petrović, P. Limão-Vieira and G. García, *J. Phys. B* **45**, 045207 (2012).

[29] A.G. Sanz, M.C. Fuss, F. Blanco, F. Carelli, F. Sebastinelli, F. Gianturco and G. García, *App. Rad. Isot*. **83B**, 68 (2014).

[30] A.G. Sanz, M.C. Fuss, F. Blanco, J.D. Gorfinkiel, D. Almeida, F. Ferreira da Silva, P. Limão-Vieira, M. J. Brunger and G. García, *J. Chem. Phys*. **144**, 128 (2013).

[31] A.G. Sanz, M.C. Fuss, F. Blanco, F. Sebastinelli, F.A. Gianturco and G. García, *J. Chem. Phys*. **137**, 124103 (2012).

[32] A.G. Sanz, M.C. Fuss, F. Blanco, Z. Mašín, J.D. Gorfinkiel, F. Carelli, F. Sebastinelli, F. Gianturco and G. García, *App. Rad. Isot*. **83B**, 57 (2014).

[33] A.G. Sanz, M.C. Fuss, F. Blanco, Z. Mašín, J.D. Gorfinkiel, R.P. McEachran, M.J. Brunger and G. García, *Phys. Rev. A* **88**, 062704 (2013).

[34] M.C. Fuss, A. Muñoz, J.C. Oller, F. Blanco, P. Limão-Vieira, A. Williart, C. Huerga, M. Téllez and G. García, *Eur. Phys. Jour. D* **60**, 203 (2010).

[35] M.C. Fuss, A.G. Sanz, A. Muñoz, F. Blanco, M. Téllez, C. Huerga and G. García, *Biomedical Engineering, Trends in Electronics, Communications and Software* (InTech, Rijeka, Croatia, 2011).

Chapter 5

Experimental Methods and Results

It is well known that biological effects of radiation primarily result from damage to the DNA molecule.[1] Consequently, understanding the fundamental mechanisms involved in radiation-induced damage in DNA is essential for the development of more efficient radiation-based biomedical technologies. DNA (deoxyribonucleic acid) is a macromolecule which consists of two antiparallel polynucleotide strands, each composed of repeated deoxyribose-phosphate units and four different nucleobases: thymine, cytosine, adenine and guanine. Thymine and cytosine are pyrimidine derivatives, whereas adenine and guanine derived from the purine molecule. These bases are covalently linked to the deoxyribose moiety (sugar) via the glycosidic C1'-N1 bond. The sugar is in turn bound to the phosphate group through the C3' and C4' hydroxyl groups (phosphodiester bonds). The two strands of DNA are held together by hydrogen bonds formed between opposite bases. As mentioned in the introduction of this thesis (Chapter 1), in living cells, DNA molecule far from being isolated, is surrounded by other biomolecules, such as oxygen molecules, water, salts and proteins (see Figure 1.1). Consequently, all of these molecules are targets for the primary radiation, leading to two different destructive processes, usually referred to as direct and indirect damage. The former, results when radiation energy is directly deposited into any of the individual DNA components (i.e., nucleobases, the sugar or the phosphate group).[2,3] Indirect processes are initiated by the species created during the interaction of the primary radiation (or SEs) with the molecules surrounding DNA, which can subsequently react with the DNA components.[4,5]

In both the direct and indirect processes, ionizing radiation generates large quantities of secondary electrons[1] (see, for instance, Figure 4.4), which have low energies with a distribution that essentially lies below 30 eV and most probably have an energy of approximately 9-10 eV.[6] As seen in Chapter 3, for electrons with incident energies below 30 eV the magnitude of the cross sections increases significantly. Thus, low-energy electrons are expected to play an important role in radiation damage. At sufficiently low energies (below ~15 eV), LEEs can efficiently attach to DNA subunits leading to the formation of transient negative ions (TNIs). As such, LEEs induce direct damage on DNA because these metastable anions may dissociate into highly reactive radicals via DEA, or decay into dissociative electronically excited states. LEEs are more likely captured by the nucleobases rather than other DNA components, owing to their higher electronegativity. This may lead to DEA on these subunits, causing either dehydrogenation of the bases[7] or their release via *N*-glycosidic (C1'-N1) cleavage.[8] Alternatively, DEA may occur on the phosphate group via electron transfer from the base to that site; this would produce cleavage of C-O bond and thus result in a single-strand break (SSB).[9-12]

However, it is well known that the processes induced by electrons impacting against DNA are strongly affected and modified in the presence of vital cellular components, particularly H_2O and O_2, which are in contact with the DNA.[13,14] As cells are comprised of 70 - 80% water, a major proportion of the primary radiation energy is absorbed by this intracellular water. Additionally, numerous studies have reported considerable damage enhancement in DNA samples when they were irradiated under high concentrations of oxygen.[13] Despite the fact that the indirect effects are believed to contribute significantly to cellular DNA damage, their underlying mechanisms remain rather unknown, in particular those produced by LEEs.

Previous chapters have been devoted to the study of single-molecule interactions that fall into the category of direct damage. In this part of the work we take a step forward and present an experimental study on the damage induced by ionizing radiation and LEEs in various forms of DNA (namely, a representative DNA subunit and supercoiled DNA), under a hydrated and aerobic environment. Three different types of experiments were undertaken, each one conducted using specific experimental techniques and yielding particular output data. As a starting point, we report a comparison between the damage induced directly in the nucleoside thymidine (dThd) by high energy electrons (10 keV) and the LEEs emitted from a tantalum surface, under vacuum conditions. Yields of free thymine (i.e., base release caused by the rupture of the *N*-glycosidic bond) were analysed by high-performance liquid chromatography (HPLC). Subsequently, we investigated the simultaneous damage to DNA components induced by soft X-rays (1.5 keV) and low-energy electrons (0 - 30 eV) in thin films of thymidine, irradiated under dry nitrogen and oxygen at standard ambient temperature and pressure (SATP). The formation of four radiation-induced products is reported, namely, free thymine and the

nucleoside modifications 5-hydroxymethyl-2'-deoxyuridine (5-HMdUrd), 5-formyl-2'-deoxyuridine (5-FordUrd) and 5,6-dihydrothymidine (5,6-DHThd), as inferred by HPLC coupled with tandem mass spectrometry analysis (LC-MS/MS). These results constitute the first measurement of products induced by LEEs irradiation of a biomolecule (e.g., thymidine) at SATP, as well as a quantitative comparison of these products with those generated by soft X-rays under exactly the same conditions. Finally, we present in this work the first results of a study on the indirect effect of LEEs with liquid water condensed on and within plasmid DNA. In particular, we studied the effect of the DNA hydration level on the damage yields induced by soft X-rays and photo-emitted low-energy electrons; thin films of plasmid DNA were irradiated under SATP conditions and at different levels of relative humidity (RH) levels up to solvation, namely, 20, 50, 80 and 100%. Formation of single- and double- strand breaks (SSBs and DSBs, respectively) were analysed with agarose gel electrophoresis.[15]

In the following sections, after describing the experimental techniques employed, results derived from each experiment are presented and discussed.

5.1. Measurements under UHV Conditions: the Direct Effect

To gain a better understanding, at the molecular level, of the underlying LEE-induced DNA damage mechanisms, measurements with isolated DNA building blocks are highly valuable. In this work, as target molecule we used the DNA subunit thymidine ($C_{10}H_{14}N_2O_5$; dThd). This molecule is a nucleoside composed of a 2-deoxyribose group (dR) joined to the pyrimidinic nucleobase thymine through the C1'-N1 *N*-glycosidic bond (see Figure 5.1). To date, the only studies on electron collisions involving this nucleoside have been reported by Abdoul-Carime *et al*.[8] and Ptasińska *et al*.[16]; they showed that LEEs are capable to induce thymidine fragmentation via DEA involving low-lying π^* resonances. Bald *et al*.[17] performed similar experiments using laser-induced acoustic desorption (LIAD) technique for thermal evaporation of the samples. More recently, fragments generated from dehydrogenated thymidine have been analysed with matrix-assisted laser desorption and ionization (MALDI) technique.[18] Further vacuum measurements on the interaction of LEEs with dThd in the condensed-phase have been provided by Zheng *et al*.[19] and then by Li *et al*.[20] The major radiation-product was identified as thymine. The yield of the nucleobase was analysed by HPLC with UV detection and LC-MS/MS.

In these initial studies, dThd samples were bombarded with a monoenergetic low-energy electron beam produced by an electron gun. In this work we use the emission of SE from a metal surface exposed to ionizing radiation as the source of LEEs. This type of LEEs source possesses a broad energy distribution and the electron flux is significantly lower than that produced by an electron gun. Thus, the quantity of material recovered and fragments produced

by this type of LEE source could be expected to be lower than that generated with the apparatuses employed in previous studies. The main purpose of the present experiment is to check whether the distribution of SE emitted from a metal surface is capable of inducing sufficient dThd radiation-products to be detected by chromatographic techniques.

In the present experiment, both thin and thick films of dThd deposited on a tantalum surface were exposed to 10 keV electrons for various time periods and under an ultra-high vacuum (UHV). The yield of free thymine was determined by HPLC-UV analysis, by calibration with authentic reference compounds.[27] For a thick film, dThd damage was mainly induced by high-energy electrons. Contrastingly, in thin films of dThd, rupture of the glycosidic bond was induced primarily by the SEs emitted from the tantalum surface, since the 10 keV electrons traverse the films with negligible attenuation. Hence, this study allows the damaging effects induced in dThd by a distribution of SEs and those induced by high-energy electrons to be compared.

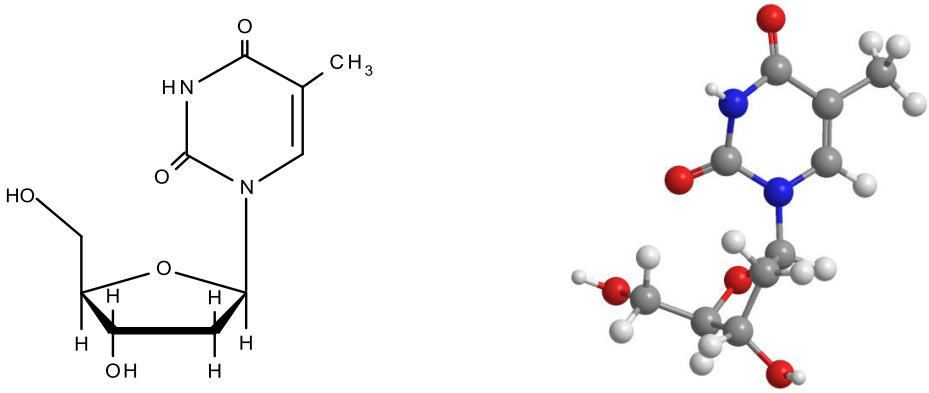

Figure 5.1: Equilibrium geometrical configuration of the present target molecule thymidine.

5.1.1. Experimental Methods and Materials

Thymidine Samples Preparation

Thymidine was purchased from Sigma–Aldrich Co., Ltd. at a stated purity of 99.5% and diluted with distilled and deionized water (ddH_2O) until a final concentration of 50 ng/mL was reached. The solution concentration was more accurately checked by measuring the optical density at 260 nm with a Synergy HT-I spectrophotometer, by assuming a molar optical density of 8.41 ODU/μmol at pH 7.0.[21]

dThd films of two different thicknesses have been prepared following the scheme developed previously for thin DNA films.[22] Under a dry atmosphere, either 600 ng of pure dThd in 12 μL of ddH_2O (i.e. low-concentrated solution) or 15.2 μg of pure dThd in 10 μL of ddH_2O (i.e. high-concentrated solution) were deposited on cleaned tantalum (Ta) substrates. Afterward, samples

were frozen at -70 °C and then lyophilized (or freeze-dried) by pumping with a hydrocarbon-free sorption pump under the pressure of 1–3 mTorr for ~two hours to form solid films. The dThd films were circular in shape with an average radius r=3.5 ± 0.1 mm. Using the known density ρ =1.45g/cm^3 for dThd,[23] and the masses m of dThd deposited on Ta prior lyophilization, their average thickness $t = m/\pi r^2 \rho$ were calculated to be ~11 nm and ~400 nm, for the thin and thick films, respectively.

The integrity of dThd samples have been checked after each step of the preparation procedure by HPLC. Liquid chromatography is a separation technique, where a small volume of liquid is injected into a column that contains porous particles (stationary phase). The individual components of the sample are moved through this column by means of a liquid, the so-called mobile phase, which is forced to traverse the column by high pressure pumps. Each of these components interacts slightly different with the column's stationary phase (depending on the polarity, mass, etc, of the product in question). Hence, the time each component employs to come out in the chromatogram, i.e., the retarding time, is characteristic of each compound. In the present experiment, the samples were separated with a HPLC Alliance HT instrument (Waters 2795) in reversed phase equipped with an octadecylsilyl silica gel (ODS-A) column (5-µm particle size, 250 length x 6.0 mm inner diameter; YMC). The products were eluted at a flow rate of 1.2 mL/min using a linear gradient of mobile phase from 0% to 10% acetonitrile, combined with 20 mM ammonium acetate buffer (pH=6.9) for 30 min. Once the components have been separated, they were collected at the exit of the column and identified with an external detection technique, in this case a dual wavelength UV absorbance detector (Waters 2487) at 210 and 260 nm. The analysis was controlled by a Millenium workstation (Waters version 4).

HPLC-UV analysis revealed negligible degradation of dThd fresh solution. Additionally, lyophilized dThd samples deposited on tantalum substrates showed minimal degradation, as can be seen in Figure 5.3 by comparison of the HPLC retention time and UV spectrum to authentic standards (in red).

Experimental Setup and Irradiation Conditions

Present measurements have been performed at the *Université de Sherbrooke Hospital Centre*. Details of the experimental setup have been reported earlier by Boudaiffa *et al.*[24], Panajotovic *et al.*[25] and Rezzaee *et al.*[26] Only a brief description of the apparatus is therefore given here. After preparation, the dry dThd samples were transferred to a UHV chamber and placed on a rotary multi-sample holder, which can transport each sample in front of the electron beam.[27] The chamber was evacuated for 24 h by a hydrocarbon-free turbomolecular pump to a

Figure 5.2: Photograph of the HPLC-UV system (Université de Sherbrooke Hospital Centre).

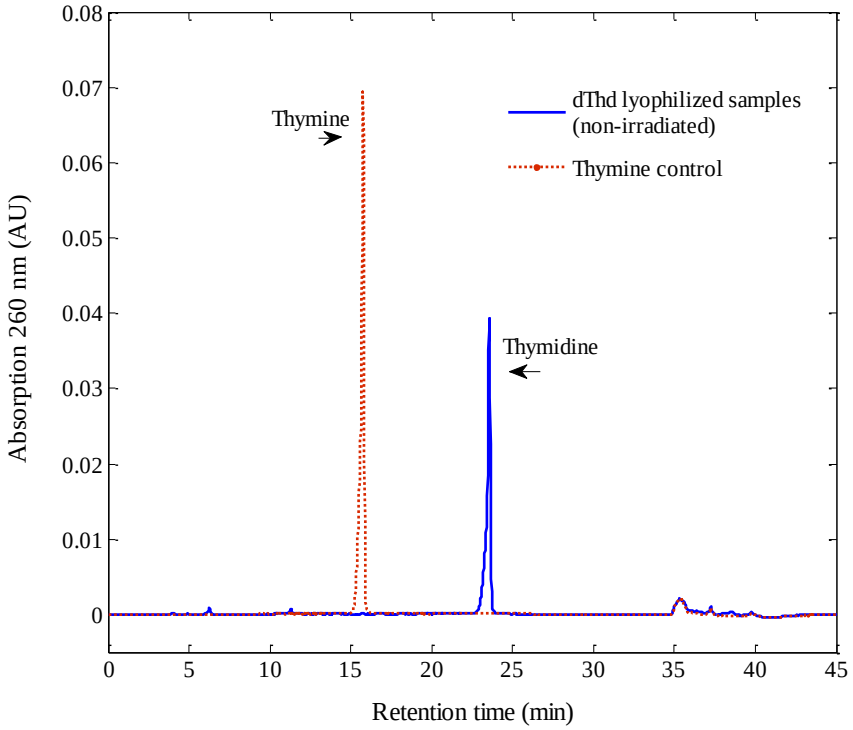

Figure 5.3: HPLC analysis of dThd samples lyophilized on a tantalum film. For comparison, an authentic thymine standard has been also analysed under the same HPLC conditions.

pressure of ~10^9 Torr. The electron irradiator consists of an electron gun producing a monoenergetic beam. The electron beam current and its diameter were measured with a phosphorescent screen placed also on the rotary multi-sample holder. After stabilization of the incident electron current at 8.0 ± 0.4 nA, giving a current density of 40×10^{10} electrons/s.cm^2, the films were individually irradiated with monoenergetic 10 keV electrons for periods between 5 and 30 minutes. Meanwhile, the other samples were protected from stray electrons by applying a repulsive potential of 9 V with respect to the cathode of the electron gun. Additionally, to assure that the damage produced in our samples was inflicted predominantly by the incident electrons, two control samples were introduced inside the chamber, which were kept under the same experimental conditions but were not irradiated. Note that even under UHV conditions, dThd samples still contains ~2.5 water molecules per nucleotide, which cannot be removed by lyophilization.

Samples Recovery and Quantification with HPLC-UV

After irradiation, samples were immediately removed from the chamber and recovered from the surface of each Ta substrate by dissolution with 30μl of phosphate buffer (0.4 M, pH 7.0) and 15μl of ddH_2O in three independent steps (15 μl/each). The recovery of thin lyophilized samples is one of most crucial steps of these experiments since, in some cases, it has been observed a fluctuation of more than 30% in their recovery.

We have checked the reliability of the recovery procedure by testing a group of 18 control samples, which contains 300 ng of thymidine-monophosphate (TMP), 250 ng of dThd and 250 ng of thymine (Thy), diluted in 60 μl of ddH_2O. These samples were deposited on tantalum substrates and freeze-dried. Immediately after lyophilization they were recovered following the procedure above mentioned, and subsequently they were analysed with HPLC-UV. From the analysis of the chromatograms it was inferred that, although the absolute amount of each compound is quite variable, their relative amount remain unaltered, to within 1.1%, compared to the fresh control solution. In other words, the recovery is equally effective for dThd and its radiation-products, such as free thymine, and we can rely on the ratio $dThd_{products}$/dThd to evaluate the damage induced by radiation.

5.1.2. Results and Discussion

Figure 5.4 shows the chromatograms of thick and thin films of dThd samples (panel (a) and (b), respectively) deposited on tantalum and irradiated during 30 minutes. Also is shown for comparison the chromatogram of dThd control samples, i.e., thymidine films that were

lyophilized and kept under the same experimental conditions as those of the irradiated samples but were not exposed to radiation. We identified two major peaks in the chromatograms, at the retention times t_{ret} ~ 15.5 min and t_{ret} ~ 24 min, which correspond to the nonmodified thymine base and the parent compound thymidine, respectively.

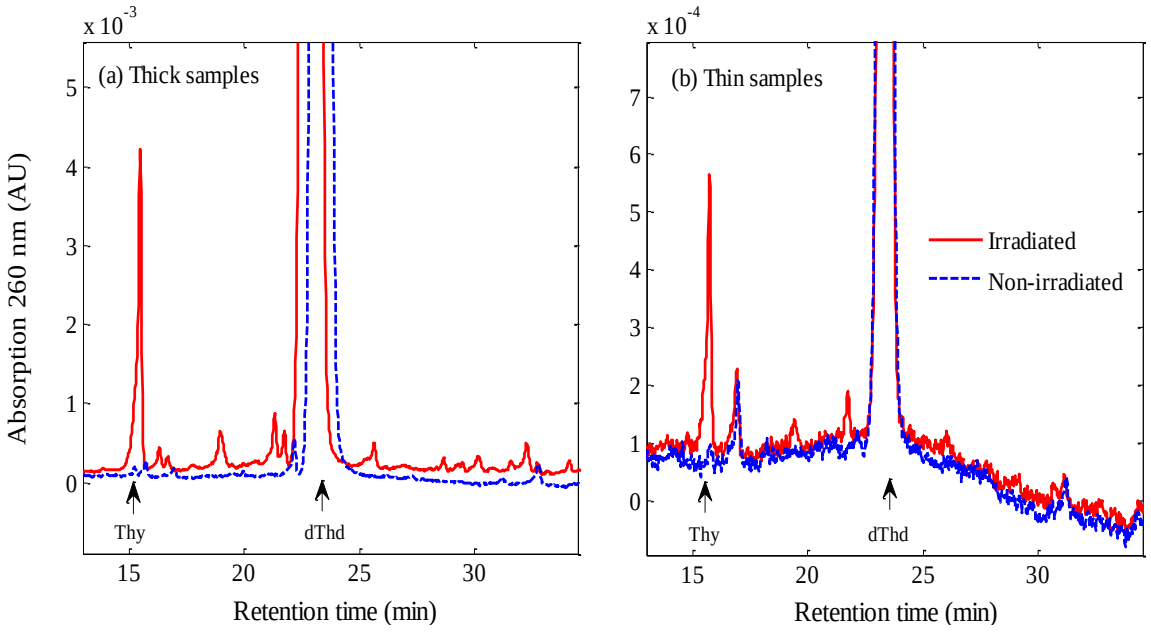

Figure 5.4: HPLC-UV analysis of (a) thick and (b) thin dThd samples irradiated during 30 minutes. For comparison, non-irradiated control dThd samples have been also analysed by HPLC-UV.

In addition, Figure 5.5 shows the variation in the proportions of unaltered dThd and free thymine as a function of the electron fluence (i.e., the exposure-response curves), both for thick and thin dThd films. Each point in the graphs corresponds to the mean value of the yields from three samples exposed to identical conditions. The error bars denote the standard deviation from these means. We assume that incident 10 keV electrons pass through the thin films suffering negligible attenuation and then interact with the tantalum substrates generating a large amount of SEs out of the surface. Although the energy spectra of the emitted electrons from the tantalum surface have not been still measured or simulated, SEs are expected to exhibit an average energy below ~10 eV.[28] This means that damage detected on thin dThd films can be attributed chiefly to SEs emitted from the metal films. In contrast, when the 10 keV electrons traverse the thick films (~ 400 nm), they are expected to deposit most part of their energy within the samples through numerous inelastic collisions (the estimated range of 10 keV electrons in biological material is ~200 nm).[29] This indicates that damage observed in a thick film of dThd results mainly from high-energy electrons rather than SEs.

Both for thin and thick films, the yield of base release vary linearly with the electron fluence. The percentage yields were derived from the initial slopes of the linear-least-squares fit of respective exposure curves and are reported in Table 5.1. This Table also provides the enhancement factor (EF) due to SEs interactions, which has been obtained by dividing the yield associated with the thin dThd samples by that measured with the thick samples, i.e., $EF = Y_{Thin}/Y_{Thick}$. Present results indicate that SEs emitted from the metal substrate under UHV conditions enhance the dThd damage by a factor of 3.3, relative to high-energy electrons.

Table 5.1: Percentage yields per 10^{16} electrons/cm^2 for the formation of base release (thymine loss from thymidine) for thick and thin samples of thymidine.

	Y_{Thick}	Y_{Thin}	$EF = Y_{Thin}/Y_{Thick}$
Formation of Thymine	1.8 ± 0.4	6.1 ± 0.6	3.3 ± 0.4

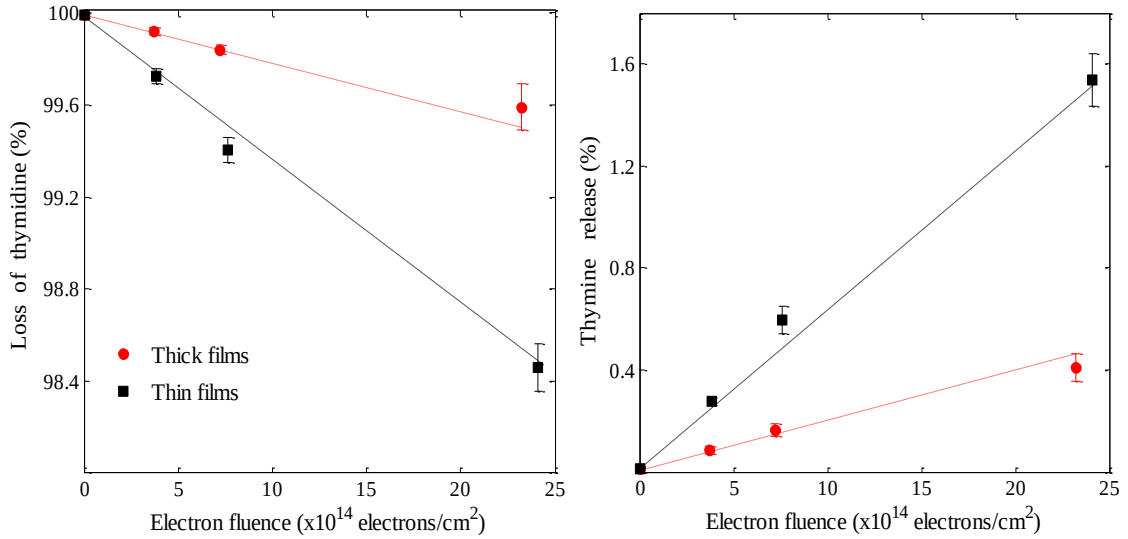

Figure 5.5: Exposure-response curves for (a) loss of thymidine and (b) appearance of free thymine (base release), in thin and thick films of dThd deposited in tantalum substrates and irradiated with 10 keV electrons under UHV.

Since the measurements were performed under UHV, induced damage observed in the samples can be attributed to direct effects. Reaction mechanisms of direct damage induced by fast electrons and LEEs to thymidine are now well established,[16, 20] and thus I only discussed them briefly here. According to the single-track simulation shown in Chapter 4, when high-energy electrons traverse biological media they undergo successive energy losses via, for example electronic excitation and ionization.[6] Under dry conditions, the principal mechanism of formation of base release is via one-electron ionization, likely involving a radical cation on the sugar moiety.[30] On the other hand, low-energy electrons ejected from the metal surface low-energy electrons can fragment the glycosidic N1-C1 bond through resonant processes. LEEs can

become trapped in the molecule into low-lying π* orbitals associated with the aromatic ring of the thymine base and form a TNI,[31] which can subsequently dissociate into a highly reactive neutral radical and an anion via DEA. Experimental evidence for the decomposition of dThd by low-energy electrons was firstly reported by Abdoul-Carime *et al.*[8] and then by Ptasińska *et al.*[16]. They showed that LEEs can break the glycosidic N1-C1 bond either at subexcitation energies, through transfer of the captured electron to sugar moiety (reaction 5.1), or at energies above 5 eV (reaction 5.2). In the latter case, the electron more likely remains on the nucleobase:

$$dThd + e^- \rightarrow dThd^{-*} \rightarrow (Thy - H)^{\bullet} + (dR\text{-}OH)^- ; \qquad (E \sim 1.2\ eV) \qquad (5.1)$$

$$dThd + e^- \rightarrow dThd^{-*} \rightarrow (Thy - H)^- + (dR\text{-}OH)^{\bullet} ; \qquad (E > 5.5\ eV). \qquad (5.2)$$

According to Ptasińska *et al.*[16], the latter DEA reaction (5.2) might be associated with a broad resonant feature located between 5.5 and 12 eV presumably of core-excited character.

In summary, present results suggests that low-energy secondary electrons can induce more efficiently the fragmentation of the glycosidic N1-C1 bond (via dissociative electron attachment[14]) than high-energy electrons. In addition, these measurements provide evidence that a distribution of SEs emitted from a metal surface upon ionizing radiation generates enough thymidine-products for chemical analysis.

5.2. The effect of Oxygen on Radiation-Induced Damage

It is well known that the damage mechanisms governed by both ionizing radiation and LEEs are strongly affected by the presence of O_2.[13] Numerous studies have reported considerable enhancement of the damage induced in DNA samples when they were irradiated under high concentrations of oxygen (see Alizadeh *et al.*[13] and references therein). For instance, cultured mammalian cells irradiated with X-rays showed a damage enhancement ratio of approximately 3 in the in presence of oxygen.[32] It has also been demonstrated that exposure to an oxygenated atmosphere doubled the damage induced in plasmid DNA by both X-rays and LEEs.[13] This radiosensitizing effect is normally attributed to the addition of oxygen to carbon-centred radicals in competition with the chemical repair of radicals by reaction with cellular thiols, a phenomenon known as the oxygen fixation hypothesis (OFH).[33] This hypothesis assumes that O_2 molecules attach to short-lived target radicals thereby irreversibly fixing the damage via the formation of peroxy radical (DNA-OO$^{\bullet}$).[34]

On the other hand, there is very little information available about the radiosensitization mechanism of O_2 in DNA components upon interaction with LEEs. Moreover, there is currently no information about the products induced by LEE irradiation for any small biomolecules at

standard ambient temperature and pressure (SATP). This situation has prompted the present study: we have measured the damage yields induced by soft 1.5 keV X-rays and photo-emitted LEEs in thin films of dThd irradiated under pure dry N_2 or O_2 at SATP. These environmental conditions required specific experimental techniques; the apparatus and technique developed by Brun *et al*.[14] and Alizadeh *et al*.[13] to investigate LEE-induced damage in plasmid DNA under well-controlled environmental conditions have been adapted to carry out analogous experiments with small DNA components. In order to differentiate between the damage induced by X-rays and that of LEEs, dThd samples were deposited on glass and tantalum substrates: whereas damage yields for the samples deposited on glass are caused by the soft X-rays, those arising from dThd films on tantalum are due to both the interaction of X-rays and LEEs emitted from the metal. This procedure affords the direct comparison of the yield of products induced by X-ray photons and those induced by LEEs under identical experimental conditions. Damage to dThd films was measured by LC-MS/MS in terms of base release and some base modifications, namely 5-HMdUrd, 5-FordUrd and 5,6-DHThd.Given that the chamber containing the samples was flushed with either nitrogen or oxygen, it was possible to examine the modifications introduced by an oxygenated environment on the LEE-induced damage.

5.2.1. Experimental Methods and Materials

The experimental procedure we followed in the present study is represented schematically in Figure 5.6. Briefly, small aliquots of pure thymidine solution were deposited on either glass or tantalum substrates with a pipette (step 1). These samples were then lyophilized (step 2) and placed in an irradiation chamber for X-ray exposure (step 3). Each sample-holder contained three samples deposited on glass and three more on tantalum. After irradiation, samples were immediately recovered (step 4) and analysed by LC-MS/MS to quantify the different dThd radiation products (step 5).

The technical procedure followed to prepare the samples (step 1 and 2) is identical to that described in the previous section. Specific details of the experimental apparatus, irradiation conditions, post-irradiation sample recovery and analysis are given below.

Thymidine Sample Preparation

In this case, only thin dThd films were prepared (see section 5.1.1). To obtain a fairly uniform thickness of approximately 10 nm, 12-μL drops of solution containing 600 ng of pure thymidine were deposited on cleaned glass and tantalum substrates and then lyophilized. Similarly to the previous experiment, purity of dThd samples was checked with HPLC after preparation of the fresh solution (50 ng/mL) and freeze-dried process, showing no detectable decomposition of the target molecule.

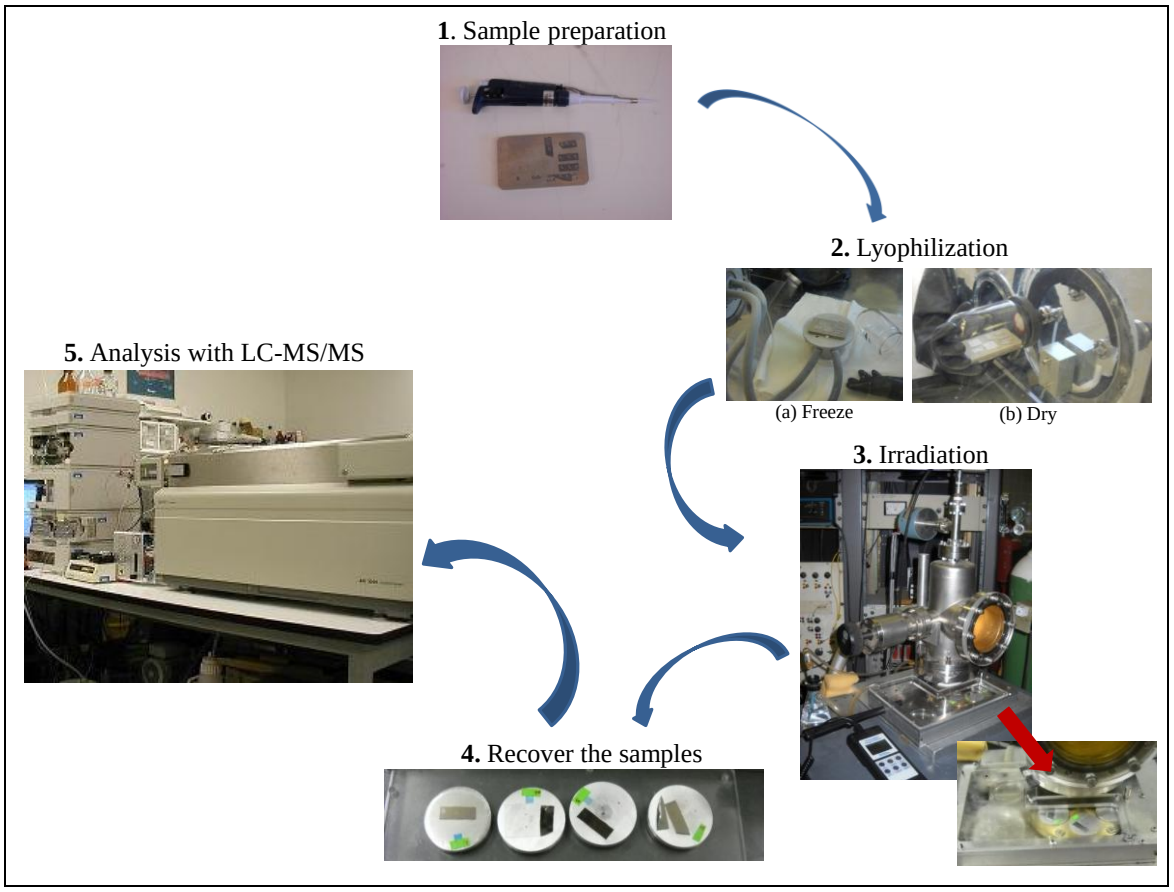

Figure 5.6: Schematic view of the main steps followed in the present experiment (see text for further details).

Experimental Setup and Irradiation Conditions

The experimental apparatus employed for the present study, placed at the *Université de Sherbrooke Hospital Centre*, was firstly developed by Cai *et al.*[28] and then improved by Brun *et al.*[14] and Alizadeh *et al.*[13,35] Here only a brief description of the present configuration is therefore given. The apparatus, shown schematically in Figure 5.7, consists on a stainless steel chamber which is connected to a Baratron gauge (A) and an adjustable leak valve (B) linked in turn to a nitrogen gas tank. The chamber is evacuated down to around 5 mTorr by means of a mechanical pump. A negative potential of 3.4 kV is applied to a concave aluminium cathode (C) through a high-voltage electrical feedthrough (D). The former is fixed in a glass-ceramic (Macor®) support (E) which is placed as a cap on a long quartz tube (F).[14] The Al K_α X-ray source was constructed based on the original designed of Hoshi *et al.*[36] A nitrogen plasma discharge with 5.5-6.0 mA current is established between the cold-cathode and an aluminium foil target (G), generating characteristic K_α X-rays of 1.5 keV energy. A portion of these X-rays, after traversing a flight tube continuously flushed with helium gas (H) and then a thin foil of mylar (I), enters into a small chamber filled with dry N_2 or O_2 at atmospheric pressure introduced by two circulation valves (L). The small chamber was devoid of humidity, as

monitored by a hygrometer. The dThd samples are placed in this chamber, specifically, on six aluminium plates (K) that are fixed at different equidistant positions around a brass rotating disk (L). The latter is monitored from the outside with a magnet. Thus, films can be placed successively in front of the source to be exposed to X-rays of varying fluence.

In order to differentiate damage induced to dThd molecules by either X-rays or LEEs, we employed two different substrates, namely, glass and tantalum.[37,38] The former is a borosilicate glass (Fisher Scientific) of 1 mm thickness; the latter is a film of 450 ± 50 nm thickness evaporated on a 0.4 mm thickness silicon wafer. In a typical run, 15 samples were deposited on tantalum, and 15 were on the glass substrate. To remove trace amounts of dThd degradation induced by environmental factors other than radiation, we included three control samples for each substrate; they were lyophilized and kept under the same environmental conditions as those of the irradiated samples, but were not exposed to X-rays. The remaining samples were exposed in groups of three to X-rays for exposures of 2, 4, 7 and 9 hours.

In order to measure the number of photons incident on individual samples, small pieces of GAFCHROMIC HD-810 radiochromatic dosimetry films (Advanced Materials Group of International Specialty Products Technologies Inc., Wayne, NJ) were placed on each plate close to the samples. Cai *et al*.[39] showed that these radiochromatic films constitute a simple dosimeter for soft X-rays. Before exposure, the GAFCHROMIC films are transparent and turn progressively blue upon X-radiation, increasing the blue intensity with the absorbed dose. After irradiation, the films were immediately retrieved and stored in the dark for 48 h at room temperature. Then, they were scanned with a HP ScanJet 4400C colour scanner. Blue and red channels images were analysed with ImageJ software.[40] The mean values resulting from the ImageJ colour analysis histograms for non-irradiated (I_o) and irradiated (I) areas of the films, permit to obtain the absorbance defined as $\log_{10}(I_o/I)$. The sensitivity of the GAFCHROMIC films had been previously calibrated by Alizadeh *et al*.[13], who estimated a conversion factor of 0.0393 min^{-1}. This factor has been used to convert the irradiation time to photon fluence (photons/cm^2) in the present experiments.

One should note that before interacting with the dThd films, the emitted X-rays are attenuated by three different environments: the helium-filled volume (x=50 mm), the mylar foil (x=2.5 μm) and, within the target-chamber, either oxygen or nitrogen gas surrounding the samples (x=1.25 mm). Using the mass attenuation coefficient and the density of these media,[41] and applying the exponential attenuation law $I_t=I_o e(^{-\mu/\rho.\rho x})$, it was found that the initial intensity of photons was reduced in 0.7% and 28.1% after traversing the helium and mylar areas, respectively. Subsequently, 14.7% and 22.9 % of soft X-rays were absorbed by the N_2 and O_2

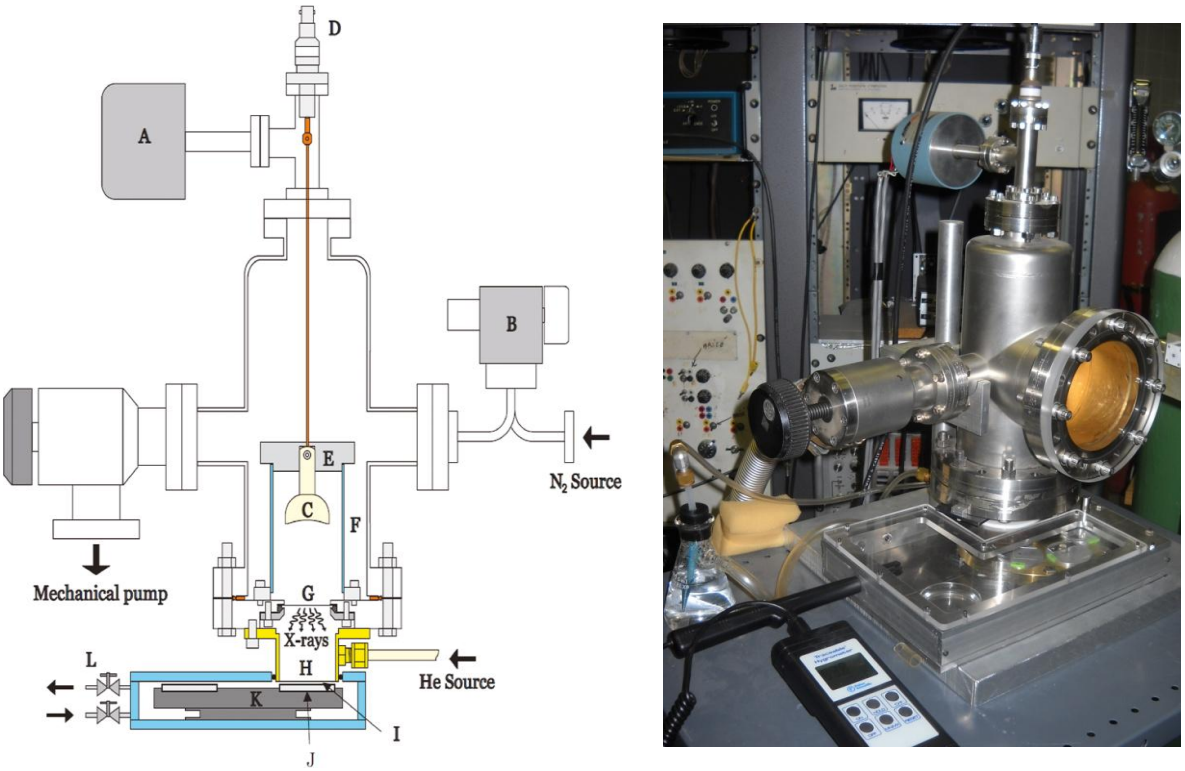

Figure 5.7: Schematic view of the experimental apparatus: (A) baratron, (B) adjustable leak valve, (C) concave aluminium cathode, (D) high voltage electric feedthrough, (E) glass-ceramic (Macor) support, (F) quartz tube, (G) aluminium, (H) He-filled volume, (I) thin foil of mylar, (J) sample holder, (K) rotating disk, and (L) gas circulation valves. (Image on the left panel taken from Alizadeh *et al.*[13]).

molecules, respectively.[13] Regarding X-rays absorption by the dThd film, given that for 1.5 keV X-rays thymidine has a mass attenuation coefficient[41] of μ/ρ=983 cm^2/g and a density[23] of ρ=1.45 g/cm^3, we calculated that 0.16% of the X-rays are absorbed within the 10 nm-thymidine films.

The remaining X-rays photons pass through the samples to reach the metal or glass interface. The interaction of the incident X-rays with the tantalum atoms generates energetic SEs within the metal via mainly the photoelectric effect. On traversing the tantalum film, these electrons suffer numerous inelastic collisions and lose progressively their energy. Hence, only a small portion of the secondary electrons reach the surface consisting essentially of LEEs. The energy distribution of SEs generated at the tantalum surface peaks at 1.4 eV with an average energy of 5.85 eV.[13] The area under the curve reveals that 95% of the photo-electrons emitted from the metal surface have energies lower than 30 eV. The electron flux and the yield of electron emission per incident photon were determined to be $(0.54 \pm 0.2)\times10^9$ electrons/$s.cm^2$ and 0.047 ± 0.005 electrons, respectively, from a previous study.[13] On the other hand, SEs ejected from the surface of the insulator substrate are assumed to be negligible compared to SEs emitted from the metallic surface.

Samples Recovery and Radiation-products Quantification by LC-MS/MS

After X-rays exposure, both irradiated and non-irradiated samples were immediately removed from the chamber and recovered from the tantalum and glass films following the procedure explained in section 6.1.1. Efficiency of the recovery on samples deposited on glass has been also checked. In this case, a group of 8 control samples (same composition as in section 6.1.1) deposited on a glass surface were lyophilized and subsequently recovered. HPLC-UV analysis showed also strong variability in the absolute amount of each compound, but their relative concentrations remain constant, to within 0.75%.

The recovered samples were then stored at -25°C before analysis by LC-MS/MS. It has been shown that LC-MS/MS is a highly sensitive and specific technique that combines liquid chromatography separation with electrospray ionization tandem mass spectrometry detection, allowing direct characterization and measurement of modified nucleosides.[42] Samples were first subjected to liquid chromatography separation by means of a conventional HPLC apparatus (Shimadzu LC- 10ADvp pumps) equipped with an auto-sampler, a degasser, column oven (CTO-10ASvp) and UV/Vis detector (SPD-10Avp) working at 220 and 260 nm. The separation was performed in reversed phase using a ODS-A column (5-μm particle size, 150 length × 2.0 mm inner diameter; YMC). Note that coupling of HPLC to mass spectroscopy requires the use of small columns. The products were eluted at low flow rate (0.25 mL/min) using a linear gradient starting with ammonium formate buffer (5 mM, pH 5) containing acetonitrile (ratio of buffer to acetonitrile = 95:5) and going to a higher percentage of acetonitrile (ratio = 80:20) in 10 minutes, followed by a wash cycle (5 min in 70% acetonitrile and additional 3 minutes to reequilibrate the column). The liquid chromatograph is coupled to an API 3000 tandem mass spectrometer system (MS/MS) through a turbo-ionspray source (MDS Sciex, Applied Biosystems). The products were detected in positive ionization with a triple-quadrupole system using the multiple reaction monitoring (MRM) mode.

Although LC-MS/MS is recognized as a suitable technique with an outstanding capability to analyse a broad variety of products, accuracy is reduced due to ion suppression. This can lead to the underestimation of the real concentration of the products, which can vary from one sample to another, affecting therefore the repeatability of a measurement for a certain radiation fluence. In order to minimize the error introduced by the LC-MS/MS analysis, it is customary to add internal standards to the samples. These compounds have the same chemical properties, and thus, they are added to the analysis to correct for losses of products during sample preparation and changes in chromatography and electrospray ionization for LC-MS/MS analyses. In the present study, isotopic labelled internal standards for thymidine, thymine, 5-FordUrd and 5-HMdUrd within +2 to +4 amu were added to samples after irradiation.[43] Key parameters for

LC-MS/MS measurement, i.e., retention times and fragmentation transitions are specified in Table 6.2. The amount of product was determined by comparison of the ion signals for the natural and isotopic compounds during the same chromatographic run. In other words, the concentration of unaltered thymidine and each dThd radiation-product has been calculated from the area of the absorbance peak ($A_{product}$) normalized by the absorbance peak area of the corresponding labelled internal standard (A_{std}), since the concentration of the latter is known:

$$C_{product} = \frac{A_{product}}{A_{std}} \times C_{std} \ . \tag{5.3}$$

Unfortunately, an isotopic labelled internal standard for 5,6-DHThd is not presently available. The calibration of this compound was carried out by external injection of a known amount of 5,6-DHThd in separate chromatographic runs before and after the injection of the sample. Thus, yields of 5,6-DHThd are affected by a higher uncertainty than the other radiation-products.

The concentration of thymine, 5-FordUrd, 5-HMdUrd and 5,6-DHThd relative to the concentration of unaltered dThd provides the percentage yields of damage induced by soft X-rays and photo-emitted LEEs as a function of dose. Note that the limit of detection for various pyrimidine derivatives ranges from 5 fmol to 1 pmol, depending on the structure.[43]

Table 5.2: LC-MS/MS retention times and fragmentation transitions for the different radiation-products observed in dThd samples irradiated with 1.5 keV photons.

	Retention time (min)	Transition (Da)	Internal standards	
			Transition (Da)	Concentration (μM)
5,6 DHThd	7.5	245.1/117.1		0.01
5-FordUrd	8.0	257.0/141.0	259.0/143.0	0.01
5-HMdUrd	7.0	259.1/125.0	261.1/127.0	0.01
Thymine	6.5	127.0/110.1	131.2/114.0	10
Thymidine	8.5	243.3/117.1	245.3/117.1	50

Calculation of *G* values

In order to quantify the damage induced by either X-rays or LEEs, the damage yields can be expressed in terms of *G* values, which refer to the number of moles of substance produced per joule of radiation energy absorbed (nmol/J) or number of damaged molecules per absorbed 100 eV (i.e., D/100 eV being 1D/100 eV = 103 nmol/J).[44] This quantity depends not only on the energy of the radiation but also on the type of radiation and the target. A detailed description of the procedure to derive *G*-values for thin films has been reported by Brun *et al*.[13] and Alizadeh

et al.[45] Briefly, G-values are calculated from the following expressions for X-rays and LEEs respectively:

$$G_X = \frac{D_{Gl}}{X_{abs} \times 1486\ eV}\ x\ 100\ eV \tag{5.4}$$

$$G_{LEE} = \frac{(D_{Ta} - D_{Gl})}{\eta_e X_{Trans} \times 5.85\ eV}\ x\ 100\ eV \tag{5.5}$$

where η_e = 0.047 ± 0.005 is the number of secondary electrons induced by each incident photon, D_{Gl} and D_{Ta} refers to the the number of damaged dThd induced in a film deposited either on a glass or tantalum substrate for a given photon fluence (Φ=10^{12} photons/cm^2), and are given by,

$$D_{Gl} = |Y_{Gl}|.\Phi.N_{dThd} \tag{5.6}$$

$$D_{Ta} = |Y_{Ta}|.\Phi.N_{dThd} \tag{5.7}$$

where $|Y_{Gl}|$ and $|Y_{Ta}|$ are the initial slopes of the linear-least-squares fit of the respective exposure curves which represent the percentage yields of damage per incident photon/cm^2 for samples deposited on glass and tantalum, respectively. N_{dThd} is the number of thymidine molecules in each sample, calculated via:

$$N_{dThd} = \frac{m\ (g).N_A(mol^{-1})}{M_W(g.mol^{-1})} = 14.91\ \times 10^{14} \tag{5.8}$$

where N_A is the Avogadro's Number, m = *600 ng* is the mass of thymidine in each film and M_W= 242.23 g/mol is the molecular weight of thymidine. Subsequently, the number of absorbed photons (X_{Abs}) in the thymidine film and the number of photons passing through the film to produce photoelectrons at the tantalum substrate (X_{Trans}) are given by:

$$X_{Abs} = \phi.S\left(1 - e^{-\frac{\mu}{\rho}\rho\frac{t}{cos\theta}}\right), \tag{5.9}$$

$$X_{Trans} = \phi.S\left(e^{-\frac{\mu}{\rho}\rho\frac{t}{cos\theta}}\right), \tag{5.10}$$

being μ/ρ = 983 cm^2/g the mass attenuation coefficient for 1.5 keV X-rays.[41] The other parameters needed are S = 0.385 cm^2, t = 10 *nm* and ρ = 1.45 g/cm^3, which are the area, the thickness the density of the thin films, respectively.

G_X and G_{LEE} are calculated within 20% and 25% errors, respectively, which mostly arise from the uncertainty on the area of the DNA film and its thickness, photon fluence, as well as the concentration of sample and η_e. It is worthy to note that the surface of the films are not strictly uniform so that some spots may exist where the local thickness is smaller than ~10 nm

and therefore LEEs are not completely thermalized. However, we have assumed that all the energy of the photo-emitted electrons is absorbed in the films. Hence, the calculated *G*-values presented here are underestimated and represent a lower limit for the real value.

5.2.2. Results and Discussion

The present experimental results permit to evaluate damage induced to thymidine molecules by either soft X-rays or LEEs, and quantify the formation of four molecular lesions: base release (thymine loss from thymidine), the oxidatively generated nucleobase modifications 5-HMdUrd and 5-FordUrd, and the reductively generated nucleobase modification 5,6-DHThd. As an example, we report in Figure 5.8 the LC-MS/MS chromatogram recorded for dThd samples deposited on Ta and irradiated under N_2 (panel a) and O_2 (panel b) atmospheres. For comparison, we also show the chromatogram recorded for the corresponding non-irradiated control samples. Each peak in the chromatogram is associated with a radiation-product: (a) free thymine (base release), (b) 5-HMdUrd, (c) 5,6 DHThd, (d) 5-FordUrd and (e) thymidine (see retention times in Table 5.2).

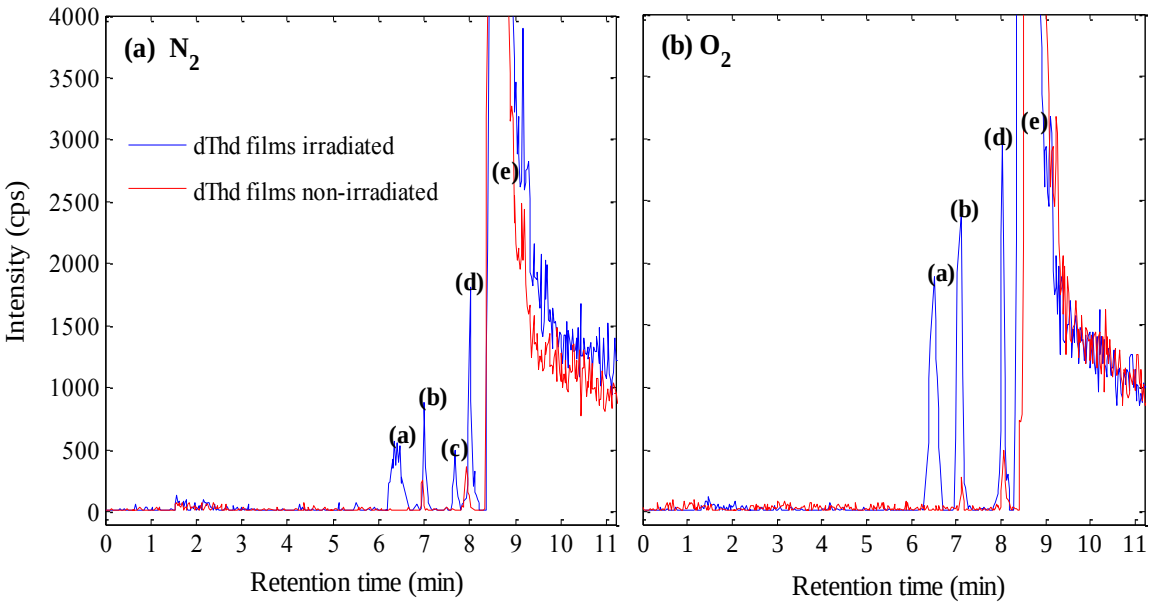

Figure 5.8: LC-MS/MS chromatogram of dThd samples deposited on tantalum. Non-irradiated control samples are compared with samples exposed to X-rays the longest, under an N_2 (panel a) and O_2 (panel b) atmosphere. Each peak in the chromatogram stands for a radiation-product: (a) free thymine (base release), (b) 5-(c) HMdUrd, (c) 5,6 DHThd, (d) 5-FordUrd and (e) thymidine.

Figure 5.9 shows the loss of dThd with increasing photon fluence (exposure-response curve) for samples deposited on tantalum and glass substrates, under N_2 (panel a) and O_2 (panel b) atmospheres. Similarly, formation of the different nucleoside radiation-products, relative to undamaged dThd, as function of the X-ray exposure for films deposited on glass and Ta is shown in Figure 5.10, also under a N_2 (panel a) and O_2 (panel b) environment. Each point in the graphs corresponds to the mean value of the yields from three samples exposed to identical conditions. The error bars denote the standard deviation from these means, i.e., the statistical error. As expected, we observe in the figures that the amount of intact dThd decreases and that of the radiation-products increases with the photon fluence, over the entire fluence range under study. A detailed analysis of the figures reveals higher yields of damage when the samples are deposited on the tantalum surface, independently of the surrounding atmosphere, in accordance with previous studies.[13] This indicates an enhancement of the nucleoside damage due to the LEEs emitted from the metal surface: damage yields observed in dThd samples deposited on glass substrate are induced by the absorbed X-rays, whereas for samples deposited on tantalum both X-rays and LEEs are responsible of are responsible of the induced damage. The difference in the yields between both substrates can be therefore attributed to the interaction of LEEs with dThd molecules. The dose-response curves also show larger loss of dThd under an oxygenated atmosphere, independently of the substrate the samples are deposited on. This leads to larger yields *of* free thymine, 5-FordUrd and 5-HMdUrd, however no 5,6-DHThd was detected in irradiated samples surrounded by O_2 (this effect is also clearly appreciated in the LC-MS/MS chromatogram reported in Figure 5.8).

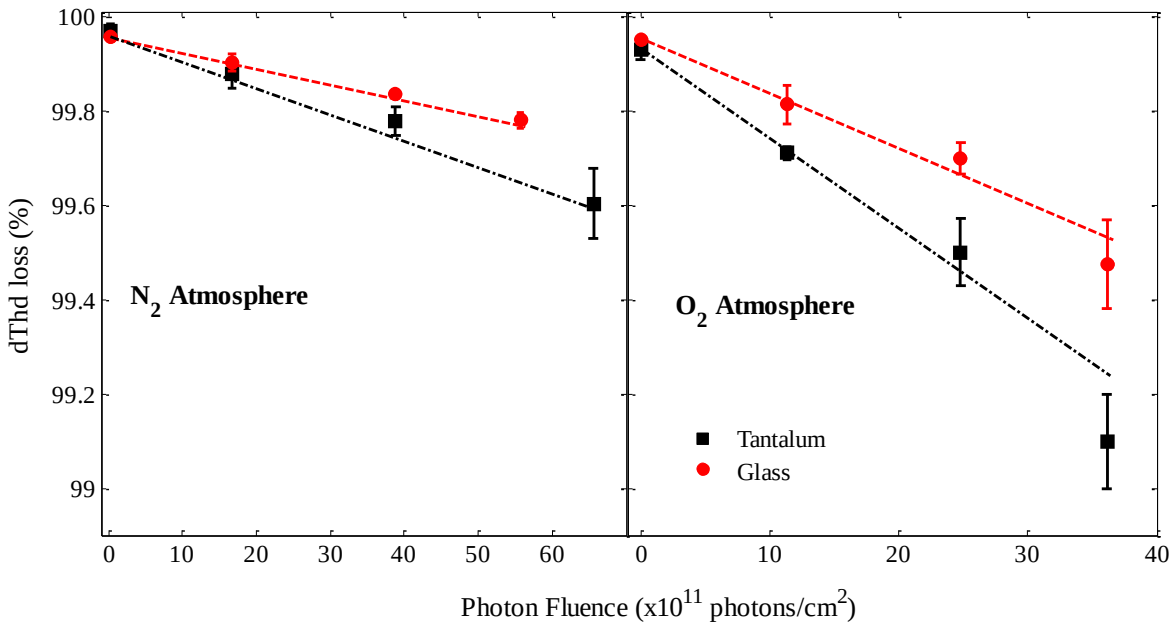

Figure 5.9: Exposure-response curves for the loss of unaltered thymidine in thin films deposited on tantalum and glass substrates and irradiated with 1.5 keV X-rays under (a) N_2 and (b) O_2 at SATP.

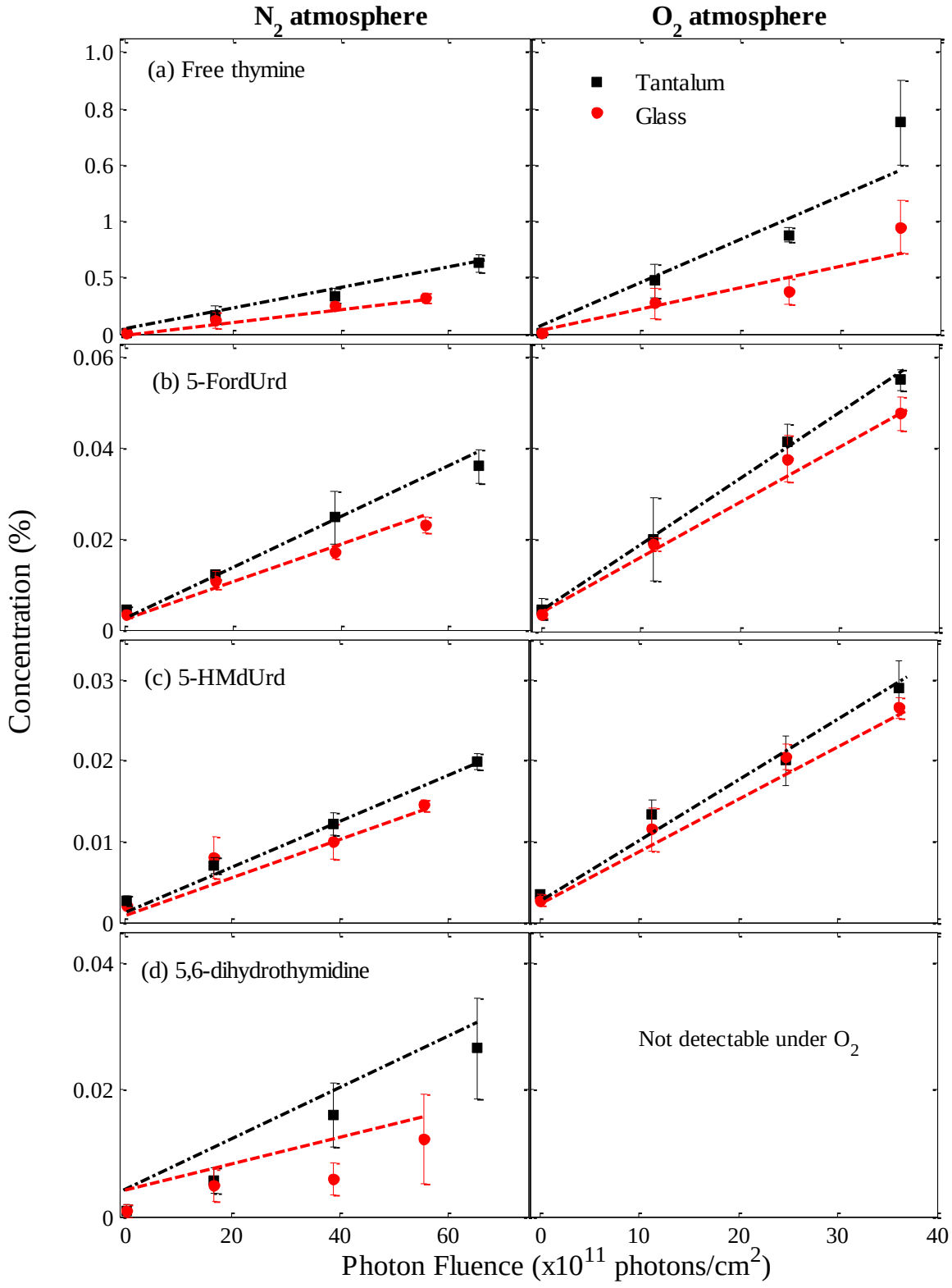

Figure 5.10: Exposure-response curves for the appearance of: (a) free thymine (base release), (b) 5-formyl-2'-deoxyuridine (5-FordUrd), (c) 5-hydroxymethyl-2'-deoxyuridine (5-HMdUrd) and (d) 5,6-dihydrothymine in thin films of thymidine deposited on either tantalum and glass substrates and irradiated by 1.5 keV X-rays under N_2 (left panel) and O_2 (right panel) at SATP.

Table 5.3: Percentage yields per 10^{14} photons/cm^2 for the formation of base release and nucleobase modifications 5-formyl-2'-deoxyuridine (5-FordUrd), 5-hydroxymethyl-2'-deoxyuridine (5-HMdUrd) and 5,6-dihydrothymidine (5,6-DHThd). G values are given in nmol/J.

	Environment	Y_{Gl}	Y_{Ta}	$EF = Y_{Ta}/Y_{Gl}$	G_X	G_{LEE}
Loss of Thymidine	N_2	-3.3 ± 0.1	-5.8 ± 0.8	1.8 ± 0.2	95 ± 15	358 ± 57
	O_2	-10.3 ± 0.1	-17.5 ± 0.1	1.7 ± 0.1	289 ± 50	1219 ± 232
	O_2 / N_2	3.1 ± 0.4	3.0 ± 0.4			
Thymine	N_2	2.6 ± 0.2	4.6 ± 0.4	1.8 ± 0.2	73.8 ± 15	286 ± 57
	O_2	8.4 ± 0.1	15.3 ± 0.2	1.8 ± 0.2	238 ± 50	1162 ± 232
	O_2 / N_2	3.2 ± 0.5	3.3 ± 0.6			
5-FordUrd	N_2	0.4 ± 0.1	0.5 ± 0.1	1.3 ± 0.1	10.2 ± 2	21.9 ± 4
	O_2	1.1 ± 0.1	1.4 ± 0.1	1.3 ± 0.1	34.1 ± 7	37.1 ± 7
	O_2 / N_2	2.8 ± 0.4	2.8 ± 0.4			
5-HMdUrd	N_2	0.2 ± 0.05	0.3 ± 0.05	1.5 ± 0.1	5.7 ± 1	16.8 ± 3
	O_2	0.6 ± 0.1	0.7 ± 0.1	1.2 ± 0.1	17 ± 3	20.2 ± 4
	O_2 / N_2	3.0 ± 0.6	2.3 ± 0.3			
5,6-DHThd	N_2	0.2 ± 0.07	0.4 ± 0.08	2 ± 0.5	5.7 ± 1	33 ± 6
	O_2	ND	ND	-	ND	ND
	O_2 / N_2	-	-			

As mentioned above, we included a set of three control samples both for glass and tantalum substrates in each experimental run, which are represented by the first points in Figures 5.9 and 5.10. Whereas thymine is not released, or lies below the detection limit of the LC-MS/MS system without X-rays exposure, it can be appreciated that dThd slightly degrades into 5-FordUrd, 5-HMdUrd and 5,6-DHThd (see also Figure 5.8). Note that somewhat larger damage can be observed in control samples deposited on the tantalum substrates, which can be attributed to the reactivity of the metal surface.[13] However, the levels of damage detected in non-irradiated samples is much lower than in the irradiated ones (~86% and ~88% less 5-FordUrd and 5-HMdUrd have been detected in non-irradiated tantalum samples within an O_2 atmosphere, up to ~90% under the other environmental conditions).

As in the previous experiment (section 5.1.2), we have employed a linear-least-square procedure to fit the data in Figures 5.9 and 5.10. The slopes of the fitted lines to the exposure-response curves give the percentage yields of the thymidine loss and radiation-products formation per photon fluence, for samples deposited on glass (Y_{Gl}) and tantalum (Y_{Ta}), and surrounded either by N_2 or O_2 molecules. Such data represent the rate of dThd degradation and

formation of thymine, 5-FordUrd, 5-HMdUrd and 5,6-DHThd. They are given in Table 5.3 along with their standard errors per 10^{14} photons/cm^2. It can be seen that among the products analysed, thymine release was the predominant channel.

Table 5.3 also provides the enhancement factors (EFs), which have being obtained by dividing the yields associated with the tantalum substrate by those associated with the glass substrate: $EF = Y_{Ta}/Y_{Gl} = 1 + Y_{LEE}/Y_{Gl}$, where $Y_{LEE} = Y_{Ta} - Y_{Gl}$ is the yield of dThd products induced by LEEs.[13] Therefore, EFs indicate the damage enhancement induced by the photo-emitted LEEs relative to the X-rays. These data show that LEEs produce an enhancement on thymidine loss by a factor of 1.8 relative to X-rays, under both N_2 and O_2 atmospheres. Similarly, formation of thymine is enhanced by a factor of 1.8 for samples deposited on tantalum relative to glass, under both N_2 and O_2 atmospheres conditions. The yield of 5,6-DHThd is enhanced by a factor of 2 on tantalum samples relative to glass, under N_2 atmosphere. Although at a smaller rate, LEEs also enhance the formation of 5-FordUrd and 5-HMdUrd relative to X-rays by a factor of 1.3/1.3 and 1.5/1.2 in each case, under N_2/O_2 atmosphere, respectively. From these results, it appears that LEEs are significantly more efficient than X-rays to induce free thymine and the reductive product 5,6-DHThd, but they are only slightly more efficient to induce the oxidatively generated base modifications. In other words, the main difference between LEE and X-ray radiation was the greater relative formation of free thymine and 5,6-DHThd in the case of LEEs. Similar results were obtained recently by Park *et al*.[30], who irradiated dried thin films of TpTpT trinucleotide with a monoenergetic beam of LEEs (10 eV) under UHV and with X-rays under ambient conditions. They found that the yields of base release and 5,6-DHThd for LEEs were more than 50% larger than for X-rays, whereas the yields of oxidation products were similar for LEE and X-ray radiation. Although these results are merely indicative, since the number of LEEs actually absorbed by the film was not known with certainty, they are in good qualitative agreement with present results.

On the other hand, it is also observed in Table 5.3 that Y_{Gl} and Y_{Ta} for thymine, 5-FordUrd and 5-HMdUrd become larger by changing the atmosphere from N_2 to O_2. This enhancement is evaluated with the ratio O_2/N_2 which shows that the formation of these products under an O_2 atmosphere is equally favoured in tantalum and glass samples, within the experimental uncertainty. In accordance with the previous results on plasmid DNA,[13] these results indicate that damage enhancement induced by LEEs tend to be independent of the surrounded atmosphere, within the experimental uncertainty.

Additionally, the damage yields can be expressed in terms of G values. Such data is also given in Table 5.3 in units of nmol/J for 1.5 keV soft X-rays and LEEs. One can see that *G* values for total damage induced by X-rays and LEEs under N_2 atmosphere are 95 ± 15 nmol/J

and 358 ± 57 nmol/J, respectively, which are comparable to those obtained in earlier studies for loss of supercoiled plasmid DNA i.e., 98 ± 20 nmol/J and 260 ± 50 nmol/J for X-rays and LEEs, respectively.[45,14] More interestingly, there is good agreement between present G_X for base release (73.8 ± 15 nmol/J) and the G_X value obtained recently by Park *et al.*[30] (G_X=72 ± 4 nmol/J) in the study of thin films of TpTpT trinucleotide. Also, it is in fair agreement with the data obtained by the group of Bernhard[46], who estimated a G value of 124 ± 8 nmol/J for free base release in d(CGCGCG)$_2$ hexamer films irradiated by X-rays at room temperature.

Note that apart from the products reported here, further radiation-induced dThd products can be generated. For instance, 2',3'-dideoxy-thymidine is known to be formed induced by X-rays and also by LEEs interaction.[47,48] Moreover, under an oxygenated atmosphere, additional oxidized nucleosides are expected to be formed.[2]

Induced damage observed in the samples can be attributed to two different reaction mechanisms: either direct or indirect damage. The former encompasses the interaction of the 1.5 KeV X-rays and SEs (including the LEEs photo-emitted from the metal surface) with thymidine, whereas the latter occurs when the species generated by the impact of the X-rays and SEs with the surrounding N_2 and O_2 reacts with thymidine.[13]

5.2.2.1. Direct Damage

Reaction mechanisms of direct damage induced by X-rays and LEEs to thymidine are well established [49,50] hence we only discussed them briefly here in the context of the present experiment. When 1.5 keV X-rays traverse the samples, a portion of them (0.16%) interacts with the thymidine molecules essentially via the photoelectric effect.[51] The generated photo/Auger electrons deposit progressively their energy within the dThd molecules leaving them either ionized (~80%) or electronically excited.[6,52] Indeed, the main pathways of formation of the different radiation-products analysed here involve one-electron ionization, either at the base or the sugar moiety.[30] These scattering interactions induced by soft X-rays are prone to occur on samples deposited on both tantalum and glass substrates.

On the other hand, there is experimental evidence that LEEs can induce base release, strand breaks, and base modifications in nucleosides, short oligonucleotides and plasmid DNA, involving a subionization process, i.e., dissociative electron attachment (DEA).[19,27] As discussed in section 5.1.2, subexcitation LEEs and electrons with energies above ~5.5 eV can induce the rupture of the *N*-glycosidic bond in thymidine (via reaction 5.1 and 5.2). Alternatively, DEA reactions can induce the loss of a neutral hydrogen radical ($H^{\bullet}$)[53,54] or ejection of the hydride ions (H^-),[55,56] depending also on the incident electron energy:

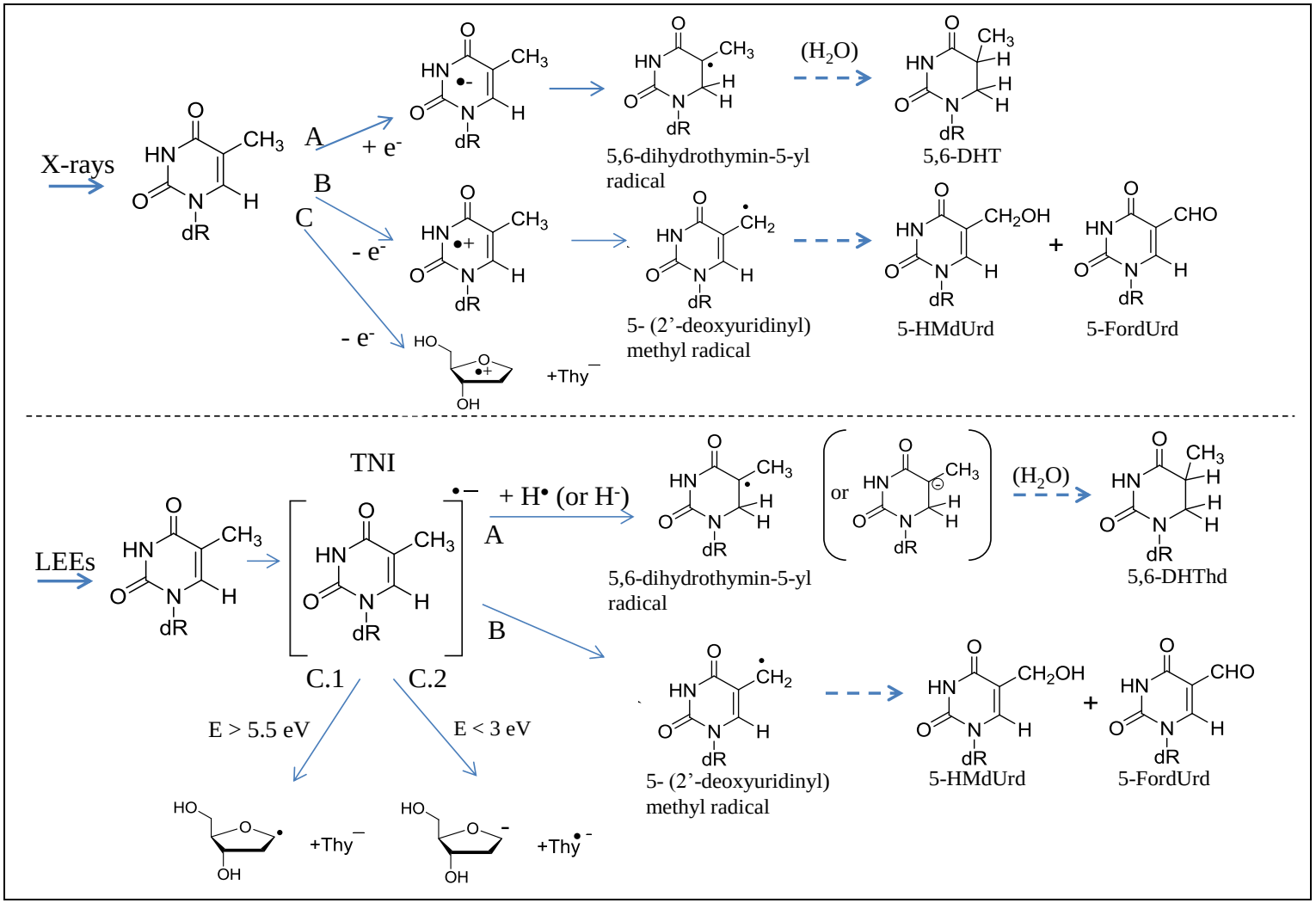

Figure 5.11: Mechanisms of damage on the nucleoside thymidine induced by X-rays through one-electron ionization reactions (top panel) or by LEEs through DEA processes (bottom panel), leading to the formation of 5,6-DHT (pathway A), 5-FordUrd and 5-HMdUrd (pathway B) and release of free nucleobase (pathway C). See text for further details.

$$dThd + e^- \rightarrow dThd^{-*} \rightarrow (dThd\text{-}H)^- + H^\bullet ; \qquad (E < 1.8\ eV) \qquad (5.11)$$

$$dThd + e^- \rightarrow dThd^{-*} \rightarrow (dThd\text{-}H)^\bullet + H^- ; \qquad (E > 5.5\ eV), \qquad (5.12)$$

The former reaction (5.11) may be associated with the second π* resonance of the base moiety, since the same fragmentation pattern has been detected in electron collisions with the isolated base.[31] Moreover, ejection of $H^\bullet$ is expected to occur from the N3 position.[53,54,57] On the other hand, the release of the hydride anion (H^-) through DEA occurs mainly at the N3, C6 and the C5-methyl group.[56,58] Additionally, H^- can be ejected from the deoxyribose moiety induced by electrons with incident electrons between 6-9 eV.[59,7] However, the contribution of the latter reaction is expected to be much lower since LEEs are preferentially captured by the base moieties.[60,61]

Given that the energy distribution of the SEs emitted from tantalum surface upon X-rays exposure ranges essentially from zero to 30 eV and peaks at 1.4 eV, with an average energy ~5.85 eV peaks, all these DEA reactions (5.1, 5.2, 5.11 and 5.12) are susceptible to occur in the present experiment. One should note that SEs with energies above 10 eV can ionize thymidine or induce nonresonant fragmentation (via either electronic excitation of high-lying dissociative states or dipolar dissociation),[30] however these reactions are likely minor in view of the low percentage of electrons within this energy. Therefore, it is reasonable to assume that photo-emitted LEEs induce damage mainly through DEA.

A summary of the different mechanisms of direct damage induced by X-rays and LEEs leading ultimately to the reductive product 5,6-DHThd(A), the oxidative products 5-FordUrd and 5-HMdUrd (B) and base release (C) is given in Figure 5.11. It is worthy to note that X-rays and LEEs induce similar radical intermediates, although the decomposition pathways are initiated via different mechanisms, i.e., via one-electron ionization or DEA, respectively.[30]

5.2.2.2. Indirect Damage

For a discussion of the indirect damage, we need to consider the species created around the thymidine molecules by the presence of N_2 and O_2. According to our calculations, 22.9% and 14.7% of soft X-rays are absorbed by O_2 and N_2 molecules, respectively, before reaching the sample surface.[13] As mentioned before, most of this absorbed energy leads to ionization reactions. X-rays photoionize the O_2 and N_2 molecules generating molecular ions and secondary electrons ($h\nu + AB \rightarrow AB^+ + e^-$).[51] The generated secondary electrons possessing energies above the ionization threshold (which for nitrogen and oxygen molecular gas is placed at is placed at 15.58 and 12.077 eV,[62] respectively) can undergo further ionization processes. Note that the total ionization cross sections for electron collisions with O_2 molecules[63] are slightly

larger than for N_2 molecules,[64] over the entire photoelectron energy range (10-1500 eV). Also it has been shown that, after single ionization oxygen molecules are more dissociative than nitrogen molecules:[65] whereas 85% of the N_2 molecules stabilize into N_2^+, only about 71% of the O_2 stabilizes into O_2^+.[65] The remaining single charged molecules may dissociate onto the ionic products N^+ and O^+, respectively:

$$\begin{aligned} e^- + N_2 &\rightarrow N_2^+ \rightarrow N^+ + N + 2e^- \\ e^- + O_2 &\rightarrow O_2^+ \rightarrow O^+ + O + 2e^- \end{aligned} \qquad (5.13)$$

Double ionization may lead to double charged fragments N^{2+} and O^{2+}, although the contribution of this channel to the total ionization cross sections is much smaller. Ionization reactions can lead to the formation of a variety of positive dissociative fragments and molecular ions.[35] Extensive discussions of the O_2 and N_2 ionization processes can be found in the literature.[66]

Additionally, other dissociative fragments can be generated. Regarding N_2, neutral dissociation occurs for incident electron energies above 10 eV. The energy distribution peaks around 60 eV with a maximum cross section 1.23×10^{-16} cm^2.[64] Neutral fragments are also produced by low energy electrons, although through another scattering mechanism: dissociative electron attachment. The resonant state N_2^{-*} dissociates onto a neutral fragment and an unstable negative ion according to the following the reaction:

$$e^- + N_2\,(x^1\Sigma_g^+) \rightarrow N_2^{-*}\,(^2\Pi_u) \rightarrow N(^4S) + N^-(^3P) \rightarrow N(^4S) + N(^4S) + e^- \qquad (5.14)$$

that is, the unstable N^- ion, which have a very short lifetime ($\tau \sim 4 \times 10^{-14}$ s)[67] will undergo autoionization emitting a near zero energy electron.[67]

Under an O_2 atmosphere, radical anions O^- may be produced also via two different electron impact mechanisms: either through nonresonant ion-pair formation induced by incident electrons with energies above 17 eV,[68] or via dissociative electron attachment, according to the reaction:

$$e^- + O_2\,(\Sigma_g^-) \rightarrow O_2^{-*}\,(^2\Pi_u) \rightarrow O^-(^3P) + O(^3P, ^1D) \qquad (5.15)$$

The energy distribution for the formation of O^- peaks around 6.5 eV,[69] being the maximum cross section[70,69] 1.4×10^{-18} cm^2. Additionally, some LEEs can participate in a three-body attachment reaction to yield the superoxide radical $O_2^{-\bullet}$:[71]

$$e^- + O_2 + O_2 \rightarrow O_2^{-\bullet} + O_2. \qquad (5.16)$$

It is important to highlight that the abovementioned N_2 and O_2 radiation-products are generated in two different regions: the free space between the mylar foil and the thymidine surface, or within the films due to the adsorption of N_2 and O_2 molecules. In the former region,

only the reactive species generated within 0.1μm (i.e., the mean free path at standard conditions) are believed to interact with the target. The point to be noted is that the species generated in this volume are due to the interaction of 1.5 keV X-rays and the SEs they produced. On the other hand, LEEs emitted from the tantalum surface reach thermalization within the thymidine films[72] where they deposit all their energy. This means that inside the Ta films, LEEs strongly interact both with the nucleoside and the N_2/O_2 molecules diffused within the dThd layers inducing DEA reactions. In particular, DEA condensed-phase cross section for O_2 peaks at 6 eV,[73] which is very close to the average energy (5.85 eV) of the LEEs emitted from the metal substrate.

In addition, one should note that whereas some of the oxygen products are highly reactive, in order to form reactive nitrogen species the presence of oxygen species (e.g., O_2 or NO_2) is required.[74] Interestingly, Alizadeh *et al*.[13] reported no detectable enhancement of conformational damage to DNA under nitrogen atmosphere compared to analogous experiments under vacuum. This means that the presence of N_2 molecules do not promote the damage induced by soft X-rays or LEEs.

According to the above discussion, we expect to find larger yields of damage on irradiated dThd in an O_2 atmosphere, where higher amount of reactive species with larger reactivities are generated. Finally, we underline that in general, in order to observe higher damage yields, oxygen must be present during radiation exposure or within microseconds after exposure to radiation.[75]

The LEE–mediated damaging mechanisms inducing the formation of 5,6-DHThd, 5-FordUrd, 5-HMdUrd and base release in dThd under N_2/O_2 atmospheres are proposed in Figure 5.12. Specific details of the different pathways of damage are given in the following subsections.

5.2.2.3. Base Release

Various studies have reported the fragmentation of the glycosidic bond in thymidine due to γ-ray or X-ray irradiation in vacuum, initiated by one-electron ionization either of the thymine base or the deoxyribose moiety.[2,49,76,77] For instance, when a radical cation on the sugar sub-unit is formed, it may undergo deprotonation most likely at the C3’ and C5’ sites, giving a C-centred radical which is in turn a precursor to base release.[78]

As mentioned before, the ability of LEEs to induce base release via DEA is well established both in the gas[8,16] and condensed phase[20,19] under vacuum. In this case, according to the energy distribution of the SEs emitted from the tantalum surface, base release may arise from both

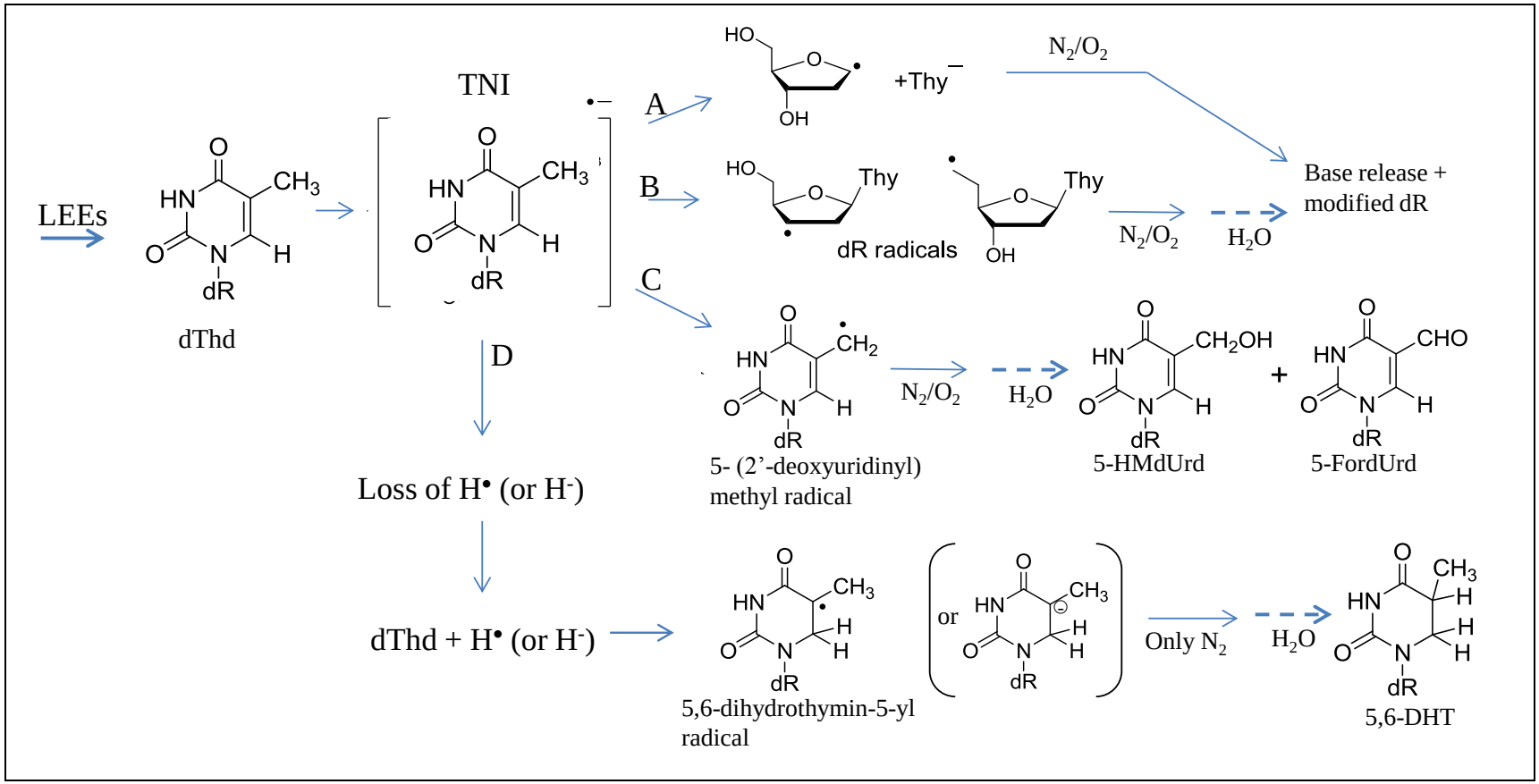

Figure 5.12: LEE-mediated pathways of damage for thymidine. Release of the base thymine occurs via DEA to the base (pathway A) or to the 2-deoxyribose (dR) moiety (pathway B). DEA can also take place from the exocyclic methyl group of dThd leading to a hydrogen anion (H-) and an 5-(2'-deoxyuridinyl)methyl radical, which may undergo a series of reactions to form 5-HMdUrd and 5-FordUrd (pathway C). From DEA reactions with dThd, hydrogen atoms (H•) or hydrogen anions (H-) are generated which can get attached to dThd to give a 5,6-dihydrothymindin-5-yl radical. Under a N_2 atmosphere, this radical may subsequently transform into 5,6-DHThd (see text for more details).

reactions 5.1 and 5.2; it can be explained by the initial formation of TNI at the base moiety followed by transfer of the electron to either the C-N bond or the C-O bonds of the sugar moiety (pathway A and B in Figure 5.12, respectively). DEA from the 2-deoxyribose moiety involves cleavage of the C-O bonds either at C5' or C3' positions giving hydroxide ion (OH-) and carbon centered radicals at C5' and C3', respectively. When dissolved in H_2O, the latter radicals undergo subsequent reactions that lead to base release (-Thy) together with modified 2-deoxyribose fragment. Thus, base release is a favoured pathway for the reaction of LEEs with DNA components.

Measurements on base release under an oxygenized environment have been reported only upon γ- or X-rays exposure. In an early work, Swarts and co-workers[79] measured the formation of unaltered nucleobases from dry salmon sperm DNA samples irradiated with γ-rays under N_2 and O_2. They found that the yield of free thymine was significantly larger within the latter environmental gas. Hoffmann and Huttermann[80] reported thymine release from freeze-dried thymidine-monophosphate samples induced by X-rays irradiation under a nitrogen and air atmosphere. They observed a linear increase on the yield of free thymine as function of dose, being ~30% larger on samples irradiated under air, which is composed by a 21% of O_2. Despite quantitative comparison is not possible with these studies, they are in qualitative agreement with the present results for samples deposited on glass, which show the significant influence of O_2 on the X-irradiated dThd samples.

The effect of O_2 can be explained mainly by the ability of O_2 to rapidly add to carbon-centred radicals (which are generated via X-rays and LEEs irradiation, as explained above),[81] giving rise to the peroxyl radicals. In particular, yield of base release by pathway B (Figure 5.12) is greater when the irradiation is carried out in O_2 compared to N_2 because O_2 adds to the initial 2-deoxyribose radicals leading to peroxyl radicals; the resulting chemistry of the peroxyl radicals facilitates base release.[82] In addition, greater base release under O_2 atmosphere can be also attributed to the large amount of highly reactive oxygen species that are formed within the samples or at the film-gas interface, which can react with thymidine molecules and finally lead to base release. For instance, Lin *et al.*[83] proposed that $O_2^{-\bullet}$ can attack the C(1') site of the 2-deoxyribose moiety inducing the release of the base, in accordance with previous studies of Cadet *et al.*[84] Alternatively, although probably at a smaller extent, oxygen can scavenge electrons from the target increasing the amount of base cation radicals, what results in larger base release as suggested by Swarts *et al.*[79] For instance, oxygen may oxidize the sugar moiety at the C(1') site. The resulting cation radical can undergo deprotonation, what alters the *N*-glycosidic bond and is susceptible to release the base.[85] Note that these reactions may compete with the possibility that excess electrons reduce the radical intermediates and regenerate the initial substrate.

5.2.2.4. Oxidative Base Modifications: 5-FordUrd and 5-HMdUrd

It is well established that ionizing radiation can induce the oxidation of dThd to 5-hydroxymethyl-2'-deoxyuridine (5-HMdUrd) and 5-formyl-2'-deoxyuridine (5-FordUrd).[86] Such compounds have been detected under different conditions, for instance, in DNA aerated aqueous solutions,[87] DNA solid films irradiated with γ-rays,[88] and also multilayer thymidine films irradiated with soft X-rays under vacuum.[89] Photoxidation mechanisms leading to the formation of these compounds have been excellently reviewed by Cadet *et al*.[86] Briefly, electron removal from the base moiety can give base-centred radical cations, which subsequently may undergo deprotonation leading to the intermediate 5-(2'-deoxyuridinyl)methyl radical.[90] The latter radical can undergo a number of reactions to explain the formation of 5-HMdUrd and 5-FordUrd.

Figure 5.10 shows larger yields of both oxidized nucleosides in samples deposited on the tantalum substrate under both environments, which is attributed to the efficient action of LEEs. The mechanism of LEE-mediated oxidation inducing the formation of 5-HMdUrd and 5-FordUrd in thymidine are proposed in Figure 5.13, which includes several pathways. The loss of hydride anions ($-H^-$) from the methyl group via DEA of electrons with incident energy of ~10 eV (reaction 5.12),[58] is the first step of a series of reactions that explains the formation of the oxidized 2'-deoxyribonucleoside compounds. The resulting transient compound is the 5-(2'-deoxyuridinyl)methyl radical (**3**), which is highly reactive and may therefore react rapidly with O_2 to form a peroxyl radical ($ROO^{\bullet}$). (**4**) This radical may be reduced by electron transfer and subsequently undergo protonation (**5**) to generate the peroxide (5-hydroperoxymethyl-2'-deoxyuridine).[91] This compound is converted either into the alcohol 5-HMdUrd (**6**) through reduction, or into the aldehyde 5-FordUrd (**7**) via dehydration (pathway A).[86,92] Additionally, the neutral C-centred radical (**3**) can be oxidized to 5-methyl-(2'-deoxyuridylyl) cation through addition of oxygen and subsequent elimination of superoxide radical anion (**8**). This is followed by addition of a H_2O molecule giving the alcohol, 5-HMdUrd. Alternatively, Park *et al*.[30] proposed that oxidation of (**3**) can also occur by means of nearby oxidizing radicals such as 5,6-dihydrothymin-5-yl radical, which is also formed in the solid samples via X-rays or LEEs irradiation and is an intermediate to 5,6-DHThd, as we will see in next section. Thus, electron transfer may occur between 5-methyl-(2'-deoxyuridylyl) radicals and 5,6-dihydrothymin-5-yl radicals to give the corresponding cation and anion, respectively (pathway B).[30] Finally, 5-HMdUrd (**6**) and 5-FordUrd (**7**) can be also formed through the Russell mechanism:[86] the combination of two 5-(2'-deoxyuridinyl)hydroperoxymethyl radicals (**3**) may form a tetroxide intermediate (**9**) which subsequently decomposes into 5-HMdUrd (**6**) and 5-FordUrd (**7**), by the release of a $^1O_2$ molecule (pathway C).

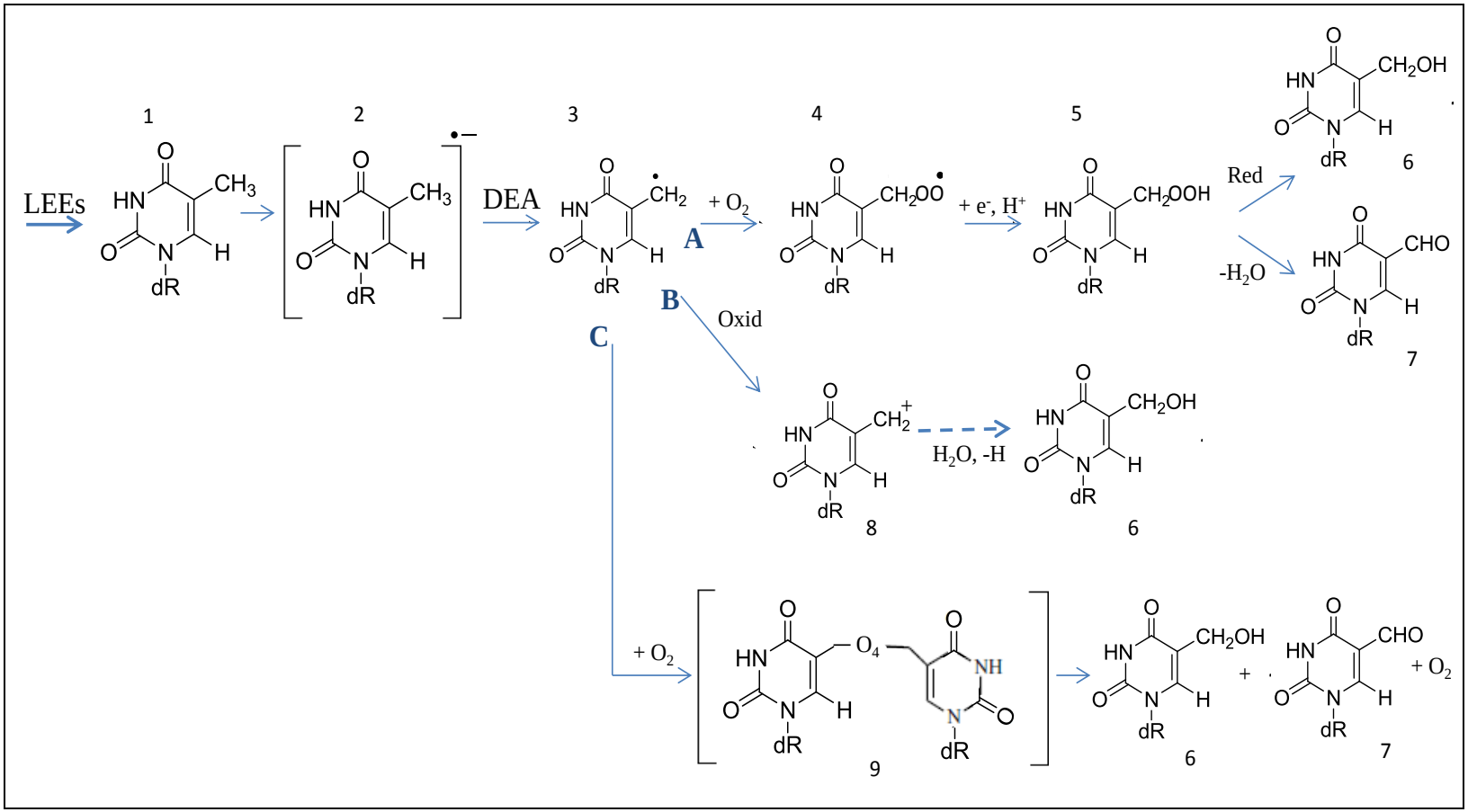

Figure 5.13: LEE-mediated oxidation pathways for thymidine (dThd, R=2-deoxyribose) leading to the formation of 5-HMdUrd (**6**) and 5-FordUrd (**7**). (see text for further details).

All the aforementioned pathways are favoured under an oxygenated atmosphere. Accordingly, we found larger yields of 5-HMdUrd and 5-FordUrd under an oxygenated atmosphere.

5.2.2.5. Oxygen-free Base Modifications: 5,6-dihydrothymidine

Earlier investigations have reported 5,6-dihydrothymidine (5,6-DHThd) to be a major radiation-induced product of thymidine and DNA samples in solid state irradiated with γ rays[88,89] and soft X-rays[89] under anoxic conditions. Formation of 5,6-DHThd upon ionizing radiation exposure was explained by initial electron addition to the pyrimidine ring, followed by protonation and then a reductive reaction.[30,93] Additionally, Park *et al.*[7,30] explained that the formation of 5,6-DHThd could be mediated by DEA of low-energy electrons. The present results are in agreement with Park *et al.*[7,30] investigation and demonstrate the larger effectiveness of LEEs to induce the formation of 5,6-DHThd compared to 1.5 keV X-rays (Figure 5.10). In this case, formation of 5,6-DHThd can be initiated by the hydride anions, (reaction 5.12), as proposed by Park *et al.*[7], and also via hydrogen radicals, which are produced by subexcitation LEEs (reaction 5.11). $H^{\bullet}$ can become attached to the 5,6-double bond of the pyrimidine ring at either the C5 or C6 site. The resulting 5,6- dihydrothymin-5(or 6)-yl radical may be reduced, (for instance, by electron transfer with the 5-methyl-(2'-deoxyuridylyl) radical; see section 5.2.2), to form an intermediate anion. The latter compound may subsequently undergo protonation with proton donors of the film or upon dissolution of the samples after irradiation (see Figure 5.14).[7,30]

More importantly, oxygen is not required for this reaction to take place.[89] In fact no 5,6-DHThd product was detected in dThd films irradiated under an O_2 environment (see Figure 5.10). This behaviour is expected since the intermediate radical reacts very quickly with O_2 molecules, inhibiting therefore the pathway to 5,6-DHThd formation. The final product resulting from the addition of oxygen to 5,6-dihydrothymin-5-yl radicals, such as 5-hydroxy-5,6-dihydrothymidine, were not measured in the present analysis.

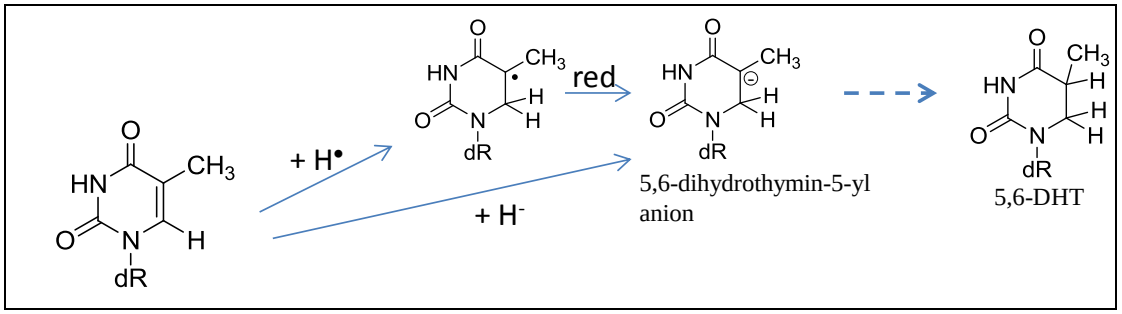

Figure 5.14: Possible mechanisms of formation of 5,6-dihydrothymidine initiated either by $H^{\bullet}$ or H^{+}, which are generated via DEA process (reaction 5.11 and 5.12, respectively).

5.3. The Effect of Hydration Level on Radiation-induced Damage.

We have already highlighted the importance of water as the solvent of life in Chapter 4. Cellular DNA is embedded in a medium that essentially consists of water, which implies that the majority (over 66%) of the radiation energy deposited in cell is absorbed by the cellular water. Thus, studies focused on the interdependence between DNA radiation damage and water content started long ago.[94,95] Initially, indirect damage induced in irradiated DNA was studied in aqueous solutions. As experimental techniques were improved, radiation studies with hydrated DNA films became possible. Baverstock *et al*.[96] used photons to irradiate lyophilized DNA films hydrated with water vapour, where presumably only bound water was present. Then, Swarts and co-workers[79] showed that the release of bases originating from γ-irradiated DNA depends on its level of hydration. Ito *et al*.[97] reported the yield of damage induced by γ-irradiation in plasmid DNA in three different environments: dry, humid and aqueous state. More recently, Yokoya *et al*.[98] discussed the effect of bound and free water on the yields of DNA strand breaks induced by γ-rays at various levels of hydration. All of these studies employed high energy radiation and assumed that $OH^{\bullet}$ radicals and charge transfer were the main causes of damage to irradiated cellular DNA.[79,99]

On the other hand, owing to the important role of LEEs in DNA breaks,[9] various studies focused on the interactions of LEEs with hydrated DNA have recently been reported. Experiments were performed with DNA subunits and short oligonucleotides embedded into multilayer films of amorphous ice, to simulate the water molecules surrounding cellular DNA.[100-102] Those results indicated the formation of new dissociative transient anions, arising from the interaction between H_2O and DNA.[103] Theoretical studies were subsequently conducted, which confirmed that the addition of water to dry DNA modifies the transient-anion manifold, the corresponding decay channels and thus the SSB and DSB yield functions.[104,105] In addition, further theoretical studies showed that when DNA molecules are immersed in an environment of polar molecules, such as water (i.e., solvation), their capability to capture electrons with near-zero energies increases significantly, via the modification of the adiabatic electron affinity (AEA) of solvated DNA bases in bulk water.[106,107]

Note that these earlier experiments were performed under UHV conditions and the water molecules were frozen within DNA. In this work, by means of the experimental setup described in section 5.2, we study the indirect effects of LEEs and soft X-rays with liquid water condensed on and within DNA at standard ambient temperature and pressure (SATP).[15] Specifically, thin films of plasmid DNA deposited on tantalum and glass substrates were exposed to 1.5 keV X-rays under different relative humidity levels, i.e., 20, 50, 80 and 100% RH. In contrast to a dilute solution of DNA, the number of H_2O molecules per nucleotide (Γ) in

these films is limited to a range of $2.5 \leq \Gamma \leq \sim 33$, where $\Gamma \leq 20$ corresponds to layers of hydration and $\Gamma = 33$ to an additional bulk-like water layer. The loss yields of supercoiled (SC) plasmid DNA and the formation of single- and double- strand DNA damages are compared at different humidity levels. As such, by increasing the DNA hydration level up to concentrations which produce bulk-like water, we shift progressively from the direct to indirect effects of LEEs.

5.3.1. Experimental Methods and Materials

Given that natural DNA possesses a double-stranded helical structure, here we employ double stranded plasmid DNA. The main advantage of working with plasmid DNA is in the post-irradiation chemical analysis. Owing to its supercoiled configuration, just one bond rupture in a plasmid DNA of a few thousand base pairs can cause a conformational change in the DNA. This huge damage amplification considerably facilitates the analysis of DNA damage. Supercoiled plasmid DNA, which corresponds to undamaged DNA, converts into a relaxed form or 'nicked circular' (C) form by induction of a single-strand break (SSB), while induction of a double-strand break (DSB) within both the SC and C forms changes the plasmid into its linear (L) form.[13] DSBs are especially important because they usually cannot be repaired by the cell.

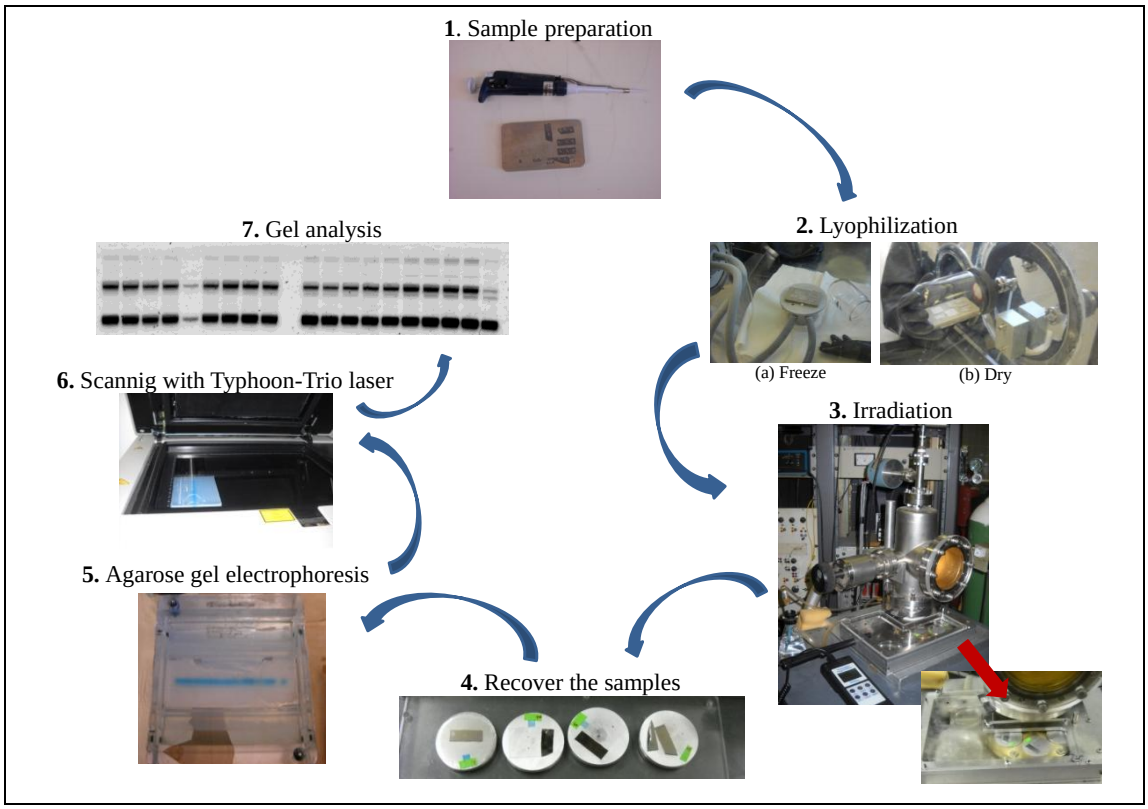

Figure 5.15: Schematic view of the main steps performed in the present experiment (see text for further details).

The experimental procedure is very similar to that followed in section 5.2.1. Principal steps of this experiment are shown schematically in Figure 5.11. Basically, small aliquots of plasmid DNA solution were deposited on glass and tantalum substrates (step 1) and lyophilized (step 2). Then, dried samples were placed in the irradiation chamber for X-rays exposure at SATP. In this case, the sample-chamber contained also a water pool to create the hydrated conditions (step 3). After irradiation, samples were immediately recovered (step 4) and loaded in an agarose gel for being electrophoresed (step 5). The gel was scanned (step 6), and the resulting image was analysed densitometrically to quantify the amount of each DNA form (step 7). Thus, this experimental procedure differs from the one employed in section 5.2.1 essentially in the manipulation of the samples. Plasmid DNA requires different treatment with regards to sample preparation, post-irradiation recovery and analysis than that of dThd. The specifics of these steps are described in more detail below.

Plasmid DNA Sample Preparation

A detailed description of sample preparation and manipulations can be found in Alizadeh *et al.*[13,35] Briefly, supercoiled DNA [pGEM-3Zf(−) bacterial plasmid DNA, 3197 base pairs, ca. 1.97×10^6 amu, Promega] was extracted from *Escherichia coli* JM109 host and purified with the QIAfilter Plasmid Giga Kit (Qiagen).[108] The DNA pellet was stored at -20 °C in TE buffer (10 mM Tris, 1 mM EDTA). Subsequently, DNA was purified using a homemade microcolumn filled with Sephadex G-50 resin on a bed of glass beads. This step is crucial to clean the DNA from TE and eliminate small molecules such as salts. After equilibration and washing with distilled and deionized water (ddH_2O), the plasmid DNA was eluted by centrifugation. The DNA concentration was determined spectrophotometrically by measuring its absorbance at 260 nm, assuming a molar absorption coefficient of 5.3×10^7 $L.mol^{-1}.cm^{-1}$ at pH 7.0 for DNA.[109] Typically, a certain amount of proteins remain linked to the DNA molecule, which has the maximal absorption at 280 nm. Hence, we can check the purity of the DNA sample by means of the ratio A_{260}/A_{280}: if this ratio is ~2.0, the concentration of proteins is low. For the plasmid DNA employed in this set of experiments the ratio A_{260}/A_{280} was > 1.89. The resulting DNA solution is diluted with ddH_2O up to reach 50 ng/µL concentration. Then, the integrity of the DNA samples after the preparation procedure has been checked by means of agarose gel electrophoresis, showing that ~96% of the extracted DNA was in supercoiled form.

To avoid charging of the films due to electrons thermalization, thin and uniform plasmid DNA films should be prepared. For this reason, 10 µl of plasmid solution at a concentration of 50 ng/µl was spread out on clean tantalum and glass surfaces, and lyophilized. The procedure followed to freeze-drying the DNA samples was the same than that employed to prepare the

thymidine films (see section 5.1.1). The film thickness is derived from the same expression used in previous sections (i.e., $t = m/\pi r^2 \rho$): considering that the dried samples had a ring shape of 6.0 ± 0.2 mm average diameter and the density[110] for plasmid extracted from *E. coli* is 1.71 g/cm^3, the mean thickness turned to be ~10 nm (i.e., a thickness of approximately 5 ML of DNA).

The resulting DNA thin films presumably contained a small amount of "structural" water (on average, 2.5 bound water molecules per nucleotide),[27] which cannot be removed by lyophilization and therefore remain bound to our "dry" DNA samples. The DNA films were rehydrated by exposing them to water vapour under N_2 atmospheric pressure at four different humidity levels (20, 50, 80 and 100% RH). More specifically, dried films were kept inside the chamber (flushed with dry N_2) where a water dish was placed to maintain a specific relative humidity (RH) condition. The humidity was monitored by a traceable hygrometer sensor (Fisher Scientific) and the temperature during the irradiation was 23 ± 1 °C. RH levels of 20% and 50% correspond to Γ=5 ± 1 and 10 ± 1, respectively, which are the strongly bound water molecules in direct contact with DNA and constitute the primary hydration layer. The 80% RH level correspond to Γ=20 ± 1, i.e., additional 8-9 water molecules which are more loosely bound to DNA and form the secondary hydration layer. Outside this shell are the non-bound water molecules that resembles bulk water, represented in this case by 100% RH (Γ=32.7).

Damage Quantification by Agarose Gel Electrophoresis

Agarose gel electrophoresis is a laboratory method employed to separate DNA fragments based on charge, size and conformation. An electric field is applied to the gel, which force the charged molecules to migrate through the gel matrix that contains small pores. Note that DNA is a negatively charged molecule, due to the phosphate groups that constitute the backbone of DNA. Hence, it will move towards the positively charged end of the gel when the current is turned on. Since the gel contains small pores, the velocity of the different molecules moving through the porous matrix depends on their size. This means that a small DNA strand will travel a greater distance and migrate further down the gel than a larger one. As a result, each DNA form produces a visible band in the gel at a certain position (see Figure 5.17).

After irradiation, the samples were immediately retrieved from the chamber and recovered from substrates with 10 μL of TE buffer. The fractions of various forms of DNA were separated by a 1% agarose gel electrophoresis run in TAE buffer (40 m*M* Tris acetate, 1 m*M* EDTA, pH 8.0) at 10 V.cm^{-1} for 7 min and 7.5 V.cm^{-1} for 68 min. In each well of the gel, we loaded 2 μL from each recovered solution containing ~100 ng of plasmid DNA, previously prestained by 3

μL of 100× SYBR® Green I (Molecular Probes™). The gel itself was stained by 8 μL of 10,000×concentration SYBR Green I. After electrophoresis, gels were scanned with the Typhoon-Trio laser scanner (GE Healthcare) using blue fluorescence mode at an excitation wavelength of 488 nm and filter type (520 BP 40). The relative amounts of each form of DNA were quantified using ImageQuant software (Molecular Dynamics). Given that binding of SYBR Green I to the SC form of DNA is weaker compared to nicked circular and linear configurations, the obtained values were corrected using a normalization factor, which in this case turned to be f=1.7.[13] In this work, we measured the amount of supercoiled (SC), circular (C) and linear (L) form of DNA, that correspond to undamaged DNA, the formation of SSBs and DSBs, respectively. As an example, we show in Figure 5.12 the gel slab obtained from plasmid DNA samples deposited on glass (left) and tantalum (right) substrates, irradiated with 1.5 keV X-rays under 20% of humidity. It can be easily identified the bands corresponding to SC, C and L forms of DNA.

One should note that plasmid DNA is a very sensitive sample and degrades quite easily. Thus, additional precautions should be taken when dealing with plasmid DNA. Any manipulation of the DNA solution, before and after irradiation, was done within a cool environment to minimize thermal degradation. In addition, the tantalum substrates were washed with alcohol and water, followed by heating during 30 min in an oven. Once the substrates had cooled down we deposited the samples. Finally, it was essential to reduce to the minimum the time the samples spent inside the chamber surrounded by water vapour.

Calculation of *G*-values

We follow the same scheme described in section 5.2.1 to calculate the G-values for the measurements according to the formulas (5.4) and (5.5). In this case, frozen-dried films of pGEM-3Zf(−) plasmid DNA, with no salt and 2.5 bound water molecules per nucleotide, have a molecular weight of $M_w = 2.25 \times 10^6\ g/mol$. Since samples contain 500 ng of DNA, the number of DNA molecules per sample is $N_{DNA} = \frac{500\ ng.N_A(mol^{-1})}{M_W(g.mol^{-1})} = 13.36\ x\ 10^{10}$.Other parameters necessaries to calculate X_{Abs} and X_{Trans} are the area S=0.283 cm^2, the thickness t = 10 nm and the density ρ = 1.71 g/cm^3 of the films,[110] together with the mass attenuation coefficient μ/ρ = 1056 cm^2/g for 1.5 keV X-rays in plasmid DNA.[41] The resulting G_X and G_{LEE} are calculated within 20% and 26% errors, respectively.

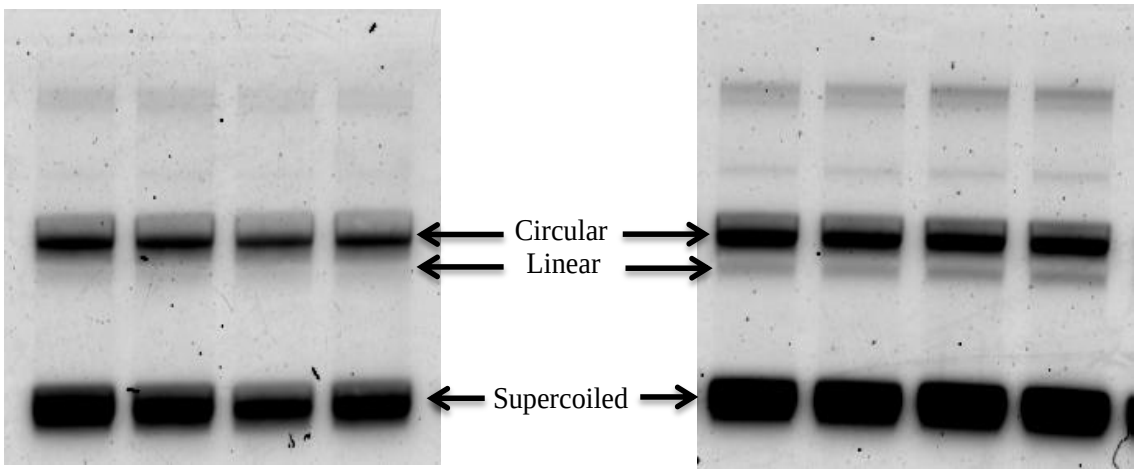

Figure 5.16: Agarose gel electrophoresis analysis of plasmid DNA films deposited on glass (left) and tantalum (right) substrates irradiated with 1.5 keV X-rays at SATP conditions and under 20% of humidity.

5.3.2. Results and Discussion

In this work, damage to plasmid DNA was evaluated by quantifying the configurational changes of the SC DNA as a function of photon fluence. Figure 5.13 shows the variation in the disappearance of SC and appearance of C and L forms of DNA with increasing photon fluence up to ~25 photons/cm^2 (i.e., the exposure-response curves), for irradiated DNA samples deposited on glass and tantalum under relative humidity (RH) levels of 20, 50, 80 and 100%. As in previous experiments, each point in these curves corresponds to the mean value of the yields from three samples, prepared under identical conditions and exposed to same photon fluence; the error bars denote the resulting standard deviation of three repeated experiments.

Present exposure-response curves for loss of SC and formation of SSBs in DNA samples deposited on both glass and tantalum substrates were fitted by means of a non-linear regression. Regarding the formation of DSB, we can see in Figure 5.13 that they lay below the limit of detection at low humidity (20% RH), whereas at higher humidity there is a linear dependence with the photon fluence. Yields of loss of SC form and DNA strand-breaks induction per incident photon/cm^2 were obtained from the gradient of the exposure-response curves at zero fluence. They are reported in Table 5.4 for samples deposited onto glass (Y_{Gl}) and tantalum (Y_{Ta}) at various representative RH (%). The Γ values corresponding to each RH with hydration shells of DNA are also specified, together with earlier results obtained with the same apparatus under N_2 at 0 % RH.[13] Note that the latter data, may correspond to damage induced via the direct effect. The yields of damage Y_{Ta} are always larger than Y_{Gl}, for dry and hydrated samples,

showing that LEEs emitted from tantalum surface can cause considerable DNA damage enhancement, in accordance with the experimental results reported in section 5.2.2. If we compare Y_{Ta} and Y_{Gl} at 0.0% RH with the values obtained at 100% RH, we can estimate that the indirect effect due to the presence of water is 64% and 74%, for samples deposited on the glass and tantalum substrates, respectively, which is in fair agreement with earlier works.[111,112]

We can also observe in Table 5.4 that by increasing RH level from 0.0% up to 80%, which corresponds to adding the primary and then secondary hydration shells to vacuum-dried DNA films, the yields of damage induced by X-rays (Y_{GI}) and LEEs with X-rays (Y_{Ta}) grow both slightly. Despite SSBs yields saturate around 80% RH for X-rays, they suffer a dramatic rise at 100% RH when samples are deposited on tantalum films. Hence, LEEs induce much more damage to DNA than photons when bulk water surrounds the molecule. This effect is reflected in the enhancement factors (EFs), that are also shown in Table 5.4. Up to 80% RH, this parameter remains fairly constant, within the experimental error, indicating that the effectiveness of LEEs in inducing damage to DNA with respect to that induced by X-ray photons remains the same after adding the first and second layer of hydration. However, once we reach the bulk-water condition *EF* for loss of SC increases substantially: from 1.2 ± 0.3 at 80% RH up to 2 ± 0.5 at 100% RH. This means that the damage induced by LEEs on DNA increases almost 100% in comparison with photons when the bulk-like layer of water is added to the second hydration layer.

These behaviours are clearly reflected in the *G* values, which are presented also in Table 5.4 for loss of SC as well as formation of C and L damages by X-rays (G_X) and LEEs (G_{LEE}). It can be seen that both G values increase slightly with Γ, but within the Γ=20-33 range G_{LEE} suffers a significant rise. *G* values obtained from X-rays are consistent with previous studies, which have shown that the waters of hydration level dramatically affect the radiation damage to DNA. In particular, good agreement is found with the data reported by the group of Sevilla *et al*.[113,114] who obtained 133 nmol/J at Γ=2.5, 145 nmol/J at Γ=5.7, 236 nmol/J at Γ=14, 300 nmol/J at Γ=18.1 and 261 nmol/J at Γ=22.5. No data on G_{LEE} has been reported before. In accordance with our previous study on thymidine and other investigations,[13,14] G values indicate that LEEs are more efficient than X-rays to induce DNA damage. In other words, supposing that X-rays and LEEs deposit the same amount of energy, LEEs induce much more damage.[14]

Yields of damage observed in the plasmid DNA are consequence of a variety of reactions. As mentioned before, they can be originated by two different mechanisms, either direct or the indirect effect. In this case, the latter effect is caused by the water molecules in contact with DNA.

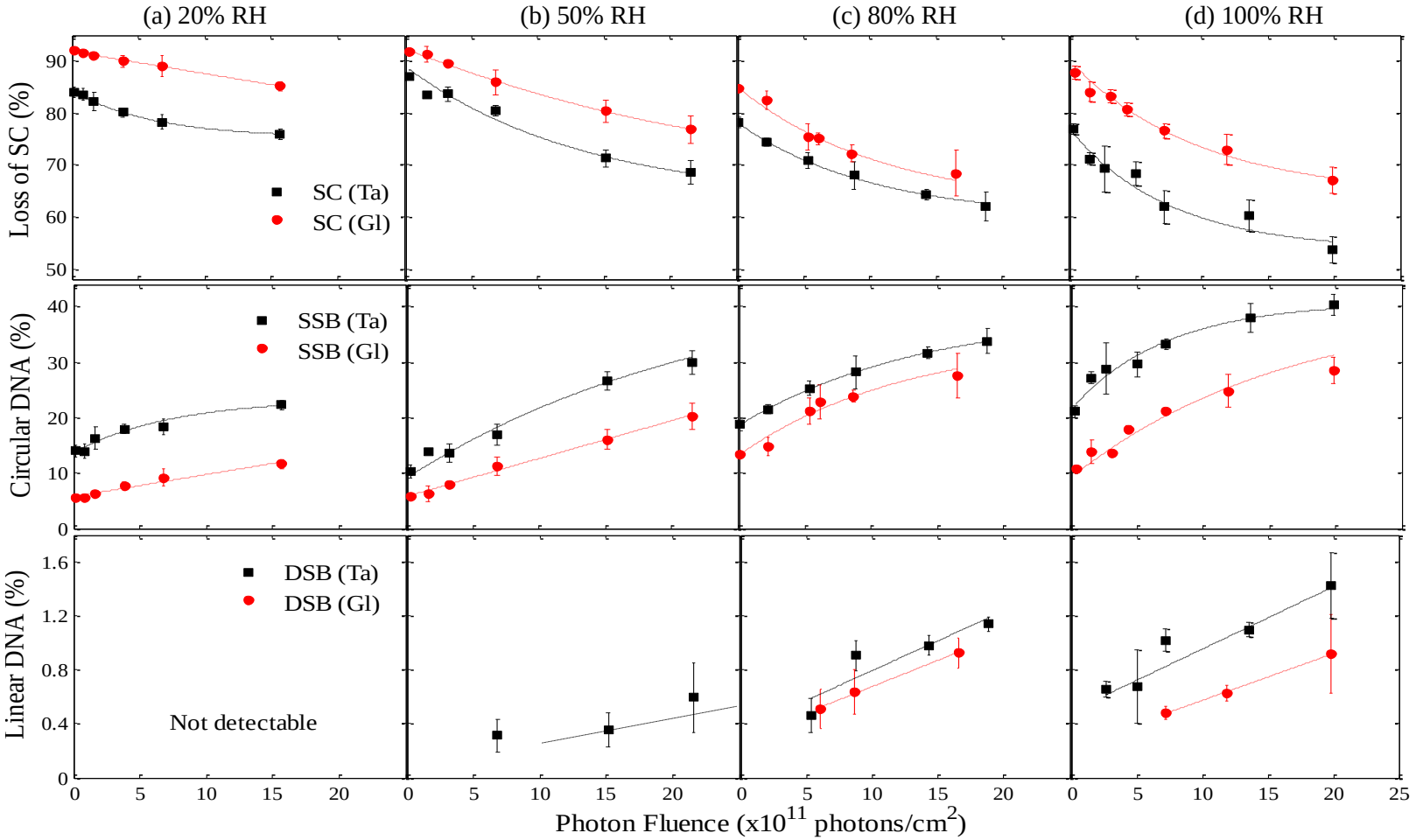

Figure 5.17: Exposure-response curves for loss of SC form (top panel) in plasmid DNA films deposited on tantalum and glass substrates and irradiated by 1.5 keV X-rays under four different hydration level under N_2 atmosphere at STAP: (a) 20% RH, (b) 50% RH, (c) 80% RH, and (d) 100% RH. Also shown, the exposure-response curves for the formation of circular (middle panel) and linear form (bottom panel), caused by SSBs and DSBs, respectively.

Table 5.4: Percentage yield per 10^{12} photons.cm^{-2} for the loss of SC and formation of SSBs and DSBs in films of plasmid DNA under various hydration level (RH %). G values are in nmol/J.

	Humidity	**DNA Form**	Y_{GI}	Y_{Ta}	$EF = Y_{Ta} / Y_{GI}$	G_X	G_{LEE}
Dry DNA	RH 0.0% **Γ = 2.5**	SC	3.6 ± 0.6	4.9 ± 0.7	1.4 ± 0.2	98 ± 20	260 ± 50
		SSB	3.3 ± 0.3	4.5 ± 0.4	1.4 ± 0.2	93 ± 19	248 ± 65
		DSB	ND	ND	-	-	-
First Hydration Layer	RH 20% **Γ = 5 ± 1**	SC	4.6 ± 0.5	5.8 ± 1	1.3 ± 0.3	126 ± 25	247 ± 64
		SSB	3.9 ± 0.3	5.0 ± 1	1.3 ± 0.3	107 ± 21	226 ± 59
		DSB	ND	ND	-	-	-
	RH 50% **Γ = 10 ± 1**	SC	7.0 ± 0.4	8.5 ± 1.6	1.2 ± 0.2	191 ± 38	309 ± 80
		SSB	6.5 ± 0.4	7.5 ± 1	1.1 ± 0.2	178 ± 36	206 ± 54
		DSB	ND	0.1 ± 0.01	-	-	21 ± 5
Second Hydration Layer	RH 80% **Γ = 20 ± 1**	SC	9.0 ± 1.7	11.0 ± 1.4	1.2 ± 0.3	246 ± 49	412 ± 107
		SSB	8.7 ± 1.7	10.0 ± 0.7	1.1 ± 0.2	238 ± 48	268 ± 70
		DSB	0.3 ± 0.02	0.4 ± 0.01	1.3 ± 0.1	8 ± 2	21 ± 5
Bulk Water	RH 100% **Γ = 33± 1**	SC	10.0 ± 1	19 ± 5	2.0 ± 0.5	274 ± 55	1852 ± 482
		SSB	9.0 ± 1	18 ± 5	2.0 ± 0.5	246 ± 49	1852 ± 482
		DSB	0.3 ± 0.02	0.4 ± 0.04	1.3 ± 0.2	8 ± 2	21 ± 5

5.3.2.1. Direct Damage

In accordance with earlier works reported by Cai *et al.*[28] Brun *et al.*[14] and Alizadeh *et al.*[13], our results indicate that LEEs are more efficient than X-ray photons to induce SSBs and DSB damage in DNA. A comprehensive review of the direct mechanisms of damage triggered by LEEs and soft X-rays on plasmid DNA has been provided by Brun *et al.*[14]. Essentially, 1.5 keV X-rays interact with DNA molecules predominantly through the photoelectric effect, producing large amount of photoelectrons and Auger electrons. These fast electrons undergo successive energy losses via, for example, vibrational and electronic excitations or ionization. The latter further generates an electron of increasingly lower energies and a hole. These reactions can

ultimately lead to strand breaks.[2,112] As mentioned before, it takes less energy to break a chemical bond with a LEE than with a photon. In addition, the threshold energy to induce a strand break in DNA with a photon is around 7 eV,[115] whereas LEEs can induce SSBs even at 0.8 eV via dissociative electron attachment (DEA).[10] Boudaiffa *et al.*[9] also demonstrated that LEEs with energies above ~ 5 eV can produce DSBs. It has been shown that strand breaks result from a local interaction, i.e. from DEA involving a basic constituent and not related to the long-range properties of DNA.[116] LEEs predominantly get attached to the nucleobases due to their high electronegativity. The four DNA bases showed clearly the presence of a low-lying shape resonance at subexcitation energies (< 3 eV).[117] The resulting TNIs may loss a hydrogen atom, predominantly from N-H bonds. This reaction initiates chemical modifications that can cause permanent damage in DNA.[121] Additionally, all DNA bases possess core-excited resonances located at electron impact energies above ~ 5 eV. TNIs of DNA bases are prone to transfer the extra electron to the phosphate group, which preferentially occupies an empty σ* orbital of the C-O bond.[118] The resulting state is dissociative, causing the C-O bond rupture, i.e., a SSB. Additionally, experiments with the individual phosphate group showed that incident electrons with energies ~8 eV induce the formation of a dissociative TNI on that subunit.[119] Alternatively, the decomposition of the sugar sub-unit, which is highly sensitive to LEE attack, would result also in a strand break.[121,117] Considering that the energy distribution of the LEEs emitted from the tantalum surface peaks around 1.4 eV, they are expected to induce considerable damage in SC DNA via DEA process. Owing to this dissociative channel, LEEs are more effective than X-ray photons to induce DNA damage: when the same amount of energy is deposited in DNA by photons and LEEs, the latter species produce more damage, as stated by Brun *et al.*[14]

5.3.2.2. Indirect Damage

There are various channels that contribute to the indirect damage when water molecules are present surrounding the DNA. Exposure to high-energy radiation leads to ionization of water molecules, what results in the formation of a water cation and a secondary electron,

$$H_2O \xrightarrow{rad} H_2O^{\bullet+} + SE(e^-)\,. \tag{5.17}$$

Within the primary hydration layer, i.e., the water molecules that are in close contact with DNA, a rapid transfer of electrons and holes from water to DNA can occur, contributing to damage,

$$\mathrm{SE(e^-) + DNA \rightarrow DNA^{\bullet -}; \quad H_2O^{\bullet +} + DNA \rightarrow DNA^{\bullet +}.} \tag{5.18}$$

Additionally, the hydroxyl radical ($OH^{\bullet}$) is generally pointed out as the main responsible for damage enhancement observed in hydrated DNA samples.[2] $OH^{\bullet}$ easily abstracts hydrogen atoms from the DNA sub-units. About 20% of $OH^{\bullet}$ interacting with DNA involve the sugar phosphate, while the remaining $OH^{\bullet}$ radicals get attached to the nucleobases.[120] These reactions produce structural damages and may ultimately lead to SSBs and DSBs in DNA.[2] There are several pathways to the formation of the hydroxyl radicals. As explained in literature,[2,121] $OH^{\bullet}$ can be created from water of hydration by ionizing radiation. The water radical cation ($H_2O^{\bullet+}$) obtained from the reaction (5.17), is a strong acid so that it transfers a proton to a near water molecule, according to the reaction:

$$H_2O^{\bullet+} + H_2O \rightarrow H_3O^{+} + OH^{\bullet} \qquad (5.19)$$

It has been pointed out that H_2O^{+} initially has the structure of a neutral water molecule[122] and therefore it may migrate rapidly by resonant electron transfer with a succession of neighboring water molecules.[123] This gives rise to the following net ionization reaction:

$$2H_2O \rightarrow H_3O^{+} + OH^{\bullet} + e_{aq}^{-} \qquad (5.20)$$

As a second source of $OH^{\bullet}$, one should consider the electronically excited states of water which can be produced both by primary ionizing radiation and the impact of SEs. H_2O^{*} states are prone to dissociate into $H^{\bullet}$ and $OH^{\bullet}$ radicals, i.e., $H_2O^{*} \rightarrow H^{\bullet} + OH^{\bullet}$. Note that the contribution of this channel is smaller compared to that produced by the ionization of water, but it is not negligible.

As can be seen in reaction 5.17, SEs constitute other major product of water ionization. They possess a broad distribution of energies from sub-excitation energies (< 5 eV) up to energies half of the primary radiation. SEs can also react with water molecules surrounding DNA and DNA itself to form free radicals, ions, and LEEs, depending on their energy. Electrons with energies below 15 eV can be captured by a water molecule to form a transient negative anion (TNI) which can dissociate via DEA or dissociative electronic excitation channels. The dominant DEA channel leads to the formation of H^{-} and $OH^{\bullet}$ radicals from dissociation of the $^2B_1$ state of H_2O^{-} at 7-11 eV incident electron energies. Smaller contributions arise from the $^2A_1$ and $^2B_2$ anionic states, which are formed near 9 and 11 eV, respectively.[14] Also above 7 eV, the electronically excited states $^{3,1}B_1$ may dissociate into $H^{\bullet}$ and $OH^{\bullet}$ radicals. Above 10 eV, ionization takes over and becomes the dominant scattering channel.[14]

Present results showed that DNA films deposited in tantalum surface, i.e., exposed to photo-emitted LEEs, suffered larger damage. The just mentioned DEA-H_2O reactions can also be triggered by these LEEs. Hence, at any RH level, larger yields of H^{-}, $H^{\bullet}$ and $OH^{\bullet}$ radicals are

generated in the tantalum samples than in those deposited on glass, which are highly efficient in causing SSBs and DSBs. Our results also indicate that when the bulk-like water layer is added, damage induced on samples deposited on tantalum increases dramatically. This means that the LEE-mediated reactions mentioned before are somewhat less efficient below $\Gamma = 20$ (i.e. within the first and second hydration layer). This behaviour can be attributed to quenching of DEA reactions of DNA sub-units due to the interaction of DNA with H_2O molecules. This effect has been reported before for smaller molecules. For instance, Lu and Sanche[124] reported that DEA resonances at energies ≥ 2 eV visible for CFCs or HCFCs on the Kr surface were almost suppressed when samples where adsorbed on H_2O ice. Similarly, electron-stimulated desorption of O^- from O_2 molecules was strongly suppressed when O_2 were adsorbed on water films.[125] Another possibility is quenching of dissociative electronically excited states of H_2O in contact with DNA. Cho *et al.*[126] reported that the probability to excite the $^{3,1}B_1$ states of H_2O by LEEs was considerably reduced in the presence of thymine. In contrast, within the bulk-like water layer there is no more contact between DNA and H_2O, and therefore DEA reactions and electronically excited H_2O states are no longer quenched, so that the production of H^-, $H^\bullet$ and $OH^\bullet$ radicals via the indirect effect of LEEs increases at 100% RH. However, only 30% of LEEs produced at the tantalum surface in our experiment have energies higher than 7eV.[13] This suggests that there is another source of damage governed by LEEs responsible for the high Y_{Ta} and G_{LEE} in the presence of bulk water.

In the condensed phase, water molecules are collectively capable of trapping electrons via solvation, i.e., the electrons get localized and stabilized in deep traps which are induced by the electrostatic interaction between the electron and the induced and permanent dipoles of the surrounding water molecules.[121] These deep traps that fully solvate the electrons, requires a significant rearrangement of the water molecules until they find the position of lowest energy. However, in the time before becoming solvated, water molecules rest in random arrangements that contain much shallower electron traps, also named precursors states. These states lie just below the conduction band of liquid water (~ -1.5 eV if we take the vacuum level as the zero energy of reference), permitting electron transfer with other quasi-bound electron states of the shallow traps.[121] Moreover, such electron states may occur in the interface between the second hydration layer and the bulk water, as suggested by Siefermann and Abel.[106] The wavefunction of the electron resting in the interface shallow traps is expected to be more extended than the corresponding one in deep traps, so that it could overlap with the wavefunction of the TNIs states of the DNA moieties. Additionally, it is well known that formation of TNIs on adsorbed molecules is not limited exclusively to electrons possessing positive energies. This means that the trapped electron with energies slightly lower than 0 eV can still trigger DEA after rapidly being transferred to a solute molecule, such as a solvated nucleobase. Note also that the

attachment of an electron to a solute molecule depends on the adiabatic electron affinity (AEA) of the molecule. It has been shown that the solvation of DNA molecules modifies their AEA, increasing significantly their ability to capture electrons lower zero.[106,107] Consequently, when a SE confined near DNA reaches a low enough energy to enter an interface trap, it may be scavenged into regions of large electron affinities such as those around nucleobases. A similar phenomena was observed by Wang and Lu,[127] who provided experimental evidence of the transfer of prehydrated electrons to DNA sub-units in aqueous solutions. We have mentioned before that electrons captured by the bases, are susceptible to get transfer to the backbone of the DNA and form a phosphate-centred radical anion.[11] If the resulting anion state is dissociative it causes a SSB and the overall reaction is called dissociative electron transfer (DET). This process is essentially the same as DEA with the difference that DET involves an electron transfer between two localized quantum states.[121] Such reaction has been already observed in electron impact experiments on dry films of DNA,[128] resulting also in a strand break.

5.4. Summary

In this Chapter we have presented an investigation into the damage induced by either ionizing radiation or LEEs in molecules of biological interest under different environmental conditions. The overall goal of this investigation was to differentiate the portion of DNA damage caused by high-energy radiation from that induced by LEE-mediated reactions. Additionally, we have provided a study of the relative contribution of the direct and indirect modes of damage caused by LEEs in an aerobic and hydrated environment.

Present results indicate that exposure of DNA molecules (or DNA sub-units) to either ionizing radiation or LEEs, both lead to a similar profile of radiation-products. However some quantitative differences were detected; under identical experimental conditions, LEEs were considerably more efficient than 1.5 keV X-ray radiation at inducing larger yields of damage. In other words, when the same amount of energy is deposited in DNA by both X-rays and LEEs, the latter species induce more damage.[14] Although both types of radiation induce similar radical intermediates and pathways of damage, the initial mechanisms are significantly different: whereas high-energy radiation involves one-electron ionization, LEEs initiate the formation of the different radiation products via a subionization process, i.e., DEA.

In an attempt to provide insight into the radiosensitization mechanism of O_2, a novel technique has been employed to investigate DNA damage in ambient conditions. Thin films of thymidine were exposed to 1.5 keV X-rays and photo-emitted LEEs under pure dry N_2 and O_2 atmospheres. LC-MS/MS analysis revealed, firstly, that LEEs enhance the loss of unaltered thymidine by a factor of 1.8 relative to X-rays, being particularly efficient at inducing free

thymine and 5,6-DHThd products. On the other hand, it was found (see yields of damage and G values in Table 5.3) that free thymine, 5-HMdUrd and 5-FordUrd were produced at a level that is approximately 3-fold higher in the presence of O_2 than under a N_2 atmosphere. This is because a larger amount of radicals and ions are formed due to the interaction of radiation with O_2 than N_2, and, further to this, they are considerably more reactive than those generated under N_2. Additionally, O_2 can react with C-centred radicals, thereby fixing the damage. O_2 reacts rapidly with C-centred radicals, thereby fixing the damage. In contrast, no 5,6-DHThd was detected when samples were irradiated under an O_2 atmosphere, indicating that O_2 molecules react with the intermediate radical compound inhibiting the pathway to the formation of 5,6-DHThd.

Finally, we have reported the effect of the DNA hydration level on damage yields induced by soft X-rays and photo-emitted low-energy electrons (LEEs) in thin films of plasmid DNA irradiated under N_2 at ambient pressure and different humidity levels, from 0 to 100% RH (Γ = 2.5 to 33, respectively). Our results showed that DNA damage induced by LEEs and X-rays increases slightly with the level of hydration until the second hydration shell is formed ($\Gamma \leq 20$). Then, the damage induced in DNA by LEEs alone increases dramatically as the hydration level reached the bulk-like conditions (i.e., Γ = 33). This means that the contribution of LEEs to indirect DNA damage arises principally from the molecules that constitutes the bulk-like water layer rather than from the water molecules that are in contact with DNA. This behaviour can be explained essentially by two mechanisms: (1) quenching of dissociative electron attachment to DNA and quenching of dissociative electronically excited states of H_2O in contact with DNA within the first and second layer of hydration. In contrast, within bulk water, these dissociative reactions are enhanced and produce large quantities of H^-, $OH^\bullet$ and $H^\bullet$ radicals. (2) Due to the modification of the AEAs of the DNA bases in bulk water, electrons captured in water-interface shallow traps may rapidly transfer to the bases of solvated DNA to form transient anions. Subsequently these anions undergo dissociation or may transfer the excess electron to the phosphate group, ultimately leading to a strand break.

Bibliography

[1] C. von Sonntag, *Free-Radical-Induced DNA Damage and its Repair, A Chemical Perspective* (Springer-Verlag, Berlin Heidelberg, 2006).

[2] S. Uehara, H. Nikjoo and D.T. Goodhead, *Radiat. Res.* ***152***, 202 (1999).

[3] M.D. Sevilla and W.A. Bernhard, *Mechanisms of Direct Radiation Damage to DNA. Radiation Chemistry, from Basics to Applications in Material and Life Sciences* (EDP Sciences, France, 2008).

[4] E.L. Alpen, *Radiation Biophysics*, (Prentice-Hall, Inc.: New Jersey, 1990).

[5] P. O'Neill, *Radiation-induced damage in DNA* In *Radiation Chemistry: Present Status and Future Trends* (Elsevier Science: Amsterdam, 2001).

[6] S.M. Pimblott and J.A. LaVerne, *Radiat. Phys. Chem.* **76**, 1244 (2007).

[7] Y. Park, Z. Li, P. Cloutier, L. Sanche and J.R. Wagner, *Rad. Res.* **175**, 240 (2011).

[8] H. Abdoul-Carime, S. Gohlke, E. Fischbach, J. Scheike and E. Illenberger, *Chem.Phys. Lett*. **387**, 267 (2004).

[9] B. Boudaïffa, P. Cloutier, D. Hunting, M. A. Huels and L. Sanche, Science **287**, 1658 (2000).

[10] F. Martin, P.D. Burrow, Z. Cai, P. Cloutier, D. Hunting and L. Sanche, *Phys. Rev. Lett.* **93**, 068101 (2004).

[11] Y. Zheng, P. Cloutier, D.J. Hunting, L. Sanche and J.R. Wagner, *J. Am. Chem. Soc.* **127**, 16592 (2005).

[12] J. Simons, *J. Acc. Chem. Res*. **39**, 772 (2006).

[13] E. Alizadeh, P. Cloutier, D. Hunting and L. Sanche, *J. Phys. Chem. B* **115**, 4523 (2011).

[14] É. Brun, P. Cloutier, C. Sicard-Roselli, M. Fromm and L. Sanche, *J. Phys. Chem. B* ***113***, 10008 (2009).

[15] E. Alizadeh, A.G. Sanz, G. García and L. Sanche, *J. Phys. Chem. Lett.* **4**, 820 (2013).

[16] S. Ptasińska, S. Denifl, S. Gohlke, P. Scheier, E. Illenberger and T.D. Märk, *Angew. Chem. Int. Ed.* **45**, 1893 (2006).

[17] I. Bald, I. Dąbkowska and E. Illenberger, *Angew. Chem. Int. Ed.* **47**, 8518 (2008).

[18] I. Bald, H.D. Flosadóttir, B. Ómarsson and O.Ingolfsson, *Int. J. Mass Spectrom.* **313**, 15 (2012).

[19] Y. Zheng, P. Cloutier, D.J. Hunting, J.R. Wagner and L. Sanche, *J. Am. Chem. Soc.* **126**, 1002 (2004).

[20] Z. Li, Y. Zheng, P. Cloutier, L. Sanche and J.R. Wagner, *J. Am. Chem. Soc.* **130**, 5612 (2008).

[21] W.A. Kibbe. *OligoCalc: an online oligonucleotide properties calculator*. Nucleic Acids Res. **35** (2007).

[22] N. Mirsaleh-Kohan, A. Bass and L. Sanche, *J. Chem. Phys.* **134**, 015102 (2011).

[23] ChemSpider. *The free chemical database*. http://www.chemspider.com/

[24] B. Boudaiffa, P. Cloutier, D. Hunting, M.A. Huels and L. Sanche, *Radiat. Res.* **157**, 227 (2002).

[25] R. Panajotovic, F. Martin, P.Cloutier, D. Hunting, and L. Sanche, *Radiat. Res*. 165, 452 (2006).

[26] M. Rezaee, P.Cloutier, A.D. Bass, M.Michaud, D.J. Hunting and L. Sanche, *Phys. Rev. E* **86**, 031913 (2012).

[27] L. Sanche, *Mass Spect. Rev*. **21**, 349 (2002).

[28] Z. Cai, P. Cloutier, D. Hunting and L. Sanche, *J. Phys. Chem. B* **109**, 4796 (2005).

[29] J.A. LaVerne and S.M. Pimblott, *Radiat. Res.* **141**, 208 (1995).

[30] Y. Park, A.R. Peoples, G.S. Madugundu, L. Sanche and J.R. Wagner, *J. Phys. Chem. B* **117**, 10122 (2013).

[31] C. Winstead, V. McKoy and S. d'Almeida Sanchez, *J. Chem. Phys.* **127**, 085105 (2007).

[32] L.D. Skarsgard and I. Harrison, *Radiat. Res.* **127**, 243 (1991).

[33] S. Lehnert. *Biomolecular Action of Ionizing Radiation*; Taylor & Francis, New York, London (2008).

[34] M. Quintiliani. *Int. J. Radiat. Biol*. **50**, 453 (1986).

[35] E. Alizadeh and L. Sanche, *Rad. Phys. Chem.* **81**, 33 (2012).

[36] M. Hoshi, D.T. Goodhead, D.J. Brenner, D.A. Bance, J.J. Chmielewski, M.A. Paciotti and J.N. Bradbur, *Phys. Med. Biol*. **30**, 1029 (1985).

[37] A. Dumont, Y. Zheng, D. Hunting and L. Sanche, *J. Chem. Phys.* **132**, 045102 (2010).

[38] M.A. Huels, B. Boudaïffa, P. Cloutier, D. Hunting and L. Sanche. *J. Am. Chem. Soc*. **125**, 4467 (2003).

[39] Z. Cai, X. Pan, D. Hunting, P. Cloutier, R. Lemay and L. Sanche, *Phys. Med. Biol*. **48**, 4111 (2003).

[40] ImageJ software (http://rsb.info.nih.gov/ij/).

[41] National Institute of Standards & Technology, NIST, http://physics.nist.gov/PhysRefData/XrayMassCoef/.

[42] S. Frelon, T. Douki, J.L. Ravanat, J.P. Pouget, C.Tornabene and J. Cadet, *Chem. Res. Toxicol*. **13**, 1002 (2000).

[43] F. Samson-Thibault, G.S. Madugundu, S. Gao, J. Cadet and J.R. Wagner, *Chem. Res. Toxicol*. **25**, 1902 (2012).

[44] Farhataziz and M.A.J. Rodgers, *Radiation Chemistry, Principles and Applications* (VCH: New York, NY, 1987).

[45] E. Alizadeh and L. Sanche, *J. Phys. Chem. B* **115**, 14852 (2011).

[46] K.K. Sharma, S. Purkayastha and W.A. Bernhard, *Radiat. Res.* **167**, 501 (2007).

[47] G.S. Madugundu, Y. Park, L. Sanche and J.R. Wagner, *J. Am. Chem. Soc*. **134**, 17366 (2012).

[48] S.A.S. Audat, C.T. Love, B.A.S. Al-Qudat and A.C.J. Bryant-Friedrich, *Org. Chem.* **77**, 3829 (2012).

[49] D.M. Close, *Radiat. Res.* **135**, 1 (1993).

[50] K. Fujii, K. Akamatsu and A. Yokoya, *Radiat. Res.* **161**, 435 (2004).

[51] M.J. Berger, J.H. Hubbell, S.M. Seltzer, J. Chang, J.S. Coursey, R. Sukumar, D.S. Zucker and K. Olsen, *XCOM: Photon Cross Sections Database. NIST* (1998).

[52] S.M. Pimblott and L.D. Siebbeles, *Nucl. Instrum. Methods Phys. Res., Sect. B* **194**, 237 (2002).

[53] H. Abdoul-Carime, S. Gohlke and E. Illenberger, *Phys. Rev. Lett.* **92**, 168103 (2004).

[54] S. Denifl, S. Ptasińska, M. Probst, J. Hrusak, P. Scheier and T. D. Mark, *J. Phys. Chem. A* **108**, 6562 (2004).

[55] S. Denifl, P. Sulzer, F. Zappa, S. Moser, B. Krautler, O. Echt, D. K. Bohme, T. D. Mark and P. Scheier, *Int. J. Mass Spectrom.* **277**, 296 (2008).

[56] S. Ptasińska, S. Denifl, V. Grill, T. D. Märk, E. Illenberger and P. Scheier, *Phys. Rev. Lett.* **95**, 093201 (2005).

[57] S. Ptasińska, S. Denifl, P. Scheier, and T.D. Mark, *J. Chem. Phys.* **120**, 8505 (2004).

[58] S. Ptasińska, S. Denifl, V. Grill, T.D. Märk, P. Scheier, S. Gohlke, M.A. Huels and E. Illenberger, *Angew. Chem., Int. Ed.* **44**, 1647 (2005).

[59] Y. Park, H. Cho, L. Parenteau, A. D. Bass and L. Sanche, *J. Chem. Phys.* **125**, 074714 (2006).

[60] Y. Zheng, J.R. Wagner and L. Sanche, *Phys. Rev. Lett.* **96**, 208101 (2006).

[61] Y. Zheng, P. Cloutier, D. Hunting, J. R. Wagner and L. Sanche, *J. Chem. Phys.* **124**, 064710 (2006).

[62] A.A. Radtsig and B.M. Smirnov, *Reference Data on Atoms, Molecules, and Ions*; (Énergoatomizdat, Moscow,1986; Springer-Verlag, Berlin, 1985).

[63] E. Krishnakumar and S.K. Srivastava, *J. Phys. B* **21**, L607 (1988).

[64] Y. Itikawa, *J. Phys. Chem. Ref. Data* **35**, 1 (2006).

[65] C. Tian and C.R. Vidal, *Phys. B: At. Mol. Opt. Phys.* **31**, 5369 (1998).

[66] (a) R.J. Van Brunt, F.W. Powell, R.G. Hircsh and W.D. Whitehead. *J. Chem. Phys*. **57**, 3120 (1972). (b) N. Zavilopulo, F.F. Chipev, and O.B. Shpenik. *Tech. Phys*. **50**, 402 (2005).

[67] J. Mazeau, F. Gresteau, R.I. Hall and A. Huetz, *J. Phys. B: Atom. Molec. Phys., Vol.* **11**, 18 (1978).

[68] M.A. Huels, L. Parenteau, M. Michaud and L. Sanche, *L. Phys. Rev. A* **51**, 337 (1995).

[69] Y. Itikawa, *J. Phys. Chem.* Ref. Data Vol. **38**, 1 (2009).

[70] D. Rapp and D.D. Briglia, *J. Chem. Phys.* **43**, 1480 (1965).

[71] D. Galuska, D. Manole, R. Vladoiu, S. Matejcik and J.D. Skalny, *J. Optoelectron. Adv. Mater* **7**, 2371 (2005).

[72] H. Nikjoo and L. Lindborg, *Phys. Med. Biol.* **55**, 65 (2010).

[73] M.A. Huels, L. Parenteau, M. Michaud and L. Sanche, *Phys. Rev. A* **51**, 337 (1995).

[74] H.Wiseman and B.Halliwell, *Biochem. J.* **313**, 17 (1996).

[75] E.J. Hall and A.J. Giaccia, *Radiobiology for the Radiologist* (Lippincott Williams & Wilkins, Philadelphia, USA 2006).

[76] E. Itälä, K. Kooser, T. Hägerth, E. Rachlew, M.A. Huels and E. Kukk, *J. Phys. Conf. Ser*. **388**, 022078 (2012).

[77] H. Levola, K. Kooser, E. Rachlew, E. Nommiste and E. Kukk, *Int. J. Mass Spect.* (http://dx.doi.org/10.1016/j.ijms.2013.08.008)

[78] Y. Razskazovskiy, M.G. Debije and W.A. Bernhard, *Radiat. Res.* **153**, 436 (2000).

[79] S.G. Swarts, M. Sevilla, D. Becker, C.J. Tokar and K.T. Wheeler, *Radiat. Res.* **129**, 333 (1992).

[80] A.K. Hoffmann and J. Hüttermann, *Int. J. Radiat. Biol.* **72**, 735 (1997).

[81] D.J. Deeble, D. Schulz and C. Von Sonntag, *Int. J. Rad. Biol.* **49**, 915 (1986).

[82] X. Li, L. Sanche L, Sevilla MD, Radiat. Res. 165, 721 (2006).

[83] P.C. Dedon, *Chem. Res. Toxicol.* **21**, 206 (2008).

[84] G.A. Russell, *J. Am. Chem. Soc.* **79**, 3871 (1957).

[85] A.A. Kuznetsova, D.G. Knorre and O.S. Fedorova, *Russ. Chem.Rev.***78**, 659 (2009).

[86] W. S. Lin, F. Wong and R. Anderson, *Bioch. Biophys. Res. Commun.* **147**, 778 (1987).

[87] J. Cadet and R. Teoule, *Int. J. Radiat. Biol.* **2**, 119 (1975).

[88] J. Cadet, T. Douki, D. Gasparutto, J.L. Ravanat and J.R. Wagner, *Encyclopedia of Radicals in Chemistry, Biology and Materials* (John Wiley & Sons, 2012).

[89] T. Douki, T. Delatour, F. Paganon and J. Cadet, *Chem. Res. Toxicol.* **9**, 1145 (1996).

[90] S.G. Swarts, D. Becker, M. Sevilla and K.T. Wheeler, *Radiat. Res.* **145**, 304 (1996).

[91] K. Akamatsu, K. Fujii and A. Yokoya, *Radiat. Res.* **161**, 442 (2004).

[92] C. Decarroz, J.R. Wagner, J.E. van Lier, C.M. Krishna, P. Riesz and J. Cadet, *Int. J. Radiat. Biol.* **50**, 491 (1986).

[93] J.R. Wagner, J.E. van Lier, M. Berger and J. Cadet, *J. Am. Chem. Soc.* **116**, 2235 (1994).

[94] G. Lin and L. Li, *Ang. Chem. Int. Ed.* 52, 5594 (2013).

[95] W. Wang and M.D. Sevilla, *Radiat. Res.* **138**, 9 (1994).

[96] J.T. Lett and P. Alexander, *Radiat. Res.* **15**, 159 (1961).

[97] D. Becker and M.D.Sevilla, *Adv. Radiat. Biol.* **17**, 121 (1993).

[98] K.F. Baverstock and S.Will, *Int. J. Radiat. Biol.* **55**, 563 (1989).

[99] T. Ito, S.C. Baker, C.D. Stickley, J.G. Peak and M.J. Peak, *Int. J. Radiat. Biol.* ***63***, 289 (1993).

[100] A. Yokoya, S.M.T. Cunniffe and P. O'Neill, *J. Am. Chem. Soc.* **124**, 8859 (2002).

[101] C. Chatgilialoglu and P. O'Neil, *Exp. Gerontol.* **36**, 1459 (2001).

[102] W.C. Simpson, T.M. Orlando, L. Parenteau, K. Nagesha and L. Sanche, *J. Chem. Phys.* **108**, 5027 (1998).

[103] M. Michaud, P. Cloutier and L. Sanche, *Phys.Rev. Lett.* **44**, 5624 (1991).

[104] R.S. Smith, N.G. Petrik, G.A. Kimmel and B.D. Kay, *Acc. Chem. Res.* **45**, 33 (2012).

[105] S. Ptasińska and L. Sanche, *Phys. Rev.* **75**, 030915 (2007).

[106] T.M. Orlando, D. Oh, Y. Chen and A.B. Aleksandrov, *J. Chem. Phys.* **128**, 195102 (2008).

[107] G.A. Grieves, J.L. McLain and T.M. Orlando, *Charged Particle and Photon Interactions with Matter, Recent Advances, Applications, and Interfaces*. (Ed. Y. Hatano, Y. Katsumura and A. Mozumder, CRC Press: Boca Raton, FL 2011).

[108] K.R. Siefermann and B. Abel, *Angew. Chem. Int. Edit.* **50**, 5264 (2011).

[109] M. Smyth and J. Kohanoff, *Phys. Rev. Lett.* **106**, 238108 (2011).

[110] QIAprep Miniprep Handbook, www.qiagen.com.

[111] K.L. Manchester, *Biotechniques* **20**, 968 (1996).

[112] R.L.P. Adams, T. Knowler and D.P. Leader, *The Biochemistry of the Nucleic Acids*, (Chapman & Hall, 10th edn, 1986).

[113] H.B. Michaels and J.W. Hunt, *Radiat. Res.* **74**, 23 (1978).

[114] C. von Sonntag, *The Chemical Basis for Radiation biology* (Taylor and Francis: London, U.K. 1987).

[115] T. La Vere, D. Becker and M.D. Sevilla, *Radiat. Res.* **145**, 673 (1996).

[116] W. Wang, D. Becker and M.D. Sevilla, *Radiat. Res.* **135**, 146 (1993).

[117] M. Folkard, K.M. Prise, B. Vojnovic, B. Brocklehurst and B.D. Michael, *Int. J. Radiat. Biol*. **76**, 763 (2000).

[118] L.G. Caron and L. Sanche, *In Low-energy Electron Scattering from Molecules, Biomolecules and Surfaces*, (Ed. P. Čársky and R. Čurík, CRC; PressTaylor and Francis Group: Boca Raton, FL 2012).

[119] X. Pan and L. Sanche, *Chem. Phys. Lett*. **421**, 404 (2006).

[120] W.A. Bernhard and D.M. Close, In *Charged Particle and Photon Interactions with Matter, Chemical, Physicochemical, and Biological Consequences with Applications*, (Ed. A. Mozumder, Y. Hatano, Marcel Dekker, Inc.: New York, NY, 2004).

[121] W.H. Hamill, *J. Phys. Chem.* **73,** 1341 (1969).

[122] E. Alizadeh and L. Sanche, *Chem. Rev*. **112**, 5578 (2012).

[123] V. De Waele, I. Lampre and M. Mostafavi, *In Charged Particle and Photon Interactions with Matter, Recent Advances, Applications, and Interfaces*. (Ed. Y. Hatano, Y. Katsumura, A. Mozumder. CRC Press: Boca Raton, FL, 2011).

[124] Q-B. Lu and L. Sanche, *J. Chem. Phys.* **120**, 2434 (2004).

[125] R. Azria, Y. Le Coat, M. Lachgar, M. Tronc, L. Parenteau and L. Sanche, *Surf. Science* **451**, 91 (2000).

[126] W. Cho, M. Michaud and L. Sanche, *J. Chem. Phys.* **121**, 11289 (2004).

[127] (a) C.R.Wang and Q.B. Lu, *Angew. Chem., Int. Ed.* **46**, 6316 (2007); (b) C.R.Wang, J. Nguyen and Q.B. Lu, *J. Am. Chem. Soc.* **131**, 11320 (2009).

[128] L. Sanche, *In Radical and Radical Ion Reactivity in Nucleic Acid Chemistry* (Ed. M.M. Greenberg, John Wiley and Sons: New Jersey, NJ, 2009).

Chapter 6

New Design of Experimental System

As we saw in Chapter 4, our Monte Carlo code (LEPTS) provides valuable information about radiation transport in biologically relevant materials. Partial validation of the model has been provided by some gas phase experiments based on determinations of macroscopic parameters as the stopping power.[1,2] However, current biomedical applications require validated models in the condensed phase.

This situation, together with the experience acquired through the joint experiments at the *Université de Sherbrooke* (see Chapter 5), motivated the design and construction of a new experimental setup. The whole project was conducted at the Radiation-Matter Interaction Laboratory (Instituto de Física Fundamental-CSIC) in collaboration with the National Laboratory for Nuclear Fusion-CIEMAT in Madrid. The apparatus will allow the radiation-induced damage in condensed biomolecular systems under different, well-controlled experimental conditions to be evaluated and ultimately may help to validate radiation interaction models in the condensed phase.

The design and calibration of the main components of the experimental system are detailed below, followed by a description of some preliminary experimental tests.

6.1. Design and Technical Characteristics

The experimental setup presented in this chapter has been designed with the intention of being highly versatile and portable, so that it can be transported to different research facilities to irradiate condensed samples using different primary beams (photons, electrons or ions). A schematic diagram of the system is shown in Figure 6.1(a), and a photograph of the actual setup can be seen in Fig. 6.1(b). The apparatus consists of an ultra-high vacuum (UHV) chamber of relatively small dimensions (see Section 6.1.1) equipped with an externally controlled sample holder that enables the condensation of biomolecular targets on metallic surfaces. This configuration generates secondary electrons (SEs) close to the samples when the underlying metal substrate is irradiated by primary radiation (see Chapter 5). The experimental procedure is based on the spectroscopic analysis of the primary beam before and after the interaction with the target, together with an energetic and angular analysis of the secondary species produced (electrons and ions). This is accomplished by means of an appropriate set of spectrometers, namely, a silicon detector and a hemispherical electrostatic analyser mounted on a [horizontal] revolving plate together with a fixed time of flight spectrometer.

Various components were specifically designed by us to meet the specifications of the chamber. In particular, the electron gun, the sample-holder, the silicon detector assembly including an external liquid nitrogen cold finger, a housing structure for radioactive sources and a focusing lens system for the hemispherical electrostatic analyser were designed using 3D mechanical CAD software (SolidWorks, Dassault Systems, France) and built in our engineering workshops (IFF-CSIC and CIEMAT). All of the materials used in these components are suitable for ultra-high vacuum purposes, i.e., stainless steel, duralumin, machineable ceramics (Macor®) and glass.

6.1.1. UHV Collision Chamber

The collision chamber is formed by a stainless steel tube of 30 cm length and 25 cm in diameter, equipped with several lateral exits of different dimensions which point radially towards the centre. Among these exists, there are two flanges, DN65 CF (conFlat) and DN100 CF, placed facing oppositely to each other. There are six more flanges, DN40 CF, forming three opposing pairs distributed at angles of 45° in between the DN65-DN100 pair. A glass viewing port is attached to the main chamber through the DN100 CF flange, providing direct visual inspection inside the vacuum vessel when experiments are running. The DN40 CF flanges hold the high-voltage feedthroughs required by the detectors, the TOF equipment, the ionization gauges and the electron gun. The chamber contains a revolving plate, which can be controlled externally and holds the electron spectrometers. The whole experimental setup is supported by

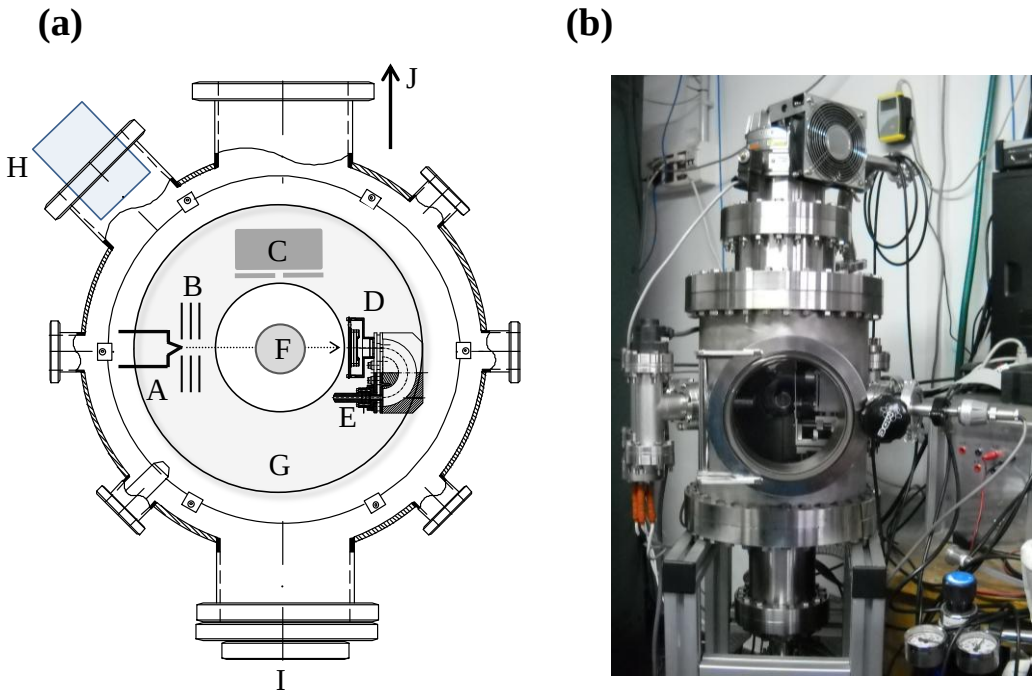

Figure 6.1: (a) Sketch of the present experimental apparatus (horizontal plane view): (A) electron emitting filament, (B) extraction and acceleration electrodes, (C) Silicon detector, (D) hemispherical electrostatic energy analyser, (E) channel electron multiplier (F) sample-holder, (G) externally-controlled rotatable plate, (H) TOF analyser, (I) glass view-port, (J) dry scroll and turbomolecular pump. (b) Photograph of the complete experimental setup.

an aluminium structure situated on a wheeled platform in order to facilitate the system's mobility.

The chamber is pumped by a combined dry scroll pump (Varian SH-110, Italy) with a turbomolecular pump (Varian V-301, Italy) system to reach a background pressure of the order of 10^{-9} Torr, as measured by a Bayard-Alpert ionization gauge (Varian UHV-24, Italy).

6.1.2. Sample-holder

We have also designed a new sample holder which is placed along the central axis of the chamber and aligned with the spectrometers on the same horizontal plane. A high purity gold mono-crystal (Au(1,1,1,)) was used as a substrate for the condensation of the molecules of interest. Various techniques exist to deposit biological compounds on metal surfaces, for example, vapour condensation, molecular self-assembly, sublimation and freeze drying,[3] of which the former is the most suitable technique for our portable chamber.

A schematic diagram of the whole sample-holder is given in Figure 6.2(a) together with a photograph of the substrate-housing (Figure 6.2b). The substrate is placed in a vertical plane

over the entrance to the molecular target (1). An effusive molecular beam is formed in a stainless steel hollow chamber (2) equipped with heating (filament) (3) and cooling (liquid N_2) circuits. Solid targets are placed inside the hollow chamber and heated to vaporization. In the case of gas-phase samples, they flow through two stainless steel pipes (4) from a source external to the chamber up to the substrate up to the substrate. The molecular vapours are then condensed on the surface of the substrate by controlling the temperature with the cooling and heating systems. The cooling system consists of two parallel single-pass-feedthroughs (5), with thermal and electrical insulation (6), which are externally connected to a liquid N_2 reservoir. A detachable tube (7) connects the feedthroughs with the substrate housing (2). The different pieces are joined together by means of commercially available fittings (Swagelok®) (8). Finally, the temperature of the substrate housing chamber is externally controlled with a thermocouple (9). The sample holder is completely hermetic and may be handled externally, so that the solid samples are formed under UHV conditions. This procedure helps to minimize sample contamination.

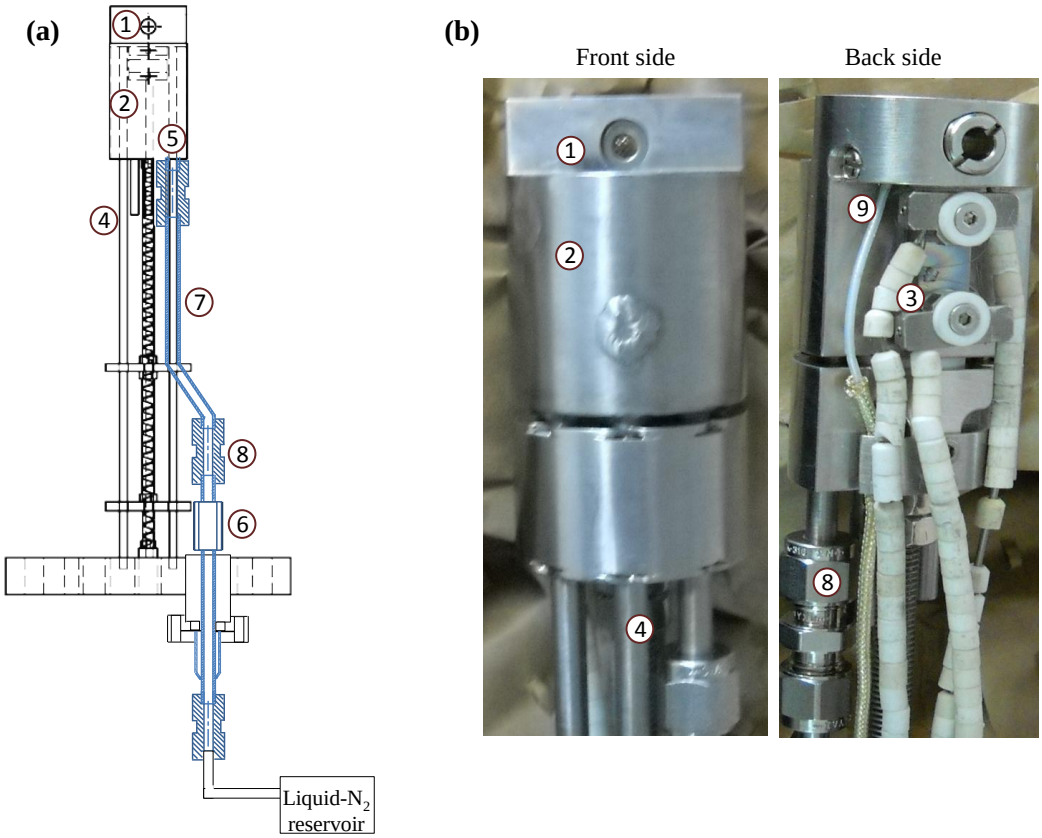

Figure 6.2: (a) Schematic diagram of the sample-holder. (b) Photograph of the substrate-housing. (see text for further details).

6.1.3. Electron Gun

The purpose-built electron gun is formed from a hairpin tungsten filament and four 4 mm thick electrodes each separated by 2 mm long "Macor®" insulators. The first electrode possesses a conical central aperture, with internal and external openings of 3 mm and 1 mm, respectively, through which the filament tip enters. The remaining electrodes also have central apertures of 1 mm in diameter. Electrons are generated by thermionic emission from the filament which is heated by a power supply (Isotech IPS1810, UK). The negative terminal of the filament is in turn connected to a negative HV source (Bertan 205B, USA). These electrons are extracted through an extraction potential (V_{ext}) applied to the first electrode. Subsequently, they are collimated and focused (V_f) by the remaining electrodes, the last of which is grounded. As a result, an electron beam of ~1 mm in diameter is generated with typical beam currents in the range of μA and an energy spread of about 0.8 eV. A schematic draw of the electron gun and the electrical connections is shown in Figure 6.3.

This electron gun can be employed as a source of primary fast electrons or to calibrate the detectors. It is incorporated into the chamber through one of the DN40 CF flanges. The distance between the gun and the detector can be externally adjusted using a telescopic extension tube.

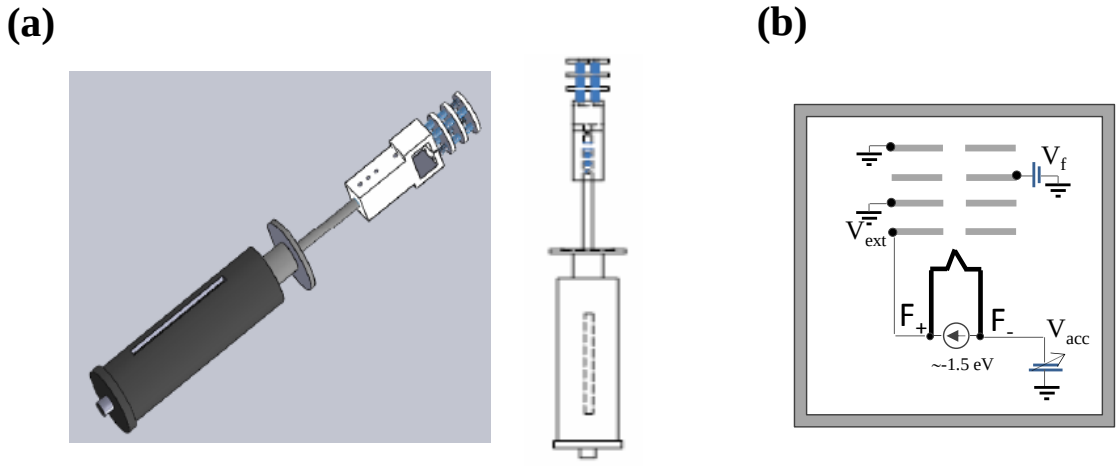

Figure 6.3: (a) Schematic draw and (b) electrical connections of the electron gun.

6.1.4. Silicon detector

A flexible duralumin assembly has been constructed for the silicon detector (see Figure 6.3a). The assembly is fully mobile and detachable. Hence, it can be placed at any position on the revolving plate (except for the location of the hemispherical electrostatic analyser) whilst also permitting movement in the vertical plane. Moreover, we also wanted to be flexible in terms of energy, hence an additional detachable piece was designed for the connection of up to four silicon detectors. Additionally, a custom-built liquid nitrogen storage vessel (Dewar) has been constructed to improve sensitivity of the detector (see Figure 6.3b) by reducing the thermal noise.

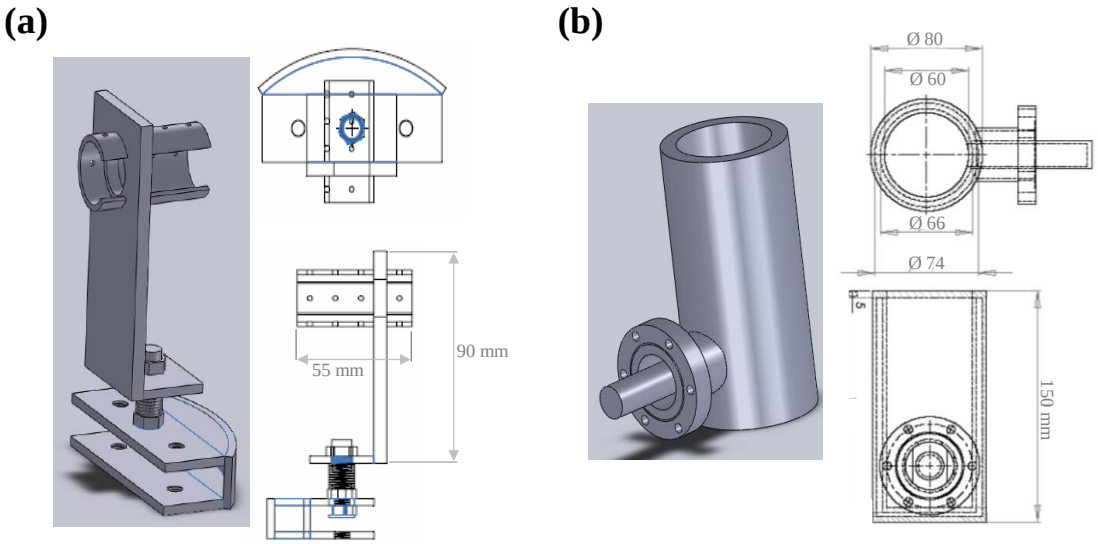

Figure 6.4: (a) Schematic draw of the silicon detector assembly and (b) the liquid nitrogen dewar.

The silicon (Si) detector itself (Ortec, USA) has a thickness of 1.008 mm thickness and an effective area of 50 mm^2. It is operated in pulse-height mode. Once the biased Si detector detects a particle (V_{bias}=~140 eV; MHV-4, Mesytec, Germany), the signal is processed by a set of electronic units. Firstly, the electron current pulses reach a charge sensitive preamplifier which outputs positive voltage pulses. These are integrated to yield a Gaussian signal and then amplified to the appropriate levels of detection (0.5 – 5 V). In this case, both stages are performed by a compact unit (MSI-8, Mesytec, Germany).The resulting pulses are collected by a pulse-height analyser (PHA; Toivel, Bulgary), which then converts the analogue signal into a digital signal (ADC) and samples the pulses into different bins (8192 channels) according to their height (energy). The output of the ADC/PHA is transferred to a PC where SpectLab (Toivel, Bulgary) software finally stores and displays the spectrum. The linearity of the ADC/PHA was verified for different input voltages ranging from 0 to 5 eV (see Figure 6.5(a)).

As an example, Figure 6.6(b) shows a calibration spectrum for the radioactive source ^{137}Cs, in which can be appreciated the beta continuum together with a small peak that corresponds to internal conversion electrons from the K shell (624 keV).

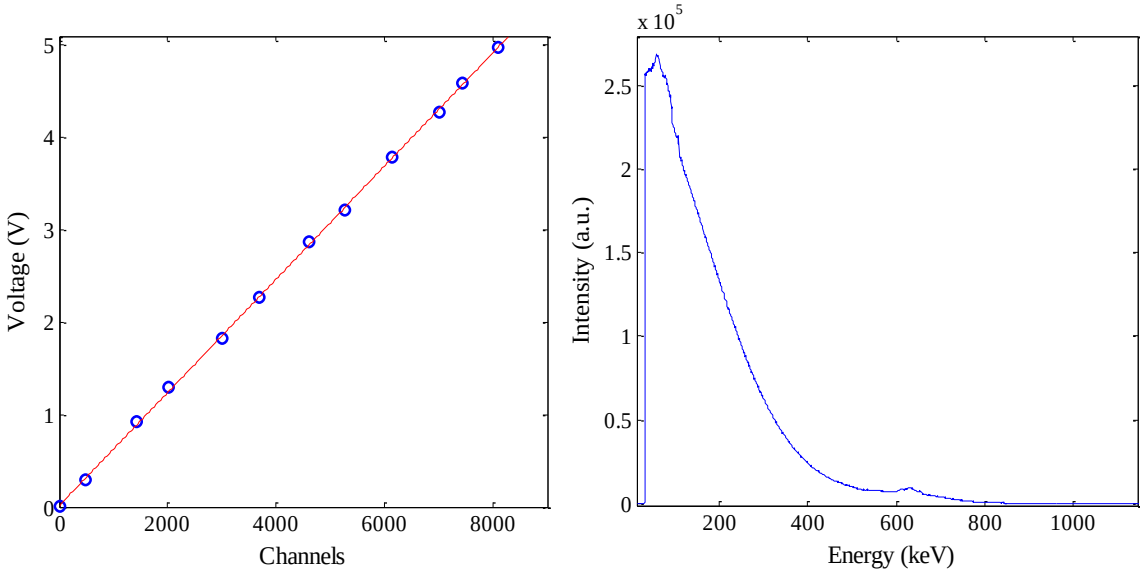

Figure 6.5: (a) Calibration voltage-to-channels of the ADC/MCA. (b) ^{137}Cs spectrum obtained with the silicon detector.

6.1.5. Hemispherical Electrostatic Analyser

To measure low-energy electrons (typically below 10 keV) a hemispherical electrostatic analyser with a two-stage microchannel plate detector has been incorporated. The analyser is electrically shielded to avoid stray fields and the entrance is equipped with a lens focusing system.

The spectrometer is used to disperse electrons as a function of their kinetic energy. It consists of two concentric duralumin hemispheres, commonly referred to as the inner and outer plates, respectively. The inner hemisphere is biased positively with respect to the outer hemisphere so that electrons entering the analyzer are forced to follow a curved path by an electrostatic field. For a constant voltage difference between the hemispheres (ΔV_p), only electrons with a certain energy (E_o), the so-called "pass energy", will pursue a circular path along the mean radius ($R_o = (R_1+R_2)/2$) semi-circle to reach the detector. Hence, this type of spectrometer is characterized by a geometrical factor (C_g), which relates ΔV_p to E_o according to:

$$E_o = C_g \Delta V_p \, . \tag{6.1}$$

The geometrical factor associated with the present spectrometer was determined to be $C_g = 0.8$, as can be seen in Figure 6.6a.

This spectrometer was operated at a constant pass energy of 41 eV (fixed analyzer transmission (FAT) mode). In order to scan the energy range of interest, the hemispheres are connected to a negative (retarding) high-voltage supply (Bertan series 362, USA) through two 24 V batteries which maintain the value of ΔV_p constant. The electrons are detected by means of the microchannel plate detector (MCP) operating in single-pulse counting mode, with a biasing voltage of ~2 keV (Bertan series 230, USA). The detection electronics used to process the signal are very similar to those employed for the Si detector: the electron current is collected by a custom-built preamplifier which provides positive voltage pulses (of the order of ~ 50 mV). These pulses are transferred to an amplifier (model 2020, Canberra, USA) and subsequently to a discriminator (constant fraction discriminator 584, Ortec, USA) which eliminates any electronic noise. The eventual resulting pulses are rectangular signals of 5 V amplitude which are collected by a data acquisition system (National Instruments USB-6259, USA) connected to a PC where a customized LabView software programme (National instruments, USA) counts and stores them for subsequent analysis. The energy resolution of this experimental system (full-width at half-maximum (FWHM)) was found to be lower than 0.9 eV (see Figure 6.6b). A scheme of the detector's electronics is shown in Figure 6.7.

The entire system, spectrometer and electronics, was calibrated for different incident energies ranging from 50 to 3750 eV (see Fig. 6.8 (a)). The electron energy loss distribution for incident energies of 500 eV in Ar is shown in Fig. 6.8 (b). Using this energy calibration, an average excitation peak is clearly discerned at around 11.5 eV and the ionization continuum arises above ~15.7 eV.

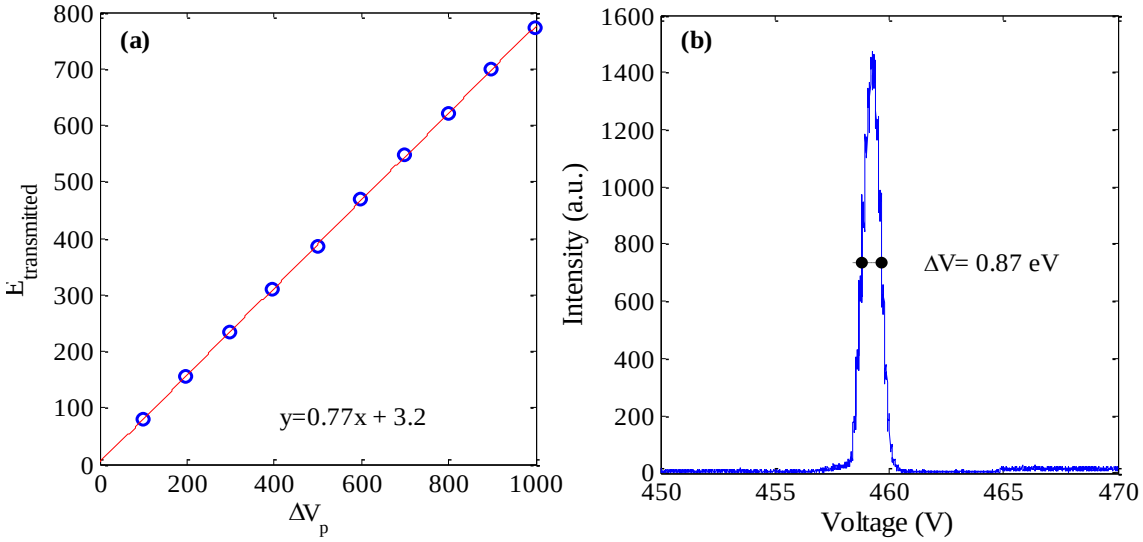

Figure 6.6: (a) Geometrical factor of the hemispherical electrostatic analyser and (b) energy resolution (FWHM) of the system.

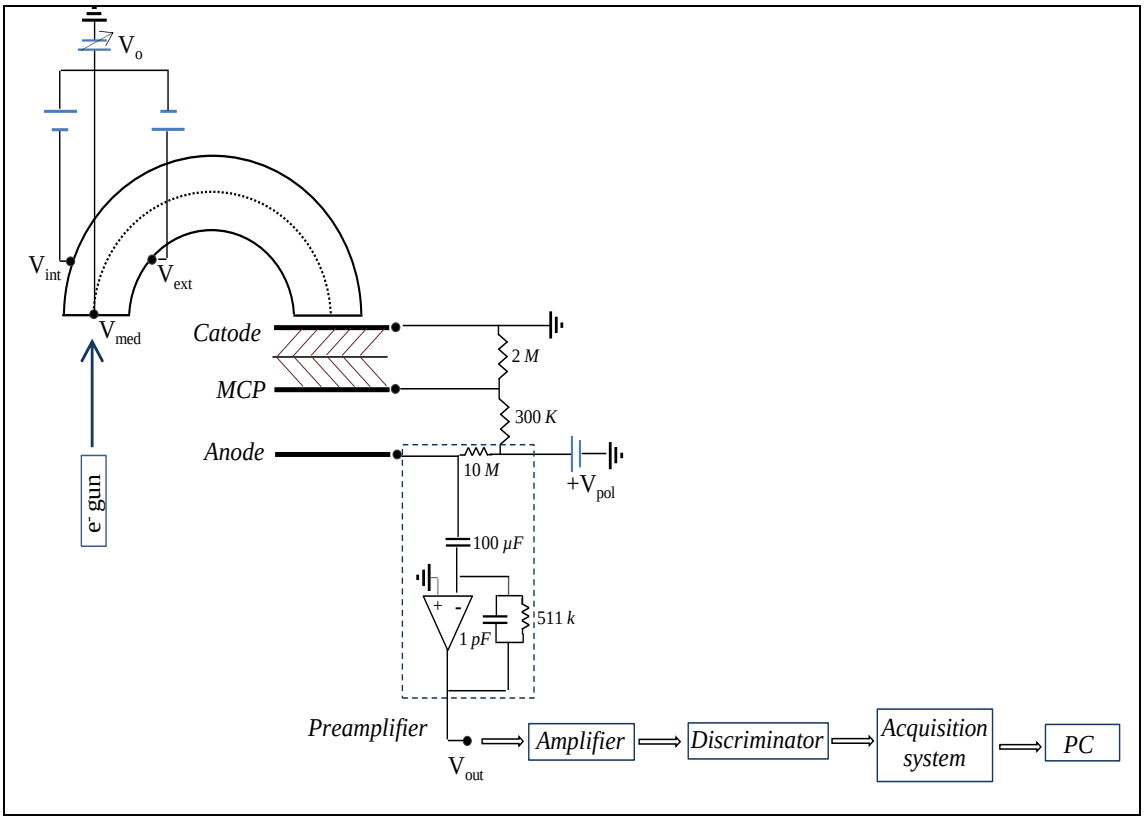

Figure 6.7: Electronic scheme of the hemispherical electrostatic analyser.

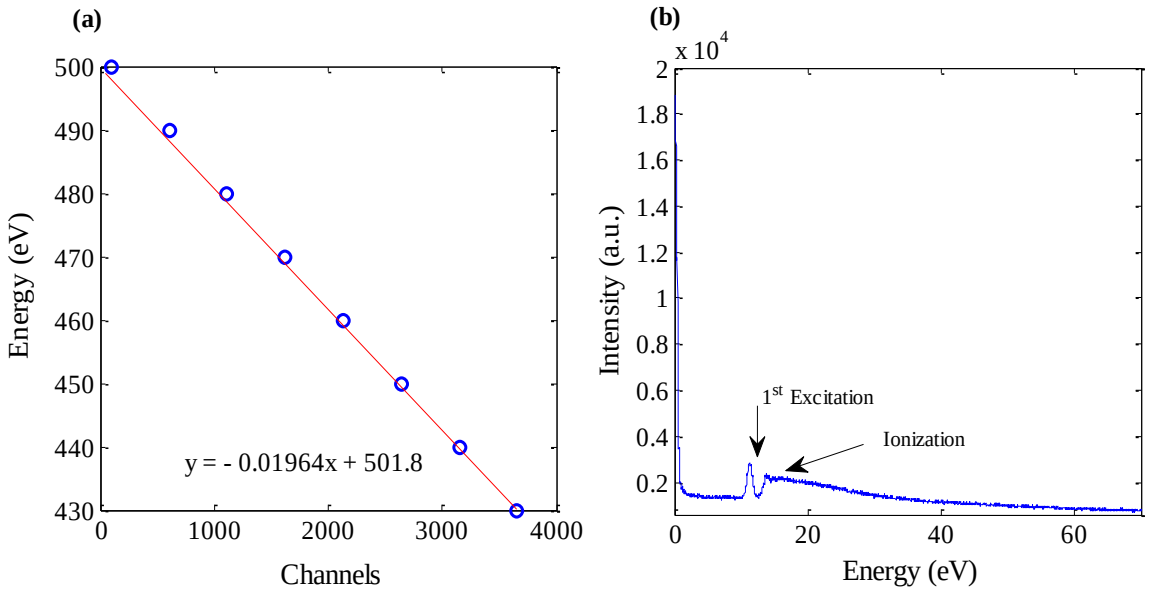

Figure 6.8: (a) Number of channels-energy calibration for the hemispherical electrostatic analyser for incident energies between 500 eV and 430 eV. (b) Electron energy loss distribution measured in Ar for 500 eV incident energy.

6.1.6 Time of Flight

When the primary radiation interacts with the condensed sample, not only secondary electrons are generated, but also positive and negative ions. Therefore, we have incorporated a time of flight mass spectrometer to analyse ion-induced fragmentation. A schematic draw and a photograph of this unit are shown in Figure 6.9. Briefly, by working in pulse mode and applying a negative voltage (0-900 eV) to the target substrate, the negative ions are accelerated towards the extractor electrode. Passing the grounded extractor (1mm wide) they are focussed with a three grid Einzel lens along the drift tube (60 cm long). Electrostatic quadrupolar lenses are used to control the direction of the beam reaching the detector (two-stage micro channel plates, MCP). Using an electronic system similar to that described above (see section 6.1.4 and 6.1.5), the length of the time of flight (TOF) between the extraction and the detection of ions is measured and stored to provide the ion intensity distributions as a function of their mass and charge properties. This spectrometer is currently being subjected to calibration procedures.

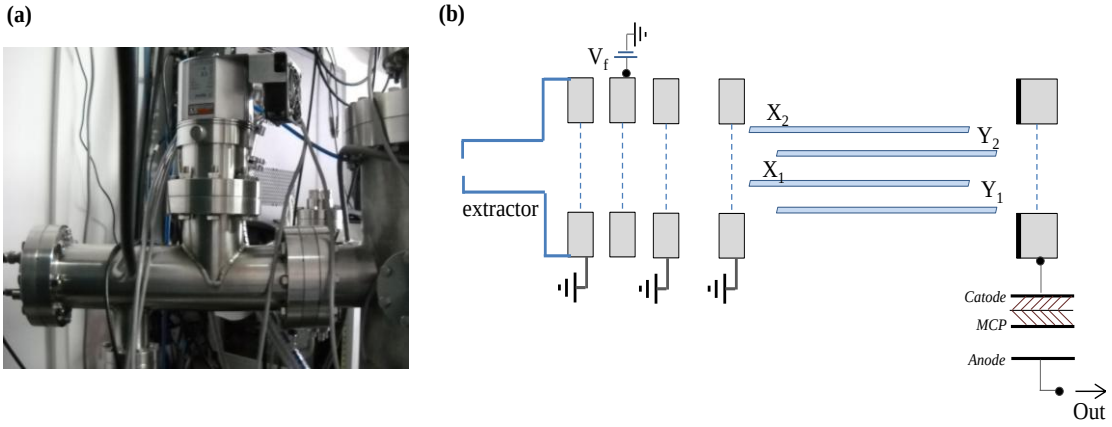

Figure 6.9: (a) Photograph and (b) schematic draw of the time of flight mass spectrometer.

6.2 Preliminary Experimental Tests

In order to validate our apparatus, some preliminary experimental tests were carried out. The chamber was carried to the European Synchrotron Radiation Facility (ESRF) in Grenoble, where gold films were irradiated with a synchrotron X-ray beam of 60 keV (0.1 % bandwidth) on the 1D17 beam line.

Firstly, the primary X-ray beam was characterized by means of a high-purity germanium (HPGe) X-ray detector (2 elements detector Canberra (50 $mm^2 \times$ 5mm and 80 $mm^2 \times$13 mm)) placed at 3 m from the source. After calibrating the detector with a ^{133}Ba radioactive sample, gold films of different thicknesses (100, 300 and 500 μm) were placed in the sample-holder and irradiated along their normal axis. The transmitted photons were collected by the germanium

detector, yielding a spectrum dominated by the photoelectric peak (with a resolution better than ~0.5%). For each sample, four independent energy spectra were recorded over different acquisition periods (t=20, 40, 60 and 120 s). The transmitted intensity was derived from the area of the relevant peaks that appeared in the spectra and was quantified using MAESTRO®-32 software. By comparing the intensity of the peaks transmitted through the different gold films with the unattenuated incident intensity (i.e., when no film was placed in the sample-holder), the linear attenuation coefficient (μ) can be derived according to the expression $I = I_o e^{-\mu t}$, where t is the sample thickness. As shown in Figure 6.10, the measured attenuation coefficient for 60 keV photons in gold is μ_{exp}=74 cm^{-1}.

Subsequently, the angular and energy distribution of the secondary electrons (SEs) emitted from the gold substrate were measured with the silicon detector, which was placed at different angles with respect to the incident beam (31°, 51°, 81°, 91°, 101° and 112°). Note that 60 keV X-ray photons interact with gold atoms mainly via photoelectric processes. This interaction causes the emission of energetic photoelectrons. Most of the photons' absorbed energy is transferred into kinetic energy of bound electrons ($E_{e^-} = E_\gamma - E_k$). From the stopping power and range tables for electrons available on the NIST website,[4] the range of 60 keV electrons in gold was found to be ~7μm. Hence, only electrons generated in films of such a thickness are ejected from the gold substrate. As an example, in Figure 6.11(a) we provide an energy spectrum of SEs emitted from the gold surface at 31º. Figure 6.11(b) presents the angular distribution of these secondary electrons, which shows that they are preferably scattered at 45° from the normal axis.

We simultaneously simulated this experiment with our LEPTS code so that comparisons could be made with the experimental output. The geometry and composition of the target, detectors and structural materials were introduced in the simulation with the help of the GAMOS tool (see Chapter 4). Photon interactions were treated with the GEANT4 code, which relies on the Evaluated Photon Data Library '97 Version for all input parameters.[5] Integral and differential electron-gold cross sections needed to simulate secondary electron interactions were calculated by using the IAM-SCAR procedure (see Chapter 2). For energies above 10 keV, as mentioned in Chapter 2, electron-target collisions can be treated within the Born-Bethe approximation. Integral elastic and inelastic cross sections were then derived from simple energy-dependent formulae at these energies.[6,7] Electron-energy loss distribution functions were given by a corrected form of the EEL spectra measured for xenon.

The simulated attenuation for 60 keV X-rays in gold was μ_{sim}=87 cm^{-1}, which is somewhat larger than the experimental value (see Figure 6.10). This discrepancy can be attributed to: (a) the input data used for the simulation, which corresponds to single-atom data; (b) photon

scattering at low angles which is interpreted by the detector as being unscattered; and (c) multiple scattering effects (the mean free path of 60 keV X-rays in gold is ~115 μm) which are not taken into account by the experimental analysis. Given these conditions, the agreement between the experiment and the simulation is regarded to be reasonably good (within ~15%). On the other hand, the simulation also provided the angular distribution of the secondary electrons emitted from the gold surface, which is in fairly good agreement with the experimental results, as can be appreciated in Figure 6.11(b).

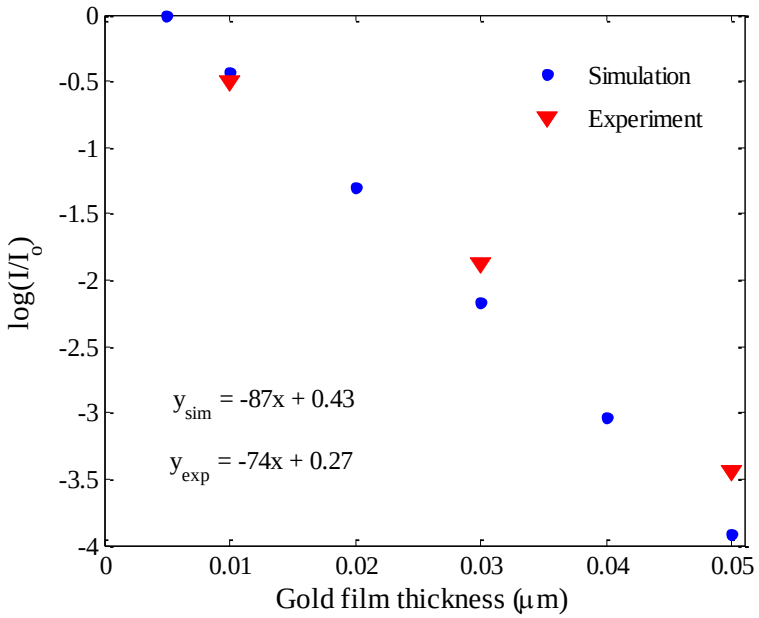

Figure 6.10: Attenuation of 60 keV X-rays beam passing through gold films.

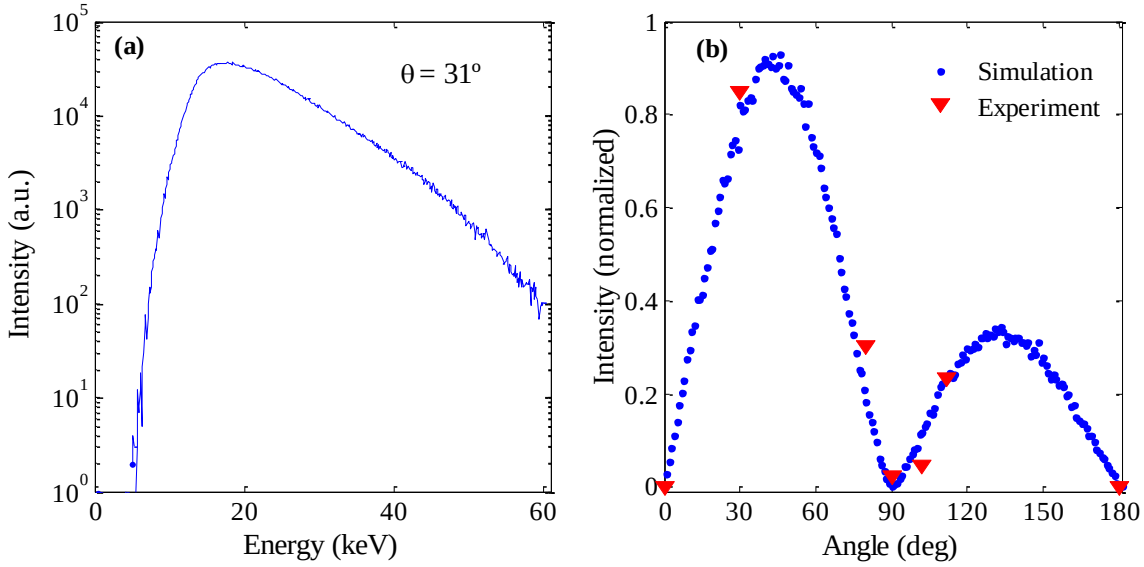

Figure 6.11: (a) Energy spectrum of secondary electrons emitted from the gold substrate at 31º. (b) Normalized angular distribution.

6.3. Summary

We have designed a versatile and portable experimental apparatus to irradiate condensed samples with different primary radiations. Some specific devices have been incorporated to permit low-energy secondary electron spectrometry (i.e. the sample holder and the hemispherical electrostatic analyser). Currently, the different elements of the experimental setup are calibrated (except the TOF detector) and well-adjusted to perform measurements over a broad energy and angular ranges.

The preliminary experimental tests indicate that our LEPTS simulation code provides an accurate representation of photon-matter interactions and a reliable characterization of the density of the target. Regarding electron interactions, current testing also showed that our simulation can provide a reasonably good description of the angular distribution of SE emitted from a gold substrate when subjected to X-ray radiation.

In summary, we have shown that the arrangement of the experimental setup is suited to conducting the experiments required in order to validate radiation interaction models in the condensed phase. The apparatus is almost ready to be transported to other experimental facilities to validate nano-scale radiation damage models for different projectiles: ions, positrons, etc.

Bibliography

[1] A. Muñoz, J. C. Oller, F. Blanco, J. D. Gorfinkiel, P. Limão-Vieira and G. García, *Phys. Rev. A* **76**, 052707 (2007).

[2] A. Muñoz, J. C. Oller, F. Blanco, J. D. Gorfinkiel, and G. García, *Chem. Phys. Lett.* **433**, 253 (2007).

[3] M. Rezaee, P. Cloutier, A.D. Bass, M. Michaud, D.J. Hunting and L. Sanche, *Phys. Rev. E*, **86**, 031913 (2012).

[4] M.J. Berger, J.S. Coursey, M.A. Zucker and J. Chang, NIST Standard Reference Database.

[5] D. Cullen, J. H. Hubbell, L. Kissel, The Evaluated Photon Data Library, ’97 Version, Technical Report UCRL-LR-50400 vol 6, Lawrence Livermore National Laboratory, Livermore, CA, 1997. Rev 5.

[6] G. García and F. Manero, *Phys. Rev. A* **57**, 1096 (1998).

[7] G. García and F. Blanco, *Phys.Rev. A* **62**, 044702 (2000)

Chapter 7

Conclusions

Within this thesis we have investigated electron and positron collisions with biologically relevant targets using both theoretical and experimental methods. From a theoretical point of view, electron-molecule scattering cross sections calculated for anthracene, hydrogen cyanide, pyrazine and pyrimidine, employing the IAM-SCAR method at high energies, and either the SA-SCE approach or R-matrix model at low energies, were found to agree well with other experimental or theoretical sources (with a numerical uncertainty of ~10%), within their respective energy region of applicability, i.e., above ~30 eV and below the ionization threshold, respectively. In the case of polar targets, we have seen that, within the IAM-SCAR methodology, more accurate elastic DCS are produced when the Dickinson correction [1] is applied for medium and large angles. Across the common overlap energies, our results showed that the IAM-SCAR model agrees slightly better with the R-matrix method (within ~10%) than with the SA-SCE approach (within ~10% at 10 eV increasing up to ~25% at 30 eV), being attributable to the omission of the absorption potential in the latter method. Finally, we have made complete sets of recommended integral elastic, inelastic and total cross sectional data available over a broad energy range: from 0.1 eV (0.01 meV in the case of anthracene) up to 10 keV, for the abovementioned representative targets. Previous scattering data for these molecules of biological interest was either non-existent or incomplete.

This combined procedure has been further employed to treat positron-molecule collisions. In particular, we have provided, for the first time, a computational investigation on positron

scattering with pyrimidine over a wide energy domain. Integral and differential cross sections were calculated using various models (within the R-matrix and IAM-SCAR methodology), which describe the polarization effects at different levels of sophistication. After verifying the agreement between the present calculated cross sections and previous experimental results, we can conclude that the R-matrix method (within the CC approximation) and the IAM-SCAR procedure (using the dipole plus quadrupole polarization (V_{d+p}) potential), provide the most reliable results, at low and high energies, respectively.

From the abovementioned computational studies it is concluded that the combination of the IAM-SCAR model with a low-energy scattering method, such as the R-matrix model or the SA-SCE approach, provides a valid and realistic approach to studying electron and positron scattering from both polar and non-polar molecular targets, over a very broad energy range. In fact, it constitutes a promising tool whenever one is aiming to get e^-/e^+ scattering data sets from multi-electron systems for radiation-interaction models (e.g. LEPTS), as it may facilitate the arduous task of compiling collisional reference data sets. Moreover, the low-energy methods provide information about resonances, which is one of the most significant routes to producing molecular damage. We would like also to point out that these scattering calculations represent an extremely helpful complement to experimental studies, since they provide information for energies and angles to which experiments do not have access. This is particularly true when dealing with polar targets, for which disconcerting disagreements were systematically encountered between experimental and theoretical integral CS. In this context, we have shown that by computing scattering cross sections under experimental conditions, i.e., emulating the technical restrictions of the experimental setup (such as the forward angular acceptance), we can provide a better interpretation of the experimental results and a more meaningful comparison between theory and experiment.

By combining appropriate data sets with the LEPTS Monte Carlo code, we can provide a molecular-level radiation interaction model capable of following the course of an incident particle and some of its products, interaction-by-interaction, from the keV region down to 1 eV. As an example, we have reported electron and positron tracks (with 15 keV incident energy) decelerating in water. Our results show that the analysis of quantities based solely on energy deposition to the medium cannot give a complete picture of the radiation effects induced in the media. By discriminating the different radiation interaction processes, LEPTS provides information not only on the energy imparted, but also about the frequency and spatial distribution of all the different collision events (provoked either by the primary particle or secondary electrons). In this sense, LEPTS introduces notable improvements in low-energy particle tracking compared to some other widely used programmes, because it considers the

occurrence of crucial scattering processes, such as DEA and Ps formation, which dramatically affect the fate of electrons and positrons, respectively, and hence the track-end structures.

From the experimental side, this work has been able to shed some light on the relative contribution of low-energy electrons (LEEs), compared to ionizing radiation, to the direct and indirect modes of damage induced in DNA. Analysis with LC-MS/MS revealed that, under identical conditions, LEEs (0-30 eV) are considerably more efficient (by a factor of ~1.8) than soft X-rays (1.5 keV) in generating radiation-induced products from thymidine, namely, base release, 5-HMdUrd, 5-FordUrd and 5,6-DHThd. Among the products analysed, thymine release turned out to be the predominant channel, which arises from N-glycosidic-bond cleavage involving a low-lying π^*-type resonance. A LEE-mediated mechanism for the formation of the oxidative products 5-HMdUrd and 5-FordUrd has been proposed, which involves the loss of hydride anions ($-H^-$) from the methyl-group via DEA of electrons with incident energy of ~10 eV. Moreover, yields of damage indicated that the loss of unaltered thymidine induced by both X-rays and LEEs are significantly (and equally) favoured in an oxygenated environment. An approximately 3-fold increase of the yield of free thymine, 5-HMdUrd and 5-FordUrd is attributed to the reaction of O_2 with initial carbon-centred thymidine radicals generated in the film during irradiation, and additionally, to the action of the reactive radicals and ions formed when ionizing radiation and LEEs interact with O_2. On the other hand, we have also reported in this work the first study on the indirect effect of LEEs with liquid water condensed on and within plasmid DNA. Interestingly, we found a dramatic increase in LEE-induced damage as hydration levels surpassed the second hydration layer and approached bulk-like conditions (G_{LEE} for the loss of SC increased from $G_{LEE}=412 \pm 107$ at 80% RH up to $G_{LEE}=1852 \pm 482$ at 100% RH, whereas G_X increased from $G_X=246 \pm 49$ at 80% RH up to $G_X=274 \pm 55$ at 100% RH). This contribution is partly due to water molecules in contact with DNA, but mostly due to highly reactive species created within the bulk-like water layer. The present experimental results indicate, therefore, that LEEs contribute considerably to indirect damage in DNA.

A new experimental apparatus was designed and constructed for the investigation of radiation damage in condensed biomolecular systems. The main advantage of this experimental system is its versatility - it allows the irradiation of biological samples with different primary beams (e.g., electrons, photons or ions). After having performed the pertinent general working tests (vacuum, mechanical and electronic systems, detectors, data acquisition systems), it has been shown that the arrangement of this experimental setup is suitable for performing the experiments required to validate radiation interaction models in the condensed phase. Currently,

the experimental apparatus is ready to perform spectroscopic measurements in research facilities.

At this point it should be mentioned that, in the course of the work that brought forth this thesis, some issues have arisen that will require resolving in future investigations. From a theoretical point of view, despite the fact we found fairly good agreement between the calculated positron-pyrimidine scattering cross sections and the available experimental measurements,[2] this level of accord was less than in the case of electron scattering. Hence, still more work is needed, in order to improve the accuracy of the calculations. As we have seen in Chapter 3, IAM-SCAR cross sections are quite sensitive to the description of the polarization effects and Ps formation. We believe that the inclusion of more multipole terms in the polarization potential would not bring about a significant improvement in the results, as it has been shown that the dipole plus quadrupole polarization potential (V_{d+p}) provides reasonably accurate results.[3,4] On the other hand, a more challenging problem is to improve on the quality of the representation of the Ps formation, for instance, by including a new effective potential in the imaginary term, which describes Ps formation by itself.

Concerning the track structure simulations, until now LEPTS have been applied to relatively simple molecules in the gas-phase, such as H_2O, ethylene, methane or THF, in the gas-phase. The next objective will be the application of LEPTS to the biomolecular targets investigated in this thesis, i.e., HCN, anthracene and the diazines, pyrimidine and pyrazine. Although we have reported in this work essential input parameters required by the simulation, i.e., integral and differential scattering cross sections, other indispensable data, such as electron energy loss spectra, is still lacking. Once all the required input parameters become available in the literature, we will include these results into the LEPTS code to simulate single particle trajectories in the said targets. In particular, owing to recent growing interest in the nucleobase analogues pyrimidine and pyrazine, the amount of reliable data is increasing quickly. Therefore, we expect to apply the simulation code to these targets in the near future. Given that pyrazine and pyrmidine are structural isomers, it will be interesting to compare the structures of the corresponding electron tracks; any differences being attributable to the strong dipole moment of pyrimidine. The following natural step will be to apply the interaction model to progressively more complex targets, for instance, molecular mixtures (e.g. a volume containing 80% of water molecules and 20% of another biomolecule, as a rough approximation of cells composition).

However, track structure simulations in liquid water remain a challenging problem due to the scarcity of elastic and inelastic cross sections in this medium. In this work (Chapter 4) we have adopted a gas-phase approximation, which is believed to be accurate above ~100 eV but introduces a significant uncertainty below that energy. Within this context, the next objective

will be correcting the gas-phase cross sections calculated with the IAM-SCAR model for condensed matter. As a first step towards this goal, electron and positron cross sections for different sizes of argon clusters have been reported recently.[5] In a similar way as we apply the SCAR procedure, some corrective factors, based exclusively on the geometry of the problem, can be introduced in order to calculate the effective cross section (σ_{eff}) of single atoms within the liquid.

Finally, one should note that although this simulation procedure describes most of the interaction processes mediated by the incident particles and the generated secondary electrons, it does not consider the damaging effects induced by other secondary species, such as charged or neutral radicals. Therefore, another major objective of molecular-level radiation interaction models is to consider the role of radicals and products generated from the environmental molecules surrounding DNA, such as H_2O and O_2. Currently, experiments to study induced fragmentation in biomolecules by electron transfer from negative ions being undertaken.[5,6] These results will serve to compile a new input interaction data base, which will ultimately be incorporated into the LEPTS code.

Bibliography

[1] A.S. Dickinson, *J. Phys. B* **10**, 967 (1977).

[2] P. Palihawadana, R. Boadle, L. Chiari, E.K. Anderson, J.R. Machacek, M.J. Brunger, S.J. Buckman and J.P. Sullivan, *Phys. Rev. A*, **88**, 012717 (2013).

[3] L. Chiari, A. Zecca, S. Girardi, E. Trainotti, G. García, F. Blanco, R. McEachran and M. Brunger, *J. Phys. B: At. Mol. Opt. Phys*. **45**, 215206 (2012).

[4] (a) R.P. McEachran, D.L. Morgan, A.G. Ryman and A.D. Stauffer, *J. Phys. B* **10**, 663 (1977); (b) R.P. McEachran, A.G. Ryman and A.D. Stauffer, *J. Phys. B: Atom. Molec. Phys.* **11**, 511 (1978).

[5] F. Blanco, A. Muñoz, D. Almeida, F. Ferreira da Silva, P. Limão-Vieira, M.C. Fuss, A.G. Sanz, and G. García, *Eur. Phys. Jour. D* **67**, 199 (2013).

[6] D. Almeida, F. Ferreira da Silva, G. García and P. Limão-Vieira, *Phys. Rev. Lett* **110**, 023201 (2013).

Capítulo 7

Conclusiones

A lo largo del presente trabajo se han investigado las colisiones de electrones y positrones con moléculas de interés biológico, usando métodos tanto experimentales como teóricos. En lo que a la teoría se refiere, se ha puesto de manifiesto que las secciones eficaces de dispersión electrón-molécula calculadas con el método IAM-SCAR, a altas energías, y con los modelos SA-SCE o R-matrix, a bajas energías, para los blancos antraceno, ácido cianhídrico, pirazina y pirimidina, coinciden con otras fuentes experimentales o teóricas, con una incertidumbre numérica de ~10%. Esto es particularmente cierto dentro de sus rangos de validez: por encima de 30 eV, y por debajo del nivel de ionización, respectivamente. En el caso de moléculas polares, dentro de la metodología de IAM-SCAR, se ha observado que la corrección de Dickinson[1] proporciona secciones eficaces diferenciales de dispersión elástica más precisas que la corrección de dipolo, originalmente aplicada en este método. Por otro lado, nuestros resultados también muestran que, en las energías dónde los diferentes modelos se solapan (~10-30 eV), el método IAM-SCAR se encuentra en mejor concordancia con el modelo R-matrix (~10%) que con el método SA-SCE (el acuerdo encontrado del ~10% a 10 eV aumenta hasta ~25% a 30 eV). Esta mayor discrepancia se atribuye a la omisión del término de absorción en el potencial modelo que utiliza el método SA-SCE. Como resultado de estos cálculos, se han facilitado tablas de datos recomendados de secciones eficaces integrales (elásticas, inelásticas y totales) de dispersión de electrones con las moléculas previamente citadas, para las cuales, los datos de probabilidad de interacción bien eran inexistentes o incompletos. Dichas tablas cubren un amplio rango de energías: desde 0.1 eV (0.01 meV en el caso de antraceno) hasta 10 keV.

Este procedimiento combinado ha sido empleado, a su vez, para estudiar la dispersión de positrones por moléculas. En particular, se ha proporcionado, por vez primera, un estudio computacional sobre las interacciones de positrones con el blanco molecular pirimidina, en un amplio rango de energías. Se han calculado secciones eficaces, integrales y diferenciales, usando varios modelos que describen los efectos de polarización con diferentes grados de sofisticación. Después de una comparación crítica entre los distintos modelos y otros resultados disponibles en la literatura, se concluye que el método de R-matrix, dentro de la aproximación CC, y el modelo IAM-SCAR, usando el potencial modelo de polarización que incluye los términos dipolo y cuadrúpolo (V_{d+p}), proporcionan los resultados más fiables, a bajas y altas energías, respectivamente.

Teniendo en cuenta los estudios computacionales arriba mencionados, se concluye que la combinación de nuestro modelo IAM-SCAR con métodos *ab-initio* de baja energía, cómo R-matrix o SA-SCE, constituye un procedimiento válido y realista para el estudio de la dispersión de electrones y positrones con sistemas moléculares, tanto polares como no polares, sobre un rango de energías muy amplio. De hecho, constituye una herramienta prometedora, de cara a la generación de conjuntos de datos de dispersión de e^-/e^+ por sistemas multi-electrónicos, para su uso en modelos de interacción (v.g. LEPTS). Puede también facilitar la ardua tarea de recopilación de extensas colecciones de datos de referencia. Además, los modelos de dispersión de baja energía permiten obtener información sobre las resonancias, que constituyen una de las principales vías de inducción de daño molecular. También queremos señalar que estos cálculos de dispersión constituyen un complemento extremadamente útil para las investigaciones experimentales, ya que proporcionan información sobre rangos de energía y ángulos donde los aparatos experimentales no pueden acceder. Esto es particularmente cierto en el caso de moléculas polares, para las cuales se han encontrado, sistemáticamente, importantes discrepancias entre las secciones eficaces integrales experimentales y teóricas. Dentro de este contexto, se ha demostrado que, calculando las secciones eficaces bajo las condiciones experimentales, es decir, emulando las restricciones técnicas (por ejemplo, el ángulo de aceptancia) del dispositivo experimental en cuestión, podemos interpretar los resultados experimentales con mayor precisión y desarrollar una comparación significativa entre teoría y experimentos.

Por otro lado, mediante la combinación de bases de datos de dispersión apropiadas con el código de Monte Carlo LEPTS, se ha proporcionado un modelo de interacción de radiación-materia a nivel molecular, el cual es capaz de seguir la historia de una partícula, y algunos de sus productos, desde su energía inicial (en el rango de los keV) hasta 1 eV. Este modelo ha sido aplicado para simular las trayectorias de positrones y electrones con 15 keV de energía inicial en agua líquida. Nuestros resultados muestran que un análisis basado únicamente en la energía

depositada en el medio, no puede proporcionar una descripción completa de los efectos de la radiación en dicho medio. Gracias a la discriminación de los diferentes procesos de interacción que pueden tener lugar, LEPTS es capaz de proporcionar información, no sólo de la energía impartida, sino también de la frecuencia y distribución espacial de todos los procesos de colisión (hayan sido provocados por las partículas primarias o los electrones secundarios). En este sentido, LEPTS introduce una mejora sustancial en el seguimiento de partículas a bajas energías, comparado con otros modelos disponibles comercialmente (v.g. PENELOPE o GEANT4). Uno de los principales motivos que nos lleva a hacer esta afirmación, es que LEPTS incluye ciertos procesos de interacción, como disociación por captura electrónica (DEA) o formación de positronio, que afectan determinantemente al destino final de los electrones y positrones, respectivamente, y por tanto, el perfil de sus trayectorias.

Desde el punto de vista experimental, este trabajo ha contribuido a clarificar la contribución de los electrones de baja energía (0-30 eV; LEEs), en comparación con la radiación ionizante, al daño directo e indirecto inducido en ADN. Se ha observado que ambos tipos de radiación producen un perfil de daño cualitativamente similar, aunque diferente en términos cuantitativos: bajo las mismas condiciones experimentales, los LEEs inducen un daño considerablemente mayor que los rayos X en ADN. Análisis de las muestras irradiadas con LC-MS/MS (espectrometría de líquidos con espectrómetro de masas tándem) ha revelado, que los LEEs son un factor ~1.8 más eficaces que los rayos X, a la hora de inducir daño en el nucleósido timidina, generando como productos: timina libre, 5-HMdUrd, 5-FordUrd y 5,6-DHThd. Entre los productos analizados, la base timina ha resultado ser el predominante, generado por la escisión del enlace N-glucosídico, en la que participa una resonancia de carácter π^*. Se ha propuesto un mecanismo, mediado por los LEEs, para la formación de los productos 5-HMdUrd y 5-FordUrd; este es desencadenado por la pérdida del anión hidruro del grupo metilo, mediante reacción DEA de electrones con energías incidentes de ~10 eV. La mayor tasa de eficacia en el daño inducido por LEEs, se mantiene cuando las muestras son irradiadas bajo un ambiente oxigenado. Nuestros resultados indicaron que, bajo tales circunstancias aeróbicas, el daño inducido en timidina aumenta considerablemente. En particular, se observó que la presencia de oxígeno triplica la tasa de generación de timina, 5-HMdUrd y 5-FordUrd. Esto se atribuye en primer lugar, a la reacción de O_2 con radicales de carbono centrados, que son producidos en las muestras durante la irradiación; y en segundo lugar, a la acción de los radicales e iones reactivos que son generados por la interacción de la radiación ionizante y los LEEs con O_2. Por otro lado, se ha estudiado la influencia que tiene el nivel de hidratación en el daño inducido por rayos X (1.5 keV) y electrones de baja energía en ADN. Es importante destacar que nuestros resultados mostraron un incremento dramático del daño inducido por los LEEs, conforme el nivel de hidratación de las muestras superaba la segunda capa de hidratación (80 %RH) y alcanzaba el

estado de solvatación (100 RH%). En particular, G_{LEE} para la pérdida de ADN superenrrollado aumentó de G_{LEE}=412 ± 107 a 80% RH hasta G_{LEE}=1852 ± 482 a 100% RH, mientras que G_X aumentó de G_X=246 ± 49 a 80% RH hasta G_X=274 ± 55 a 100% RH. Esta contribución se origina en parte por las moléculas de agua en contacto con el ADN (primera y segunda capa de hidratación), pero en mayor medida por las especies altamente reactivas generadas en la capa libre de agua (100% RH). Por lo tanto, nuestros resultados muestran que los LEEs contribuyen considerablemente al daño indirecto inducido en ADN.

Un nuevo sistema experimental ha sido diseñado y construido de cara al estudio del daño inducido por radiación en sistemas biomoleculares condensados. La principal ventaja de este dispositivo es su versatilidad, ya que permite la irradiación de muestras biológicas con diferentes haces primarios (v.g. electrones, fotones e iones). Después de haberse llevado a cabo las pruebas oportunas de funcionamiento general (vacío, sistemas mecánicos y electrónicos, detectores, programas de control y toma de datos), se ha concluido que el diseño actual de la cámara de colisión es apropiado para realizar los experimentos pertinentes, que permitirán la validación de los modelos de interacción, cómo LEPTS, en fase condensada. Actualmente, el sistema experimental está validado para realizar medidas espectrométricas en grandes instalaciones.

Llegados a este punto, se debe señalar que, en el curso del trabajo que ha dado lugar a la presente tesis, han surgido algunos asuntos que deberán ser afrontados en futuras investigaciones. Desde el punto de vista teórico, a pesar de que los datos de dispersión de positrones con pirimidina, obtenidos con nuestros modelos, muestran una coincidencia bastante alta con los datos experimentales,[2] el nivel de concordancia es ligeramente inferior que en el caso de dispersión de electrones. Por lo tanto, se hace patente la necesidad de trabajar más de cara a la mejora del comportamiento de nuestros cálculos. Cómo se ha visto en el Capítulo 3, las secciones eficaces obtenidas mediante el método IAM-SCAR, son bastante sensibles a la descripción de los efectos de polarización y la formación de positronio. Desde nuestro punto de vista, la inclusión de más términos de multipolo en el potencial de polarización no llevaría aparejada una mejora significativa en los resultados, ya que, cómo se ha visto, los proporcionados usando el potencial de polarización V_{d+p} son suficientemente razonables.[3,4] Por otro lado, uno de los principales retos es mejorar la calidad de la representación de la formación de positronio, por ejemplo, mediante la inclusión de un nuevo potencial efectivo en el término imaginario, que lo describa por sí mismo.

En cuanto a la simulación de Monte Carlo de trayectorias de partículas, hasta ahora, LEPTS ha sido aplicada a moléculas relativamente sencillas: agua, etileno, metano y THF, en fase gaseosa. El próximo objetivo será aplicar LEPTS a las moléculas estudiadas en esta tesis, a

saber, ácido cianhídrico, antraceno y las diazinas, primidina y pirazina. Aunque en este trabajo se han proporcionado datos de entrada imprescindibles para la simulación (como son las bases de datos de secciones eficaces integrales y diferenciales), todavía faltarían otros datos de entrada indispensables, cómo los espectros de pérdida de energía. Tan pronto como estos últimos datos estén disponibles en la literatura, se incorporarán en nuestro código para simular las trayectorias de partículas en los blancos previamente citados. En particular, debido al creciente interés por los análogos de las bases nitrógenadas, pirimidina y pirazina, la cantidad de datos fiables para estos blancos moleculares es cada vez mayor. Así pues, esperamos poder aplicar nuestro modelo a estos blancos moleculares próximamente. Dado que las moléculas pirimidina y pirazina son isómeros estructurales, será interesante comparar los perfiles de las trayectorias generadas para ambas moléculas, ya que cualquier diferencia en las mismas puede ser atribuida esencialmente al fuerte momento dipolar permanente de la molécula pirimidina. Como evolución lógica, el siguiente paso será aplicar la simulación a blancos progresivamente más complejos, cómo por ejemplo, mezclas moleculares (v.g. un volumen conteniendo 80% de moléculas de agua y 20% de otra biomolécula, cómo una burda aproximación a la composición celular).

Por otro lado, la simulación de trayectorias de partículas en agua líquida continúa suponiendo un reto, debido principalmente a la escasez de datos de dispersión en este medio. En el presente trabajo (Capítulo 4), se han empleado datos obtenidos (supongo que te refieres a obtenidos, si no, son los datos los que están en fase gaseosa) en fase gaseosa a modo de aproximación, lo que es considerado fiable para energías incidentes por encima de ~100 eV. Sin embargo esta aproximación, a su vez introduce una incertidumbre relevante a energías por debajo de dicho umbral. Dentro de este contexto, el siguiente objetivo sería la corrección de los datos de dispersión en fase gaseosa calculados con IAM-SCAR para fase condensada. Como primer paso hacia esta meta, secciones eficaces de dispersión de electrones con clústers de argón han sido facilitados recientemente. De la misma forma que aplicamos el procedimiento de SCAR, factores de corrección basados exclusivamente en consideraciones geométricas pueden ser introducidos, con el fin de calcular secciones eficaces efectivas (σ_{eff}) de átomos simples dentro de un líquido.

Finalmente, debemos señalar que, aunque nuestra simulación describe la mayoría de los procesos de interacción en los que se ven involucradas las partículas primarias y los electrones secundarios generados, no considera los daños inducidos por otras especies secundarias, como los radicales neutros o positiva/negativamente cargados. Por lo tanto, otro objetivo primordial de los modelos de interacción a nivel molecular, será considerar el papel que juegan los radicales y demás productos generados a partir de las moléculas que rodean el ADN, como H_2O y O_2. Actualmente, la fragmentación de biomoléculas mediante transferencia electrónica desde iones negativos se está estudiando experimentalmente.[5,6] Estos resultados servirán para recopilar

una nueva base de datos de interacción, que finalmente se incorporará al programa de simulación LEPTS.

Bibliografía

[1] A.S. Dickinson, *J. Phys. B* **10**, 967 (1977).

[2] P. Palihawadana, R. Boadle, L. Chiari, E.K. Anderson, J.R. Machacek, M.J. Brunger, S.J. Buckman and J.P. Sullivan, *Phys. Rev. A*, **88**, 012717 (2013).

[3] L. Chiari, A. Zecca, S. Girardi, E. Trainotti, G. García, F. Blanco, R. McEachran and M. Brunger, *J. Phys. B: At. Mol. Opt. Phys*. **45**, 215206 (2012).

[4] (a) R.P. McEachran, D.L. Morgan, A.G. Ryman and A.D. Stauffer, *J. Phys. B* **10**, 663 (1977); (b) R.P. McEachran, A.G. Ryman and A.D. Stauffer, *J. Phys. B: Atom. Molec. Phys.* **11**, 511 (1978).

[5] F. Blanco, A. Muñoz, D. Almeida, F. Ferreira da Silva, P. Limão-Vieira, M.C. Fuss, A.G. Sanz, and G. García, *Eur. Phys. Jour. D* **67**, 199 (2013).

[6] D. Almeida, F. Ferreira da Silva, G. García and P. Limão-Vieira, *Phys. Rev. Lett* **110**, 023201 (2013).

List of Figures

1.1 Structure of DNA molecule 5

3.1 Equilibrium geometrical configuration of anthracene molecule 45

3.2 Convergence tests of the partial wave expansion and the size of the physical box for the electron-anthracene scattering problem calculated with the ePOLYSCAT code 46

3.3 Partial elastic cross sections for electron scattering from anthracene for the contributing symmetries A_g, B_{1g}, B_{2g}, B_{3g}, A_u, B_{1u}, B_{2u} and B_{3u}, computed with the ePOLYSCAT code 47

3.4 Eigenphase sums together with their first derivatives for the scattering symmetries of anthracene computed with the ePOLYSCAT code 48

3.5 Wavefunctions for the resonant electron in anthracene associated with the metastable anions found at energies below ~5 eV and the corresponding spatial maps of the virtual molecular orbitals, calculated with the ePOLYSCAT code 50

3.6 (Left panel) Elastic DCS for electron-anthracene collisions down to 10^{-6} eV of incident energy and (right panel) integral elastic cross sections in the totally symmetric IR *A*1g, together with the corresponding eigenphase sum, computed with the ePOLYSCAT code 51

3.7 Backward integral scattering cross sections versus total elastic cross sections computed with the ePOLYSCAT code and comparison to experimental data . . . 52

3.8 Elastic DCS for electron scattering from anthracene at some incident energies computed with the ePOLYSCAT code and the IAM-SCAR model 54

3.9 Comparison of the present elastic DCS for electron scattering from anthracene at 1 keV incident energy obtained with IAM-SCAR to previous experimental data . . 54

3.10 Elastic DCS for electron scattering from anthracene computed with the IAM-SCAR method and comparison to experimental data for benzene 55

3.11 Integral elastic cross sections for electron scattering from anthracene computed with the ePOLYSCAT code and with the IAM-SCAR method 55

3.12 Integral inelastic and total cross sections for electron scattering from anthracene computed with the ePOLYSCAT code and the IAM-SCAR method 57

3.13 Equilibrium geometrical configuration of pyrazine molecule 59

3.14 Elastic DCS for electron scattering from anthracene computed with the IAM-SCAR method at some selected energies and comparison to other experimental and theoretical results 61

3.15 Integral elastic cross sections for electron scattering from pyrazine computed with the IAM-SCAR method and comparison to other experimental and theoretical results 62

3.16 Integral inelastic cross section for electron scattering from pyrazine computed with IAM-SCAR method and comparison to the R-matrix results 64

3.17 TCS for electron scattering from pyrazine 64

3.18 Equilibrium geometrical configuration of HCN molecule 68

3.19 Convergence tests of the partial wave expansion and the size of the physical box for the electron-anthracene scattering problem calculated with the ePOLYSCAT code 69

3.20 Partial elastic cross sections for electron scattering from HCN for the contributing symmetries Π, Σ, Δ and Φ, calculated with the ePOLYSCAT code 70

3.21 Eigenphase sums for the symmetries of HCN in which we found a maximum in the corresponding cross sections calculated with the ePOLYSCAT code 70

3.22 Computed scattering wavefunction (right side) and the corresponding virtual orbital wavefunction (left side) for the $^2\Pi$ and $^2\Sigma$ resonant states of HCN, calculated with the ePOLYSCAT code 71

3.23 Computed variations in the resonant features (E_r and Γ_r) of the π^* resonance as function of both C-H and C≡N stretching 72

3.24 Spatial resonant wavefunctions (real part) for the π^* resonance as function of the stretching of both C-H and C≡N bonds 73

3.25 Computed real part of the potential energy surface (PES) for the $^2\Pi$ (N+1)-electron state upon C-H and C≡N stretching 73

3.26 Computed variations in the resonant features (E_r and Γ_r) of the σ^* resonance as function of both C-H and C≡N stretching 74

3.27 Spatial resonant wavefunctions (real part) for the σ^* resonance as function of the stretching of both C-H and C≡N bonds 75

3.28 Computed real part of the PES for the $^2\Sigma$ (N+1)-electron resonant state as function of the stretching of both C-H and C≡N bonds 75

3.29 Computed variations in the resonant features (E_r and Γ_r) of the π^* resonance as the molecule is bent from linearity up to θ=60º and spatial resonant wavefunction (real part) at θ=60º for the A' resonant state 76

3.30 Integral elastic cross section for electron scattering from HCN computed with the ePOLYSCAT code and the IAM-SCAR method, and comparison to other experimental and theoretical results 78

3.31 Elastic CS values for HCN integrated over a restricted angular range 78

3.32 Elastic DCS for electron scattering from HCN computed with the ePOLYSCAT−POLYDCS procedure and the IAM-SCAR+rotations model at some incident energies, and comparison to other experimental and theoretical results . . 79

3.33 Integral inelastic and total cross sections for electron scattering from HCN computed with the ePOLYSCAT−POLYDCS procedure and the IAM-SCAR+rotations model, and comparison to other experimental and theoretical results 80

3.34 Equilibrium geometrical configuration of pyrimidine molecule 83

3.35 Partial elastic cross sections for the scattering symmetries of pyrimidine calculated with the R-matrix method at the SEP level including different number of virtual orbitals 84

3.36 Partial elastic cross sections for the scattering symmetries of pyrimidine calculated with the R-matrix method at the CC level 86

3.37 Summed elastic cross sections for electron scattering from pyrimidine calculated with the R-matrix method at the SEP and Close-Coupling level 86

3.38 Elastic DCS for electron scattering from pyrimidine calculated with the IAM-SCAR+rotations model at some incident energies, and comparison to other experimental and theoretical results 88

3.39 Integral elastic cross section for electron scattering from pyrimidine computed with the IAM-SCAR method, and comparison to other experimental and theoretical results 89

3.40 Electronically inelastic cross sections for electron scattering from pyrimidine computed with the IAM-SCAR method, and comparison to other experimental and theoretical results 90

3.41 Total cross sections for electron scattering from pyrimidine computed with the IAM-SCAR+rotations procedure, and comparison to other experimental and theoretical results 91

3.42 Comparison of the calculated DCS for electron scattering from anthracene, pyrazine and pyrimidine 94

3.43 Comparison of the calculated integral elastic CS for electron scattering from anthracene, pyrazine and pyrimidine 95

3.44 Comparison of the calculated integral TCS for electron scattering from anthracene, pyrazine and pyrimidine 95

3.45 Partial elastic cross sections for positron scattering from pyrimidine calculated with R-matrix at the Static level 97

3.46 Convergence tests for the positron-pyrimidine scattering problem calculated with the R-matrix model at the SEP level 98

3.47 Partial elastic cross sections for positron scattering from pyrimidine calculated with R-matrix at the CC level 99

3.48 Integral elastic cross sections for positron scattering from pyrimidine computed with the R-matrix method and the IAM-SCAR model 102

3.49 Integral elastic cross sections, dipole corrected, for positron scattering from pyrimidine computed with the R-matrix method and the IAM-SCAR model, and comparison to other experimental results 102

3.50 Elastic DCS, dipole corrected, for positron scattering from pyrimidine calculated with the IAM-SCAR model and the R-matrix method at some incident energies, and comparison to other experimental results 103

3.51 Inelastic integral CSs for positron scattering from pyrimidine computed with the R-Matrix approach and the IAM-SCAR method, and comparison to other experimental results 105

3.52 Total cross sections, dipole corrected, for positron scattering from pyrimidine computed with the R-matrix method and the IAM-SCAR model, and comparison to other experimental results 106

4.1 Integral cross section values for electron scattering from vapour water employed for the simulation 123

4.2 Integral cross section values for positron scattering from vapour water employed for the present simulation 124

4.3 Flow diagram of a single track simulation with the LEPTS code 126

4.4 Trajectories of single electrons with an initial energy of 15 keV traversing water until complete thermalization 127

4.5 Trajectories of single positrons with an initial energy of 15 keV traversing water until complete thermalization 129

5.1 Equilibrium geometrical configuration of thymidine 136

5.2 Photograph of the HPLC-UV system 138

5.3 HPLC analysis of dThd samples lyophilized on a tantalum film 138

5.4 HPLC-UV analysis of thick and thin dThd samples irradiated during 30 minutes under UHV 140

5.5 Exposure-response curves for loss of thymidine and appearance of free thymine, in thin and thick films of dThd deposited in tantalum substrates and irradiated with 10 keV electrons under UHV 141

5.6 Schematic view of the main steps of the experimental procedure followed to measure the effect of oxygen on radiation-induced damage 144

5.7 Schematic view and photograph of the experimental apparatus employed to irradiate biological samples under standard ambient temperature and pressure (SATP) . . . 146

5.8 LC-MS/MS chromatogram of dThd samples deposited on tantalum substrates and exposed to X-rays during 9 hours, under an N_2 and O_2 atmosphere 150

5.9 Exposure-response curves for the loss of unaltered thymidine in thin films deposited on tantalum and glass substrates and irradiated with 1.5 keV X-rays under N_2 and O_2 at SATP 151

5.10 Exposure-response curves for the appearance of: (a) free thymine, (b) 5-FordUrd, (c) 5-HMdUrd and (d) 5,6-dThd in thin films of thymidine deposited on tantalum and glass substrates and irradiated with 1.5 keV X-rays under N_2 and O_2 at SATP . . . 152

5.11 Scheme of the mechanisms of damage induced by X-rays, through one-electron ionization reactions, and LEEs, through DEA channel, on the nucleoside thymidine . . 156

5.12 Scheme of the LEE-mediated pathways of damage for thymidine under a N_2 and O_2 atmosphere 160

5.13 Scheme of the LEE-mediated oxidation pathways for thymidine leading to the formation of 5-HMdUrd and 5-FordUrd 163

5.14 Scheme of the possible mechanisms of formation of 5,6-dihydrothymidine . . . 164

5.15 Schematic view of the main steps of the experimental procedure followed to measure the effect of hydration level on radiation-induced damage 166

5.16 Example of an agarose gel electrophoresis analysis for plasmid DNA samples . . 170

5.17 Exposure-response curves for loss of SC form, and formation of SSBs and DSBs, in plasmid DNA films deposited on tantalum and glass substrates and irradiated by 1.5 keV X-rays under 20, 50, 80 and 100 % relative hydration level under N_2 atmosphere at STAP 172

6.1 Schematic view and photograph of the experimental setup designed and constructed for the irradiation of condensed biological samples 187

6.2 Schematic draw and photograph of the home-made sample-holder 188

6.3 Schematic draw and photograph of the home-made electron gun 189

6.4 Schematic draw and photograph of the home-made silicon detector assembly and liquid nitrogen dewar 190

6.5 (a) Calibration voltage-to-channels of the ADC/MCA and (b) Cs spectrum obtained with the silicon detector 191

6.6 (a) Geometrical factor of the hemispherical electrostatic analyser and (b) energy resolution (FWHM) of the system 192

6.7 Electronic scheme of the hemispherical electrostatic analyser 193

6.8 Electron energy loss distribution measured in Ar for 500 eV incident energy . . . 193

6.9 Schematic draw and photograph of the time of flight mass spectrometer 194

6.10 Attenuation curve of 60 keV X-rays beam passing through gold films of various thicknesses 196

6.11 (a) Energy spectrum of secondary electrons emitted from a gold substrate at 31º, upon 60 keV X-rays irradiation. (b) Normalized angular distribution of secondary electrons emitted from a gold substrate upon 60 keV X-rays irradiation 196

List of Tables

3.1 Computed resonant parameters for the anthracene molecule 48

3.2 Computed scattering length for scattering in the A_{1g} IR 52

3.3 Recommended integral elastic, electronically inelastic and total cross sections for electron scattering from anthracene in the energy range from 10^{-5} to 10000 eV . . . 58

3.4 Recommended elastic, electronically inelastic and total integral cross sections for electron scattering from pyrazine in the energy range from 0.1 to 10000 eV 65

3.5 Dipole moment of various biomolecules 66

3.6 Computed geometrical properties and dipole moment of HCN, obtained with the ePOLYSCAT code using different atomic basis sets and comparison with the experimental values 68

3.7 ePOLYSCAT computed resonant parameters for HCN 71

3.8 Recommended elastic, electronically inelastic and total integral cross sections for electron scattering from HCN in the energy range from 0.1 to 10000 eV 81

3.9 Resonance parameters (eV) and polarizability values ($Å^3$) computed for the different SEP and CC models for pyrimidine 87

3.10 Recommended integral cross sections for electron scattering from pyrimidine in the energy range from 0.1 to 10000 eV 92

3.11 Details of the optimization tests performed for the positron-pyrimidine scattering study 96

3.12 Elastic cross sections for positron scattering from pyrimidine computed with the R-matrix approach at the SP and CC levels 106

3.13 Integral cross sections for positron scattering from pyrimidine in the energy range 1-10000 eV, calculated with the IAM-SCAR approach 107

4.1 Information provided by the LEPTS model for 15 keV electrons in water, both for the whole irradiated volume and a selected nano-volume 128

4.2 Information provided by the LEPTS model for 15 keV positrons in water, both for the whole irradiated volume and a selected nano-volume 129

5.1 Percentage yields per 10^{16} electrons/cm^2 for the formation of free thymine for thick and thin samples of thymidine, deposited in tantalum substrates and irradiated with 10 keV electrons under UHV 141

5.2 LC-MS/MS retention times and fragmentation transitions for the radiation-products observed in dThd samples irradiated with 1.5 keV photons 148

5.3 Percentage yields per 10^{14} photons/cm^2 and *G* values (in nmol/J) for the formation of base release, 5-FordUrd, 5-HMdUrd and 5,6 DHThd, in dThd samples irradiated under N_2 and O_2 at SATP 153

5.4 Percentage yield per 10^{12} photons.cm^{-2} and *G* values (in nmol/J) for the loss of SC and formation of SSBs and DSBs in films of plasmid DNA irradiated under various hydration level (RH %) 173

List of Publications

[1] A.G. Sanz, F. Sebastianelli and F.A. Gianturco, Following resonant compound states after electron attachment: A quantum modelling of the dynamical evolution in molecular anions, in: G.García and M.C. Fuss (Ed.), *Radiation Damage in Biomolecular systems*, Springer, Heidelberg, 2012.

[2] M.C. Fuss, A.G. Sanz, A.Muñoz, F. Blanco, M. Téllez, C. Huerga and G. García, LEPTS—a Radiation-Matter Interaction Model at the Molecular Level and its Use in Biomedical Applications, in: A. N. Laskovski (Ed.), Biomedical Engineering, Trends in Electronics, Communications and Software, InTech, Rijeka, Croatia, 2011.

[3] A.G. Sanz, M.C. Fuss, A. Muñoz, F. Blanco, P. Limão-Vieira, M.J. Brunger, S.J. Buckman and G. García, Modelling low energy electron and positron tracks for biomedical applications, *International Journal of Radiation Biology* 88, 71 (2012).

[4] M.C. Fuss, R. Colmenares, A.G. Sanz, A. Muñoz, J.C. Oller, F. Blanco, T.P.T. Do, M.J. Brunger, D. Almeida, P. Limão-Vieira and G. García, Electron interactions with tetrahydrofuran, *Journal of Physics: Conference Series* 373, 012010 (2012).

[5] A.G. Sanz, M.C. Fuss, F. Blanco, F. Sebastinelli, F.A. Gianturco and G. García, Electron scattering cross sections from HCN over a broad energy range (0.1-10 000 eV): Influence of the permanent dipole moment on the scattering process, *The Journal of Chemical Physics* 137, 124103 (2012).

[6] M.C. Fuss, A.G. Sanz, A. Muñoz, T.P.T. Do, K. Nixon, M.J. Brunger, M.J. Hubin-Franskin, J.C. Oller, F. Blanco and G. García, Interaction model for electron scattering from ethylene in the energy range 1–10 000 eV, *Chemical Physics Letters* 560, 22 (2013).

[7] A.G. Sanz, F. Carelli, F. Sebastianelli, F.A. Gianturco and G. García, Dynamics of formation of anthracene anions in molecular clouds and protoplanetary atmospheres *New J. Phys.* **15,** 013018 (2013).

[8] A.G. Sanz, M.C. Fuss, F. Blanco, Z. Mašín, J.D. Gorfinkiel, F. Carelli, F. Sebastinelli, F. Gianturco and G. García, Electron scattering cross section calculations for polar molecules over a broad energy range, *Applied Radiation and Isotopes* 83, 57 (2014).

[9] M.C. Fuss, A.G. Sanz, A. Muñoz, F. Blanco, M.J. Brunger, S.J. Buckman, P. Limão-Vieira and G. García, Current prospects on Low Energy Particle Track Simulation for biomedical applications, *Applied Radiation and Isotopes* 83, 159 (2014).

[10] A.G. Sanz, M.C. Fuss, F. Blanco, F. Carelli, F. Sebastinelli, F. Gianturco and G. García, Electron scattering cross sections from anthracene over a broad energy range (0.00001-10 000 eV), *Applied Radiation and Isotopes* 83, 68 (2014).

[11] R. Colmenares, A.G. Sanz, M.C. Fuss, F. Blanco and G. García, Stopping power for electrons in pyrimidine in the energy range 20-3000 eV, *Applied Radiation and Isotopes* 83, 91 (2014).

[12] M.C. Fuss, A.G. Sanz, F. Blanco, J.C.Oller, P. Limão-Vieira, M.J. Brunger and G. García, Total electron scattering cross sections from pyrimidine as measured using a magnetically confined experimental system, *Physical Review A* 88, 042702 (2013).

[13] A.G. Sanz, M.C. Fuss, F. Blanco, Z. Mašín, J.D. Gorfinkiel, R.P. McEachran, M.J. Brunger and G. García, Cross-section calculations for positron scattering from pyrimidine over an energy range from 0.1 to 10000 eV, *Physical Review A* 88, 062704 (2013).

[14] A.G. Sanz, M.C. Fuss, F. Blanco, J.D. Gorfinkiel, D. Almeida, F. Ferreira da Silva, P. Limão-Vieira, M.J. Brunger and G. García, An investigation into electron scattering from pyrazine at intermediate and high energies, *The Journal of Chemical Physics* 144, 128 (2013).

[15] F. Blanco, A. Muñoz, D. Almeida, F. Ferreira da Silva, P. Limão-Vieira, M.C. Fuss, A.G. Sanz and G. García, Modelling low energy electron and positron tracks in biologically relevant media, *The European Physical Journal D* 67, 199 (2013).

[16] E. Alizadeh, A.G. Sanz, G. García, and L. Sanche, Radiation Damage to DNA: The Indirect Effect of Low-Energy Electrons, The Journal of Physical Chemistry Letters 4, 820 (2013)

[17] E. Alizadeh,[†] A.G. Sanz,[†] G.S. Madugundu, G. García, J.R. Wagner and L. Sanche, Thymidine Decomposition Induced by Low-Energy Electrons and Soft X-rays under N_2 and O_2 Atmospheres, Radiation Research, *Radiation Research* (accepted for publication; [†] these authors contributed equally to this work).